



Searches for supersymmetry in events with three leptons at the ATLAS Detector

Stewart Martin-Haugh

Declaration

I hereby declare that this thesis has not been and will not be submitted in whole or in part to another University for the award of any other degree.

Signature:

Stewart Martin-Haugh

UNIVERSITY OF SUSSEX

STEWART MARTIN-HAUGH, DOCTOR OF PHILOSOPHY

SUPERSYMMETRY SEARCHES IN TRILEPTON EVENTS WITH THE ATLAS DETECTORSUMMARY

This thesis presents searches for supersymmetry in $\sqrt{s} = 7$ TeV and 8 TeV proton-proton collisions at the LHC using data collected by the ATLAS detector in 2011 and 2012. Events with exactly three electrons or muons and missing transverse energy were selected, since these can be a striking signature of supersymmetry with low Standard Model background. Additional kinematic criteria were investigated and applied in order to increase the sensitivity to supersymmetric signals. Standard Model backgrounds were estimated by a combination of Monte Carlo simulations and data-driven techniques. The agreement between data and background predictions was validated before analysing data in the signal regions. No significant excess was recorded in any of the analyses performed: the results were therefore interpreted as lower bounds on the masses of supersymmetric particles in a variety of different model scenarios.

Acknowledgements

I would like to acknowledge help and support (technical and moral) from many people, in many forms since 2009. I would not have been able to complete this work without my supervisors, Antonella De Santo and Fabrizio Salvatore. I always enjoyed working with Anthony Rose and learnt a lot from him, as well as the other Sussex ATLAS students: Nicky Santoyo, Ed Leming, Zara Grout and Yusufu Shehu. Tina Potter was always there to help with easy and difficult questions. Valeria Bartsch and Emyr James both helped me with various tasks. It was a pleasure to work in the ATLAS multilepton SUSY group: Sam King, Steve Farrell, Basil Schneider, Lukas Marti, Tobias Kruker, Sigve Haug, Anadi Canepa and Zoltan Gecse all deserve special mention. I learnt a great deal from the UK students at CERN, and particularly my neighbours and pseudo-neighbours from *Rue de l'Athenée*: Will Buttinger, Caterina Doglioni, Nick Edwards, Jack Goddard, Robert King, Adrian Lewis, Sarah Livermore, Bryn Mathias, James Robinson, Ailsa Sparkes and Chris Young. Many members of the ATLAS collaboration (too many to mention) also gave me the benefit of their time and expertise. Finally, I would like to thank Ellie Davies and my parents.

Contents

List of Tables	xii
List of Figures	xv
1 Introduction	1
2 The Standard Model and Supersymmetry	3
2.1 The Standard Model	3
2.1.1 Introduction	3
2.1.2 Gauge theories	4
2.1.3 Radiative corrections	5
2.1.4 Electroweak interactions and symmetry breaking	5
2.1.5 Quantum chromodynamics	10
2.1.6 Limitations of the Standard Model	10
2.2 Supersymmetry	12
2.2.1 An extra symmetry of nature	13
2.2.2 Dark matter	13
2.2.3 The hierarchy problem	14
2.2.4 Gauge coupling unification	14
2.2.5 The supersymmetric Higgs sector	15
2.3 The Minimal Supersymmetric Standard Model	16
2.3.1 Supersymmetric masses	16
2.3.2 Supersymmetric mass spectra	18
2.3.3 Supersymmetry and gravity	20
2.4 Models of supersymmetry	20
2.4.1 General gauge mediation	21
2.4.2 Phenomenological alternatives to supersymmetry breaking	24
2.4.3 Simplified models	27

2.5 Summary	28
3 The LHC and ATLAS detector	31
3.1 The LHC	31
3.2 The ATLAS detector	33
3.2.1 ATLAS detector geometry and kinematics	33
3.3 ATLAS general detector design	35
3.4 ATLAS detector components	36
3.4.1 ATLAS Inner Detector	36
3.4.2 ATLAS Magnet System	39
3.4.3 ATLAS Calorimeter System	40
3.4.4 ATLAS Muon Spectrometer	45
3.5 ATLAS Trigger System	46
3.5.1 Level 1 Trigger	48
3.5.2 ATLAS High Level Trigger	50
3.5.3 Trigger chains and menus	52
4 Simulation and reconstruction	53
4.1 Event generation	54
4.1.1 Parton distribution functions	54
4.1.2 Matrix element	55
4.1.3 Parton showers, hadronisation and the underlying event	55
4.1.4 Summary of event generator properties	55
4.1.5 Storage of event generator information	56
4.1.6 Pile-up	56
4.2 Detector simulation	57
4.2.1 Full event simulation	57
4.2.2 Trigger simulation	57
4.2.3 Fast simulation	57
4.2.4 Digitisation	58
4.3 Summary of Monte Carlo samples used in the analysis	58
4.3.1 Monte Carlo samples used in 2011	58
4.3.2 Monte Carlo samples used in 2012	59
4.4 Reconstruction and identification	59
4.4.1 Inner Detector tracks	61

4.4.2	Vertices	62
4.4.3	Leptons	63
4.4.4	Electrons	63
4.4.5	Muons	65
4.4.6	Gluon and light flavour jets	67
4.4.7	Jet reconstruction	68
4.4.8	Heavy flavour jets	69
4.4.9	Tau leptons	69
4.4.10	Summary of object reconstruction and calibration	71
4.4.11	Missing transverse energy	72
5	Overview of three-lepton supersymmetry searches	74
5.1	Analysis overview	74
5.2	Event quality requirements	78
5.2.1	Dataset selection	78
5.2.2	Trigger	79
5.2.3	Event selection for data quality purposes	81
5.2.4	Corrections to MC event weights	82
5.3	Signal region optimisation	83
5.3.1	Discriminating variables	84
5.3.2	Optimisation procedure	85
5.3.3	Optimisation of jet veto	86
5.3.4	Optimisation of E_T^{miss}	88
5.3.5	Optimisation of $m_{\ell\ell}$	88
5.3.6	Optimisation of m_T and lepton p_T	90
5.3.7	Signal region choices	94
5.3.8	Removing overlap between signal regions	94
5.4	Cutflows for final signal regions	95
5.4.1	SRnoZa	95
5.4.2	SRnoZb	96
5.4.3	SRnoZc	96
5.4.4	SRZa	96
5.4.5	SRZb	97
5.4.6	SRZc	97
5.5	Potential improvements to choice of SRs	97

6 Background estimation and systematic uncertainties	108
6.1 Background estimation	108
6.1.1 Sources of leptons in SM backgrounds	108
6.1.2 Matrix method	109
6.1.3 Measurement of weighted average fake rates	111
6.1.4 Measurement of the electron conversion scale factor	112
6.1.5 Measurements of real lepton efficiency and weighted average fake rates	115
6.2 WZ normalisation (2011 only)	117
6.2.1 Summary of background estimation	117
6.3 Systematic uncertainties	118
6.3.1 Uncertainties on the irreducible background	118
6.3.2 Summary of irreducible background uncertainties	121
6.3.3 Uncertainties on the reducible background	122
6.3.4 Uncertainties on the SUSY signal samples	123
7 Results and interpretation	129
7.1 Validation of background prediction	129
7.1.1 2011 analysis	129
7.1.2 2012 analysis	129
7.1.3 Summary	131
7.2 Results in signal regions	135
7.2.1 2011 analysis	135
7.2.2 2012 analysis	135
7.3 Statistical interpretation	139
7.3.1 Introduction	139
7.3.2 SUSY models	139
7.3.3 Statistical procedure	142
7.3.4 Treatment of systematic uncertainties	144
7.3.5 Simultaneous fit	145
7.3.6 Combining signal regions	145
7.3.7 Model-independent limits	146
7.4 Interpretation in SUSY scenario grids	146
7.4.1 Interpretation in GGM models	147
7.4.2 Interpretation in the phenomenological MSSM	148
7.4.3 Interpretation in simplified models of direct gaugino production . . .	154

7.4.4	Summary of interpretations	154
7.4.5	Comparison with CMS	155
7.4.6	Implications for dark matter searches	156
7.4.7	Implications for supersymmetry	156
7.5	Conclusions	157
A	Details of MC samples	158
B	Tables of systematics	164
	Bibliography	167

List of Tables

2.1	Particle content of the Standard Model before electroweak symmetry breaking	9
2.2	Particle content of the MSSM before EW symmetry breaking	17
3.1	Expected resolutions of each ATLAS sub-detector	37
3.2	The number of layers, extent in η and granularity of the calorimeters	42
4.1	Cross sections and effective integrated luminosity of the main MC samples used in the 2012 analysis	60
4.2	Summary of object reconstruction properties	71
5.1	Predicted number of three lepton SM events with preliminary selection . . .	76
5.2	Summary of irreducible and reducible background naming conventions . . .	77
5.3	Leptonic triggers used in the 2011 analysis	80
5.4	Leptonic triggers used in the 2012 analysis	81
5.5	Signal region nomenclature	84
5.6	The selection requirements for the 2011 signal regions	94
5.7	The selection requirements for the 2012 signal regions	94
5.8	Cutflow for SRnoZa	97
5.9	Cutflow for SRnoZb	98
5.10	Cutflow for SRnoZc	99
5.11	Cutflow for SRZa	100
5.12	Cutflow for SRZb	101
5.13	Cutflow for SRZc	102
6.1	Observed events in the muon conversion validation region in data and MC samples with the 2012 dataset	114
6.2	Statistical and systematic uncertainties for the electron conversion scale factor	115
6.3	Summary of scale factors and efficiencies in the 2012 analysis	118

6.4	The % effect of the dominant ($> 10\%$ for any background) systematic uncertainties on irreducible SM yields in SRZ for the 2012 analysis	122
6.5	The % effect of the dominant ($> 10\%$ for any background) systematic uncertainties on irreducible SM yields in SRZ for the 2012 analysis	123
6.6	Systematic uncertainties for the reducible background in the signal regions .	123
7.1	The selection requirements for the 2011 signal regions	129
7.2	Expected numbers of events from SM backgrounds and observed numbers of events in 2011 data	130
7.3	The selection requirements for the 2012 signal regions	130
7.4	Expected numbers of events in the validation regions from SM backgrounds and observed numbers of events in 2012 data	131
7.5	Expected numbers of events from SM backgrounds and observed numbers of events in 2011 data	135
7.6	Expected numbers of events from SM backgrounds and observed numbers of events in data in 2012 signal regions	136
7.7	Model independent limits in the 2012 analysis	147
7.8	Comparison of the analysis presented here (“ATLAS”) and a similar search by the CMS collaboration. CMS data taken from [1].	156
A.1	The triboson samples used for this thesis. The LO cross section and k -factors (for NLO normalisation) are reported. The integrated luminosities corresponding to the total statistics in each sample are also given.	158
A.2	The ALPGEN $t\bar{t} + V$ samples used for this thesis. The LO cross section are k -factors (for NLO normalisation) are reported. The integrated luminosities corresponding to the total statistics in each sample are also given.	159
A.3	Diboson samples used for this thesis. The LO cross section, k -factors (for NLO normalisation) and filter efficiencies are reported. The integrated luminosities corresponding to the total statistics in each sample are also given. Samples labelled with (S) are used for systematics studies only. . .	160

A.4 Top-quark samples used for this thesis. The samples are generated with 0.111 $W \rightarrow \ell\nu$ branching ratio; for setting the k -factors the $\text{BR}(W \rightarrow \ell\nu)$ reference of 0.1080 is used (in agreement with the PDG2010 value). The $t\bar{t}$ cross section is normalised to approximate NNLO. The integrated luminosities corresponding to the total statistics in each sample are also given.	161
A.5 ALPGEN Z/γ^* +jets samples used for this thesis. The integrated luminosities corresponding to the total statistics in each sample are also given.	162
A.6 ALPGEN W +jets samples used for this thesis. The integrated luminosities corresponding to the total statistics in each sample are also given.	163
B.1 The % effect of all systematic uncertainties on irreducible SM yields in SRZ for the 2012 analysis	165
B.2 The % effect of all systematic uncertainties on irreducible SM yields in SRZ for the 2012 analysis	166

List of Figures

2.1	Fermionic and bosonic Higgs couplings	7
2.2	Feynman diagrams for vector boson scattering.	8
2.3	The consistency between the measured W , top and Higgs masses	8
2.4	QCD interactions	11
2.5	Parton distribution functions	11
2.6	One-loop corrections to the Higgs mass	14
2.7	Running of the three gauge coupling constants with energy scale Q	15
2.8	Example interactions in GGM models	22
2.9	GGM spectra	24
2.10	Cross sections for GGM models	25
2.11	An example pMSSM spectrum	27
2.12	Feynman diagram for $\tilde{\chi}_2^0 \tilde{\chi}_1^+$ production	29
2.13	Cross sections for simplified models	30
3.1	Artist's impression of the LHC accelerator and experiments	32
3.2	Average interactions per bunch crossing ($\langle\mu\rangle$) in 2011 and 2012	33
3.3	Peak instantaneous luminosity during 2011 and 2012 operation	34
3.4	A schematic of the ATLAS detector	36
3.5	Cutaways of the ATLAS inner detector	38
3.6	A cross section of the ATLAS inner detector in the η - z plane	39
3.7	Probability of a high threshold hit from transition radiation of the TRT as a function of particle momentum and Lorentz factor	40
3.8	The ATLAS magnet system	41
3.9	A cutaway of the ATLAS calorimeter system	43
3.10	The amount of material, measured in nuclear interaction lengths, in the calorimetry system as a function of pseudo-rapidity	43
3.11	A sketch of a cross section of the ATLAS electromagnetic calorimeter barrel	44

3.12 A section of the ATLAS Tile Calorimeter	45
3.13 A cutaway of the ATLAS muon detector system	47
3.14 The flow of data in the ATLAS trigger system	48
3.15 Example muon trajectories for the barrel (RPCs) and endcap (TGCs)	49
3.16 A diagram of the L1 trigger system	50
4.1 Flow chart showing the processing of real and simulated data in ATLAS	53
4.2 An outline of event generation	56
4.3 Electron reconstruction efficiency in 2012 data as a function of $\langle \mu \rangle$	65
4.4 Muon reconstruction efficiency in 2010 data	67
5.1 Trigger efficiency as a function of offline electron p_T , for single electron triggers in 2011	80
5.2 Optimisation of $b - \text{tagging}$ rejection	87
5.3 Optimisation of E_T^{miss} in Z -rich signal regions	88
5.4 Optimisation of E_T^{miss} in Z -depleted signal regions	89
5.5 SFOS pairs from $\tilde{\chi}_2^0$ decays	89
5.6 Optimisation of $m_{\ell\ell}$	90
5.7 Optimisation of m_T in Z -depleted signal regions	91
5.8 Optimisation of m_T in Z -rich signal regions	92
5.9 Optimisation of m_T in SRZc	93
5.10 Expected significance in Model A in 2012 SRnoZ signal regions	103
5.11 Expected significance in Model A in 2012 SRZ signal regions	104
5.12 Expected significance in Model B in 2012 SRnoZ signal regions	105
5.13 Expected significance in Model B in 2012 SRZ signal regions	106
6.1 Sources of leptons in SM events	109
6.2 Sources of leptons in SM events, arranged by p_T	110
6.3 Sources of leptons in 2012 signal regions	125
6.4 Feynman diagrams for initial and final state internal conversion	126
6.5 Data/MC comparison for the muon conversion validation region	126
6.6 Invariant mass of dimuon pair and muon conversion candidate	127
6.7 η (top) and p_T (bottom) of electron conversion candidate in the conversion control region	127
6.8 Invariant mass of dimuon pair and electron conversion candidate in the conversion control region	128

6.9	Fake rates and scale factors for conversion electrons	128
7.1	Kinematic distributions in VRnoZa	132
7.2	Kinematic distributions in VRnoZa	132
7.3	Kinematic distributions in VRnoZb	133
7.4	Kinematic distributions in VRnoZb	133
7.5	Kinematic distributions in VRZa	134
7.6	Kinematic distributions in VRZb	134
7.7	Distributions of E_T^{miss} and m_T in SRnoZa, SRnoZb and SRnoZc	137
7.8	Distributions of E_T^{miss} and m_T in SRZa, SRZb and SRZc	138
7.9	Percentages of weak and strong production in GGM higgsino grid	140
7.10	Percentages of weak and strong production in GGM wino co-NSLP grid . .	140
7.11	Cross sections in the pMSSM grids	141
7.12	Excluded regions in two GGM models	148
7.13	Excluded regions in the pMSSM scenario with $M_1 = 100$ GeV	151
7.14	Excluded regions in the pMSSM scenario with $M_1 = 140$ GeV	152
7.15	Excluded regions in the pMSSM scenario with $M_1 = 250$ GeV	153
7.16	Excluded regions in simplified models of direct gaugino production in the 2011 analysis	154
7.17	Excluded regions in simplified models of direct gaugino production in the 2012 analysis	155

Chapter 1

Introduction

I can't believe it's possible to select invaluable truths from a lot of careening and colliding of particles in the air, which is completely senseless and not worth a jot to anyone!

Stanisław Lem [2]

This thesis presents a search for supersymmetry in final states with exactly three leptons (electrons or muons) at the ATLAS detector. Chapter 2 discusses the Standard Model and motivates supersymmetry as a possible extension. Specific supersymmetric models studied in this thesis are introduced here. The ATLAS detector at the LHC was used in this search - technical details of the detector design and operation are discussed in Chapter 3. Specialised software is used to simulate proton-proton collisions in the ATLAS detector and reconstruct the particles produced in real and simulated events - this is discussed in Chapter 4. Chapter 5 introduces the three-lepton analysis. Analysis of data from the ATLAS experiment is a collaborative activity, and this work is no exception. I detail my contributions to the analysis below. Estimation of backgrounds by data-driven methods and the evaluation of systematic uncertainties are both discussed in Chapter 6. The results of the data analysis are given in Chapter 7, as is the interpretation in terms of supersymmetric models. Comparison to analyses undertaken by CMS, an experiment with similar search capabilities, and a discussion of the consequences for supersymmetry as a whole, are given at the end of the Chapter.

The work in this thesis was performed within the ATLAS multilepton supersymmetry analysis group. I was responsible for the estimation of the electron conversion background in

2011 and 2012 (Section 6.1.4.2) and contributed to the optimisation of 2012 signal regions (Section 5.3). I evaluated systematic uncertainties on the electron conversion estimate, and those relating to the PDF sets. The other systematic uncertainties on the background prediction were calculated by other analysis group members and ATLAS performance groups: I applied these to produce final plots of various quantities in the 2012 signal and validation regions (Sections 7.1.2 and 7.2.2), made public in [3]. I also interpreted 2011 data in the GGM scenarios (Section 7.4.1), and worked on the combination of the 2011 data with results from the dilepton selection for weak SUSY searches (Section 7.4.2.1). Plots with “ATLAS Preliminary” or “ATLAS” labels are public and cited as such. Public plots I created are referenced as such in their caption, and all plots without ATLAS labels are my own, and shown publicly in this thesis for the first time. Tables are my own unless stated otherwise.

Chapter 2

The Standard Model and Supersymmetry

And yet its very completeness
signals that there is more to be
done.

Neal Stephenson [4]

2.1 The Standard Model

2.1.1 Introduction

A theory of Nature can be classified by its predictive power, or equivalently by the number of free parameters within the theory. Consider a hypothetical theory containing only a database of every experiment performed, without formulae or laws linking the results: such a theory would have no predictive power, since every new result would have to be introduced by hand. One goal of a scientific theory is to predict phenomena with as few free parameters as possible: a theory with fewer free parameters which explains the same experiments is preferable to a theory with more free parameters. The most predictive theory imaginable (a “Theory of Everything”) would have no free parameters at all, while correctly predicting the outcome of any physical experiment.

Perhaps the best example of a predictive theory that we have is the Standard Model [5] (SM), which explains many distinct physical phenomena (including the behaviour of light, radioactive decay, aspects of the structure of the elements and the burning of stars)

with only 19 free parameters¹. Some puzzles remain: for example, neutrino masses and oscillation are not explained [7], gravity is not included in the theory [8], and there is no explanation for dark matter [9]. Neutrino masses and gravity are not considered in this work: dark matter is discussed in Section 2.2.2.

The Lagrangian for the SM is given by

$$\mathcal{L}_{\text{SM}} = \mathcal{L}_{\text{QCD}} + \mathcal{L}_{\text{Electroweak}} + \mathcal{L}_{\text{Higgs}}, \quad (2.1)$$

where \mathcal{L}_{QCD} refers to Quantum Chromodynamics, discussed in Section 2.1.5, $\mathcal{L}_{\text{Electroweak}}$ and $\mathcal{L}_{\text{Higgs}}$ refer to the electroweak theory and Higgs sector, discussed in Section 2.1.4. When minimised, \mathcal{L}_{SM} gives rise to a set of dynamical equations; the behaviour of these different aspects of the theory is discussed in the following sections. Although the SM successfully explains many phenomena, there are good reasons to investigate SM extensions, as discussed in Section 2.1.6. Supersymmetry, one of the best motivated extensions with significant predictive power, is discussed in Section 2.2. The main focus of original work presented in this thesis is a search for evidence of supersymmetry.

2.1.2 Gauge theories

Consider classical electrodynamics. This theory is invariant under the transformation of the potential A_μ (where μ is a Lorentz index) by

$$A_\mu \rightarrow A_\mu - \partial_\mu \lambda. \quad (2.2)$$

In classical electrodynamics, gauge invariance first emerged as a coincidental symmetry [10], but with time it has proven to be of fundamental and far-reaching importance. In quantum electrodynamics A_μ is promoted to a quantum field, and identified with the photon field. The photon is the *gauge boson* for the theory, and the gauge symmetry in equation (2.2) is identified with the conservation of electric charge. The group governing the transformation is the unitary group of order one, denoted $U(1)$. The strong and weak forces are associated with *non-abelian* gauge groups: such groups have non-vanishing commutators between the generators for their gauge fields ($[A_\mu, A^\nu] \neq 0$), with the consequence that gauge bosons can self-interact. The introduction of non-abelian gauge groups to physics is due to Yang and Mills [11]. Quantum chromodynamics (QCD) and the weak theory are mediated by gauge bosons invariant under the non-abelian groups $SU(3)$ and $SU(2)$ respectively. Both gauge symmetries conserve their own analogues of electric charge: this is discussed in more detail in Sections 2.1.5 and 2.1.4.

¹These are the charged fermion masses and mixings, coupling constants, Z boson mass and Higgs mass: relations between the parameters allow for other choices, as well as the so-called “ θ -parameter” [6].

2.1.3 Radiative corrections

Variables in quantum field theories are frequently defined perturbatively: predictions are defined to lowest order (“tree level”), and receive corrections by expansions in the coupling constant of the theory. These corrections form an infinite series, but usually only the first few terms are important, in which case the expansion may be truncated. Quantum corrections to masses may be positive or negative: the fundamental implications of this for the SM are discussed in Section 2.2.3, and practical implications for supersymmetric theories are discussed in Section 2.3.1. The fundamental coupling constants of the strong, weak and electromagnetic forces also vary as a function of energy: this is known as running of coupling constants. The high energy behaviour of these coupling constants is discussed in Section 2.2.4.

2.1.4 Electroweak interactions and symmetry breaking

Weak interactions (as observed in β -decay for example) initially appear very different from electromagnetic interactions: weak interactions are short- rather than infinite-ranged. The weak interactions also do not respect parity: only left-handed (right-handed) particles (anti-particles) participate in the weak interaction. The special unitary group of order two ($SU(2)_L$) describes the weak interactions: L refers to the *chiral* or left-handed nature of the theory. The conserved quantum number T^3 , known as the third component of weak isospin, is defined to equal $\pm \frac{1}{2}$ for left-handed particles and zero for right-handed particles. The non-observation of right-handed neutrinos is incorporated into the theory: left-handed charged leptons form doublets $T^3 = (+\frac{1}{2}, -\frac{1}{2})$, (e_L, ν_L) , while the right-handed charged leptons form $T^3 = 0$ singlets (e_R) . The three generations of quarks are similarly divided into left-handed T^3 doublets (u, d) :

$$L_q^1 = \begin{pmatrix} u \\ d \end{pmatrix}, \quad L_q^2 = \begin{pmatrix} c \\ s \end{pmatrix}, \quad L_q^3 = \begin{pmatrix} t \\ b \end{pmatrix} \quad (2.3)$$

and right-handed singlets with $T^3 = 0$:

$$R_u^{1,2,3} = u_R, c_R, t_R \quad (2.4)$$

$$R_d^{1,2,3} = d_R, s_R, b_R. \quad (2.5)$$

Weak interactions are mediated by gauge bosons with $T^3 = (1, 0, -1)$, allowing for the conservation of T^3 at each vertex. Despite the distinctions between the electromagnetic and weak interactions, it is possible to unify the forces into a single theory [12, 13, 14]:

this is known as the *electroweak* theory and has predicted new phenomena (notably weak neutral currents [15]) as well as accurately describing the weak and electromagnetic forces. Unifying the electromagnetic and weak forces initially leads to a theory with three massless gauge bosons ($W_\mu^{i=1,2,3}$) mediating the weak force, and a single gauge boson (B_μ) mediating the electromagnetic force. Additionally, this theory predicts massless charged leptons and quarks, and two massless complex scalars, associated with the new electroweak symmetry. The predictions of massless weak gauge bosons and massless fermions are at odds with the observations of the weak force, which is known to act only at short range (and must therefore be mediated by massive particles) and measurements of charged lepton and quark masses. Several papers [16, 17, 18, 19, 20] showed a possible solution: one degree of freedom from one complex scalar is absorbed into a single, massive boson known as the Higgs boson. Additionally, the W_μ^i and B_μ bosons mix and acquire mass. This solution is known as electroweak symmetry breaking. The W^\pm , Z and A fields are formed from a superposition of the W and B fields - the three remaining degrees of freedom from the two complex scalars are “eaten” to form the longitudinal components of the W and Z fields. The W , Z and A fields are given by

$$W_\mu^\pm = \frac{(W^1 \mp iW^2)}{\sqrt{2}}, \quad (2.6)$$

$$Z_\mu = \frac{-g'B_\mu + gW_\mu^3}{\sqrt{g^2 + g'^2}}, \quad (2.7)$$

$$A_\mu = \frac{gB_\mu + g'W_\mu^3}{\sqrt{g^2 + g'^2}}, \quad (2.8)$$

where $g = e/\cos\theta_W$ and $g' = e/\cos\theta_W$ are electroweak coupling parameters. The angle θ_W is known as the Weinberg angle. During electroweak symmetry breaking, the bosons acquire masses given by

$$m_W = \frac{gv}{2}, \quad (2.9)$$

$$m_Z = \frac{(g^2 + g'^2)v}{2}, \quad (2.10)$$

where $v = 246.22$ GeV is the Higgs vacuum expectation value. This does not solve the problem of the massless fermions, and the theory is therefore not fully consistent [21] (as well as at odds with observations). Fermions can, however, acquire mass through interactions with the Higgs boson - after electroweak symmetry breaking, there are Higgs-fermion interaction terms and new Higgs-fermion mass terms. Interactions between the Higgs boson and fermions/gauge bosons are shown in Figure 2.1.

The value of v may be determined precisely from muon decays [22] while e is known to

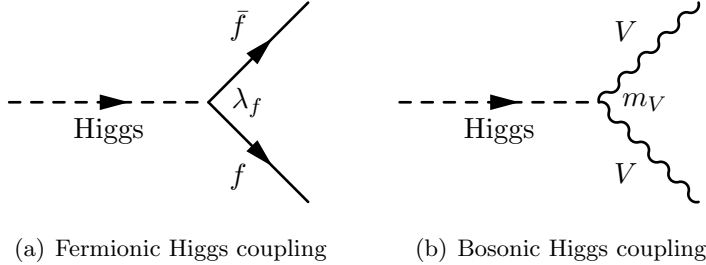


Figure 2.1: Fermionic and bosonic Higgs couplings. In (a), λ_f is the Yukawa coupling, proportional to the observed fermion mass. In (b), the Higgs only couples to the weak gauge bosons ($V = W, Z$), and not the photon or gluon, with strength proportional to m_V .

high precision from various atomic measurements [23], and θ_W remains a free parameter of the theory. Direct measurements of W and Z masses strongly constrain the theory: the ratio m_W/m_Z is very precisely predicted. The non-zero Higgs vacuum expectation value v means that it permeates the entire vacuum: all other known fields have zero vacuum expectation value. The Higgs boson can in fact *only* account for fermion masses if it has non-zero vacuum expectation value. The mass of the Higgs boson is a free but highly constrained parameter of the theory. Without a Higgs boson, the SM has intrinsic problems: the simplest problem to state is the behaviour of the vector boson scattering amplitudes $VV \rightarrow VV$, shown in Figure 2.2. The cross section σ increases without bound as a function of energy [24]:

$$\sigma(VV \rightarrow VV) \approx \frac{E^4}{m_W^4}. \quad (2.11)$$

At energies above $E \approx 1$ TeV the cross section violates unitarity: the probability of the process occurring in a collision exceeds 100%. Interactions moderated by a Higgs boson, as shown in Figure 2.2(b), introduces additional contributions to the cross section which cancel the electroweak contributions shown in Figure 2.2(a). The cancellation is dependent on the mass of the Higgs boson: in order to maintain unitarity, m_H must be approximately 1 TeV or lower.

There are two options: either new physics modifies the vector boson scattering cross sections at high energies, or there is a Higgs boson with a mass less than 1 TeV. At the time of writing, the ATLAS [25] and CMS [26] collaborations have observed a particle with mass between 125 and 127 GeV consistent with the SM Higgs boson. Figure 2.3 shows the compatibility between the measured Higgs mass m_H and other SM parameters. The blue contours show 95% and 68% confidence levels for the W mass m_W and other electroweak parameters except m_W and top mass m_t , while the grey contours show 95%

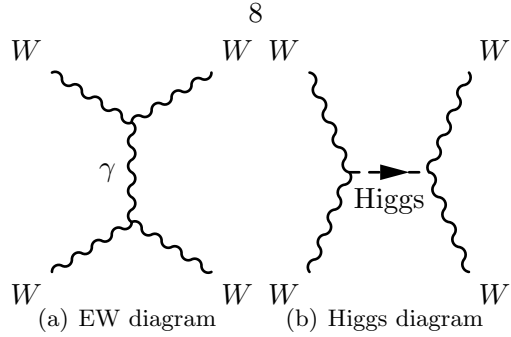


Figure 2.2: Feynman diagrams for vector boson scattering. An electroweak (EW) diagram with an intermediate photon is shown in (a), while a diagram mediated by a Higgs boson is shown in (b).

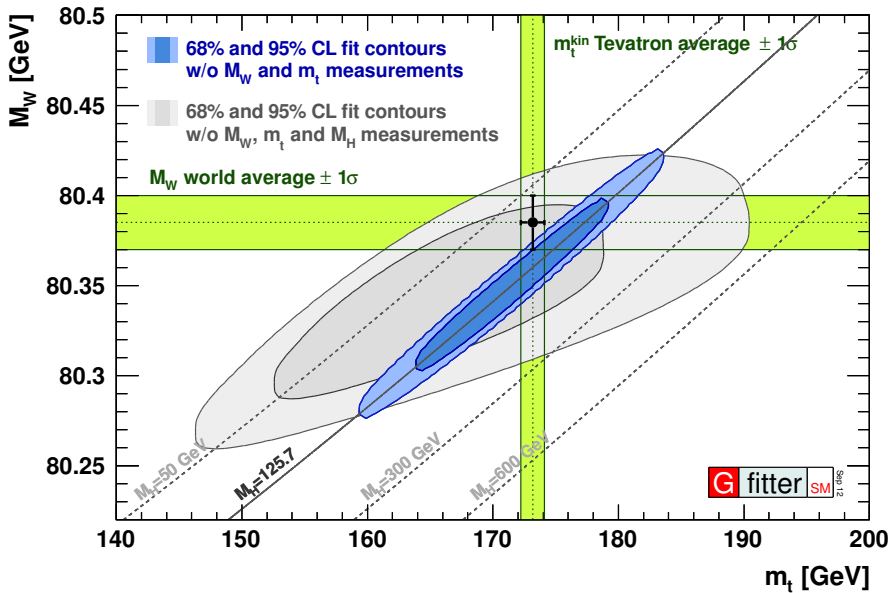


Figure 2.3: The consistency between the measured W , top and Higgs masses. Taken from [27].

and 68% confidence levels for the direct m_H , m_W and m_t measurements. The black data point shows the m_W and m_t measurements alone. The blue and grey ellipses are consistent with the data point at 95% and 68% confidence level respectively. Excluding the direct measurement, precision electroweak data gives a best fit value [27] of $m_H = 94^{+25}_{-22}$ GeV, consistent with the measured value. In this thesis, it is assumed that the observed particle is either the SM Higgs boson or perhaps the lightest supersymmetric Higgs boson to be introduced in Section 2.2.5. The final particle content of the SM before electroweak symmetry breaking is given in Table 2.1.

Name	Symbol	Spin
Mass sector		
Quarks ×3 families	(u_L, d_L) u_R d_R	
Leptons ×3 families	(ν_L, e_L) e_R	
Higgs sector		
Higgs boson	H^0	0
Gauge sector		
Gluons	g	
W bosons	W^\pm, W^0	1
B boson	B^0	

Table 2.1: Particle content of the Standard Model before electroweak symmetry breaking. After electroweak symmetry breaking, the W and B bosons mix to form photons and W and Z bosons, and the quarks and charged leptons acquire mass.

2.1.5 Quantum chromodynamics

Quantum chromodynamics (QCD) is the theory of the strong nuclear force. It predicts that protons and neutrons are not fundamental particles, and are in fact made up of fractionally charged particles known as quarks. Interactions between quarks are mediated by gauge bosons known as gluons, which exchange colour, the strong force analogue of electric charge. There are three colours, usually referred to as red, green and blue (r, g, b). Quarks carry either r, g or b charge, while anti-quarks carry anti-red, green or blue ($\bar{r}, \bar{g}, \bar{b}$). Free coloured particles have never been observed [28]: only colourless “singlet” states are observed. Colour singlet states (hadrons) are formed by a triplet of red, green and blue quarks (baryons), or pairs of $r\bar{r}, g\bar{g}, b\bar{b}$ (mesons). Tetraquark and pentaquark states could in principle be realised in Nature, but have yet to be observed. Eight gluons mediate the force: each gluon carries a linear combination of colours and anti-colours. Like W and Z bosons, gluons carry the charge of their gauge group and hence participate in the interaction: gluon self-interactions are shown in Figure 2.4(b) and 2.4(c). The gauge group for QCD is $SU(3)_c$.

Like the weak and EM coupling constants, the QCD coupling constant α_S is dependent on the energy of the process. The strength of the interaction decreases as energy increases and vice versa. This weakness of coupling strength at high energy is known as asymptotic freedom. An important consequence of asymptotic freedom is that high-energy QCD processes are calculable in perturbation theory, while low-energy QCD processes are not. Phenomenological models used to approximate such effects are discussed in Section 4.1. In addition to its constituent “valence” quarks, a hadron will contain a sea of virtual $q\bar{q}$ pairs (“sea quarks”) and gluons. The total momentum of a hadron is distributed probabilistically among its partons, each of which has momentum fraction x . The probability of finding a parton of type p with momentum x is given by the *parton distribution function* (PDF): this distribution is not calculable perturbatively, but may be extracted from experimental data, as discussed in Section 4.1.1. Examples of PDFs are shown in Figure 2.5.

2.1.6 Limitations of the Standard Model

As previously mentioned, the SM predicts many phenomena very precisely, but still has several deficiencies. Dark matter, as discussed in more detail in Section 2.2.2 cannot be identified with any known particles, the gauge couplings do not naturally unify (Section 2.2.4), and the Higgs boson mass is unstable when radiative corrections are applied (the

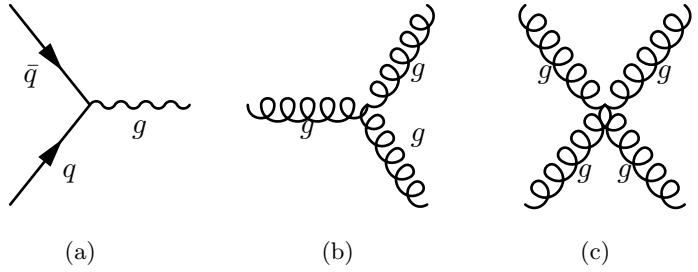


Figure 2.4: QCD interactions.

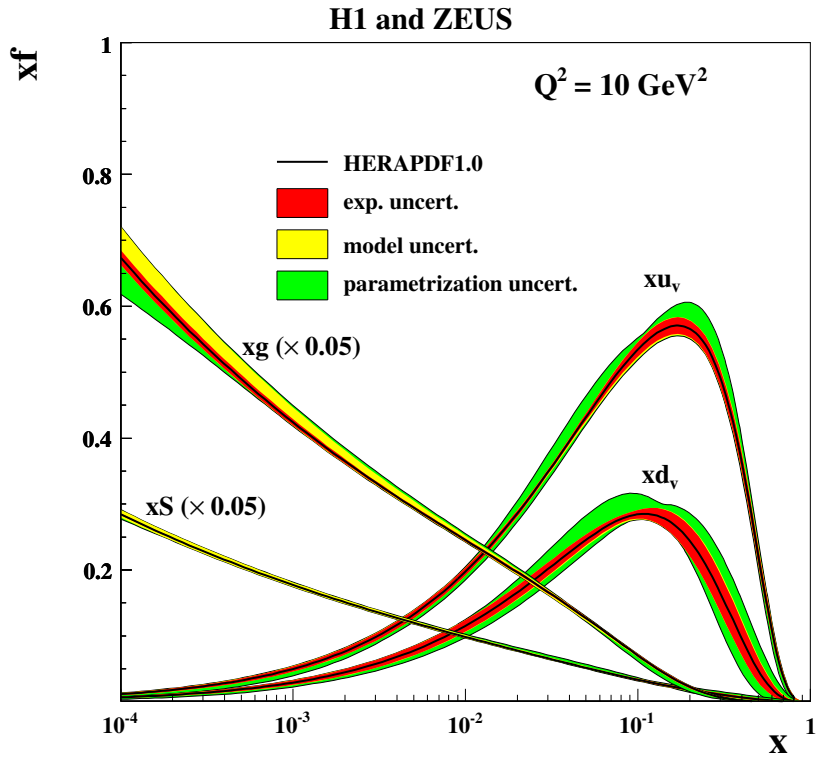


Figure 2.5: Parton distribution functions for up and down valence quarks (u_v, d_v), gluons (g) and sea quarks (S). Q^2 is the energy scale squared at which the proton is probed, while x is the momentum fraction of a given parton, and f is its PDF. Taken from [29].

“hierarchy problem”, discussed in detail in Section 2.2.3). These difficulties may be overcome by supersymmetry, as described in Section 2.2. In addition to these difficulties, no deeper explanation for the values and quantity of the 19 free parameters in the SM has been found. A more fundamental theory would have fewer free parameters, or at least an explanation for the observed values. Finally, no quantum theory of gravity has been developed: deviations from the classical theory of general relativity are expected at very small length scales, but the relative weakness of the gravitational force makes it difficult to observe such deviations: none have been observed so far [30].

2.2 Supersymmetry

Supersymmetry (SUSY) was proposed in various guises from 1966 onwards [31, 32, 33, 34, 35, 36, 37, 38, 39]. It is defined by an operator Q , which transforms bosons into fermions and *vice versa*:

$$Q|\text{Boson}\rangle = |\text{Fermion}\rangle \quad (2.12)$$

$$Q|\text{Fermion}\rangle = |\text{Boson}\rangle \quad (2.13)$$

Particles related by this transformation are referred to as superpartners or sparticles, and a set of two superpartners is called a *supermultiplet*. The superpartners of SM particles are known as superparticles or sparticles. Standard Model boson superpartners are given the suffix “ino” (wino, bino etc) while fermion superpartners are given “s” as a prefix (squarks, sleptons, sneutrinos). In equations, sparticles are given a tilde (\tilde{W} for the wino, \tilde{u} for the up squark etc).

Postulating supersymmetry for the SM almost exactly doubles its particle content - although two Higgs supermultiplets are required, as discussed in Section 2.2.5. It does not introduce any new parameters, as supersymmetric transformations do not transform any particle quantum numbers except spin. Since baryon (B) and lepton (L) number are accidental symmetries of the Standard Model (that is to say, the absence of B and L -violating interactions appears to arise from cancellation of terms rather than a principle of symmetry), supersymmetry also adds the possibility of B- and L-violating interactions. Limits on processes that violate B and L are generally very stringent, so for supersymmetry to exist in Nature, B , L or some combination thereof must be conserved, or only slightly violated. In all the supersymmetric models considered here, the symmetry imposed is R -parity, where $R = (-1)^{3(B-L)+2S}$ (with S as the particle spin). Normal particles have $R = 1$, while sparticles have $R = -1$. Interactions considered in this thesis are required to

conserve R -parity multiplicatively at each vertex. This has two important phenomenological consequences: firstly, sparticles can only be pair-produced in colliders, and secondly the lightest supersymmetric particle (LSP) is stable. Motivations for supersymmetry are explored in the next few sections.

2.2.1 An extra symmetry of nature

The forms of any additional symmetries in a realistic quantum field theory with chiral interactions are highly constrained by the Coleman-Mandula theorem [40], as generalised by Haag, Lopuszanski and Sohnius [41]. The theorem states that, in addition to Poincaré symmetry, the only additional continuous symmetry such a theory may exhibit is supersymmetry.

2.2.2 Dark matter

Measurements of the rotation curves of galaxies (first performed in the 1930s [42, 43]) show that galaxies rotate more quickly than would be expected from observations of their visible matter. There are two possible explanations: either general relativity must be modified on galactic distance scales, or “dark matter”, i.e. matter that does not interact electromagnetically, is responsible for the additional galactic mass. Several additional observations including gravitational lensing [44] and measurements of the cosmic microwave background [45] are consistent with the dark matter hypothesis, although modifications to general relativity are still investigated [46].

A possible candidate for dark matter would be a new type of particle without electromagnetic interactions, present throughout the universe (although there are possible alternatives such as Massive Compact Halo Objects [47]). Neutrinos lack electromagnetic interactions, but are disfavoured by cosmic microwave background data [48]. Many direct searches for dark matter particles have been performed: the most stringent at the time of writing were conducted by the CDMS-II [49] and XENON-100 [50] experiments.

Many models of supersymmetry (including those considered here) propose a colourless, electrically neutral, weakly interacting LSP compatible with astronomical observations [51, 52].

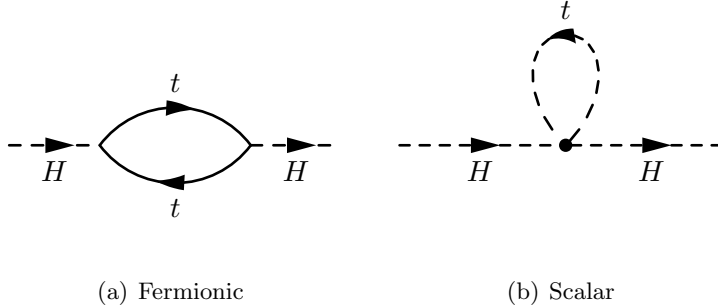


Figure 2.6: One-loop corrections to the Higgs mass from (a) a fermion (the top quark) and (b) a scalar (the top squark).

2.2.3 The hierarchy problem

The Higgs mass receives radiative corrections from all SM particles. For example, there is a correction due to the top quark Yukawa coupling λ_t :

$$\Delta M_H^2 = -\frac{|\lambda_t|^2}{8\pi^2} \Lambda_{UV}^2 \quad (2.14)$$

shown in Figure 2.6a). This correction is quadratically divergent proportionally to Λ_{UV}^2 : Λ_{UV} is the highest scale at which the theory is valid. If the SM is valid up to the Planck scale $O(10^{19})$ GeV, the correction is dramatically larger than the observed Higgs mass. The difference between the scale of electroweak physics at $O(100$ GeV) and the Planck scale (and the absence of any new phenomena at any intermediate energy scale), which manifests in these corrections to the Higgs mass, is known as the hierarchy problem [53, 54, 55, 56]. If, however, a new scalar with mass m_S exists, it gives rise to a correction of the form:

$$\Delta M_H^2 = \frac{|\lambda_S|^2}{16\pi^2} \Lambda_{UV}^2. \quad (2.15)$$

Two scalar particles with Yukawa couplings equal to that of the top quark will exactly cancel the corrections to the Higgs mass. The same argument applies for all SM fermions, and it has been shown that the correction continues to all orders [57, 58, 59, 60, 61, 62]. In supersymmetry, the two scalars required for each fermion are partners for the left- and right-handed fermions.

2.2.4 Gauge coupling unification

As discussed in Section 2.1.3, the SM predicts that gauge couplings are energy-dependent, and the change in strength as a function of the energy scale is calculable given a value at some fixed scale. The EM and weak couplings increase with energy, while the strong coupling constant decreases with energy. The coupling constants do not meet at any single point in the SM, while it is possible to make them meet at high energies in the Minimal

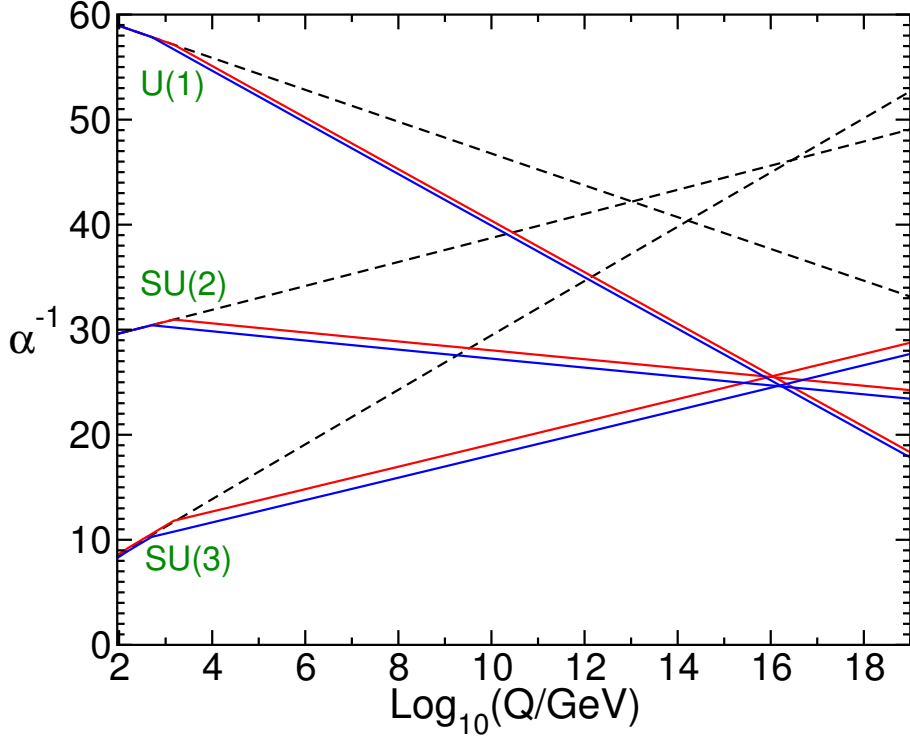


Figure 2.7: Running of the three gauge coupling constants with energy scale Q , in the SM (dotted line) and SUSY (red and blue bands). From [67].

Supersymmetric SM [63, 61, 64, 65, 66] (the simplest extension to the SM, discussed in Section 2.3. In Figure 2.7, taken from [67], the dotted lines are the SM predictions, while the red and blue lines indicate the band of allowed values in the MSSM. Gauge coupling unification is attractive because it allows the three independent gauge couplings to be subsumed into a single free parameter, and may hint at a deeper level of physics. However, gauge coupling unification is predicted to occur at 10^{16} GeV which is not currently directly accessible to experiment, although it is possible that unification at this scale could have observable effects at the TeV scale or lower such as proton decay [68].

2.2.5 The supersymmetric Higgs sector

Each SM particle has a single superpartner, except for the Higgs boson. Anomaly cancellation [69] is required for a consistent field theory: in particular the sums

$$\sum_{f_L} Y^3 = \sum_{f_L} T_3^2 Y = 0 \quad (2.16)$$

over the hypercharges Y and third component of isospin (T_3) of all left-handed fermions must be satisfied. A single higgsino \tilde{H} spoils the relation and two Higgs supermultiplets are required instead. One of the supermultiplets is denoted (H_u^+, H_u^0) and couples to up-

type quarks only, while the other is denoted (H_d^0, H_d^-) and couples to down type quarks only. The members of the two supermultiplets mix to form five mass eigenstates - the lightest Higgs boson (h^0) is a linear combination of H_u^0 and H_d^0 , and there are three additional Higgs bosons: H^0 (heavy, CP-even), A^0 (CP-odd), H^+ and H^- and associated superpartners. The up- and down-type Higgs bosons have separate vacuum expectation values $v_u = v \sin \beta$ and $v_d = v \cos \beta$, and the vacuum expectation value of h_0 is then given by $\sqrt{v_u^2 + v_d^2} = v$, matching $v = 246.22$ GeV in order to reproduce the known m_W and m_Z . The mixing angle β is a free parameter of the theory. The ratio of expectation values $v_u/v_d = \tan \beta$ is important for the sleptons and squark masses, as discussed in Section 2.3.2.

2.3 The Minimal Supersymmetric Standard Model

The Minimal Supersymmetric Standard Model (MSSM) is defined simply as the Standard Model with supersymmetric versions of all the matter particles, and two Higgs doublets for theoretical consistency. The final particle content of the MSSM is given in Table 2.2. All of the sleptons and gauginos except the gluino (as the only coloured sparticle) can mix, so the mass eigenstates are generally not the flavour or gauge eigenstates given in the table. Neutral higgsinos and gauginos ($\tilde{H}^0, \tilde{W}^0, \tilde{B}$) mix to form four *neutralinos*, $\tilde{\chi}_{i=1,2,3,4}^0$, while the charged higgsinos and wino ($\tilde{H}^\pm, \tilde{W}^\pm$) mix to form two *charginos*, $\tilde{\chi}_{i=1,2}^\pm$.

2.3.1 Supersymmetric masses

Without additional assumptions, supersymmetric particles have the same quantum numbers as their SM counterparts, including mass. This is at odds with experiment: for instance, limits on slepton masses extend to at least one hundred times the electron, muon and tau masses [70]. This would seem initially to be a disaster for supersymmetry, but supersymmetric particles share a common property: they are *allowed* to have masses in the absence of electroweak symmetry breaking [67], while SM particles are *forbidden* from having masses without electroweak symmetry breaking, as discussed in Section 2.1.4. Supersymmetric masses can then be added to the theory on an *ad hoc* basis - this is known as explicit supersymmetry breaking [67]. In order to solve the hierarchy problem, the Lagrangian must be expressed as

$$\mathcal{L} = \mathcal{L}_{\text{SUSY}} + \mathcal{L}_{\text{breaking}} \quad (2.17)$$

Name	Spin 0	Spin 1/2
Mass sector		
Squarks, quarks × 3 families	$(\tilde{u}_L, \tilde{d}_L)$ \tilde{u}_R \tilde{d}_R	(u_L, d_L) \tilde{u}_R \tilde{d}_R
Sleptons, leptons × 3 families	$(\tilde{\nu}_L, \tilde{e}_L)$ \tilde{e}_R	(ν_L, e_L) \tilde{e}_R
Higgs sector		
Higgs, higgsinos	(H_u^+, H_u^0) (H_d^0, H_d^+)	$(\tilde{H}_u^+, \tilde{H}_u^0)$ $(\tilde{H}_d^0, \tilde{H}_d^+)$
Gauge sector	Spin 1	Spin 1/2
Gluons, gluinos	g	\tilde{g}
W bosons, winos	W^\pm, W^0	$\tilde{W}^\pm, \tilde{W}^0$
B bosons, binos	B^0	\tilde{B}

Table 2.2: Particle content of the MSSM before EW symmetry breaking. Taken from [67].

where $\mathcal{L}_{\text{SUSY}}$ contains interactions that conserve supersymmetry (and in particular the couplings with the Higgs sector), while $\mathcal{L}_{\text{breaking}}$ contains new mass terms and interactions not present in the SM. This is known as *soft supersymmetry breaking*. The new mass terms give new corrections to the Higgs mass: in order for these corrections to be small the new mass terms cannot rise much above the TeV scale [67].

The possible additional supersymmetric mass terms (using the notation and conventions of [5]) are as follows:

1. Three gaugino masses: M_1, M_2, M_3 .
2. Five scalar masses squared for the squarks and sleptons: $M_{\tilde{Q}_L}, M_{\tilde{U}_R}, M_{\tilde{D}_R}, M_{\tilde{L}_L}, M_{\tilde{E}_R}$. Here \tilde{Q}_L refers to the supermultiplet containing a weak doublet of left-handed up- and down-type fermions while \tilde{U}_R and \tilde{D}_R refer to the supermultiplets formed by the right-handed up- and down-type quark singlets.
3. Three Higgs interaction terms A_i for the up and down type squarks and sleptons: A_U, A_D, A_E respectively.
4. Three scalar masses squared: $m_1^2 + |\mu|^2, m_2^2 + |\mu|^2, B\mu$, which emerge from the supersymmetric Higgs scalar potential [67].

These parameters determine the mixing between the flavour eigenstates and hence the phenomenology of supersymmetric theories. The exact dependence of the mass eigenstates on these terms is discussed in detail in Section 2.3.2. These extra terms may be added to the theory “by hand”, but this increases the number of free parameters of the theory as well as being conceptually unsatisfying. Different approaches to these extra terms are discussed in Section 2.4.

2.3.2 Supersymmetric mass spectra

The general properties of supersymmetric mass terms and their consequences for phenomenology are discussed here.

2.3.2.1 Gauginos

Since the gluino has colour charge, it cannot mix with the other gauginos. The gluino mass is therefore given by M_3 . The other gauginos form linear superpositions: their masses are given by mixing matrices, and depend on the parameters M_1, M_2 and μ . The chargino

masses are found by the singular value decomposition of the following mixing matrix:

$$M_C = \begin{pmatrix} M_2 & \frac{1}{\sqrt{2}}gv_u \\ \frac{1}{\sqrt{2}}gv_d & \mu \end{pmatrix} \quad (2.18)$$

which gives two observable states [71]:

$$\begin{aligned} M_{\tilde{\chi}_1^\pm, \tilde{\chi}_2^\pm}^2 = \frac{1}{2}(&|\mu|^2 + |M_2|^2 + 2m_W^2 \mp [(|\mu|^2 + |M_2|^2 + 2m_W^2)^2 \\ &- 4|\mu|^2|M_2|^2 - 4m_W^2 \sin^2 2\beta + 8m_W^2 \sin 2\beta \operatorname{Re}(\mu M_2)]^{1/2}) \end{aligned} \quad (2.19)$$

where the \mp on the right hand side is negative for the $\tilde{\chi}_1^\pm$ and positive for the $\tilde{\chi}_2^\pm$ (fixing $m_{\tilde{\chi}_1^\pm} < m_{\tilde{\chi}_2^\pm}$). Similarly, the mixing matrix for the physical neutralino states is given by

$$M_N = \begin{pmatrix} M_1 & 0 & -\frac{1}{2}g'v_d & \frac{1}{2}g'v_u \\ 0 & M_2 & \frac{1}{2}gv_d & -\frac{1}{2}gv_u \\ -\frac{1}{2}g'v_d & \frac{1}{2}g'v_d & 0 & -\mu \\ \frac{1}{2}g'v_u & -\frac{1}{2}g'v_u & -\mu & 0 \end{pmatrix} \quad (2.20)$$

which may be diagonalised to give the four observable neutralino states. The exact expressions are rather lengthy but may be found in [72]. For the models considered here, the most important features are as follows:

- If M_2 is much smaller than M_1 and $|\mu|$ and of the order of m_Z , the $\tilde{\chi}_1^0$ and $\tilde{\chi}_1^\pm$ form wino co-NLSPs ($\tilde{W}^\pm, \tilde{W}^0$) with degenerate or nearly degenerate masses.
- If $\mu > \{M_1, M_2\}$, the gaugino masses are independent of μ : there is no decrease in cross section for gaugino production as μ increases past this point.

2.3.2.2 Squarks and sleptons

The left- and right-handed charged fermions (f_L, f_R) represent distinct degrees of freedom in the SM, as they have different weak quantum numbers. The left- and right-handed charged sfermions (\tilde{f}_L, \tilde{f}_R), as scalars, are neither left- nor- right-handed and can therefore mix. In general, the sfermions can form admixtures between generations: most of these are prohibited by the requirement that supersymmetry does not introduce large flavour-changing neutral currents [73]. The left and right-handed first and second generation squarks form seven approximately mass-degenerate pairs which do not mix:

$$(\tilde{e}_R, \tilde{\mu}_R), (\tilde{\nu}_e, \tilde{\nu}_\mu), (\tilde{e}_R, \tilde{\mu}_R), (\tilde{u}_R, \tilde{c}_R), (\tilde{d}_R, \tilde{s}_R), (\tilde{u}_R, \tilde{c}_R), (\tilde{d}_R, \tilde{s}_R) \quad (2.21)$$

The up- and down-type quarks form distinct pairs since they respectively interact with the H_u and H_d Higgs supermultiplets. The third generation can have far higher masses,

due to the larger Yukawa and A-parameters, and large mixing is permitted between the left-and right-handed stau, stop and sbottom components. This mixing is dependent on the value of $\tan \beta$: for $\tan \beta \gtrsim 10$, significant mixing is expected. Large values of $\tan \beta$ break the flavour-blindness of supersymmetry, leading to enhanced branching ratios in supersymmetric decays to third generation particles [74].

2.3.2.3 Higgs sector

The masses of A_0 , H_0 and H^\pm are not bounded by theory: at tree level their mass terms are proportional to $1/\sin \beta$, which can be arbitrarily large. However, there is a striking prediction for the mass of the lightest Higgs boson, h^0 :

$$m_{h^0} < m_Z |\cos 2\beta| \quad (2.22)$$

The lightest Higgs mass is therefore bounded below the Z mass without radiative corrections: the largest of these comes from the stop mass [75]. It is possible to tune these corrections in order to meet the observed lightest Higgs mass of ≈ 126 GeV [76].

2.3.3 Supersymmetry and gravity

Despite nearly a century of effort, a complete quantum theory of gravity has not been found. Nevertheless, the long-range and tensor nature of the gravitational force already implies that gravity is mediated by a massless spin-2 boson, known as the graviton. Since supersymmetry transformations reduce spin by a factor of $1/2$, the superpartner of the graviton (the gravitino \tilde{G}) has spin $3/2$. A gravitino does not have weak or electromagnetic interactions, and is therefore a possible dark matter candidate if it is the LSP.

2.4 Models of supersymmetry

The motivations and parameters of the three different types of supersymmetric models examined in this work are discussed in detail. The models considered all lead to additional events with three leptons not found in the SM, which is the focus of the experimental searches presented.

Each model considered uses a distinct solution to the problem of supersymmetry breaking:

1. General Gauge Mediation (GGM) [77] postulates a hidden sector of particles which do not interact with SM particles, but impart masses to SUSY particles. This is discussed further in Section 2.4.1.

2. The phenomenological MSSM [78] uses existing experimental data and conservative assumptions to constrain the possible values for the masses. This is discussed further in Section 2.4.2.
3. Simplified models [79, 80] set the masses of a subset of superparticles to values accessible by experiment, and the other masses to infinity (or at least to experimentally inaccessible values). This is discussed further in Section 2.4.3.1.

Other examples of supersymmetry breaking mechanisms include minimal supergravity [81, 82, 83, 84, 85, 86], anomaly-mediated supersymmetry breaking [87, 88] and gauge-mediated supersymmetry breaking (GMSB) [89, 90, 91, 92, 93].

Several benchmark points for each family of models are examined in detail. By convention, each set of benchmark points is chosen by varying two SUSY parameters while keeping all others the same. The set of benchmark points defines a “grid” in the space of the two parameters. The numerical simulation of the grids investigated in this work is discussed in Sections 4.3.1.2 and 4.3.2.2.

2.4.1 General gauge mediation

Gauge-mediated supersymmetry breaking (GMSB) hypothesises the existence of a hidden sector of heavy particles which do not interact with the SM. “Messenger” particles are introduced, which interact with both the hidden and SM sectors. Loop diagrams involving the messenger particles are responsible for the supersymmetric mass terms. In such models, the gravitino is the LSP, and is approximately massless. The phenomenology of such models is largely determined by the choice of next-to-lightest sparticle (NLSP), as all decay chains will end with a decay of the form:

$$\text{NLSP} \rightarrow (\text{SM partner of NLSP}) + \text{LSP} \quad (2.23)$$

General gauge mediation (GGM) makes the additional assumption that, in the limit that the hidden and SM sectors are no longer linked by the messenger particles, the SM sector reproduces the MSSM. Under these assumptions, seven free parameters remain in the model:

- The three gaugino masses M_1 , M_2 and M_3 , defined in Section 2.3.1
- The Higgs parameters $\tan \beta$ and μ , defined in Section 2.3.1
- The choice of NLSP and corresponding mean lifetime (τ). The mean lifetime governs whether decays are prompt or macroscopically displaced.

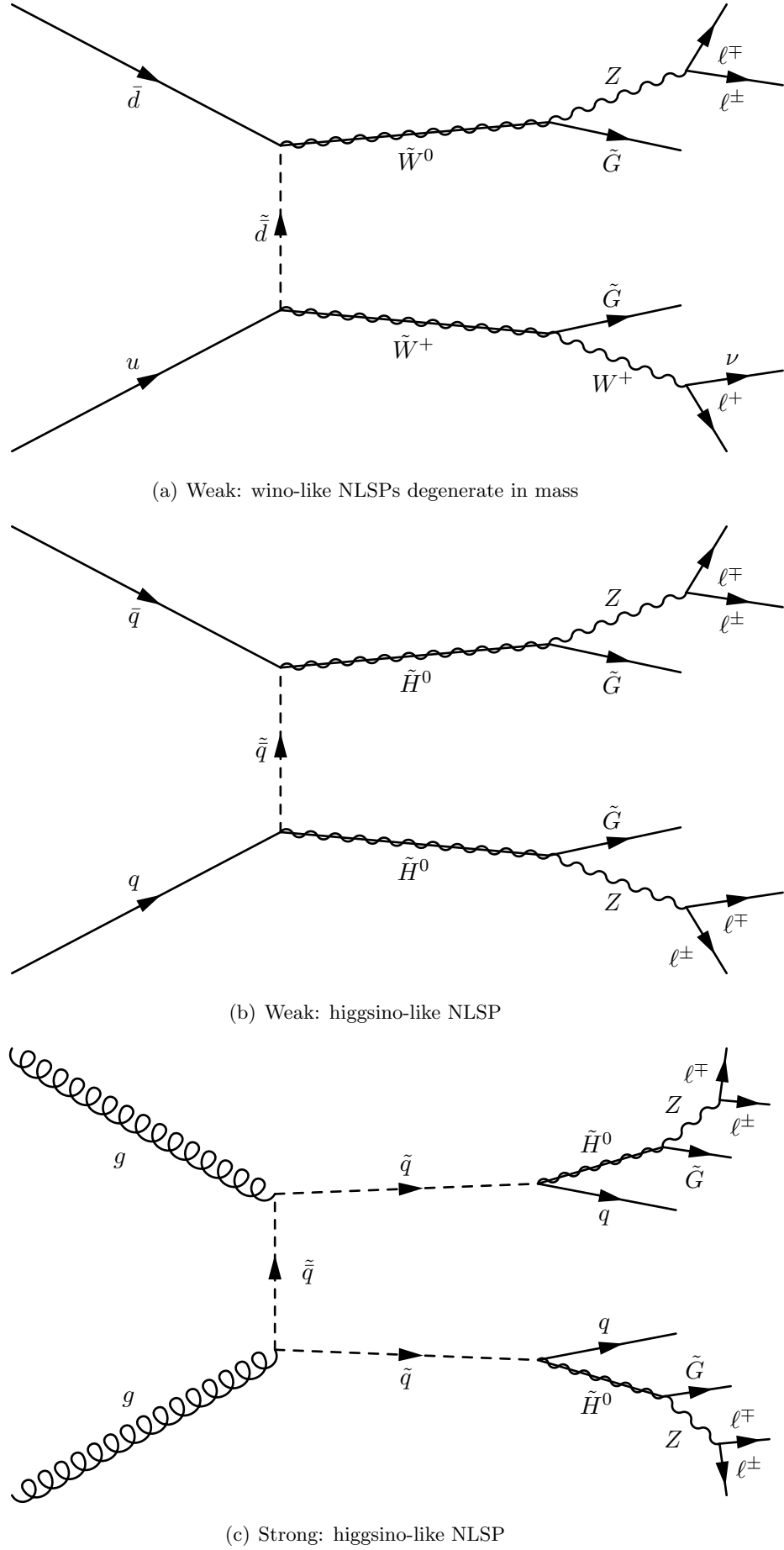


Figure 2.8: Example interactions in GGM models. Here, weak and strong refer to the force mediating each decay. Wino-like co-NLSPs are $\tilde{\chi}_1^0$ and $\tilde{\chi}_1^\pm$ with near-degenerate masses, while higgsino-like NLSPs are $\tilde{\chi}_1^0$ with predominant higgsino composition.

2.4.1.1 Wino and higgsino NLSP GGM models

Two models are considered here: one with neutral higgsino NLSP, and one with wino co-NLSPs. Both models assume prompt NLSP decays with $c\tau = 0.1$ mm, which have similar phenomenology to the other SUSY scenarios considered in this work. The phenomenology of such models is treated in [94].

In the model with a near-degenerate $\tilde{\chi}_1^0$ (mainly \tilde{W}^0) and $\tilde{\chi}_1^\pm$ (mainly \tilde{W}^\pm) co-NLSPs which decay preferentially to $Z\tilde{G}$ and $W^\pm\tilde{G}$. This model has $|m_2| \ll |\mu|$ and $|m_2| < |m_1|$, with $m_1 = \mu = 1.5$ TeV, $\tan\beta = 2$. The values of the gluino and NLSP masses in are set to the following values to define phenomenological grids:

- The \tilde{g} masses vary between 300 and 1000 GeV in increments of 100 GeV. The first two \tilde{W} masses are 120 and 150 GeV, and subsequent masses are incremented by 100 GeV, starting at 200 GeV. If this leads to equal masses, a 10 GeV cut on the \tilde{W} mass is imposed to keep the \tilde{W} lighter than the \tilde{g} leading to points like $(m_{\tilde{W}}, m_{\tilde{g}}) = (390, 400)$ GeV.

In the model with an NLSP that is mainly higgsino \tilde{h}^0 , the decays $\tilde{\chi}_1^0 \rightarrow Z + \tilde{G}$ can dominate. Intermediate decays involving $\tilde{\chi}_1^\pm \rightarrow W^\pm + \tilde{\chi}_1^0$ can lead to multilepton final states. This model has parameters $|\mu| \ll |m_1|, |m_2|$, and $m_1 = m_2 = 1$ TeV, with $\tan\beta = 1.5$. The values of the gluino and NLSP masses in are set to the following values to define phenomenological grids:

- The \tilde{H} masses vary between 110 and 890 GeV, while \tilde{g} masses vary between 300 and 900 GeV in increments of 100 GeV. The first few \tilde{H} masses are 110, 115, 120 and 150 GeV, and subsequent masses are incremented by 100 GeV, starting at 200 GeV. When the gluino and higgsino masses are equal, 10 GeV cuts on the \tilde{H} masses are used to keep the \tilde{H} lighter than the \tilde{g} .

The grid spacings and cross sections at each point are shown in Figure 2.10. The cross sections in the wino co-NLSP model points simulated range between 2.4×10^{-3} and 6.9 pb, while those for the higgsino NLSP model range between 3.7×10^{-3} and 13.5 pb. The technical details of the cross section calculation are discussed in Section 4.3.1.2 and 4.3.2.2. Possible decay chains are shown in Figure 2.8, and example spectra are shown in Figure 2.9.

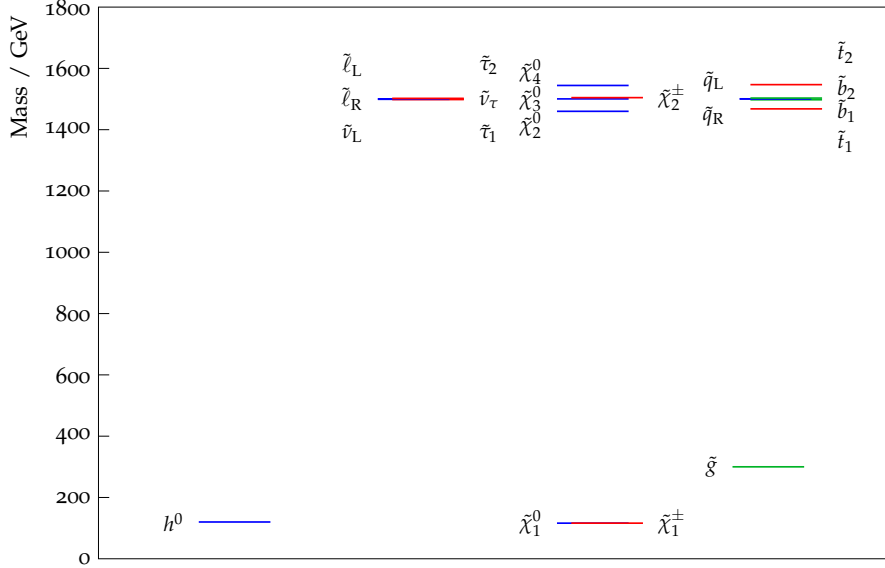
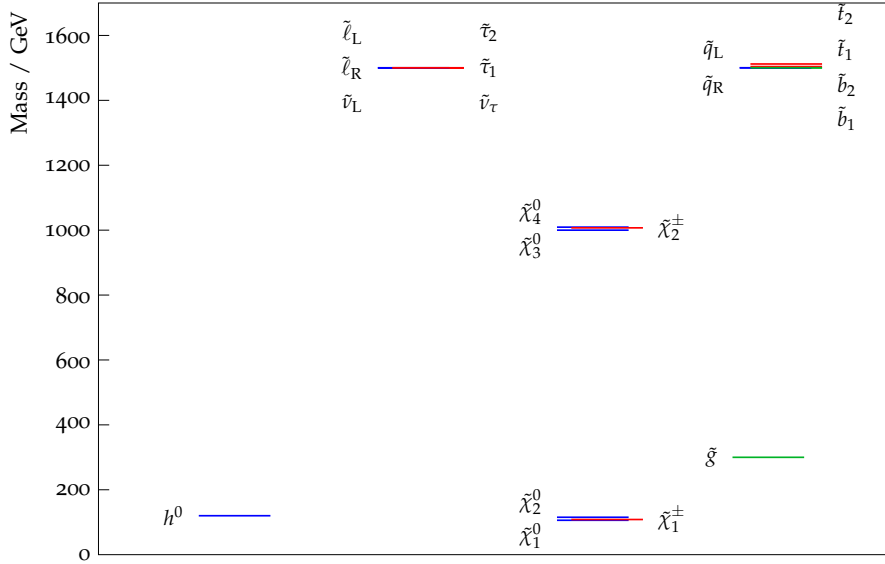
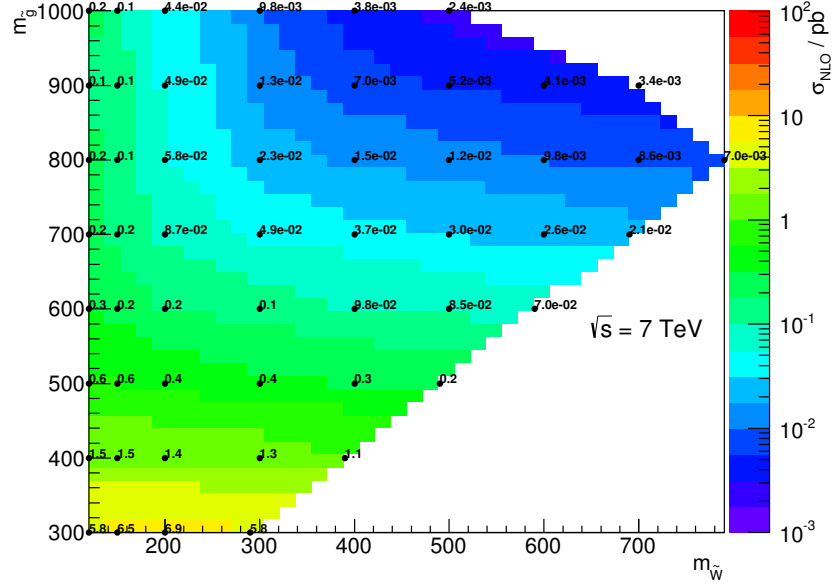
(a) Wino co-NLSP ($m_{\tilde{g}} = 300$ GeV, $m_{\tilde{W}^0, \tilde{W}^\pm} = 120$ GeV)(b) Higgsino NLSP ($m_{\tilde{g}} = 300$ GeV, $m_{\tilde{H}} = 115$ GeV)

Figure 2.9: GGM spectra for $m_{\tilde{g}} = 300$ GeV and a) $m_{\tilde{W}^0, \tilde{W}^\pm} = 120$ GeV and b) $m_{\tilde{H}} = 115$ GeV. The other Higgs sector particles have masses of approximately 2 TeV and are omitted from the plot. Generated using PySLHA [95].

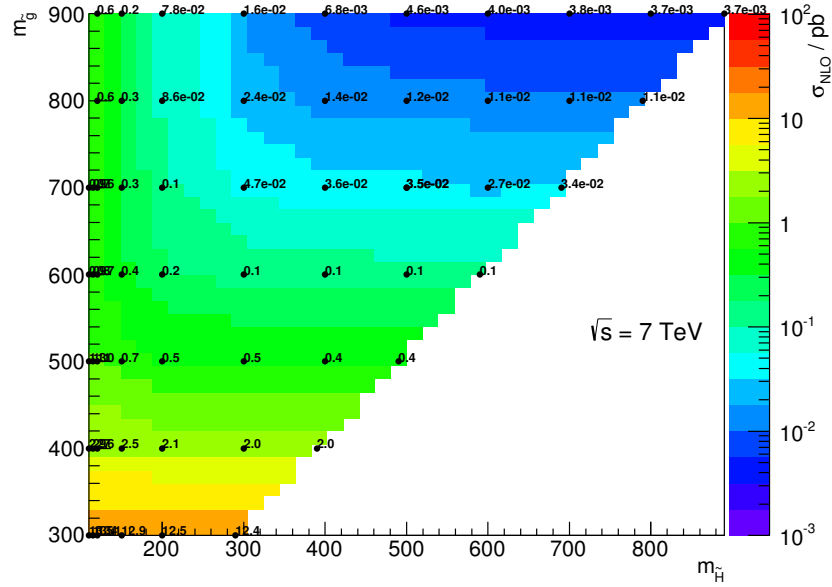
2.4.2 Phenomenological alternatives to supersymmetry breaking

Models exist which do not specify the exact form of SUSY breaking mechanism, leaving the 124 free parameters of the MSSM unconstrained. The phenomenological MSSM (pMSSM) [78] constrains the parameters by the following assumptions:

- no new flavour-changing or CP-violating interactions [73];



(a) Wino co-NLSP



(b) Higgsino NLSP

Figure 2.10: Cross sections for simulated points in the two GGM models.

- the LSP is the lightest neutralino;
- the Yukawa couplings of the first two generations are negligible;
- the dark matter density observed by WMAP [96] is set as an upper bound on the LSP density, allowing for additional possible non-SUSY sources of dark matter;

- contributions to the invisible width of the Z boson are ≤ 2 MeV;

With these assumptions applied, only 19 out of the original 124 parameters are left. These are as follows:

- the three gaugino masses M_1 , M_2 and M_3 ;
- the Higgs parameters m_A , $\tan \beta$ and μ ;
- the squared masses for the first and second generation squarks and sleptons: $M_{\tilde{Q}_{12}}^2$, $M_{\tilde{U}_{12}}^2$, $M_{\tilde{D}_{12}}^2$, $M_{\tilde{L}_{12}}^2$, $M_{\tilde{E}_{12}}^2$;
- the squared masses for the third generation squarks and sleptons: $M_{\tilde{Q}_3}^2$, $M_{\tilde{U}_3}^2$, $M_{\tilde{D}_3}^2$, $M_{\tilde{L}_3}^2$, $M_{\tilde{E}_3}^2$;
- the A -parameters for the third generation: A_t , A_b and A_τ .

2.4.2.1 Direct gaugino production in the pMSSM

A pMSSM scenario sensitive to direct gaugino production is explored. This model has heavy (> 1 TeV) squarks and gluinos, leading to low hadronic activity. Additionally, $\tan \beta = 6$ ensures equal branching ratios to all quark and lepton generations. Different values of M_1 , M_2 and μ are chosen for each grid, leading to significant variation in the proportion of higgsino and gaugino in the charginos and neutralinos. Three values of M_1 (100, 140 and 250 GeV) are chosen, with M_2 and μ taking the values 100, 110, 120, 140, 160, 180, 210, 250, 300 and 350 GeV. Left-handed sleptons are taken to have masses above 1 TeV, while right-handed sleptons are placed midway between the two lightest neutralinos:

$$m_{\tilde{\ell}_R} = \frac{m_{\tilde{\chi}_1^0} + m_{\tilde{\chi}_2^0}}{2}. \quad (2.24)$$

The masses are degenerate across all generations and the third generation A -parameters are set equal to zero. An example spectrum for the point $M_1 = 100$ GeV, $M_1 = 160$ GeV, $\mu = 160$ GeV is shown in Figure 2.11. The chargino masses vary across the other grid points according to Equation (2.19), while the neutralino mixing varies as discussed in Section 2.3.1. The parameters are chosen to exceed the LEP bounds on chargino masses ($m_{\tilde{\chi}_1^\pm} = 103.5$ GeV) [97]. The absence of light left-handed sleptons reduces the probability of leptonic decays, but also reduces the number of free parameters required to specify the grids: the results are therefore conservative and somewhat more general. The mass of the lightest Higgs m_{h_0} is set to 119.4 GeV, close to the observed Higgs-like particle mass of 125–127 GeV (the grid parameters were defined before the Higgs discovery). Higgs decays

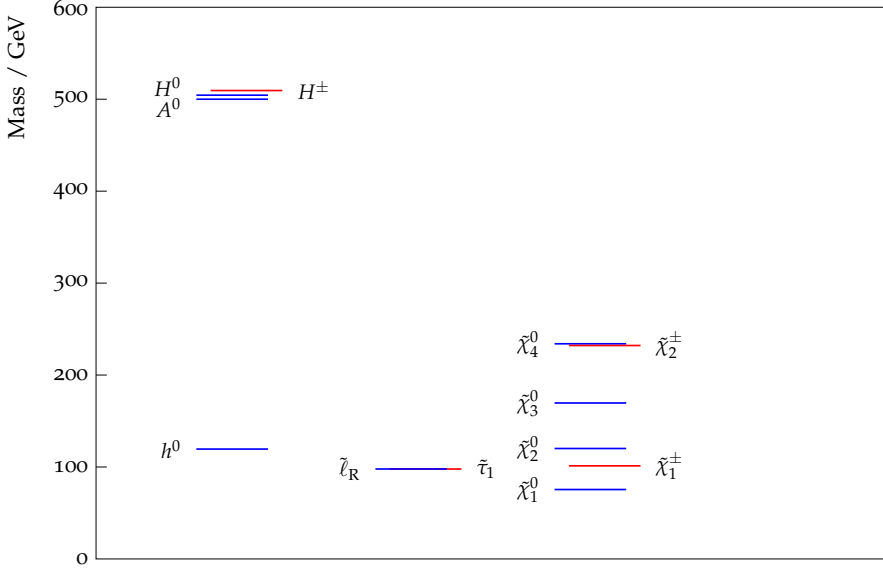


Figure 2.11: An example pMSSM spectrum with parameters $M_1 = 100$ GeV, $M_2 = 160$ GeV, $\mu = 160$ GeV. All other SUSY particles have masses of approximately 3 TeV and are omitted from the plot. Generated using PySLHA [95].

in any case make up a very small proportion of the events in these scenarios. The cross sections for the pMSSM grid used vary between 0.1 and 100 pb - the cross sections for all generated points are shown in Figure 7.11.

2.4.3 Simplified models

Only a few parameters of a theory can be explored in a realistic search: the 124 parameters of the MSSM must therefore be reduced. In GGM and the pMSSM, this is done by introducing additional model assumptions. An alternative is to reduce the content of the theory to two or three particle masses and branching ratios: these characteristics define a *simplified model*. Such models cannot be exactly realised in Nature, but have the advantage of being more amenable to experimental searches, and more general, since fewer assumptions have been made about the nature of new physics. Simplified models can also be seen as the building blocks of realistic models: the observable sector of a given model is determined entirely by its particle content and possible decays.

2.4.3.1 Simplified models of direct gaugino production

In these models, the $\tilde{\chi}_2^0$ and $\tilde{\chi}_1^\pm$ are assumed to be degenerate in mass, and to have no entirely \tilde{W}^0 and \tilde{W}^\pm respectively. Two models of $\tilde{\chi}_2^0\tilde{\chi}_1^\pm$ production are considered in this thesis. Firstly, ‘‘Model A’’ with intermediate slepton/sneutrino decays is defined. This

model contains left-handed sleptons and sneutrinos: right-handed sleptons and sneutrinos are ignored. All slepton generations are mass degenerate, as are sleptons and sneutrinos. The left-handed sleptons and neutralinos satisfy the mass relation

$$m_{\ell_L} = \frac{m_{\tilde{\chi}_2^0} + m_{\tilde{\chi}_1^0}}{2} \quad (2.25)$$

Branching ratios to $e/\mu/\tau$ are equal, as required by lepton universality and expected in realistic models with low $\tan\beta$ [74]. Benchmark points are simulated with masses from $m_{\tilde{\chi}_1^\pm}, m_{\tilde{\chi}_2^0} = 112.5$ GeV to 750 GeV, and $m_{\tilde{\chi}_1^0}$ between 12.5 and 607.5 GeV. From equation (2.25), the choice of $m_{\tilde{\chi}_1^\pm}, m_{\tilde{\chi}_2^0}$ and $m_{\tilde{\chi}_1^0}$ determines the slepton mass: this varies between 62.5 and 625 GeV.

Secondly, ‘‘Model B’’ with intermediate gauge boson decays is defined. In this model, the decays $\tilde{\chi}_2^0 \rightarrow Z + \tilde{\chi}_1^\pm$ and $\tilde{\chi}_1^\pm \rightarrow W^\pm + \tilde{\chi}_1^0$ are constrained to always occur. Benchmark points are defined with $m_{\tilde{\chi}_1^\pm}, m_{\tilde{\chi}_2^0}$ masses between 100 and 500 GeV, with $m_{\tilde{\chi}_1^0}$ between 0 and 450 GeV.

Feynman diagrams for $\tilde{\chi}_2^0 \tilde{\chi}_1^\pm$ production in both models are shown in Figure 2.12, and the cross sections are shown in Figure 2.13. The cross sections for Model A vary between approximately 6.5 and 10^{-3} pb, while those for Model B vary between approximately 0.3 and 10^{-3} pb.

2.4.3.2 Alternate models and search paradigms

The models chosen here, with the exception of GGM, have heavy squarks and gluinos (pMSSM) or none at all (simplified models). Clearly, supersymmetry with light squarks and gluinos may be manifested in nature, and dedicated searches have been performed (see [98] for example). These searches, and many others performed with search strategies sensitive to other models (for instance, those R -parity violating models) are complementary to those presented here.

2.5 Summary

The Standard Model of particle physics has been presented in some detail, and the motivation for supersymmetry as an extension has been discussed. The supersymmetric models considered in this work (GGM, the phenomenological MSSM and simplified models) were discussed in some detail. In order to test the Standard Model and search for evidence of supersymmetry or other new physics, the Large Hadron Collider (LHC) and associated detectors were constructed: the LHC and ATLAS detector are discussed in detail in

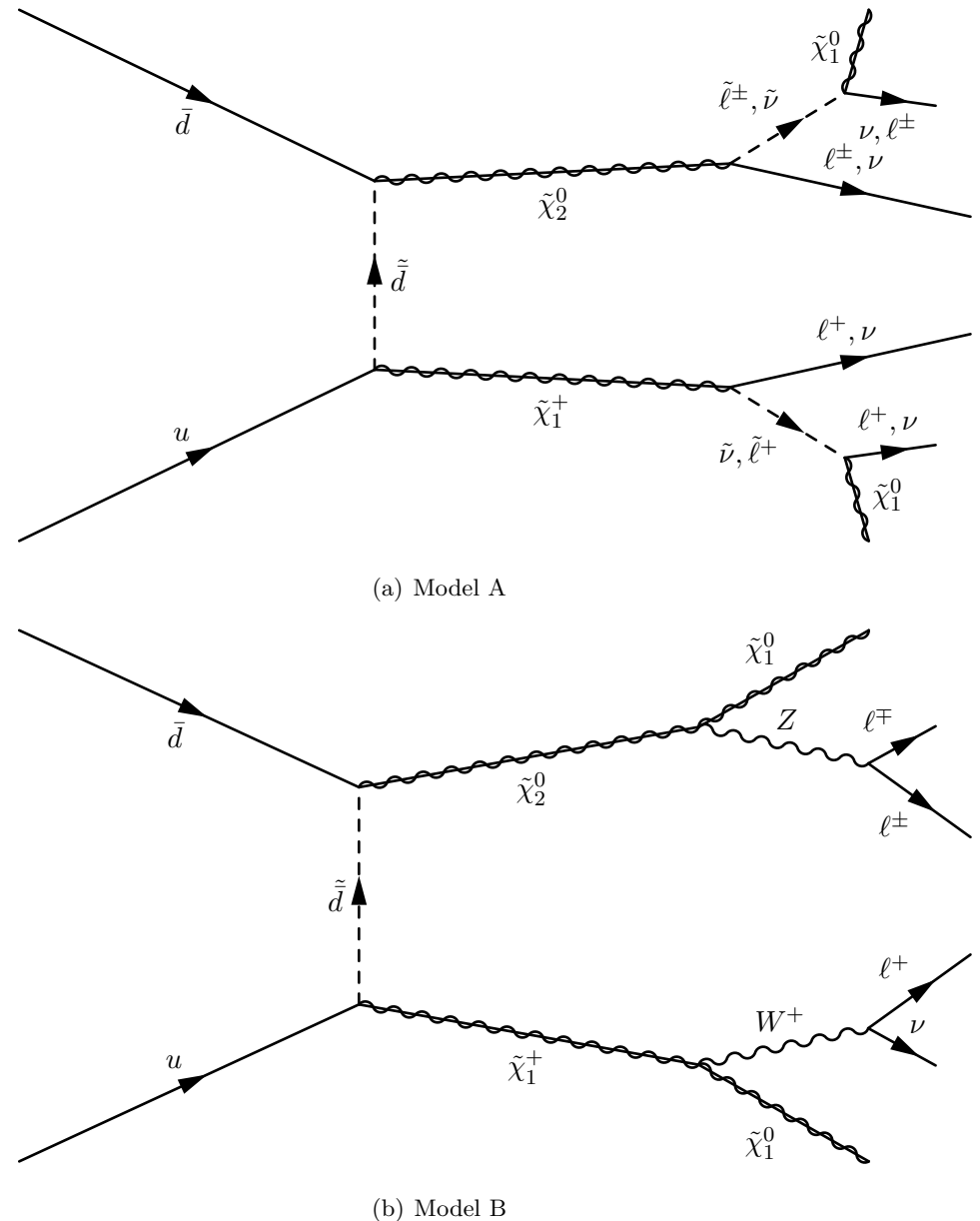
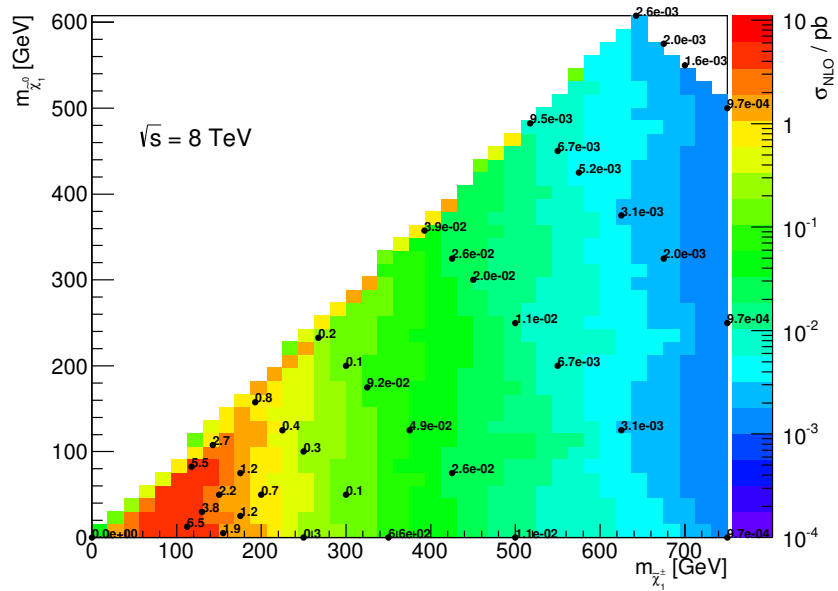
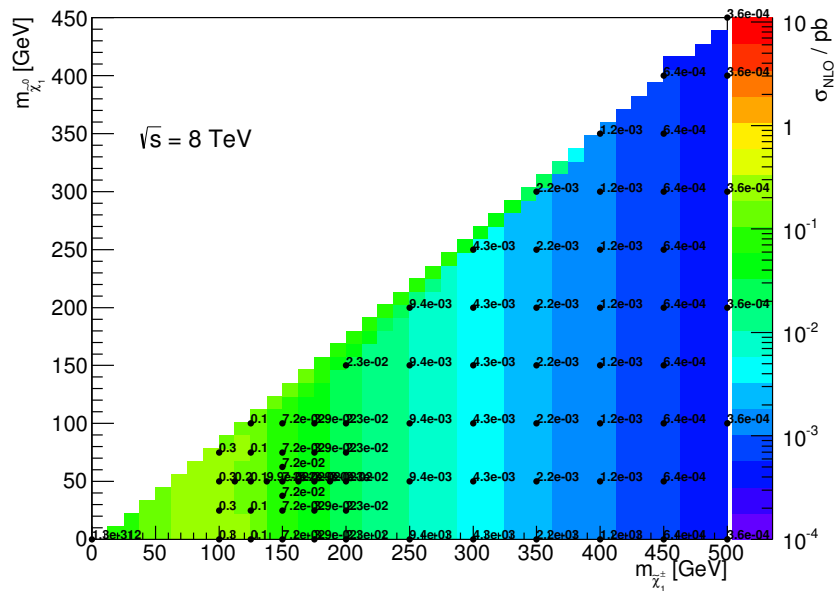


Figure 2.12: Feynman diagram for $\tilde{\chi}_2^0\tilde{\chi}_1^\pm$ production, with intermediate decays via sleptons and sneutrinos (a) and gauge bosons (b).



(a) Model A



(b) Model B

Figure 2.13: Cross sections for simulated points in the two simplified models.

Chapter 3.

Chapter 3

The LHC and ATLAS detector

The days of simple experiments
are over.

John Fowles [99]

3.1 The LHC

The Large Hadron Collider (LHC) is a synchrotron of 27 km circumference at CERN, near Geneva [100]. An artist’s impression of the LHC is shown in Figure 3.1. It was designed to provide proton-proton collisions at a nominal centre of mass energy of $\sqrt{s} = 14$ TeV, and is fed by a sequence of progressively more powerful accelerators. The first is the linear accelerator Linac 2, accelerating beams up to 50 MeV, followed by the small Proton Synchrotron Booster (PSB) at energies up to 1.4 GeV, then the Proton Synchrotron (PSB) at energies up to 28 GeV, followed by the medium-sized Super Proton Synchrotron (SPS) up to 450 GeV. To date, only collisions at $\sqrt{s} = 7$ TeV (2010–2011) and $\sqrt{s} = 8$ TeV (2012) have been achieved, as well as short periods of operation at two lower energies ($\sqrt{s} = 2.36$ TeV and $\sqrt{s} = 2.76$ TeV). Neither of the lower energy datasets is considered in this work. The LHC has also been used to accelerate lead ions, but only results from proton collisions are considered here. The LHC was designed to provide enough data at high enough energy to discover or exclude the existence of a Higgs boson and physics beyond the Standard Model. Such processes have cross sections of $O(1 \text{ fb})$, so it follows that the LHC must provide several inverse femtobarns worth of data in order to be able to make any statements about the existence of such processes. The instantaneous luminosity of a collider colliding two proton beams divided into distinct bunches is given by [5]:

$$\mathcal{L} = f \frac{n_1 n_2}{4\pi\sigma_x\sigma_y} \quad (3.1)$$

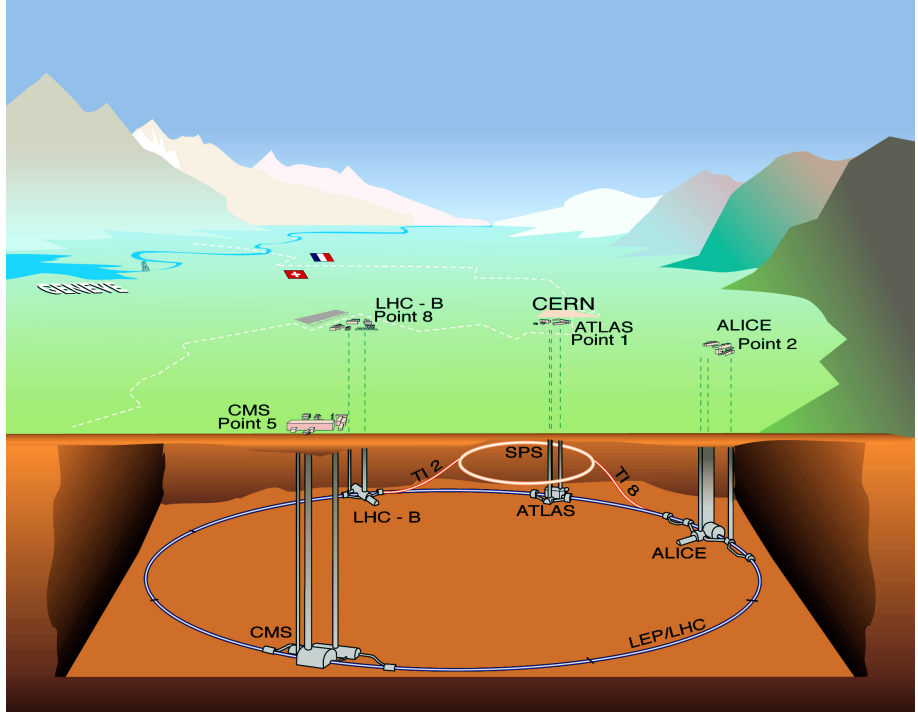


Figure 3.1: Artist’s impression of the LHC accelerator and experiments. From [101].

where f is the frequency of bunch collisions, n_1 and n_2 are the number of protons in bunches 1 and 2, and σ_x and σ_y are the horizontal and vertical RMS beam sizes. Clearly, in order to maximise the number of collisions, f , n_1 and n_2 must be maximised, and the transverse beam area must be minimised. In 2011 and 2012, f was 20 MHz, each bunch was composed of approximately 10^{11} protons, and the linear beam sizes were both approximately 0.1 mm. The LHC has a design instantaneous luminosity of $1.0 \times 10^{34} \text{ cm}^{-2} \text{ s}^{-1}$. It achieved peak instantaneous luminosities of $4 \times 10^{33} \text{ cm}^{-2} \text{ s}^{-1}$ in 2011, and $7.7 \times 10^{33} \text{ cm}^{-2} \text{ s}^{-1}$ in 2012. In 2011 the LHC delivered an integrated luminosity of over 5 fb^{-1} , and in 2012 provided approximately 21 fb^{-1} . The collision of two bunches is referred to as a bunch crossing: most of the protons in each bunch will not interact with each other: the average number of interactions per bunch crossing ($\langle \mu \rangle$) of 9.1 in 2011 and 20.0 in 2012 [102], as shown in Figure 3.2. The increase in instantaneous luminosity over time is shown in Figure 3.3. In order to measure the properties of the collisions, four large particle detectors are situated at collision points around the LHC, with additional smaller detectors at other locations. The two large, multi-purpose detectors, ATLAS [103] and CMS [104], have comparable capabilities for a wide range of Standard Model (SM) physics measurements and searches for new physics. The other large detectors (LHCb [105], ALICE [106]) are specialised for the study of B-physics and heavy ion physics respectively.

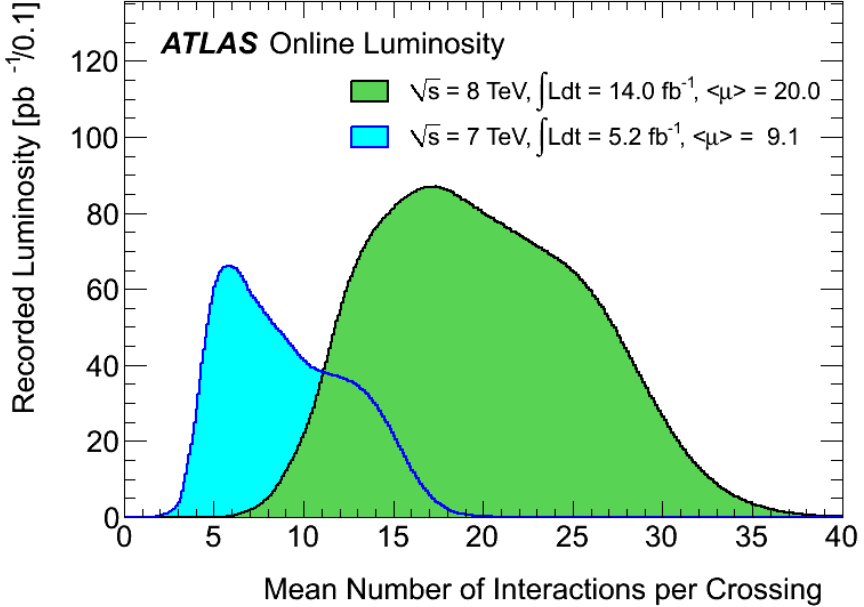


Figure 3.2: Average interactions per bunch crossing ($\langle \mu \rangle$), normalised to the integrated luminosity collected at a given $\langle \mu \rangle$, recorded by the ATLAS detector in 2011 and 2012.

3.2 The ATLAS detector

The ATLAS (A Toroidal LHC ApparatuS) detector [103] is one of two general-purpose detectors at the LHC. Its basic shape is that of a cylinder with axis of symmetry centred on the beam pipe. Starting from the concentric layer closest to the beam pipe, it consists of a central tracking system, hermetic electromagnetic and hadronic calorimeters, a solenoidal magnet and a muon tracking system with surrounding toroidal magnets, shown in Figure 3.4. Most of the sub-detectors are separated into separate “barrels” in the centre of the detector with additional sections at each end (“endcaps”). Generally, the barrel elements are arranged with axial segments (relative to the beampipe), while the endcaps have radial segments.

3.2.1 ATLAS detector geometry and kinematics

ATLAS uses a right-handed cylindrical co-ordinate system [103], with origin defined as the nominal interaction point and the z -axis is coincident with the beam direction. The y co-ordinate points upwards, while the x coordinate points out of the LHC ring. Since the detector is approximately symmetric around the z -axis, detector sides are defined as follows: side A has $z > 0$ and side C has $z < 0$. The ϕ angle is in the plane perpendicular to the z -axis, while θ is the angle from the z -axis. The transverse momentum of a particle

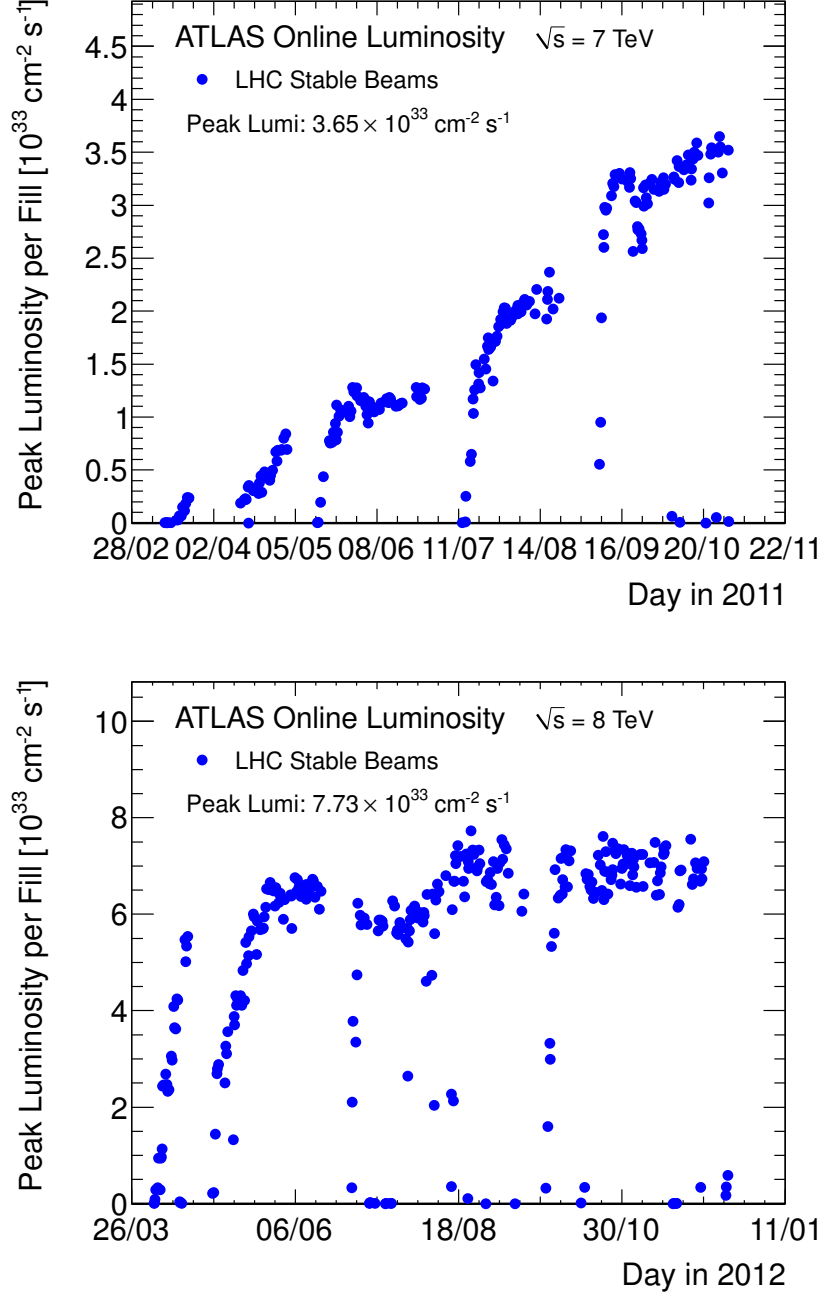


Figure 3.3: Peak instantaneous luminosity during 2011 and 2012 operation. Taken from [102].

is defined as:

$$p_T = \sqrt{p_x^2 + p_y^2} \quad (3.2)$$

where p_x and p_y are the x and y components of momentum respectively. When measuring the kinematics of particles at a collider, it is convenient to use the *rapidity*, y , defined as:

$$y = \frac{1}{2} \left(\frac{E + p_z}{E - p_z} \right) \quad (3.3)$$

where E is the particle's energy and p_z is the component of the particle momentum in the z -direction. The sum and difference of rapidities is invariant under boosts in the z -direction [5]. If the particle is massless, the rapidity reduces to the *pseudo-rapidity*, η :

$$\eta = -\ln \left(\tan \left(\theta / 2 \right) \right) \quad (3.4)$$

For stable, high- p_T particles produced in LHC collisions, the distinction between y and η is negligible, and η may therefore be used as a angular coordinate instead of θ . To quantify the distance between two particles 1 and 2, with coordinates (η_1, ϕ_1) and (η_2, ϕ_2) , the distance parameter $\Delta R = \sqrt{(\eta_1 - \eta_2)^2 + (\phi_1 - \phi_2)^2}$ is often used. When imposing a condition of spatial proximity on particles 1 and 2, the requirement $\Delta R < R_{\text{max}}$ defines a cone of radius R_{max} around one of the two particles, within which the second particle must be found for it to be declared “matched” to the particle in question.

The magnitude and direction of the longitudinal momentum $|p_z|$ of collision products depend on the unknown initial momenta of the constituent quarks and gluons in each parton, so the total momentum in an event cannot be determined. However, since the initial momentum in the transverse plane (perpendicular to the beam direction) is approximately zero, it follows that the final transverse momentum is also zero. An imbalance in the total transverse momentum (p_T^{vis}) of the visible collision products therefore indicates the presence of additional invisible particles. The *missing transverse energy* (E_T^{miss}) is defined as

$$\vec{E_T^{\text{miss}}} = -\vec{p_T^{\text{vis}}} = -\sum_{\text{vis}} \vec{p_T} \quad (3.5)$$

where the sum runs over all visible particles. The E_T^{miss} is the magnitude of the total momentum vector of any invisible or otherwise undetected particles.

3.3 ATLAS general detector design

ATLAS is designed to measure SM processes and search for new physics. In many cases, high momentum leptons and light and heavy-flavour jets are expected, as well as (depending on the process) significant E_T^{miss} . The design of ATLAS, like all collider detectors, is based on the requirements of accurate momentum and energy measurement, hermeticity and fast detector readout. The momentum of charged particles is measured in an inner tracker, and muon momentum is additionally measured in a dedicated muon spectrometer. The paths of charged particles in the inner tracker are bent by a 2 T solenoidal magnet, while those of muons in the muon spectrometer are bent by toroidal magnets with fields of up to 1 T. Electromagnetic and hadronic calorimeters measure energy deposition

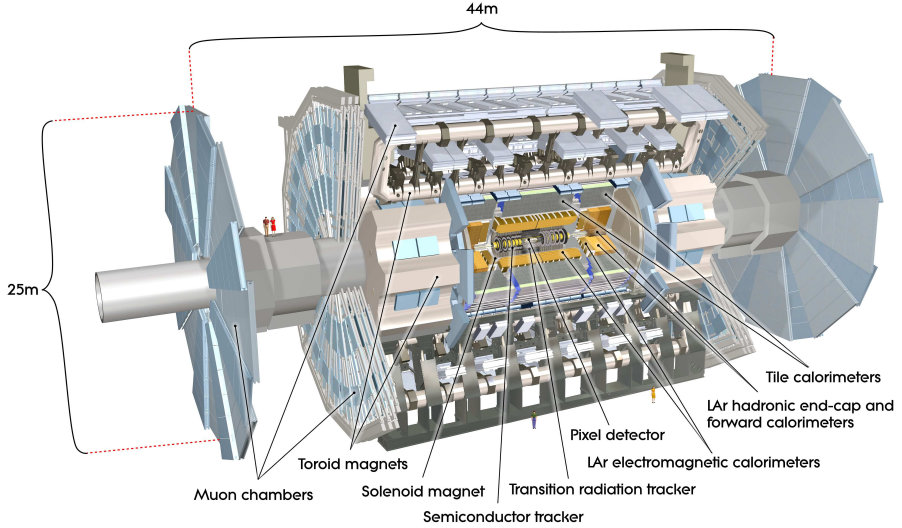


Figure 3.4: A schematic of the ATLAS detector (from [103]).

from electrons, photons, muons and hadrons. Electromagnetic and hadronic showers from particles up to $|\eta| < 4.9$ are expected to be fully contained by the calorimeters. The calorimeters and muon spectrometer are both used in the trigger to reject/accept events every bunch crossing: this requires a delicate interplay of detector and algorithm design. The design p_T and energy measurement resolutions for each subdetector are shown in Table 3.1, for both trigger-level and offline selections.

The following sections discuss in some detail the different sub-detectors which make up the ATLAS detector, as well as the trigger system. There are additional detectors not relevant to the work presented here: ALFA [107], used for measurements of elastic scattering at very high η ; the ZDC [108] situated 140 m from the interaction point; used for forward calorimetry measurements; LUCID [107], used for luminosity measurements the BCM [107] used to measure beam losses and luminosity; and the MBTS, used to trigger events of interest for non-perturbative QCD.

3.4 ATLAS detector components

3.4.1 ATLAS Inner Detector

The ATLAS inner tracking system, shown in Figure 3.5, is designed to detect tracks from charged particles within $|\eta| < 2.5$ with high momentum resolution ($\sigma_{p_T}/p_T = 0.05\% p_T + 1\%$). It is made up of three concentric sub-detectors: two silicon detectors (the Pixel and Semiconductor Tracker (SCT) detectors) and the Transition Radiation Tracker (TRT). The cylindrical geometry of the inner detector is shown in the three-dimensional schematics

Detector type	Subdetector	Section	$ \eta $ (max., min.)		Resolution type	Design resolution
			Trigger	Offline		
Tracking	ID		$(0, 2.5)$		σ_{p_T}/p_T	$1\% + 0.05\% p_T$
		MS	$(0, 2.4)$	$(0, 2.7)$		10% at $p_T = 1$ TeV
Calorimetry	ECAL		$(0, 2.5)$	$(0, 3.2)$	σ_E/E	$0.7\% + 10\%/\sqrt{E}$
		Barrel	$(0, 3.2)$			$3\% + 50\%/\sqrt{E}$
	HCAL	Endcaps	$(3.1, 4.9)$			$10\% + 100\%/\sqrt{E}$

Table 3.1: Expected resolutions of each ATLAS sub-detector. Measured resolutions are discussed in Chapter 4. Here, the trigger and offline columns refer to whether the appropriate $|\eta|$ range is used by the trigger system, or available once the event has been recorded. Taken from [103].

in Figure 3.5, while the η - z plane geometry is shown in Figure 3.6. The tracking algorithms used in the trigger and offline tracking selection are discussed in Sections 3.5.2.3 and 4.4.1 respectively.

3.4.1.1 Pixel Detector

The Pixel detector consists of three concentric layers of silicon sensors encircling the beampipe. It extends out to $|\eta| < 2.5$ - as may be seen in Figure 3.6, three layers will be traversed by a charged particle. A cluster of signals on a sensor (known as a hit) defines a space-point.

3.4.1.2 ATLAS Semiconductor Tracker

The SCT barrel consists of four concentric layers of silicon microstrips, while the endcap consists of nine layers of silicon microstrips. The barrel extends to $|\eta| < 1.7$, while the endcaps extend from $1.2 < |\eta| < 2.5$. Each module consists of two identical sensors with 768 silicon strips on each side, aligned at a stereo angle of 40 mrad. In the barrel, the inner sensor layer is oriented parallel to the beampipe, while in the endcaps the inner sensor strips point towards the beampipe. A charged particle passing through a module will activate one or more strips on each module side: the intersection point between activated strips on opposite layers intersect defines a space-point.

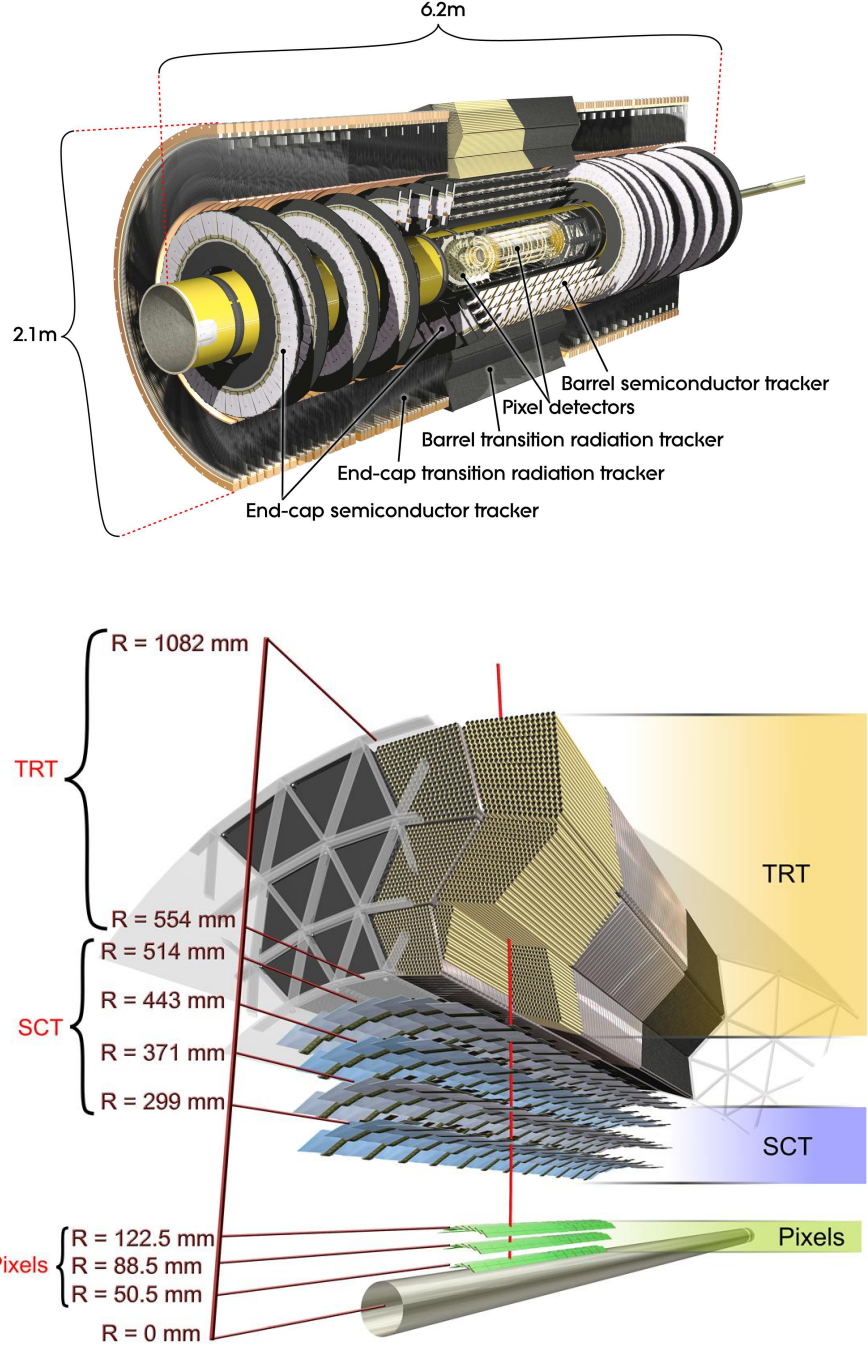


Figure 3.5: Cutaways of the ATLAS inner detector (from [103]).

3.4.1.3 ATLAS Transition Radiation Tracker

The Transition Radiation Tracker (TRT) is a cylindrical detector extending to $|\eta| < 2.0$ considering both barrel and endcap, and consists of nearly 300,000 straw tubes of plastic filled with a $\text{Xe}-\text{CO}_2 - \text{O}_2$ gas mixture, with a central gold-plated tungsten wire. When

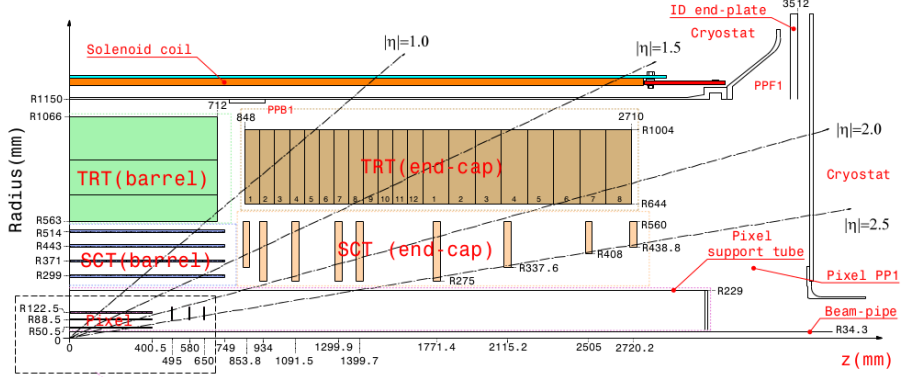


Figure 3.6: A cross section of the ATLAS inner detector in the η - z plane (from [103]).

a charged particle traverses the straw, it ionises the gas, and the ionisation electrons drift towards the wire.

Transition radiation occurs when a charged particle crosses between media with different dielectric constants: the energy radiated is proportional to the Lorentz factor $\gamma = E/mc^2$ of the charged particle. Transition radiation at X-ray frequencies is recorded as an additional, higher energy hit (known as a high-threshold hit) in the TRT. A significant chance of transition radiation at X-ray frequencies occurs for electrons of approximately 1 GeV, and for other particles only for upwards of 200 GeV due to the dependence on mass. The probability of radiation for pions and electrons as a function of energy and Lorentz factor is shown in Figure 3.7. Since a high-threshold hit is only likely for electrons, its presence is used to discriminate against pions [109]. The “low” threshold required to register a hit is 300 eV, while the “high” threshold for transition radiation is between 6 and 7 keV [110]. The TRT barrel extends from $|\eta| < 1.0$, while the endcaps extend from $0.8 < |\eta| < 2.0$. The overlap means that, as shown in Figure 3.6, tracks with $0.8 < |\eta| < 1.0$ can have hits in both the TRT barrel and an endcap. A typical track will have approximately 36 hits, which allows for improved estimation of track parameters when combined with the Pixel and SCT hits.

3.4.2 ATLAS Magnet System

ATLAS has a two-part magnet system consisting of a solenoid and toroidal system, shown schematically in Figure 3.8. The solenoid and toroids provide a magnetic field for the inner detector and muon spectrometer respectively. The ATLAS solenoidal magnet is a 2 T superconducting magnet, with an inner (outer) diameter of 2.46 (2.56) m and axial length of 5.8 m. The superconducting toroidal magnet system comprises a central barrel and two endcap toroids, providing fields of 0.5 and 1 T respectively. The barrel toroid has

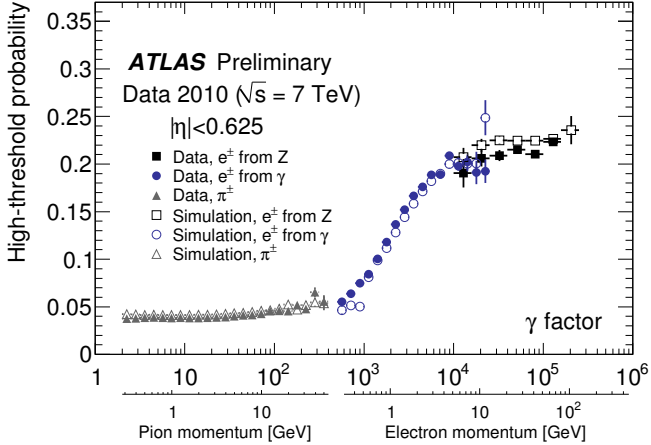


Figure 3.7: Probability of a high threshold hit from transition radiation of the TRT as a function of particle momentum and Lorentz factor. The probability of radiation remains low for pion candidates up to tens of GeV. In this plot, only particles in the barrel region ($|\eta| < 1.0$) are considered. From [109].

an axial length of 25.3 m, inner diameter 9.4 m, and outer diameter 20.1 m. All solenoid and toroid coils are made of NbTi, which maintains a high magnetic field while remaining relatively thin [103] - this reduces unmeasured energy loss in the magnets.

3.4.3 ATLAS Calorimeter System

The ATLAS electromagnetic and hadronic calorimeters are shown in Figure 3.9, and discussed in more detail in Sections 3.4.3.1 and 3.4.3.2 respectively. Electromagnetic showers can be measured with higher precision than hadronic showers, with design resolutions of $10\% \sqrt{E} + 0.7\%$ for the electromagnetic calorimeter and up to $100\% \sqrt{E} + 10\%$. They have a combined coverage of $|\eta| < 4.9$. Both calorimeters are “sampling” calorimeters: in each detector, different materials are used to initiate particle showers and to measure the resulting energy. Particle energy is lost in one layer, then measured in the following layer, and this pattern is repeated throughout each calorimeter. The ATLAS calorimeters are non-compensating: namely, they respond differently to electromagnetic and hadronic showers. The electromagnetic calorimeter is designed to measure electron and photon energy loss through electromagnetic showers. In an electromagnetic shower, electrons and photons lose energy through a cascade of electromagnetic interactions with the calorimeter. The hadronic calorimeter is designed to measure the energy loss of hadrons losing energy in hadronic showers, which are cascades of nuclear interactions with the calorimeter. The radiation length (X_0) is defined [5] as the distance over which on average an electron loses

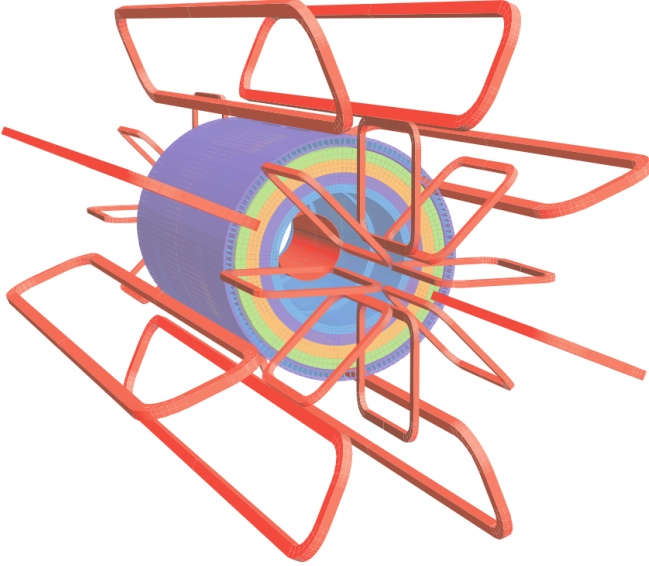


Figure 3.8: The ATLAS magnet system. In this drawing, the solenoid is the innermost red ring, while the next four rings (shown in various shades of blue, orange and green) are different sections of the electromagnetic and hadronic calorimeters. The outermost ring is the Tile Calorimeter, which acts as a flux return yoke for the magnet due to its high steel concentration. The large red loops are the barrel toroids, while the small red loops make up one set of endcap toroids, with a corresponding set on the other side. From [103].

all but $1/e$ of its energy in a given medium, while the nuclear interaction length (λ_I) is defined as the distance that a strongly interacting particle travels on average before losing all but $1/e$ of its energy through nuclear interactions. The electromagnetic calorimeter is more than $22 X_0$ thick in the barrel and more than $24 X_0$ thick in the endcap. The hadronic calorimeter is approximately $10 \lambda_I$ thick throughout the whole detector - the total number of radiation lengths of the calorimeters (including dead material) as a function of η are shown in Figure 3.10, derived from simulation. The other important characteristic of the calorimeters is their granularity, defined as the smallest measurable ($\Delta\eta, \Delta\phi$) segment. Details about the calorimeters' geometry and granularity are given in Table 3.2.

3.4.3.1 ATLAS electromagnetic calorimeter

The EM calorimeter barrel extends from $0 < |\eta| < 1.475$, and the endcaps from $1.375 < |\eta| < 2.5$. The solenoidal magnet is surrounded by the EM calorimeter - in order to reduce the amount of dead material, they share a common vacuum vessel. The EM calorimeter is formed of consecutive layers of lead absorber plates and liquid argon (LAr) instrumented by electrodes, arranged in an “accordion” geometry shown in Figure 3.11. Up to $|\eta| = 1.8$,

Component	Section	No. layers	$ \eta $ (min., max.)	Granularity ($\Delta\eta \times \Delta\phi$)	
				Min.	Max.
ECAL barrel	Presampler	1	(0, 1.52)	0.025×0.1	
	Calorimeter	3	(0, 1.35)	0.025×0.025	0.05×0.025
		2	(1.35, 1.475)		
ECAL endcap	Presampler	1	(1.5, 1.8)	0.025×0.1	
	Calorimeter	2	(1.375, 1.5)	0.05×0.025	0.1×0.1
		3	(1.5, 2.5)		
		2	(2.5, 3.2)		
				Granularity ($\Delta x \times \Delta y$ [cm])	
HCAL barrel	Calorimeter	3	(0, 1.0)	0.1×0.1	0.2×0.1
HCAL extended barrel		3	(0.8, 1.7)	0.1×0.1	0.2×0.1
HCAL endcap		4	(1.5, 3.2)	0.1×0.1	0.2×0.2
FCAL		3	(3.1, 4.9)	3.0×2.6	5.4×4.7

Table 3.2: The number of layers, extent in η and granularity of the calorimeters. Taken from [103].

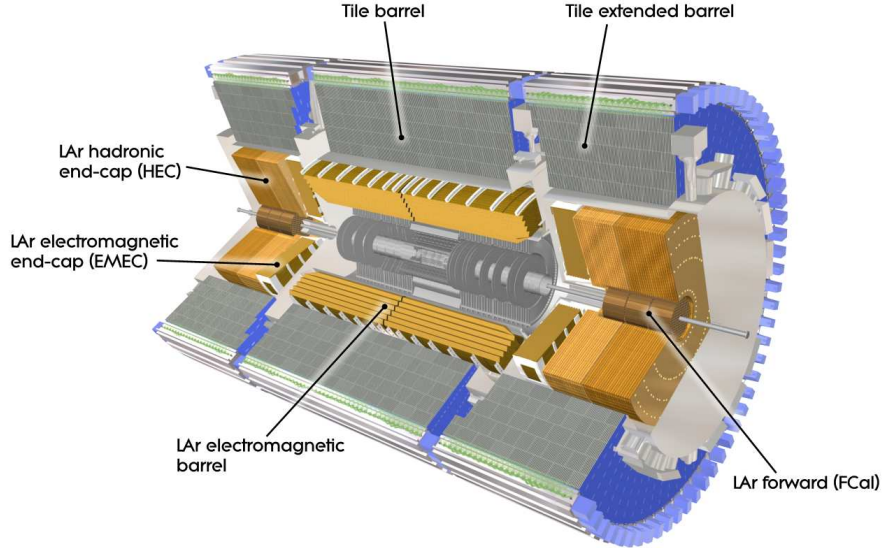


Figure 3.9: A cutaway of the ATLAS calorimeter system. Taken from [103].

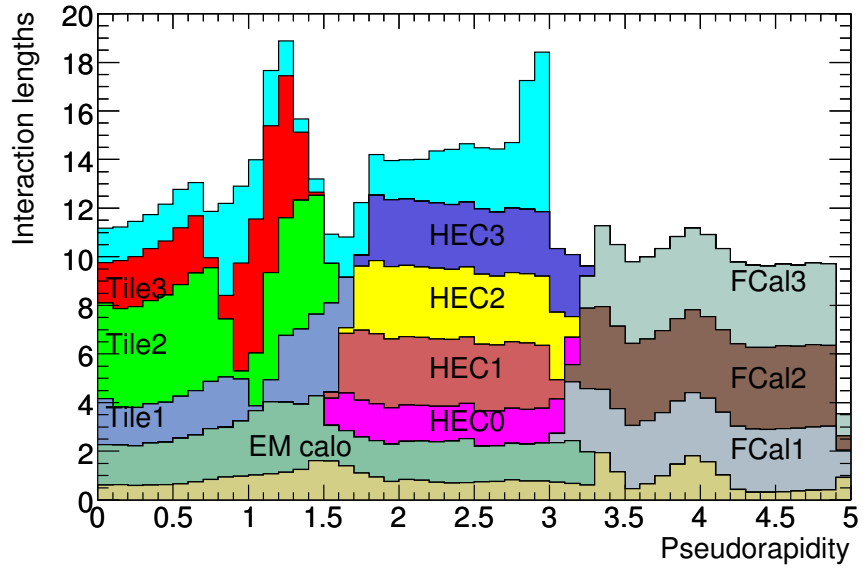


Figure 3.10: The amount of material, measured in nuclear interaction lengths, in the calorimetry system as a function of pseudo-rapidity. Material in the central solenoid and associated systems is shown in beige, while material in the muon spectrometer is shown in light blue. The values shown are simulated. Taken from [103].

the first layer of the calorimeter functions as a *presampler*. Since the presampler has no initial lead absorbing layer, it measures particle energy before any significant showering occurs. This helps mitigate the loss of energy in the ID and magnet system. After the presampler, there are two or three layers (depending on η range) of sampling calorimeter

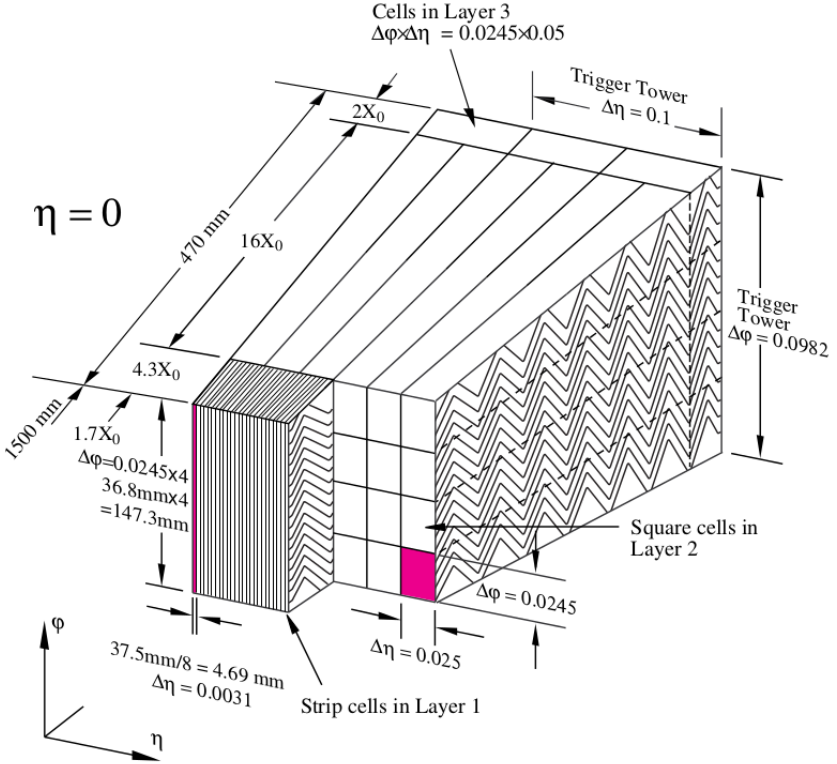


Figure 3.11: A sketch of a cross section of the ATLAS electromagnetic calorimeter barrel. Taken from [103].

as detailed in Table 3.2. The first sampling layer is used to distinguish between prompt photon production and photons from neutral pion decays, by distinguishing single and double showers. The second sampling layer contains the majority of the shower, and is used for the main energy measurement. Higher energy showers can extend to the third sampling layer: since hadronic showers generally deposit more energy, the absence of deposits in this layer is used to distinguish EM and hadronic showers.

3.4.3.2 ATLAS hadronic calorimeter

The hadronic calorimeter is formed of three parts: a barrel of concentric layers of steel and scintillating tiles, two endcaps of copper/LAr, and a forward calorimeter of alternating layers of copper/tungsten and scintillating tiles. The central hadronic (“Tile”) calorimeter, a section of which is shown in Figure 3.12, extends over the range $0 < |\eta| < 1.0$, while the two extended hadronic barrels cover the range $0.8 < |\eta| < 1.7$. Both barrels share the same LAr vacuum vessel as the EM calorimeter. The hadronic endcap calorimeters (HEC) are each made of two separate wheels, extending between $1.5 < |\eta| < 3.2$. The wheels are made of alternating layers of tungsten and liquid argon. The forward calorimeter (FCAL)

extends over $3.1 < |\eta| < 4.9$. It consists of three modules: the innermost of alternating layers of copper/LAr and the outer two comprising alternate tungsten/LAr layers.

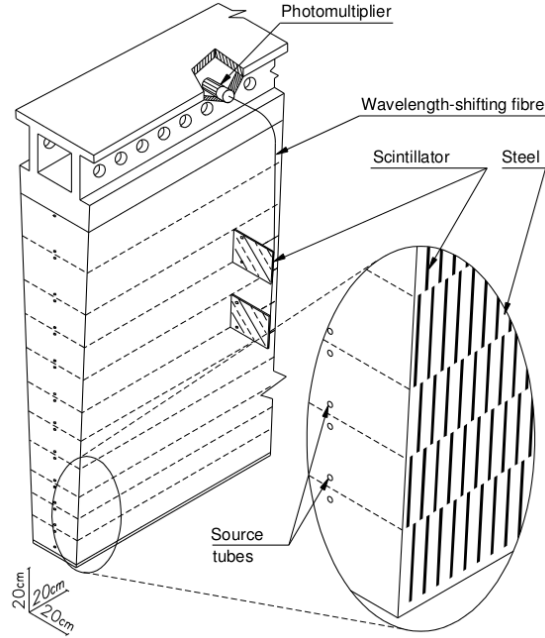


Figure 3.12: A section of the ATLAS Tile Calorimeter. The strips of steel and scintillator are visible in the cutaway: the offset between each plate increases the calorimeter granularity. Photomultiplier tubes and wavelength-shifting fibres provide readout. Adapted from [103].

3.4.4 ATLAS Muon Spectrometer

Muons and neutrinos are the only particles which traverse the entire detector, but neutrinos are highly unlikely to interact at all during their trajectory. Muons do not interact strongly and their electromagnetic energy loss through *bremsstrahlung* is suppressed relative to that of electrons by a factor of $(m_e/m_\mu)^4 \approx 5.4 \times 10^{-10}$. Muons leave a track in the inner detector, small energy deposits in the calorimeters, and an additional track segment in the muon spectrometer. The bending magnetic field for the muon spectrometer is provided by the barrel toroids for $|\eta| < 1.4$, and by the endcap toroids between $1.6 < |\eta| < 2.7$. In the intermediate or “transition” region, $1.4 < |\eta| < 1.6$, the magnetic field is provided by both the barrel and endcap toroids.

Unlike the other ATLAS sub-detectors, the muon spectrometer has separate components for fast muon triggering online, and for precision muon reconstruction offline. Monitored Drift Tubes (MDTs) are installed in the range $0 < |\eta| < 2.0$. At $\eta = 0$, there is a gap in the muon chambers required for detector access. In the barrel, the MDTs are arranged axially,

and in the endcaps they are arranged radially, fanning out from the z -axis. The MDTs are drift tubes of 29.970 mm diameter filled with Ar/CO₂ gas, and a central wire held at a constant potential of 3080 V. Faster multi-wire proportional chambers [111] known as Cathode Strip Chambers (CSCs) are used at $2.0 < |\eta| < 2.7$. The use of faster detectors is necessitated by the higher event rate in the forward direction (i.e. closer to the beam axis). The CSCs are arranged radially, fanning out from the z -axis, as shown in Figure 3.13. Both the MDTs and CSCs are drift chambers: the gas is ionised by the passing muon, and ionisation electrons are then attracted to, and read out by either one (MDT) or several (CSC) wires. The time taken for electrons to reach the wire is known as the *drift time*. The drift times in the MDT and CSC chambers (approximately 100 ns), are too long to allow the use of MDTs and CSCs in the first trigger level, which requires the detector to be read out in less than 50 ns (the bunch crossing time). There are therefore dedicated trigger chambers covering the range $|\eta| < 2.7$, which are again of two different types: Resistive Plate Chambers (RPCs) at $|\eta| < 1.05$, and Thin Gap Chambers (TGCs) at $1.05 < |\eta| < 2.7$. The change in technology is again due to the increased rate at higher η . The RPCs use parallel electrode-plates rather than wires to detect muons, while the TGCs are multi-wire proportional chambers. In addition to their triggering capability, the RPCs and TGCs are used to measure the curvature from the toroidal magnetic field, which is in the $R - \theta$ plane. Several regions of the MS have fewer chambers. At $\eta \approx 0$, control systems for the ID, calorimeters and solenoidal magnet are installed, and the base of the MS has 9 rows of “feet”, which support the entire ATLAS detector. Except in the feet region, each RPC is paired with MDT layers: the lack of space here necessitates smaller RPCs without paired MDTs. Additionally, in 2011 the regions between $1.1 < |\eta| < 1.3$ had fewer chambers than the original design: the missing chambers were installed between the 2011 and 2012 running periods.

3.5 ATLAS Trigger System

The LHC bunch crossing time was 50 ns in 2011 and 2012: this corresponds to a bunch crossing frequency of 20 MHz. It is infeasible to process or store data generated at this rate, so a triggering system is used in order to reject events not classed as interesting and hence reduce the rate of accepted events to a maximum of 400 Hz, a manageable rate that can be read out from the detector and stored. The ATLAS trigger is a three-level system with each stage selecting progressively fewer events with a more complex selection in order to reach the 400 Hz required. Since data not recorded by the detector are lost for good,

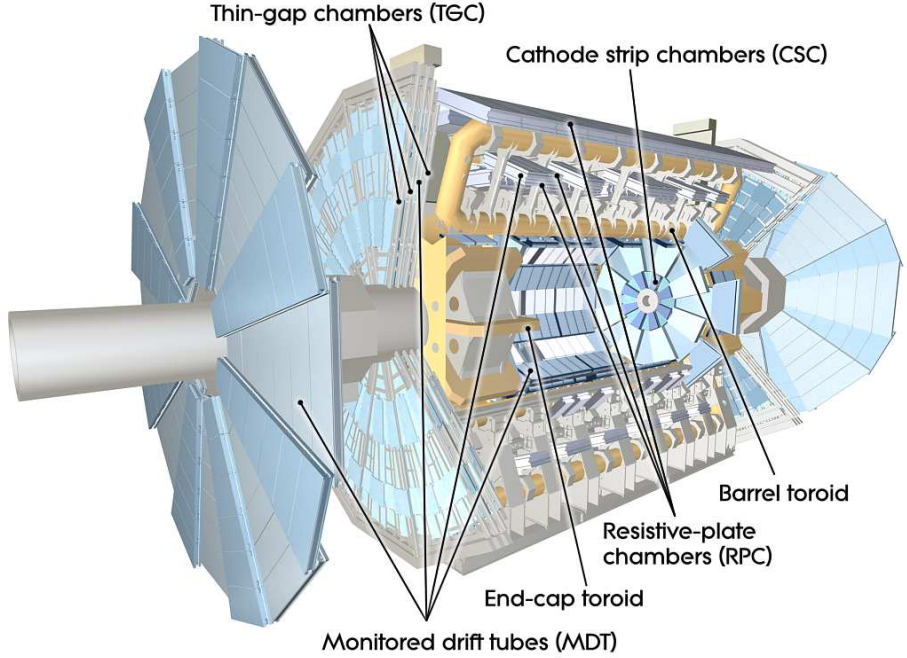


Figure 3.13: A cutaway of the ATLAS muon detector system. From [103].

it is vital to select as many events with interesting properties as possible, and to try to avoid bias in the events selected.

The three trigger levels are known as Level 1 (L1), Level 2 (L2) and Event Filter (EF). L2 and EF together form the “High Level Trigger” (HLT). L1 is the lowest level, and uses fast custom electronics, while the HLT uses software algorithms implemented on standard PCs. The L1 trigger uses coarse granularity information from the calorimeters and muon system, while the HLT has access to the full detector information. The Inner Detector is not used at L1. The L2 only has access to the event information in a Region of Interest (RoI), a broad region in η and ϕ , while the EF has access to the full event in all detector subsystems. If an event fails any of the stages (L1, L2, EF), it is permanently rejected.

The L1 and HLT trigger systems are discussed in detail in Sections 3.5.1 and 3.5.2.

The L1 trigger system reads data directly from the subdetectors. The L1 custom electronics systems pass their decision for the event to the Central Trigger Processor (CTP), which decides whether to accept the event. During this L1 decision time, the full event data is stored in front-end pipelines. If the L1 trigger system accepts the event, the Readout Buffers (ROBs) send information in the RoIs to the L2. The L2 trigger receives information from the calorimeter and muon systems, as well as new information from the ID. If the L2 trigger system accepts the event, event fragments from all RoIs are combined in the Event Builder (EB), stored in the Full Event Buffer and sent to the EF. If the EF trigger

system accepts the event, it is sent from the Full Event Buffer to permanent storage and further processing. This sequence of trigger operation is shown as a flowchart in Figure 3.14.

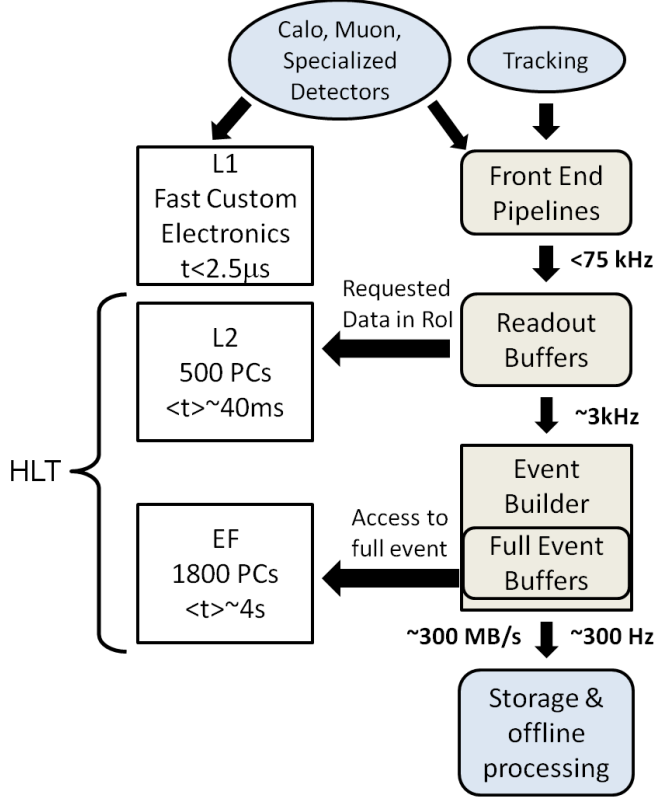


Figure 3.14: The flow of data (shown as black arrows) in the ATLAS trigger system. The acronyms used are defined in Section 3.5. The three trigger levels are shown on the left, while temporary and permanent storage/data processing units are shown on the right. Adapted from [112].

3.5.1 Level 1 Trigger

3.5.1.1 Level 1 Calorimeter Trigger

The L1 calorimeter trigger system (L1Calo) [113] uses signals in coarse granularity ($\Delta\eta \times \Delta\phi = 0.1 \times 0.1$ in the central calorimeters, and larger segments in the FCAL) segments of the EM and hadronic calorimeters, known as *trigger towers*. For electrons and photons, a 2×2 square of trigger towers with a local maximum (horizontal or vertical pairs of towers) above a given threshold forms an RoI. Isolation requirements may be imposed by requiring, for instance, an energetic 2×2 square surrounded by towers below a given threshold. No isolation requirements were used for the triggers in this work. Additionally,

the background from jets faking electrons may be reduced by requiring low energy in the HCAL behind an electron/photon candidate. Details of the L1Calo jet and tau triggers, which are not used in this work, are found in [112].

3.5.1.2 Level 1 Muon Trigger

The L1 muon trigger system (L1Muon) makes use of the RPC and TGC detectors only (as these are the only parts of the muon system that can be read out quickly enough for use). The RPCs are used for muons seen in the barrel, while the TGCs are used for endcap muons. Sequences of hits in three layers of TGC or RPC detectors are used to find muon candidates. The thresholds for low- p_T muons to pass the trigger are below approximately 10 GeV, while those for high- p_T muons are above above GeV. The paths taken by high and low- p_T muons are shown in Figure 3.15.

Muon candidates from the barrel and endcap triggers are combined into threshold multiplicities - an example threshold multiplicity would be two distinct muons with $p_T > 6$ GeV. Up to six such threshold multiplicities can be read out for every event.

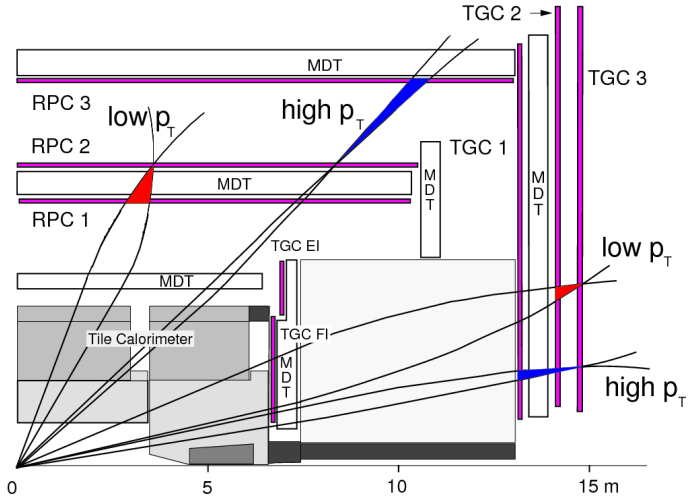


Figure 3.15: Example muon trajectories for the barrel (RPCs) and endcap (TGCs). The first layers (TGC EI and TGC FI) are not used in the trigger, but rather for precision tracking. From [114].

3.5.1.3 Level 1 Central Trigger Processor

The output from the L1Calo and L1Muon systems (referred to as trigger conditions) is sent to the Central Trigger Processor (CTP) [115]. Up to 256 trigger conditions can be processed by the CTP. In addition to the input from L1Calo and L1Muon, random and periodic timed triggers are used for monitoring and calibration. Up to 256 combinations of

these trigger conditions may be used to accept events. An example of such a combination of trigger conditions would be a single EM signal above 14 GeV combined with a single muon signal above 6 GeV. The OR of the 256 trigger combinations is used to accept events. Once an event has been accepted (L1Accept), the CTP vetoes subsequent L1Accepts for a short period in order to prevent too much data being sent to the front-end buffers - this is known as a *simple dead-time* mechanism. Additionally, the number of L1Accepts in a given period is limited for the same reason - this is known as a *complex dead-time* mechanism. In 2011 and 2012, the simple dead-time was set to 5 bunch crossings, and the complex dead-time limited to 8 L1Accepts in 416 bunch crossings. A diagram of the L1 trigger system is shown in Figure 3.16.

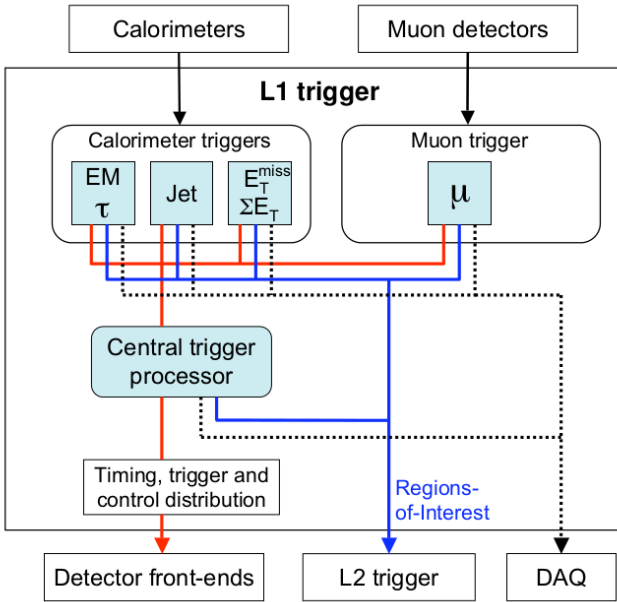


Figure 3.16: A diagram of the L1 trigger system. The flow of data to the detector front-ends, L2 trigger and data acquisition systems are shown in red, blue and black respectively. Information from the calorimeters and muon detectors is sent to the respective trigger systems. The information is then combined by the CTP, which also returns timing and control information to the detectors. If the CTP decides to accept the event, full detector information in RoIs is sent to the L2 trigger. From [103].

3.5.2 ATLAS High Level Trigger

The High Level Trigger (HLT) uses farms of PCs running software-based algorithms to select and reject events. As previously discussed, it is further subdivided into two levels: Level 2 uses specialised fast algorithms, while the Event Filter uses the same selection

algorithms as the offline event reconstruction discussed in Section 4.4. In 2011 (2012), 1193 (1205) PCs were used in the L2 farm, while 448 PCs were used in the EF farm in both years [116].

3.5.2.1 ATLAS Level 2 Trigger System

The Level 2 (L2) trigger uses specialised fast software algorithms to further reduce the rate to a maximum of 5.5 kHz (6.5 kHz) in 2011 (2012), with a maximum processing time of 40–45 ms [116]. In addition to the calorimeter and muon trigger systems, the inner detector is used at this level to further select events with tracks - tracking information is used in the electron, muon and tau triggers. The L2 system also operates at the RoI level only. If an event passes the L2 trigger, information from the RoI is sent to the next trigger system, the Event Filter.

3.5.2.2 ATLAS Event Filter Trigger System

The final trigger layer is the Event Filter (EF). The output rate of the EF was 400 Hz in 2011 and 2012 [116]. It makes use of the whole detector and the same algorithms as in ATLAS offline event reconstruction, as discussed in section 4.4, but configured to reject or accept an event in a maximum of 1 s [116] to constrain the overall output rate.

3.5.2.3 Inner Detector High Level Trigger

Information from the inner detector systems is not used at L1: the time to process an event increases as a function of the number of additional pileup events, as these will deposit additional hits in the inner detector. Since the tracking algorithms used in ATLAS are combinatoric in nature, this rise is much steeper than for the calorimeter systems, which rely on energy thresholds. The rate in the muon tracking chambers is lower since only muons reach the chambers. Two separate algorithm strategies [117] were used for trigger tracking throughout 2010–2012. Both strategies start by identifying a primary vertex, using the hit occupancy for the event, plotted as a function of z . The point with the highest hit occupancy is taken as the primary vertex co-ordinate. The algorithms generate final tracks from space-points using a Kalman filter [118], a general type of linear filtering algorithm that iteratively compensates for the effect of noise on a signal. For tracking algorithms, the signal is the true trajectory of the particle, while the noise in the system is the effect of mis-association of space-points to the true trajectory.

3.5.2.4 Calorimeter High Level Trigger

Electron reconstruction at L2 is performed within $\Delta\eta \times \Delta\phi = 0.4 \times 0.4$ RoIs, using trigger towers (defined in Section 3.5.1.1) of $\eta \times \phi = 0.025 \times 0.025$. Clusters of towers likely to come from electrons are then found with the offline electron reconstruction algorithm described in Section 4.4.4. The same procedure is followed for the EF, except that the clustering is performed in the entire detector, rather than just the ROI. Calorimeter clusters found at L2 and EF are matched with inner detector tracks in order to identify electron candidates. The calorimeter HLT is also used to identify jet candidates and events with significant E_T^{miss} : this is described in more detail in [119, 120].

3.5.2.5 Muon High Level Trigger

The L2 and EF muon trigger makes use of the MDT and CSC systems at reduced and full detector granularity respectively [114]. Muons found by the muon HLT are checked for compatibility with track candidates in the inner detector: compatible candidates are referred to as combined muons, while those found solely by the muon HLT are referred to as standalone muons. The algorithms used in the EF muon triggers are described in Section 4.4.5.

3.5.3 Trigger chains and menus

Since interesting physics events can have many different possible signatures, multiple trigger algorithms are run in parallel at each level of the trigger. In order to be recorded, an event must pass a combination of L1, L2 and EF algorithms known as a *chain*. As an example, take the single electron trigger chain *e20_medium*. This chain begins with the *L1_EM14* trigger, which has a threshold of 14 GeV and uses EM trigger towers. The detector information in the ROI provided by the *L1_EM14* trigger is then sent to the *L2_e20_medium* trigger, which has a 20 GeV threshold, and finally the full detector information is sent to the *EF_e20_medium* trigger, which again has a 20 GeV threshold. The full set of trigger chains running during data taking is known as the trigger menu. The upper limits on the various trigger input and output rates increase with additional collision energy and pileup: for this reason, the trigger menus changed between 2011 and 2012, and within the different 2011/2012 data taking periods. The trigger chains used in this work are detailed in Section 5.2.2.

Chapter 4

Simulation and reconstruction

Trying to unweave, unwind,
 unravel
 And piece together the past and
 the future.

T. S. Eliot [121]

The ATLAS detector uses a software framework known as Athena [122], based on the GAUDI framework [123]. The Athena framework implements event generation (see 4.1), simulation of particle interactions with the detector (see 4.2), digitisation and finally reconstruction (see 4.4) of particle objects by a common set of Python steering commands. The full chain of processing steps is shown in Figure 4.1, for both data and simulated collision events.

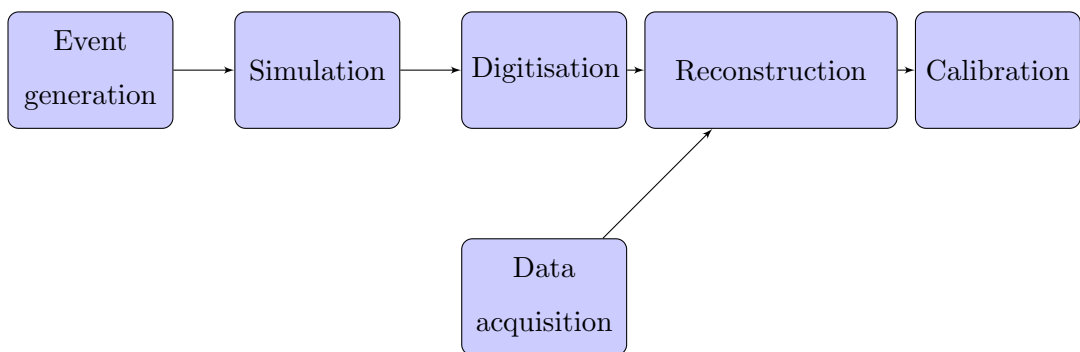


Figure 4.1: Flow chart showing the processing of real and simulated data in ATLAS.

4.1 Event generation

The physics processes described in Chapter 2 are simulated by computer codes known as Monte Carlo (MC) event generators [124]. Event generators use a combination of perturbative and phenomenological calculations to provide randomly distributed “events” of a given type (for example, $pp \rightarrow WZ \rightarrow \ell^+\ell^-\nu$) with stable final state particles.

Different physics models are used for the high momentum transfer (Q^2) part of the event, known as the *hard process*, and for the low energy parts of the event, known as *soft processes*. Since QCD is a strongly coupled theory, as discussed in Section 2.1.5, soft processes cannot be calculated perturbatively. Instead, they are approximated by phenomenological models including parameters determined from data. The full sequence of processes going into a theoretical prediction, shown in Figure 4.1 is discussed in detail in the next few sections.

4.1.1 Parton distribution functions

Parton distribution functions (PDFs) describe the probability of quarks and gluons within the colliding protons having a given fraction x of the overall momentum. PDFs, denoted $f_a(x, Q^2)$ are functions of the momentum fraction, parton species a and momentum transfer Q^2 . The factorisation theorem [125] states that the differential cross section $d\sigma$ of any hard process can be written in the form

$$d\sigma = \sum_{i,j} \int_0^1 dx_i \int_0^1 dx_j \quad d\sigma_{i,j}^{\text{part}} f_i(x_i, Q^2) f_j(x_j, Q^2) \quad (4.1)$$

Here i and j are the indices of the interacting partons with momentum fractions x_i , x_j and $d\sigma_{i,j}^{\text{part}}$ is the differential cross section of the hard process between partons i and j with momentum fractions x_i , x_j . Since the PDFs are functions only of the momentum fraction they are independent of the hard process. The PDFs themselves are not calculable in perturbation theory, but their evolution as a function of Q^2 is calculable via the so-called DGLAP equations [126, 127, 128]. To generate a set of usable PDFs, all that is needed is an ansatz functional form for each PDF, and a set of experimental data. In practice, PDFs are extracted from complex fits to a wide range of experimental data [129]. The main signal and background processes in three-lepton searches have quark-antiquark initial states, so the uncertainties on sea-quark distributions are important for the search presented here. Uncertainties arising from PDFs are important for the search presented in this thesis, as discussed in Section 6.3.1.3.

4.1.2 Matrix element

Since the hard process involves a large momentum transfer, it may be calculated using standard quantum field theory techniques - this is often referred to as the matrix element calculation. Such calculations are performed as an expansion in α_S , at increasingly high orders of α_S : leading order (LO) $O(\alpha_S)$, next-to-leading order (NLO) at $O(\alpha_S^2)$ and so on. Techniques to evaluate matrix elements are discussed in detail in [130, 131] and references therein.

4.1.3 Parton showers, hadronisation and the underlying event

Quarks radiate gluons ($q \rightarrow qg$), while gluons can decay to quark-antiquark pairs ($g \rightarrow qq$) or split into two gluons ($g \rightarrow gg$), and these processes may repeat. At high Q^2 , this is calculated as an additional correction to the matrix element calculation (*hard emission*), but at low Q^2 this is not possible: phenomenological models known as *parton showers* (PS) are used. The PS approximation is valid at Q^2 above the QCD scale ($O(\text{GeV})$). PS models have been developed by the HERWIG [132, 133, 134], PYTHIA [135, 136] and SHERPA [137] collaborations. At intermediate Q^2 , gluon/quark radiation may be treated as a hard emission or part of the PS: this can lead to double-counting of the total radiation in a given event. The CKKW [138] and MLM [139] schemes are used to determine whether emissions form part of the matrix element or PS.

After successive showers, the energy of the partons in the PS will fall to the threshold for bound state production (*hadronisation*). Since hadrons are only formed at low energy, only phenomenological models exist: several versions are provided by HERWIG, PYTHIA and SHERPA.

The *underlying event* (UE) [140] refers to the observed behaviour of the partons not participating in the hard process. These “spectator” partons hadronise to form colour singlet states: this hadronisation is described by phenomenological models developed by the JIMMY [141], PYTHIA and SHERPA collaborations.

Free parameters for the different PS, UE and hadronisation models (summarised in [124]) are tuned to data. For ATLAS, these “tunes” are discussed in detail in [142, 143, 144, 145, 146]. An outline of event generation is shown in Figure 4.2.

4.1.4 Summary of event generator properties

SHERPA, HERWIG++ and PYTHIA 6/PYTHIA 8 provide matrix elements at LO and have internal PS and UE models. HERWIG handles PS but lacks a UE model and is therefore

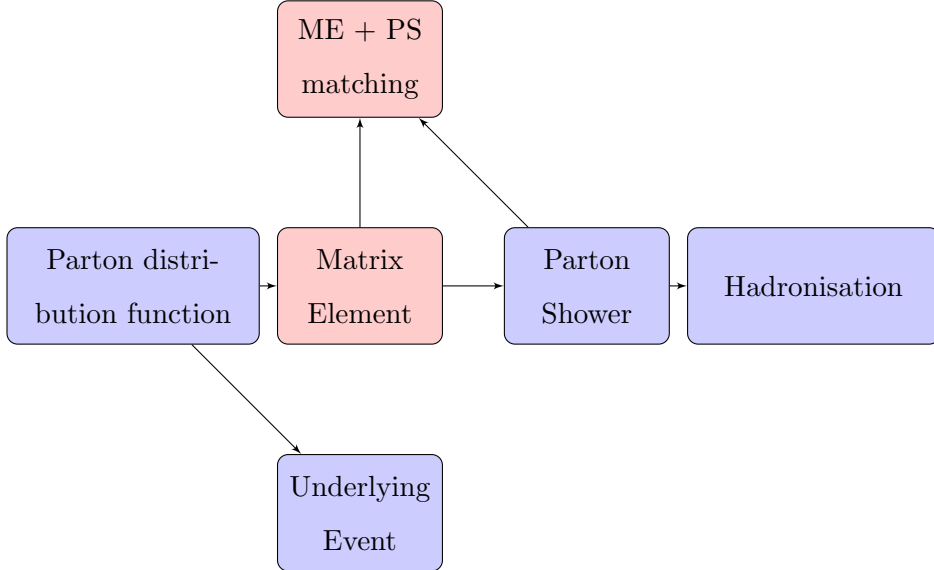


Figure 4.2: An outline of event generation. The non-perturbative parts of the calculation are in blue boxes, while the perturbative matrix element calculation is in pink.

always interfaced to JIMMY for UE simulation. ALPGEN and MADGRAPH both provide matrix elements at LO and are interfaced to HERWIG/JIMMY and PYTHIA respectively. MC@NLO [147] and POWHEG [148] both provide matrix elements at NLO and are interfaced to HERWIG/JIMMY and PYTHIA respectively. MCFM [149, 150, 151] and FEWZ [152, 153] are used to provide total cross sections for SM processes at NLO and NNLO respectively.

4.1.5 Storage of event generator information

Each event generator stores at least the identities and four-vectors of the initial and final state particles, and in some cases the intermediate, possibly virtual particles (vector bosons, SUSY particles etc) involved in the process. These are referred to as *truth particles*. Intermediate truth particles can only represent a single possible quantum mechanical history for an event and are therefore not used directly in the analysis. Final state truth particles are used in MC measurements of reconstruction efficiency, by checking whether (for instance) a lepton candidate corresponds to a true lepton. In this analysis the matching of truth and reconstructed particles is done geometrically, by requiring the truth and reconstructed particles to match within $\Delta R < 0.1$.

4.1.6 Pile-up

Each hard interaction at the LHC is accompanied by up to forty additional soft interactions (see Figure 3.2). In order to compare data to simulation, additional interactions are added

to simulated events. The $\langle \mu \rangle$ of the MC events is designed to match the $\langle \mu \rangle$ of the data sample it is to be compared to. In practice, since simulation generally happens during data-taking rather than afterwards, the $\langle \mu \rangle$ distributions will not match exactly, and simulated MC events will therefore be reweighted to the observed $\langle \mu \rangle$ distribution in data.

This procedure is referred to as *pile-up reweighting*.

The cross sections for SUSY signal processes, as well as the relevant backgrounds ($O(\text{ fb})$), are so small compared to those for soft interactions ($O(\text{ mb})$ [154]) that it is vanishingly unlikely that two hard interactions will occur in the same event. It is therefore sufficient to simulate additional soft proton-proton interactions and overlay these onto the simulation of the hard process.

4.2 Detector simulation

4.2.1 Full event simulation

Accurate simulation of the interaction of hadrons and charged leptons with the ATLAS detector depends on accurate modelling of energy loss and radiation in the different sub-detectors. The passage of particles through the detector is simulated by the GEANT4 [155] framework: phenomenological parameters for the models of energy loss and radiation used are calibrated using data from test beam experiments (see for example [156, 157, 158, 159]). The success of this simulation is also dependent on precise knowledge of the detector geometry. This is known approximately from the detector design, but was only fully validated by *in-situ* measurements of alignment [160, 161, 162] and active/dead material [163].

4.2.2 Trigger simulation

After the passage of the final state particles through the detector is complete, the event is passed to a complete simulation of the ATLAS trigger. The L1, L2 and EF trigger systems are simulated, and a set of triggers similar to that used in data acquisition is applied. Information is stored in the event record indicating whether the event passed each trigger simulated.

4.2.3 Fast simulation

Full event simulation can be very time-consuming: *fast simulation* is significantly simplified and can therefore allow for the simulation of more events in the same timescale.

This is of particular importance in cases when the total number of events simulated is a limiting factor for the analysis, such as the production of SUSY signal samples (discussed in Sections 4.3.1.2, 4.3.2.2). The ATLAS fast simulation package, known as ATLFAST-II [164, 165], uses parameterised response functions to model electromagnetic and hadronic showers [166] and a simplified detector geometry and treatment of scattering to model interactions in the ID [167].

4.2.4 Digitisation

After full or fast simulation, the response of the ATLAS detector to the simulated signals is simulated. If a signal is above the threshold for a given readout channel it is added to the total set of data read out from the simulated event. The effects of cross-talk, noise and other aspects of the data acquisition systems are then simulated as detailed in [168] and references therein.

4.3 Summary of Monte Carlo samples used in the analysis

In the following Sections, a summary of the different background samples used in 2011 and 2012 is given. The cross sections and integrated luminosities of the samples used in 2012 is shown in Table 4.1. In order to minimise the statistical error due to the sample size, the integrated luminosity of the sample must be at least the size of the actual dataset. The full set of samples used in 2011 and 2012, with ATLAS-specific dataset names, is given in Appendix A.

4.3.1 Monte Carlo samples used in 2011

4.3.1.1 Background samples

Samples of WZ and ZZ production are simulated with SHERPA, while HERWIG + JIMMY is used for WW production. SHERPA correctly treats contributions from singly resonant boson production, as well as the ordinary doubly resonant process. Production of W/Z bosons in association with heavy/light flavour jets is also simulated with ALPGEN interfaced to HERWIG + JIMMY. Z +jets samples are divided into “Drell-Yan”, for γ^* production below the Z peak ($10 \text{ GeV} < m_{\ell\ell} < 60 \text{ GeV}$), and high mass Z +jets with $m_{\ell\ell} > 60 \text{ GeV}$. MADGRAPH interfaced to PYTHIA is used for $t\bar{t} + W$, $t\bar{t} + Z$, and $t\bar{t} + WW$, processes. The diboson (WW , WZ , ZZ) yields are normalised to the MCFM NLO calculation, while the single and pair-produced top quark calculations are normalised to approximate NNLO

calculations [169]. The $t\bar{t} + W$, $t\bar{t} + Z$, $t\bar{t} + WW$, processes are normalised to NLO calculations [170, 171]. $W/Z + \text{jets}$ processes are normalised to NNLO calculations performed by FEWZ [152, 153]. WZ and ZZ samples are also produced in POWHEG interfaced to HERWIG to evaluate the theoretical uncertainty for these processes. All background samples pass through full simulation.

4.3.1.2 Signal samples

The simplified model samples, with SUSY parameters defined in Section 2.4.3, were all simulated in HERWIG. The spectra for the pMSSM samples were generated using ISASUSY [172], and the events were generated in HERWIG. The GGM samples, with parameters defined in Section 2.4.1, have spectra generated by SDECAY [173] and the events generated by HERWIG.

4.3.2 Monte Carlo samples used in 2012

Only differences between the 2011 and 2012 analyses are stated here.

4.3.2.1 Background samples

All diboson processes (WW , WZ , ZZ) are simulated by SHERPA. Again, additional WZ and ZZ samples used to treat the theoretical uncertainties on diboson production are simulated by POWHEG. Triboson processes (WWW and ZWW production) are evaluated for the analysis, and their simulation is performed using MADGRAPH. POWHEG interfaced to PYTHIA is used instead of MC@NLO for $t\bar{t}$ production, while ACERMC [174] is used for t -channel single top production (other single top processes are still simulated in MC@NLO). The POWHEG $t\bar{t}$ process is passed through ATLFEST-II rather than full simulation. Other processes contribute negligibly to the total background.

4.3.2.2 Signal samples

The 2012 analysis focuses on the interpretation of simplified models: pMSSM and GGM samples are not considered for this dataset.

4.4 Reconstruction and identification

Objects (electrons, muons, tau leptons, jets, and missing energy) are reconstructed from ATLAS detector information in exactly the same way for MC and data. This initial reconstruction is loose enough that the resulting objects may be used for many different

Process	Generator	Cross section pb	$\int \mathcal{L} dt \text{ fb}^{-1}$
$WZ \rightarrow 3\ell\nu$		10.24	258.6
$WW \rightarrow \ell\nu\ell\nu$	SHERPA	5.83	454.6
$ZZ \rightarrow 4\ell$		8.74	167.2
$ZZ \rightarrow 2\ell 2\nu$		0.54	1465.2
$WWW \rightarrow 3\ell 3\nu$		7.65×10^{-3}	9800
$ZWW \rightarrow 4\ell 2\nu$	MADGRAPH +PYTHIA 8	2.33×10^{-3}	32250
$ZZZ \rightarrow 4\ell 2\nu$		0.50×10^{-3}	151500
$t\bar{t} + (W \rightarrow \ell\nu)$		7.66×10^{-2}	1673.6
$t\bar{t} + (W \rightarrow \text{jets})$	ALPGEN + PYTHIA 8	0.15	1678.9
$t\bar{t} + (Z \rightarrow \nu\nu)$		0.04	1592.3
$t\bar{t} + (Z \rightarrow \ell\ell)$		0.03	1835.8
$t\bar{t} + (WW \rightarrow \ell\nu\ell\nu)$	MADGRAPH +PYTHIA 8	9.2×10^{-4}	10880
$t\bar{t}$ (semi- and fully-leptonic)	POWHEG +PYTHIA 8	128.6	231.8
s -channel single top	MC@NLO + HERWIG	1.80	836.5
t -channel single top	ACERMC +PYTHIA 8	28.4	94.8
$Z + \text{light jets}$ (Drell-Yan)		3448.2	118.9
$Z + \text{light jets}$		13094.6	445.1
$Z + c\bar{c}$		93.92	375.7
$Z + b\bar{b}$		45.68	235.5
$W + \text{light jets}$	ALPGEN + PYTHIA 8	3658.9	74.2
$W + c$		1287.0	30.1
$W + c\bar{c}$		461.1	24.0
$W + b\bar{b}$		153.2	24.9

Table 4.1: Cross sections and effective integrated luminosity of the main MC samples used in the 2012 analysis. The cross sections are given at NLO for all processes except Z and $W + \text{jets}$.

analyses. The additional selection criteria are then applied in order to increase the purity of the selected objects. Finally, *measured* object properties are calibrated and *simulated* object properties are corrected in order to match this calibration. Objects used in this analysis were reconstructed in line with official performance group guidelines from ATLAS.

Algorithms used for reconstruction generally behave *iteratively*, starting from a set of simple objects (e.g. track hits or calorimeter deposits) and constructing a new object (e.g. an ID track or calorimeter cluster). The iterative algorithms used to reconstruct objects in the ID, calorimeters and MS are described below.

Algorithms to identify objects behave *discriminatively*, by starting with a sample of final objects and systematically rejecting objects not matching a set of pre-defined criteria. Discriminative algorithms are used to reduce a sample containing a combination of true and false objects in unknown proportion to a sample containing predicted combinations of true and false objects. Simple discriminative algorithms are also used to select the seed objects for iterative reconstruction algorithms. Discriminative algorithms may be further subdivided into *cut-based* and *multivariate* techniques. Cut-based techniques use a set of criteria motivated by physical considerations and cut values determined entirely by analysing pure samples of signal and background objects, and optimising the different cut values by hand. Multivariate techniques use a large number of physically motivated variables to generate a *discriminant*, a single number which summarises the final discriminatory performance of the variables when various cuts are applied. It is generally prohibitive to analyse so many variables by hand, so signal and background samples are fed to a multi-dimensional optimisation algorithm seeking to simultaneously maximise the efficiency at selecting true objects and rejecting fake objects. The two multivariate techniques used in this work are the Artificial Neural Network [175] (ANN) and Boosted Decision Tree [176] (BDT).

4.4.1 Inner Detector tracks

Charged particles leave tracks in the ID: these tracks are later matched to electron, muon, hadronic tau and jet candidates. Tracks are reconstructed using three different algorithms [177]. The *inside-out* algorithm starts from hits in the Pixel detector and uses a Kalman filter approach [118] to add hits while moving outwards through the Pixel and SCT detectors. These tracks are then checked for compatibility with hits in the TRT, and extended into the TRT if this is the case. The inside-out algorithm is designed for *primary*

particles, defined as particles produced either in the initial parton-parton interaction or from a short-lived particle that decays before reaching the first layer of the Pixel detector. The *back-tracking* algorithm essentially takes the opposite approach: tracks are reconstructed from hits in the TRT, moving inwards, and then hits from the Pixel and SCT detector are added. Finally, TRT-only tracks are formed using only hits in the TRT. Tracks can be fully parameterised using the following variables, referred to as track parameters, which must be defined relative to an origin:

- The space co-ordinates η and ϕ are defined by the track direction when extrapolated to the origin.
- d_0, z_0 : d_0 is the distance of closest approach of the track to the origin, z_0 is the component of d_0 in the z plane, and $z_0 \sin \theta$ is the projection of d_0 onto the z axis.
- The transverse momentum, p_T , is defined by the bending radius R of the track in the solenoidal magnetic field B , according to the formula p_T [GeV] = $0.3 \times B$ [T] $\times R$ [m].

Generally, track parameters are defined relative to the position of the *primary vertex*, defined in Section 4.4.2 as the likely position of the hardest interaction in the event. The standard track selection used in this work is defined to be $|\eta| < 2.5$, $d_0 < 1.5$ mm, $z_0 \sin \theta < 1.0$ mm (both defined relative to the primary vertex) and $p_T > 1$ GeV, ≥ 2 hits in the Pixel detector and ≥ 7 hits in the SCT. Additional tracking selections are listed when used.

4.4.2 Vertices

The point in space at which two particles interact or a single particle decays is defined as a *vertex*. It is only possible to reconstruct vertices with sufficient accuracy using ID tracks. Vertices are found by extrapolating from at least two tracks back to a common interaction point. The tracks used for vertex finding are required to have the standard selection defined in Section 4.4.1 and $p_T > 500$ MeV. Due to pileup, data and simulated events usually contain several vertices, most of which are from soft interactions, as discussed in Section 4.1.6. The primary vertex, hypothesised to be the source of the hardest interaction, is defined by finding the vertex with the greatest $\sum p_T^2$ from the associated tracks. Decays of particles with decay lengths measurable at ATLAS, including b -quarks and hadrons are known as secondary particles. Such particles will generate tracks emanating from a displaced vertex measurably displaced relative to the primary vertex: this is known as

a secondary vertex. For the analyses discussed in this work, collision events are only considered if they have a primary vertex with at least five associated tracks.

4.4.3 Leptons

From this point onwards, the term lepton is understood to mean electrons or muons only. In the following sections, electron/muon identification and calibration is discussed. Two levels of selection criteria are defined, for both electrons and muons:

- **Loose** leptons are identified with high efficiency and low purity
- **Tight** leptons are identified with low efficiency and high purity

Tight leptons are used for the final event selection, while loose leptons are used in the background estimation (Section 6.1).

4.4.4 Electrons

Electrons leave ID tracks and energy deposits in the EM calorimeter, and are generally not penetrating enough to reach the HCAL. Only electron candidates to which ID tracks are associated are considered in this work. The energy deposits are used as input to a sliding window algorithm [178] with a window size of 3×7 towers in the calorimeter barrel with granularity matching the second layer of the ECAL ($\Delta\eta \times \Delta\phi = 0.025 \times 0.025$). The window is moved around the ECAL, one step in the η or ϕ co-ordinate at a time, until the whole calorimeter has been covered. Any windows with a local maximum in total energy (> 3 GeV) are then stored as so-called pre-clusters. The pre-clusters are then geometrically matched to inner detector tracks by requiring a minimum $\Delta\eta$ and $\Delta\phi$ between the track and the pre-cluster - the requirements are $\Delta\eta < 0.05$ and $\Delta\phi < 0.05$ in the direction that the extrapolated track bends due to the magnetic field and $\Delta\phi < 0.1$ in the opposite direction. The change in $\Delta\phi$ requirement helps identify bremsstrahlung: radiated photons are emitted parallel to the electron direction before radiation, and the electron then bends more due to its decreased momentum. The electron cluster is then reconstructed using 3×7 (5×5) towers in the barrel (endcap) centred around the originally determined cluster centre. The electron energy is then determined using the measured energy in the cluster and corrected for estimates of the energy deposited before the electron reaches the calorimeter and outside the cluster (leakage). Energy deposited beyond the ECAL is referred to as longitudinal leakage, while energy deposited outside the cluster edge is referred to as lateral leakage. These corrections are parameterised by the energy measured

in the presampler (up to $|\eta| < 1.8$) and in the first calorimeter layer for $|\eta| > 1.8$. The electron ϕ and η are determined by the track ϕ and η extrapolated back to the electron vertex.

4.4.4.1 Electron identification

Criteria to reject muons, photons (both converted and unconverted), $\pi^0 \rightarrow \gamma\gamma$, charged pions and other hadrons falsely reconstructed as electrons are applied. Three levels of electron identification are used: in ATLAS jargon they are identified as LOOSE++, MEDIUM++ and TIGHT++ [179]. The three levels apply successively stricter selection criteria, and additionally include the criteria of the previous selection (making MEDIUM++ and TIGHT++ strict subsets of LOOSE++ and MEDIUM++ respectively). Cuts applied at LOOSE++ level reject hadrons and $\pi^0 \rightarrow \gamma\gamma$ through cuts on calorimetric variables such as lateral and longitudinal leakage, and impose loose requirements on track quality and matching to the cluster. The cuts applied at MEDIUM++ level impose tighter track quality and matching requirements, as well as a loose cut on the ratio of high-threshold TRT hits to total TRT hits (TRT ratio) to reject hadrons and muons in particular. The TIGHT++ cuts impose additional track quality and matching criteria, a tighter cut on the TRT ratio and rejection of any electrons with a track matching either electron from $\gamma \rightarrow e^+e^-$ candidates. Loose electrons are required to pass MEDIUM++ identification.

4.4.4.2 Electron calibration

The electron energy scale is calibrated by comparing the mass spectra of the $J/\psi \rightarrow ee$, $W \rightarrow e\nu_e$ and $Z \rightarrow ee$ resonances in simulation and data [179]. Initial calibration was performed using test-beam data [180].

4.4.4.3 Electron tight selection

Leptons from heavy flavour decays or jet misidentification are usually geometrically close to other tracks, while the opposite is true for leptons from electroweak or SUSY processes. This is not true for additional pileup interactions, which may coincidentally be close to the lepton.

In 2011, the isolation requirement was

$$\sum_{\Delta R < 0.2} p_T^{\text{tracks}} < 0.10 p_T^e \quad (4.2)$$

while in 2012, the isolation requirement was

$$\sum_{\Delta R < 0.3} p_T^{\text{track}} < 0.16 p_T^e \quad (4.3)$$

where the sum is over all tracks within $\Delta R < 0.2$, p_T^{track} is the track p_T and p_T^e is the electron candidate p_T . In both 2011 and 2012, the tracks are selected using the standard tracking criteria defined in Section 4.4.1, which includes impact parameter cuts to remove tracks associated with pileup interactions. In addition to the isolation requirements, tight electrons must pass the *tight++* cuts detailed in Section 4.4.4.1. A cut on the “ d_0 significance” is also imposed:

$$\begin{aligned} \frac{|d_0|}{\sigma(d_0)} &< 6 \text{ (2011)} \\ \frac{|d_0|}{\sigma(d_0)} &< 5 \text{ (2012)} \end{aligned} \quad (4.4)$$

where $\sigma(d_0)$ is the error on d_0 measured in the ID. This serves to remove electron candidates with well-measured displaced vertices, and helps reduce the background from heavy flavour decays. Figure 4.3 shows the efficiency of electron identification as a function of $\langle \mu \rangle$.

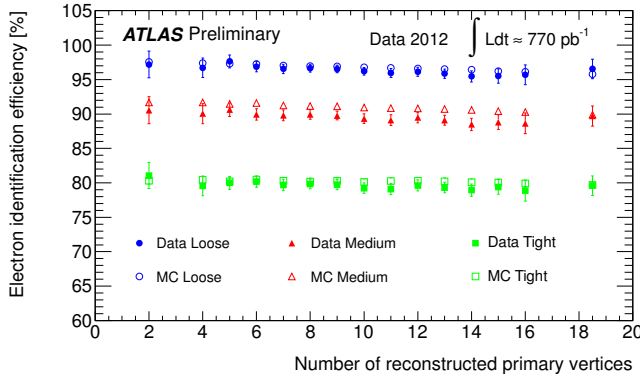


Figure 4.3: Electron reconstruction efficiency in 2012 data as a function of $\langle \mu \rangle$, measured in Z boson decays. The labels “loose”, “medium” and “tight” correspond to *loose++*, *medium++* and *tight++* as defined in Section 4.4.4.1. From [181].

4.4.5 Muons

Muons are the only known particles which traverse and interact with the entire detector: neutrinos pass through the detector with a negligible interaction probability. Muons leave tracks in the ID, small energy deposits in the calorimeters and tracks in the MS. Muons are mainly faked by charged pions - pions generally leave larger energy deposits in the calorimeters and rarely reach the muon spectrometer. Three muon reconstruction algorithms

are used in ATLAS: STACO, MUID and MUTAG [182, 183]. MUID is not considered in this work. The STACO algorithm forms straight line track segments from hits in the precision tracking (MDT and CSC) chambers. Due to the high efficiency of the precision tracking chamber drift tubes, segments without a hit in a drift tube crossed by the segment are discarded. Hits from the trigger chambers are then associated to the segment. Track candidates are then built from segments and combined, starting from the outer chambers and working inwards towards the centre of the detector. Track parameters are measured in the first precision tracking chambers, and then extrapolated back to the ID, correcting for energy loss in the calorimeters. ID tracks with compatible track parameters are then associated to MS tracks. The final track parameters are then found by a statistical combination of the ID and MS track parameters. Some regions of the MS have fewer chambers, as discussed in Section 3.4.4. In these regions, MUTAG is used. MUTAG starts from inner detector tracks and extrapolates them to single MS segments in inner stations, correcting for energy loss as is done for STACO muons. The MUTAG algorithm is also useful for muons with $p_T < 6$ GeV, which are less likely to reach the outer chambers.

4.4.5.1 Muon identification

Muons at all $|\eta|$ ranges may pass STACO reconstruction, while central muons ($|\eta| < 1.05$) may alternatively pass MUTAG reconstruction. All muons are required to have ≥ 3 TGC hits.

4.4.5.2 Muon calibration

The muon momentum scale is calibrated by comparing the invariant mass spectrum of the $J/\psi \rightarrow \mu\mu$ and $Z \rightarrow \mu\mu$ boson between simulation and data. Initial calibration of the muon momentum scale was obtained from test-beam measurements [158].

4.4.5.3 Muon tight selection

Muons are also required to be well isolated, for the reasons discussed in Section 4.4.4.3. For 2011 data, the isolation requirement is

$$\sum_{\Delta R < 0.2} p_T^{\text{tracks}} < 1.8 \text{ GeV} \quad (4.5)$$

while for 2012 data, the isolation requirement is

$$\sum_{\Delta R < 0.3} p_T^{\text{tracks}} < 0.16 p_T^\mu \quad (4.6)$$

As before, a d_0 significance cut is applied:

$$\frac{|d_0|}{\sigma(d_0)} < 3. \quad (4.7)$$

This is more stringent than the electron d_0 significance cut, since electron bremsstrahlung leads to longer d_0 tails. Muon reconstruction efficiency as a function of η is shown in Figure 4.4.

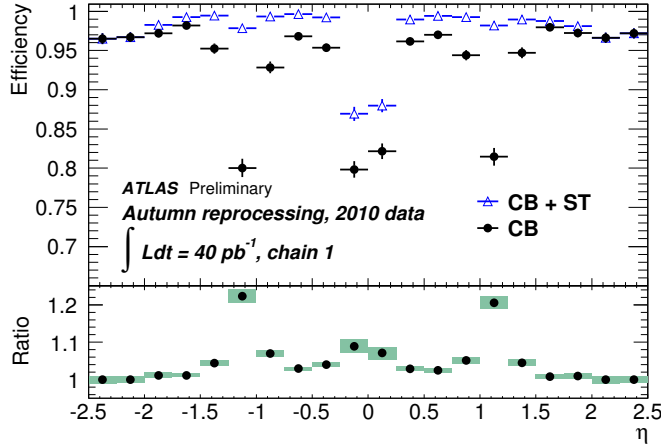


Figure 4.4: Muon reconstruction efficiency in 2010 data as a function of η , measured in Z boson decays. From [184].

4.4.6 Gluon and light flavour jets

Jets are reconstructed starting from topological clusters (“topo-clusters” in ATLAS jargon) [185]. The topo-cluster formation algorithm [178] is an iterative procedure starting from a seed cell with a signal to noise ratio $S/N \geq 4$, where S is the energy measured in the seed cell and N is defined as the RMS of the cell energy measured in random bunch crossings. Any neighbouring cells with $S/N \geq 2$ are then added to form a cluster. Neighbouring cells are then added to the seed to form a topo-cluster. All cells neighbouring the cluster cells are added to form an initial topo-cluster. This cluster is then used in an additional splitting step: every calorimeter cell with energy > 500 MeV is tested for a local maximum, and any cell passing this criterion is used as a trial seed for a new topo-cluster. Topo-clusters are then defined to have zero mass, energy equal to the sum of the energy of their constituent calorimeter cells and direction determined from the weighted averages of the ϕ and η of the constituent calorimeter cells, as described by equation (4.8)

$$(\eta, \phi)_{\text{topo-cluster}} = \frac{\sum E_c(\eta, \phi)_c}{\sum E_c}, \quad (4.8)$$

where E_C and $(\eta, \phi)_C$ are the total energy and (η, ϕ) coordinates of the constituent cells respectively.

4.4.6.1 Jet calibration

Before being used as constituents of jets, topo-clusters are calibrated. For the analysis of 2011 data, the topo-clusters were initially calibrated as if they were formed by EM showers only (“EM scale”), and then corrected to the energy scales of hadronic showers (jet energy scale). For the analysis of 2012 data, local cluster weighting (LCW) calibration was used. LCW uses an algorithm to determine whether topo-clusters originate from a hadronic or EM shower. The energy measured in the hadronic topo-clusters is then corrected according to the simulated response of single hadrons in the cells. Finally, corrections for energy deposition in dead material and the effects of noise are applied. Further details about jet calibration may be found in [186].

4.4.7 Jet reconstruction

The topo-clusters with either EM scale or LCW calibration are provided as input to the anti- k_T [187] recombination algorithm with distance parameter $R = 0.4$. The anti- k_T algorithm works iteratively: in the first step the distance parameter d_{ij} is calculated. The distance parameter is defined as

$$d_{ij} = \left(\frac{1}{k_{T_i}^2}, \frac{1}{k_{T_j}^2} \right) \frac{\Delta R_{ij}}{R^2} \quad (4.9)$$

where i and j are topo-cluster indices, k_T is the transverse momentum of each topo-cluster, $\Delta R_{ij} = \sqrt{\Delta\phi_{ij}^2 + \Delta\eta_{ij}^2}$ is the distance between the two topo-clusters, and R is a free parameter determining the size of reconstructed jets. The topo-clusters i and j which minimise d_{ij} are then combined to form larger individual clusters. In the next iteration, the larger individual clusters, as well as any remaining initial topo-clusters are combined according to the same procedure. This is repeated until all remaining topo-cluster pairs satisfy

$$\Delta R_{ij} > R. \quad (4.10)$$

These are the final jets returned by the algorithm [185]. In this work, jets are reconstructed with $R = 0.4$.

Jets found by the anti- k_T algorithm are robust against the effects of infrared and collinear radiation, and are usually cone-shaped. Cone-shaped jets are better suited to calibration

than more irregular shapes, as the energy deposition will tend to spread out smoothly from the geometric centre of the reconstructed jet.

4.4.8 Heavy flavour jets

It is possible in principle to distinguish jets originating from b - and c -quark decays (heavy flavour jets or HF) from gluon- and light (u, d, s) quark-initiated jets (light flavour jets or LF). Discrimination is possible because heavy flavour (HF) jets differ in two important ways from light flavour (LF) jets:

1. The b - and c -quark lifetimes are long enough that HF jets can be measured to originate from a secondary vertex. The vertex d_0 is used as a discriminant.
2. If the secondary vertex is reconstructed, tracks within the jet cone can be examined for compatibility with b and c hadron decays

From the HF jet algorithms available, two were used in this work: the JETFITTER-COMBNN and MV1 algorithms. JETFITTERCOMBNN combines information from method 2 into a neural network to make a final decision and was used in 2011, while the MV1 algorithm combines information from methods 1 and 2 into an artificial neural network to make a final decision and was used in 2012. The efficiencies and mis-tag rates for these algorithms are measured using the methods detailed in [188, 189, 190], while the energy calibration is performed using the methods detailed in [191]. Efficiencies, mis-tag rates and associated systematics are only provided by the ATLAS flavour tagging group for $\text{MV1} > 0.122, 0.595, 0.772$ and 0.980 , corresponding to $85\%, 75\%, 70\%$ and 60% efficiency respectively. Of these, $\text{MV1} > 0.122$ is used to define b -jets in this work: the choice is motivated in Section 5.3 by considering the effect on signal and background. Similarly, efficiencies, mis-tag rates and associated systematics are only available for four JETFITTERCOMBNN scores: of these, $\text{JETFITTERCOMBNN} > 1.8$, which corresponds to 60% efficiency, is used to define b -jets.

4.4.9 Tau leptons

Tau leptons are the only leptons heavy enough to decay hadronically, which they do in approximately 60% of cases [5]. Tau decays occur within the beampipe, so leptonic decays are effectively indistinguishable from prompt production of light leptons, and are treated as such in this work.

Hadronic decays may be further divided into:

$$\tau^- \rightarrow \pi^- + \geq 0 \pi^0 + \nu_\tau \quad (\text{"1-prong", branching ratio} \approx 85\%) \quad (4.11)$$

$$\tau^- \rightarrow \pi^- \pi^+ \pi^- + \geq 0 \pi^0 + \nu_\tau \quad (\text{"3-prong", branching ratio} \approx 15\%) \quad (4.12)$$

While “5-prong” and higher modes exist, their low branching fractions and the difficulty of their reconstruction make them negligible. Tau candidates are seeded starting from anti- k_T jets calibrated according to the local hadron calibration scheme. The η and ϕ of the tau candidate are defined exactly as the weighted average η and ϕ of the seed topocluster, exactly as for light jets. Tracks within $\Delta R = 0.2$ of the seed jet with the selection defined in Section 4.4.1 are associated to the tau candidate. The number of prongs of the tau-candidate is equal to the number of these so-called core cone tracks. Tracks within $0.2 < \Delta R < 0.4$ of the jet centre (a region known as the isolation annulus) are used to discriminate against jets reconstructed as tau candidates.

4.4.9.1 Tau identification

Jets, electrons and muons can all be falsely reconstructed as tau candidates. Jets are distinguished from tau candidates by variables related to the width of the showers and proportional energy deposited in the ECAL and HCAL, as well as the width of the cone defined by the tracks in the core cone. Additionally, for 3-prong tau candidates it is possible to reconstruct the secondary vertex corresponding to the appreciable tau time-of-flight, although not with significant precision. Electrons are distinguished from 1-prong tau candidates using the TRT ratio defined in Section 4.4.4, as well as the relative proportion of energy deposited in the ECAL and HCAL. Muons generally do not deposit significant energy in the ECAL or HCAL, but may be falsely matched to tau candidates if there is a mis-association or the muon deposits an anomalous amount of energy. To reject muons with mis-associated energy deposits, variables related to the proportion of cluster E_T to p_T are used, since these are expected to be uncorrelated. Muons with anomalously large energy deposits are expected to pass through the ECAL and hence leave a larger deposit in the HCAL than a true tau candidate. In this case, variables related to the relative proportion of energy deposits in the ECAL and HCAL are again used. BDT algorithms are used to discriminate against jets and electrons, while a cut-based selection is used to reject muons [192].

Object	ID type	ID quality	Isolation	Minimum p_T	η (max., min.)
Electron	Cut-based	Loose	None	10 GeV	(0,2.5)
		Tight	Track-based		
Muon	Cut-based	Loose	None	10 GeV	(0,2.4)
		Tight	Track-based		
Tau	Multivariate	Loose	None	20 GeV	(0,2.5)
		Tight			
Jet	Cut-based	Loose	None	20 GeV	(0,4.9)
		Tight			
b -jet	Multivariate	Tight			(0, 2.5)

Table 4.2: Summary of object reconstruction properties. Note that b -jets are an additional level of jet reconstruction.

4.4.9.2 Tau calibration

The proportion of energy deposited by tau candidates in the calorimeters is expected to differ from that deposited by jets, due to the mixture of charged and neutral pions in the tau decay. Tau leptons are calibrated from semi-leptonic $Z \rightarrow \tau\tau$ decays [193].

4.4.10 Summary of object reconstruction and calibration

The reconstruction properties for electrons, muons, taus, jets and b -jets are summarised in Table 4.2.

4.4.10.1 Overlap removal

If different objects are geometrically close (i.e. within a ΔR cone of a given size), this can indicate a problem with reconstruction. Overlap removal is performed with loose objects. If two electrons are found within $\Delta R < 0.1$, this can indicate false additional track-cluster matching: in this case, the lowest p_T electron is removed from the event. Electron candidates may also be found by jet algorithms: if an electron and jet are found within $\Delta R < 0.2$ of each other, only the electron is retained, which is justified by the higher purity of electron identification. Jets may contain leptons from semi-leptonic b and c -quark decays, as discussed in Section 4.4.8. Lepton isolation cuts are usually effective at removing such non-prompt leptons, but only if the jet is within $\Delta R < 0.2$ ($\Delta R < 0.3$ in 2012) of the lepton. Additional discrimination against semi-leptonic b - or c -quark decays is achieved by requiring that all leptons are $\Delta R < 0.4$ from jets. High energy muons can

radiate photons, and these photons may be falsely reconstructed as electron candidates. In this case, the muon is not well reconstructed. If an electron is found within $\Delta R < 0.1$ of a muon, both objects are removed from the event.

4.4.11 Missing transverse energy

The missing transverse energy (E_T^{miss}) is defined as the vector sum of transverse energy measured in the ECAL and HCAL, as well as tracks from muons measured in the MS. Clusters associated to the different objects are summed in the following order: electrons, photons, hadronically decaying taus, jets, and finally muons. Soft jets, defined to have $10 \text{ GeV} < p_T < 20 \text{ GeV}$, as well as jets with $p_T > 20 \text{ GeV}$ are used. Additionally, energy deposits from cells not associated to object clusters are added to the E_T^{miss} vector. The total calorimetric contribution to the E_T^{miss} is given by

$$E_{x(y)}^{\text{miss,calo}} = -(E_{x(y)}^e + E_{x(y)}^\gamma + E_{x(y)}^\tau + E_{x(y)}^{\text{jets}} + E_{x(y)}^{\text{softjets}} + E_{x(y)}^{\text{calo}\mu} + E_{x(y)}^{\text{CellOut}}) \quad (4.13)$$

where for the generic particle object “obj” E_x^{obj} and E_y^{obj} are defined as

$$E_x^{\text{obj}} = \sum_{i=1}^{N_{\text{cell}}} E_i \sin \theta_i \cos \phi_i \quad (4.14)$$

$$E_y^{\text{obj}} = \sum_{i=1}^{N_{\text{cell}}} E_i \sin \theta_i \sin \phi_i \quad (4.15)$$

The $\sum p_T$ from muons in the MS is added to the calorimetric E_T^{miss} in order to give a total E_T^{miss} of :

$$E_{x(y)}^{\text{miss}} = E_{x(y)}^{\text{miss,calo}} - p_{x(y)}^{\text{MS}\mu} \quad (4.16)$$

The E_T^{miss} magnitude and ϕ direction are then given by

$$E_T^{\text{miss}} = \sqrt{(E_x^{\text{miss}})^2 + (E_y^{\text{miss}})^2} \quad (4.17)$$

$$\phi_{E_T^{\text{miss}}} = \arctan(E_y^{\text{miss}}/E_x^{\text{miss}}) \quad (4.18)$$

4.4.11.1 Missing energy calibration

Electrons, muons, taus and jets are calibrated as detailed in the relevant subsections (4.4.4, 4.4.5, 4.4.9 and 4.4.6 respectively), and no additional calibration is applied to the CellOut and SoftJets terms. More details may be found in [194].

4.4.11.2 Missing energy definitions

The following objects are used to form the E_T^{miss} :

- Loose jets (covering $|\eta| < 4.9$) with $p_T > 20$ GeV;
- Loose electrons with $p_T > 20$ GeV (10 GeV) in 2011 (2012);
- Loose muons with $p_T > 20$ GeV.

The contributions from soft jets and additional energy deposits (discussed above) are added to these objects to define the E_T^{miss} .

Chapter 5

Overview of three-lepton supersymmetry searches

Two analyses are presented in this chapter: an analysis of the full dataset (4.7 fb^{-1}) collected at $\sqrt{s} = 7 \text{ TeV}$ in 2011, and an analysis of the full dataset (20.7 fb^{-1}) collected at $\sqrt{s} = 8 \text{ TeV}$ in 2012. In the following, the former is referred to as the 2011 analysis, and the latter as the 2012 analysis. The full analysis strategy is sketched here and subsequently expanded upon.

5.1 Analysis overview

All signal regions are defined to have exactly three leptons ($\ell = e, \mu$). Events with three leptons are rare in the SM and a possible SUSY signature, as explained in Chapter 2. Since lepton number is conserved at each vertex, both in the SM and in R -parity conserving SUSY, an odd number of neutrinos, sleptons or sneutrinos must also be produced in each event. The SUSY events must also contain an even number of LSPs: these increase the possible E_T^{miss} . To discriminate against SM backgrounds, all signal regions require at least 50 GeV of E_T^{miss} , with the exact value optimised in different signal regions to improve discrimination between signal and background.

Leptons are required to pass tight identification, and isolation cuts, as defined in Section 4.4.4.3 for electrons and 4.4.5.3 for muons. All leptons must have p_T of at least 10 GeV (higher depending upon the trigger requirements for the event (defined in Section 5.2.2)). Only events with two same flavour opposite charge sign leptons (known as SFOS pairs, $\{e^\pm, e^\mp\}$ or $\{\mu^\pm, \mu^\mp\}$) are considered: such leptons, when produced promptly, must emanate from the same vertex to conserve lepton number. No constraint is placed on the

flavour or charge of the third lepton, but if it has the same flavour as the SFOS pair, it forms a second SFOS pair ($\{e^\pm, e^\pm, e^\mp\}$ or $\{\mu^\pm, \mu^\pm, \mu^\mp\}$). All signal regions require at least one SFOS pair, and the invariant mass of such pairs is always required to exceed 12 GeV in order to avoid low mass resonances (J/ψ , Υ etc).

To summarise, the preliminary selection for all signal regions is given by

- Exactly three leptons passing tight selection;
- At least one SFOS pair with $m_{\text{SFOS}} > 12$ GeV;
- $E_T^{\text{miss}} > 50$ GeV.

The non-negligible SM backgrounds for this selection at 8 TeV and 20.7 fb^{-1} with this selection are shown in Table 5.1, as well as two example benchmark SUSY points. The dominant background is the $WZ \rightarrow \ell\ell\nu\nu$ process (usually referred to simply as WZ), which makes up 71% of the background. The signal scenarios are representative of the SUSY events considered in this work: they are an order of magnitude smaller than the total SM background with this selection.

In addition to processes such as WZ and $WWW \rightarrow 3\ell 3\nu$, there are backgrounds with four leptons such as $ZZ \rightarrow 4\ell$ and $ZWW \rightarrow 4\ell\nu\nu$, which only contribute if a lepton is missed by reconstruction algorithms. Production of W/Z with associated light jets contributes if at least one jet is falsely reconstructed as a lepton. Additionally, there are contributions from single or double top production, and W/Z with associated semi-leptonic b - and c -jet decays (*heavy flavour*), and photons converting to electron-positron pairs in the detector (*electron conversions*). By contrast, leptons in the SUSY models considered here are produced exclusively in $W/Z/\gamma^*$, leptonic tau and sparticle decays.

For the purposes of background estimation, leptons may be classified into two broad categories depending on their origins:

- *real*, or prompt leptons, originating from W , Z/γ^* , leptonic tau and sparticle decays;
- *fake*, or non-prompt leptons, originating from conversions and light/heavy flavour.

Processes with three or more real leptons form the *irreducible backgrounds*, while those with fewer than three real leptons form the *reducible backgrounds* - the categorisation of different background processes is shown in Table 5.2. Kinematic variables are used to reduce the contribution of irreducible backgrounds, as discussed in Section 5.3. Reducible background contributions are minimised by event and lepton identification requirements (discussed in Section 5.2), and measured in control regions to improve the prediction in

Selection (2012 dataset)	Exactly 3 leptons, SFOS pair, $E_T^{\text{miss}} > 50 \text{ GeV}$
$WZ \rightarrow \ell\ell\ell\nu$	1085.7 ± 10.9
$t\bar{t}$	163.0 ± 4.6
$Z + \text{jets}$	129.5 ± 21.0
$ZZ \rightarrow \ell\ell\ell\ell$	89.3 ± 2.3
$t\bar{t}+V$	35.8 ± 0.5
Tribosons	11.0 ± 0.2
Single top	8.8 ± 2.0
$WW \rightarrow \ell\nu\ell\nu$	3.7 ± 0.5
$ZZ \rightarrow \ell\ell\nu\nu$	0.2 ± 0.1
$\Sigma \text{ SM}$	1528.5 ± 24.4
Example SUSY point (Model A, via $\tilde{\ell}/\tilde{\nu}$)	
$m_{\tilde{\chi}_1^\pm}, m_{\tilde{\chi}_2^0} = 250 \text{ GeV}$	27.4 ± 0.5
$m_{\tilde{\chi}_1^0} = 0 \text{ GeV}$	
Example SUSY point (Model B, via W/Z)	
$m_{\tilde{\chi}_1^\pm}, m_{\tilde{\chi}_2^0} = 500 \text{ GeV}$	36.0 ± 0.7
$m_{\tilde{\chi}_1^0} = 0 \text{ GeV}$	

Table 5.1: Predicted number of SM events with a preliminary selection of exactly three leptons, at least one SFOS pair and $E_T^{\text{miss}} > 50 \text{ GeV}$ at $\sqrt{s} = 8 \text{ TeV}$. Basic data quality requirements and selection criteria are applied to the samples, as discussed in Section 5.2. Quoted errors are statistical only.

Category	Group	Process
	Dibosons	$WZ \rightarrow \ell\ell\nu\nu$ $ZZ \rightarrow \ell\ell\ell\ell$
Irreducible	Tribosons	ZWW ZZZ WWW
	Top	Dileptonic $t\bar{t}$ Wt s/t -channel t production
Reducible	Top+ X	$t\bar{t} + W$ $t\bar{t} + Z$ $t\bar{t} + WW$
	$V+$ jets	Drell-Yan $Z+$ jets $W+$ jets
	Dibosons (reducible)	$ZZ \rightarrow \ell\ell\nu\nu$ $WW \rightarrow \ell\nu\ell\nu$

Table 5.2: Summary of irreducible and reducible backgrounds, and terms used to refer to the different backgrounds.

the signal regions, as discussed in Section 6.1. Systematic and statistical uncertainties on the background prediction were evaluated, as discussed in Section 6.3.

The data analysis is *blind*: signal regions were optimised according to the simulated background prediction, without reference to data. The background prediction was tested in several distinct *validation regions* (VRs): validation regions are distinct from control regions in that they are not used to constrain the background prediction. The validation regions were defined with $E_T^{\text{miss}} < 50$ GeV (to remove possible signal contamination), and additional selection criteria to enhance contributions from specific backgrounds. The definitions of the validation regions and the resulting distributions and tables are given in Section 7.1.

Since good agreement between data and the background prediction was observed in the validation regions, data in the signal regions were analysed. No significant excess over the background prediction was observed in any signal region, in 2011 or 2012: the data were therefore interpreted as exclusions of SUSY scenario points at 95% confidence level. Additionally, results from a separate analysis group [195] were added to the 2011 analysis

to improve the pMSSM exclusion limits.

All of the final results presented in this thesis have previously been made public by the ATLAS collaboration, but additional details and an emphasis on my own contributions are given here. All the 2011 analysis results except the GGM interpretation were published in [196]. The GGM scenarios were not included in the journal publication since they contain contributions from both weak and strong production, while weak production alone was the focus of the published article. However, they were made public in an earlier conference note [197] describing the 2011 analysis. The results of the 2012 analysis shown here were made public in [3].

5.2 Event quality requirements

A subset of the data recorded at ATLAS are discarded by data-quality selection criteria for analysis. The criteria used to eliminate these data are listed below. Unless stated otherwise, the same selection criteria were used in 2011 and 2012. For consistency, the same procedures were usually applied for data and simulated events - exceptions are noted as they appear. Additional corrections to the MC event weight to account for differences in efficiency are covered in Section 5.2.4.

5.2.1 Dataset selection

5.2.1.1 2011

Between April and October 2011, 5.25 fb^{-1} worth of proton-proton collisions at $\sqrt{s} = 7 \text{ TeV}$ were recorded by the ATLAS detector. However, of these only a subset is suitable for analysis. The event reduction is achieved by requiring that, for the selected data events, the LHC was providing stable collisions, all subdetectors were operational, and both the ATLAS solenoidal and toroidal magnet systems were operating at nominal conditions. The data are then subdivided into periods labelled from A-M depending on running conditions. The data in period A were taken with different running conditions and are therefore excluded from the analysis. Once data quality criteria are applied, the total event statistics for 2011 corresponds to an integrated luminosity of 4.7 fb^{-1} .

5.2.1.2 2012

Between April and December 2012, 23.3 fb^{-1} at $\sqrt{s} = 8 \text{ TeV}$ were recorded by the ATLAS detector. Similarly to the 2011 case, also for 2012 data, only a subset of the total event

statistics are suitable for analysis. Also in this case, the data are subdivided into periods A–M according to the running conditions. Data in periods K and M are not suitable for the analysis and are excluded. For 2012, the total integrated luminosity considered for further analysis amounts to 20.7 fb^{-1} once data quality criteria are applied.

5.2.2 Trigger

The trigger chains chosen for the analysis are based on light lepton (electron, muon) signatures. For both electrons and muons these are unprescaled (accepting all valid events) with the lowest p_T threshold available, in order to accept as many events as possible. The increase in instantaneous luminosity (discussed in Section 3.1 and shown in Figure 3.3) throughout the 2011 and 2012 data taking necessitated the use of tighter triggers in the later periods, particularly for the single electron and muon triggers. The triggers used in 2011 are defined in Table 5.3. In the electron trigger the **medium** selection criteria (similar to the offline **MEDIUM++** criteria discussed in Section 4.4.4.1) are applied in periods K–M in order to reduce the background from jets faking electrons. Additionally, in period M, electron candidates with significant energy deposits in the hadronic calorimeter are vetoed at L1 (this is denoted **vh** in Table 5.3). In the context of muon triggers, **loose** and **medium** refer to the use of 10 and 11 GeV p_T thresholds for the L1 muon trigger, rather than the tightness of the selection criteria. Leptons selected by the trigger are required to be within the plateau of the trigger efficiency: an example trigger efficiency as a function of reconstructed (“offline”) lepton p_T is shown in Figure 5.1. Since the turn-on of the efficiency curve is so steep, a small mis-calibration of electron energy can lead to a large over- or under-estimate of trigger efficiency. Events are selected if they pass any of the triggers in Table 5.3, as long as the offline lepton matched to the trigger object has p_T above the threshold given in parentheses next to the trigger.

In 2012, the adopted trigger chains were used for all data periods. In addition to the **vh** cut (defined previously), isolation (denoted by **i**) was applied to both electrons and muons. The sum of track p_T within a cone $\Delta R < 0.2$ around a lepton candidate is required to be less than 10% (12%) of the electron (muon) p_T for the lepton candidate to be considered isolated. The tracks in the cone must obey the standard tracking requirements defined in Section 4.4.1. The isolation requirements may be summarised as follows:

$$\begin{aligned} \sum_{\Delta R < 0.2} p_T^{\text{track}} &< 0.10 p_T^e \\ \sum_{\Delta R < 0.2} p_T^{\text{track}} &< 0.12 p_T^\mu \end{aligned} \quad (5.1)$$

Data period	B–H	I	J	K	L–M
Single e	e20_medium		e22_medium		e22vh_medium1
p_T threshold (GeV)				e 25	
Single μ	mu18			mu18_medium	
p_T threshold (GeV)				μ 20	
Double e	2e12_medium		2e12T_medium		2e12Tvh_medium
p_T threshold (GeV)				$2 e$ 17	
Double μ				2mu10_loose	
p_T threshold (GeV)				2μ 12	
Combined $e\mu$				e10_medium_mu6	
p_T threshold (GeV)				e 15, μ 10	

Table 5.3: Leptonic triggers used in the 2011 analysis. The p_T thresholds are chosen to be within the plateau of the trigger efficiency.

where the sum is over all tracks within $\Delta R < 0.2$, p_T^{track} is the p_T for tracks in the cone and p_T^e (p_T^μ) is the electron (muon) candidate p_T .

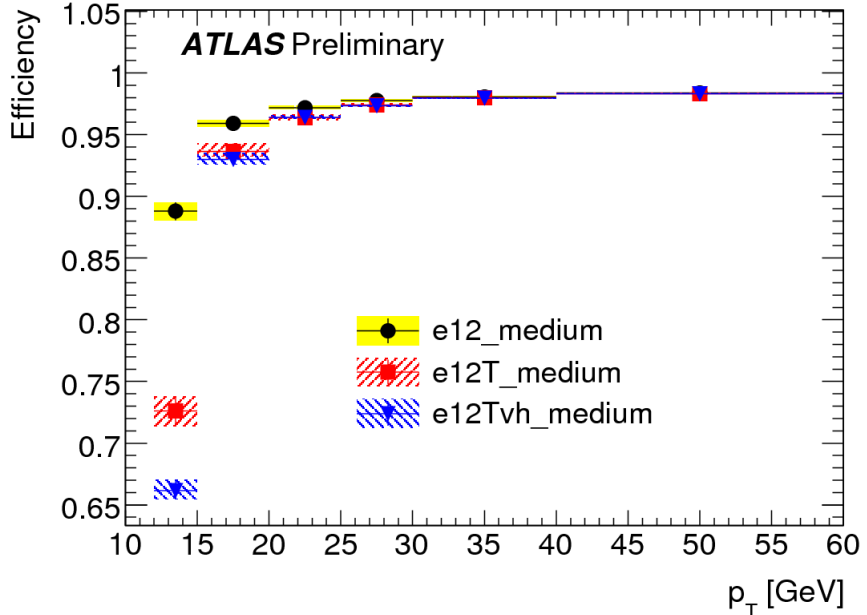


Figure 5.1: Trigger efficiency as a function of offline electron p_T , for single electron triggers in 2011. Taken from [198].

Trigger type	Detail	Offline threshold [GeV]
Single isolated e	el_e24vhi_medium1	e 25
Single isolated μ	mu24i_tight	μ 25
Double e	2e12Tvh_loose1 e24vh_medium1_e7_medium1	e 14, e 14 e 25, e 10
Double μ	2mu13 mu18_tight_mu8	μ 14, μ 14 μ 18, μ 10
Combined $e\mu$	e12Tvh_medium1_mu8 mu18_tight_e7_medium1	e 14, μ 10 μ 18, e 10

Table 5.4: Leptonic triggers used in the 2012 analysis. The p_T thresholds of the offline leptons are chosen to be within the plateau of the trigger efficiency. Note that the same triggers were used in all data periods.

5.2.3 Event selection for data quality purposes

Various selection criteria are applied to events before leptons, jets and all other event objects are selected. Events are required to have a primary vertex with at least five associated tracks. Events are vetoed if jets do not pass quality criteria defined in [199], which seek to remove events with fake jets caused by detector noise, cosmic ray muons, interactions between protons and residual gas left in the beam pipe, as well as interactions away from the main interaction point. A dedicated veto for muons from cosmic rays is imposed by requiring that reconstructed muons fail at least one of the following cuts:

- $z_0 \sin \theta > 1$ mm
- $d_0 > 1$ mm

Events with poorly reconstructed muons are also vetoed. Such muons have poorly measured q/p , where q is the particle charge and p is the momentum, both measured in the ID. The criterion used to reject such events is

$$\frac{\sigma_{q/p}}{|q/p|}(\mu) \geq 0.2 \quad (5.2)$$

where $\sigma_{q/p}$ is the error on the q/p measurement provided by the track fit, d_0 and z_0 are the impact parameter and the projection of the impact parameter onto the z -axis respectively (both defined in Section 4.4.1).

5.2.3.1 Lepton selection

So that it can have triggered the event, at least one of the three leptons in each event is required to have p_T above the offline thresholds given in Tables 5.3 and 5.4 for 2011 and 2012 respectively. Other leptons in the event must have p_T above 10 GeV. In 2012, events containing medium tau candidates (as defined in Section 4.4.9) are vetoed. An offline lepton candidate must be found within $\Delta R = 0.15$ of the lepton found by the trigger used in the event. Leptons at this stage are only required to pass loose selection - tight selection is applied in the final pre-selection detailed in Section 5.2.3.3.

5.2.3.2 Jet selection

Jets are reconstructed as detailed in Section 4.4.6 and required to have $p_T > 20$ GeV. Jets within the full acceptance of the forward and central calorimeters are used, corresponding to $|\eta_{\text{jet}}| < 4.9$.

5.2.3.3 Final pre-selection

After overlap removal (discussed in Section 4.4.10.1), further tight selection criteria are applied to all electrons and muons as detailed in Sections 4.4.4.3 and 4.4.5.3. SFOS pairs with $m_{\ell\ell} < 12$ GeV are removed from the event, in order to remove background from low mass resonances (Υ , J/ψ etc). The tight electrons, muons and jets are then used to form the E_T^{miss} , as detailed in Section 4.4.11. In addition to these objects, clusters not associated with jets or electrons as well as jets with $p_T < 20$ GeV are added to the total E_T^{miss} . Finally, pre-selected events are required to have exactly three leptons.

5.2.4 Corrections to MC event weights

The response and geometry of the ATLAS detector is not perfectly described by simulation, nor are the tracks and calorimeter deposits left by simulated objects identical to those left by objects in data. Additionally, the running conditions for a given subset of data may not match those in a set of simulated events. Corrections for these deficiencies in simulation are applied to reweight individual MC events - these corrections are provided by ATLAS performance groups.

5.2.4.1 Pile-up reweighting

As discussed in Section 4.1.6, the average number of interactions per event ($\langle \mu \rangle$) is not completely well modelled in Monte Carlo. Weights are therefore applied to simulated

events so that the distribution of $\langle \mu \rangle$ agrees between data and Monte Carlo.

5.2.4.2 Lepton efficiency reweighting

Scale factors to correct for data/MC differences in reconstruction efficiency are provided by the electron [179] and muon [200] performance groups, and these are applied to all lepton candidates. These scale factors depend on the kinematics of the observed leptons. The product of all efficiency scale factors for the leptons in the event is then applied as an overall event weight.

5.2.4.3 Flavour tagging efficiency reweighting

The presence or absence of b -tagged jets is used to classify events. Differences between the flavour-tagging efficiency and misidentification rates in data and MC are accounted for by an η - and p_T -dependent scale factor. The scale factors also depend on the flavour-tagging score (discussed in Section 4.4.8). Scale factors are provided by the flavour-tagging performance group [188, 189, 190], and only derived at specific MV1 values over a range of efficiencies. As is done for leptons, the product of these weights is then applied to the event as a whole.

5.2.4.4 Trigger reweighting (2011 only)

The efficiency of the trigger simulation (discussed in Section 4.2.2) can also differ significantly from the actual trigger efficiency in data. Additionally, vetoing MC events according to a simulated trigger decision reduces the available MC event statistics. Instead of applying the trigger simulation directly, the *trigger reweighting* procedure circumvents these problems - events are reweighted by η - and p_T -dependent trigger efficiency scale factors instead of being rejected. This procedure was applied in 2011 due to observed disagreement in trigger efficiency and in order to retain MC event statistics.

For the selections used in this work, measured and simulated trigger efficiencies were found to agree to within $< 1\%$ in 2012, with all triggers used having close to 100% efficiency. Trigger reweighting was therefore not applied to the 2012 dataset.

5.3 Signal region optimisation

The signal regions are then divided into two complementary sets: one with on-shell Z boson candidates and one without on-shell Z boson candidates. An event is considered to have an on-shell Z boson candidate if the mass of the candidate dilepton pair is within

10 GeV of $m_Z = 91.2$ GeV: ($|m_{\ell\ell} - m_Z| < 10$ GeV). The presence or absence of a Z boson indicates the type of SUSY decay and leads to different backgrounds. Signal regions with a Z -candidate veto are denoted “SR1” in 2011 and “SRnoZ” in 2012, while those with a Z -candidate veto are denoted “SR2” in 2011 and “SRZ” in 2012. Additionally, the level of background suppression in the signal region is indicated by a, b, c in loose to tight order. Three signal regions were defined in 2011, two with Z -candidate vetoes (SR1a, SR1b), and one with a Z -candidate request (SR2). Six signal regions, three with Z -candidate requests (SRZa, SRZb, SRZc), and three without (SRnoZa, SRnoZb, SRnoZc) were defined in 2012. The naming conventions for the SRs are summarised in Table 5.5. The different loose and tight signal regions have sensitivity to different scenarios: when statistically combined, a single insensitive region does not affect the sensitivity of the combination, as discussed in Section 7.3.

Analysis	Name	Z boson candidate	Acceptance
2011	SR1a	Veto	Loose
	SR1b		Tight
2012	SR2	Request	Tight
	SRnoZa		Loose
	SRnoZb	Veto	Medium
	SRnoZc		Tight
	SRZa		Loose
	SRZb	Request	Medium
	SRZc		Tight

Table 5.5: Signal region nomenclature for the 2011 and 2012 analysis.

5.3.1 Discriminating variables

Several discriminating variables are used to discriminate between signal and background, on top of the basic selection (exactly three light leptons, at least one SFOS pair and $E_T^{\text{miss}} > 50$ GeV). SUSY weak production of gauginos will have limited hadronic activity, so it is possible to use **jet multiplicity and flavour** to reduce the background. The presence of at least one b -tagged jet can indicate $t\bar{t}$ production.

Also, the total **missing transverse energy** in SUSY events is expected to generally be higher than that in Standard Model backgrounds, due to the presence of LSPs as well as

neutrinos. This is dependent on the particular event kinematics (LSPs produced nearly back-to-back will not contribute significantly to the E_T^{miss}) and on the LSP mass.

If an SFOS pair indeed emanates from a single intermediate particle, the **invariant mass** of the intermediate particle may be fully reconstructed. An invariant mass requirement ($m_{\ell\ell}$) is used in order to veto or select Z boson production, as well as to reject known low-mass resonances (J/ψ , Υ etc). Requiring an upper threshold on $m_{\ell\ell}$ increases sensitivity to scenarios with low mass splitting (given by $|m_{\tilde{\chi}_2^0} - m_{\tilde{\chi}_1^0}|$).

The **transverse mass** between a visible (ℓ) and invisible particle (E_T^{miss}) is defined as

$$m_T = \sqrt{2(E_T^{\text{miss}} p_T^\ell (1 - \cos \Delta\phi(\ell, E_T^{\text{miss}})))}, \quad (5.3)$$

where $\Delta\phi(\ell, E_T^{\text{miss}})$ is the angle between the ℓ and E_T^{miss} in the transverse plane. Transverse mass is the analogue of invariant mass in the transverse event plane. It exhibits an endpoint and a sharp peak at the mass (m_i) of the invisible particle produced. When observed, the sharp peak is broadened by a combination of experimental and theoretical effects. In SM $W \rightarrow \ell\nu$ decays, the peak is at $m_i = m_W$. Selecting events with $m_T > m_W$ therefore leads to a reduction in backgrounds with real W bosons and improved sensitivity to SUSY signals with higher mass intermediate particles. Conversely, requiring $m_T < m_W$ increases sensitivity to SUSY signals with lower mass intermediate particles.

In events with only one SFOS pair ($\{\mu^+ \mu^- e^\pm\}$ or $\{e^+ e^- \mu^\pm\}$) the lepton not forming part of the SFOS pair is the only choice for $m_T(\ell, E_T^{\text{miss}})$: since the SUSY models considered in this work do not violate flavour, the SFOS pair must come from the same leg of the decay (unless emanating from leptonic tau decays). In uniform flavour events ($\{eee\}$ or $\{\mu\mu\mu\}$), there is an ambiguity as to which lepton to use: in this case the SFOS pair with mass closest to m_Z is first searched for, and the lepton not forming part of the SFOS pair closest to the Z mass is used to form the m_T . This prescription is used for all transverse mass calculations in these analyses. The **lepton p_T** also has a sharp peak at half the invisible particle mass ($m_i/2$), but no endpoint and therefore has less rejection power than m_T . It is still useful for selecting high mass intermediate particles.

5.3.2 Optimisation procedure

The SRs are formed by maximising the expected significance Z_N where

$$Z_N = \Phi^{-1}(1 - p_0(S, B, \Delta B)). \quad (5.4)$$

Here Φ^{-1} is the cumulative distribution of the standard Gaussian and S and B are the number of expected signal and background events for a given scenario. ΔB is the back-

ground uncertainty and p_0 is the background-only p -value (that is, the chance of a dataset being recorded that is more signal-like than $S + B$, given the background-only hypothesis), as discussed in more detail in Section 7.3). The p -value is evaluated with 30% background uncertainty, which is similar to the overall background uncertainty in the 2011 analysis. The algorithm for the approximation of the p -value is detailed in [201]. In order to avoid problems with numerical instability, the algorithm is truncated to allow a maximum $Z_N = 8$.

Plots of the various event variables for signal and background are shown in the subsequent Sections, as well as the effects of varying thresholds on these variables as a function of Z_N . Different signal benchmark points are chosen to demonstrate each cut. The decrease in the number of signal and background events remaining as the various thresholds are increased leads to fluctuations in the Z_N plots: the final cut values chosen are far from these points.

The final expected significance for all points in Model A and Model B, with the 30% background uncertainty are shown in Figures 5.10, 5.10 5.12 and 5.13, and the effect of all cuts on SM backgrounds and selected benchmark points is shown in tabular form in Section 5.4.

5.3.3 Optimisation of jet veto

Since signal events from simplified models and pMSSM samples are not expected to have significant hadronic activity, vetoing jets can reduce the Standard Model background. In particular, $t\bar{t}$ events will almost always contain two b -decays, and consequently up to two correctly b -tagged jets. This motivates a veto on b -tagged jets. Details of the b -tagging algorithm MV1 are given in Section 4.4.8. Figure 5.2(a) shows the number of b -tagged jets, and b) the significance of a veto on events with a b -tagged jet passing $MV1 > X$, as X increases. By comparison, the number of jets (c), the p_T of all jets (d) and the significance of a veto on events with $p_T < X$ GeV as X increases (e) are shown. For the samples considered, vetoing all b -jets is found to be more effective than vetoing light jets. The use of the $MV1 > 0.122$ threshold yields slightly higher significance than tighter b -jet selections. The specific value $MV1 = 0.122$ is chosen, as systematic uncertainties for the algorithm were only provided for a few points, as discussed in Section 4.4.8. All subsequent optimisation is performed with this b -jet veto.

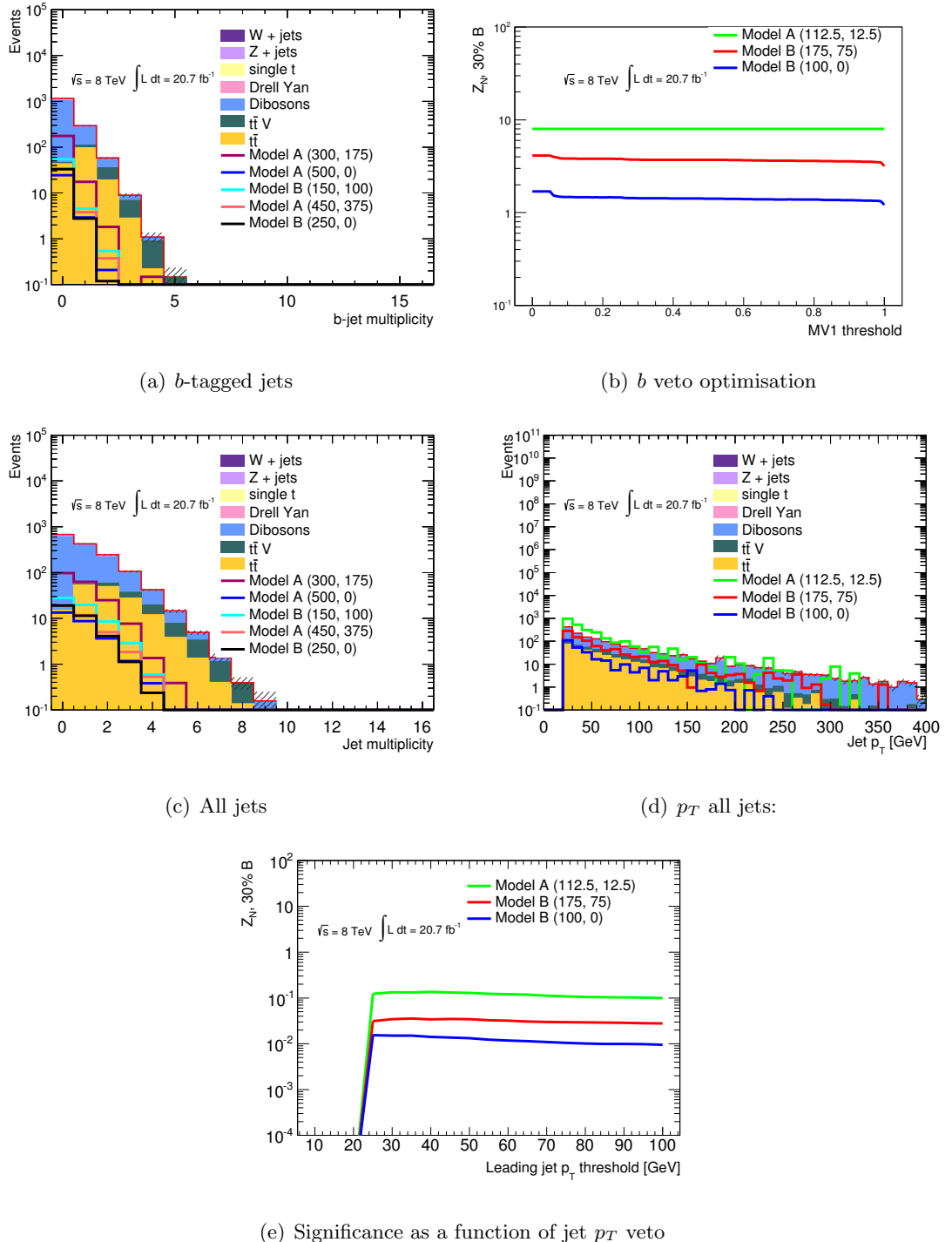


Figure 5.2: In (a), the number of *b*-tagged jets using $MV1 > 0.122$ for three lepton events with an SFOS pair and $E_T^{\text{miss}} > 50$ GeV. In (b) the significance Z_N for SUSY benchmark points as a function of the MV1 threshold for the *b*-jet veto. The number of jets for the same selection (c) and the p_T of the leading jet (d). The expected significance Z_N for SUSY benchmark points as the upper cut on the leading jet p_T is varied (e).

5.3.4 Optimisation of E_T^{miss}

As previously discussed, E_T^{miss} is an important discriminant between SUSY and SM events. In order to maximise the sensitivity to as many SUSY points as possible, E_T^{miss} values between 50 GeV and 120 GeV were investigated for each SR.

Figure 5.3(a) shows the E_T^{miss} distribution for a selection with standard preselection, a Z -candidate veto and a b -jet veto. Figure 5.3(b) shows that E_T^{miss} values between 100 and 150 GeV optimise the significance for the signal points considered. Similarly, Figure 5.4 shows an optimal significance for E_T^{miss} values between 70 and 150 GeV. Signal regions with $E_T^{\text{miss}} > 75$ GeV, $75 \text{ GeV} < E_T^{\text{miss}} < 120$ GeV and $E_T^{\text{miss}} > 120$ GeV are chosen in order to maximise sensitivity to a variety of different scenarios.

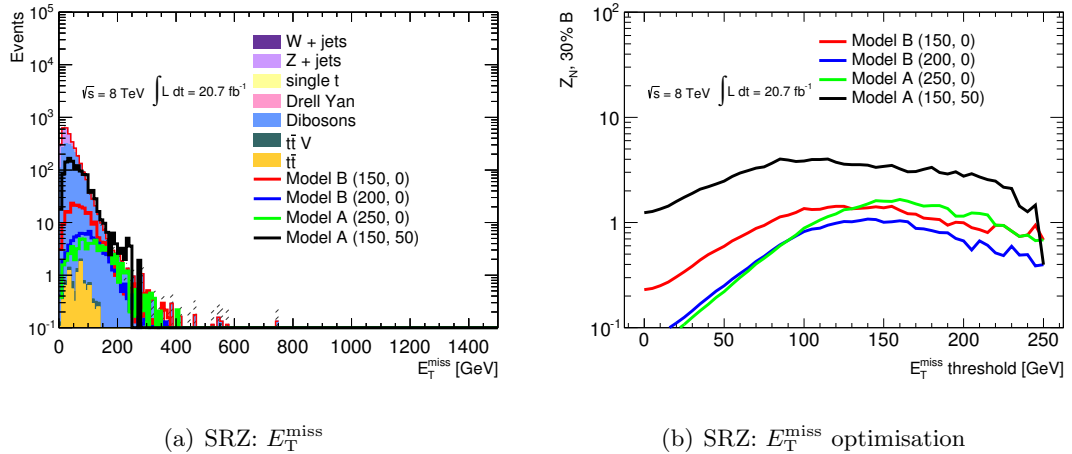


Figure 5.3: The E_T^{miss} distribution in three lepton events where a SFOS lepton pair is present, Z candidates are requested and a b -jet veto is applied (a). The expected significance for SUSY benchmark points as a cut on E_T^{miss} is varied (b).

5.3.5 Optimisation of $m_{\ell\ell}$

The invariant mass of an SFOS pair from the $\tilde{\chi}_2^0$ decay via sleptons in Model A, shown in Figure 5.5, has a kinematic endpoint which is a function of the difference between the $\tilde{\chi}_2^0$ and $\tilde{\chi}_1^0$ masses [202]. An upper threshold on $m_{\ell\ell}$ is used to select events with a low $m_{\tilde{\chi}_2^0} - m_{\tilde{\chi}_1^0}$. Figure 5.6 shows (a) the $m_{\ell\ell}$ for SM backgrounds and selected SUSY signal points and (b), the Z_N score for the same SUSY signal points as the threshold is raised. A signal region (SRnoZa) with an upper threshold for $m_{\ell\ell}$ is defined: the effect of varying this upper threshold is shown in Figure 5.6. A cut of $m_{\ell\ell} < 60$ GeV was found to be optimal for the low mass splitting regime. An additional SR (SRnoZb) was defined with $60 \text{ GeV} < m_{\ell\ell} < 81.2 \text{ GeV}$. Together with a third signal region (SRnoZc) with a Z -veto but

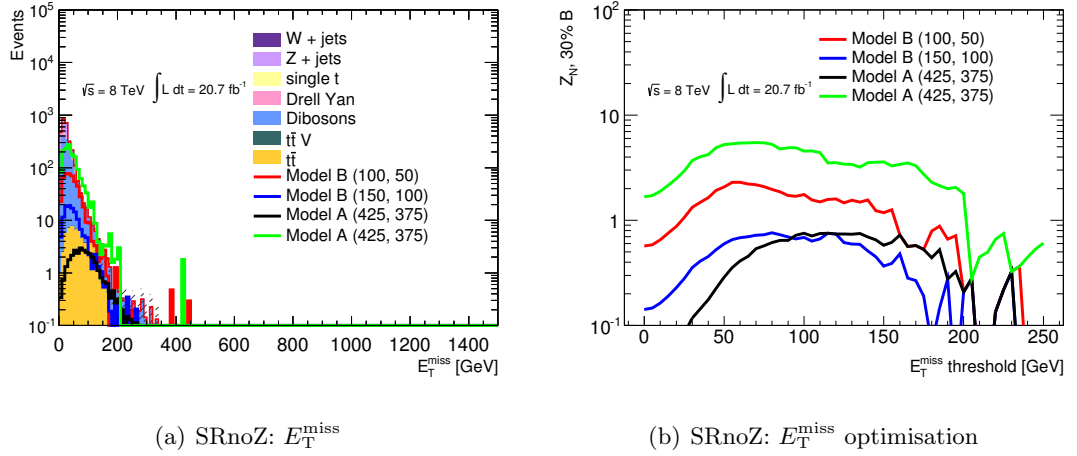


Figure 5.4: The E_T^{miss} distribution in three lepton events where a SFOS lepton pair is present, Z candidates are vetoed and a b -jet veto is applied (a). The expected significance for SUSY benchmark points as a cut on E_T^{miss} is varied (b).

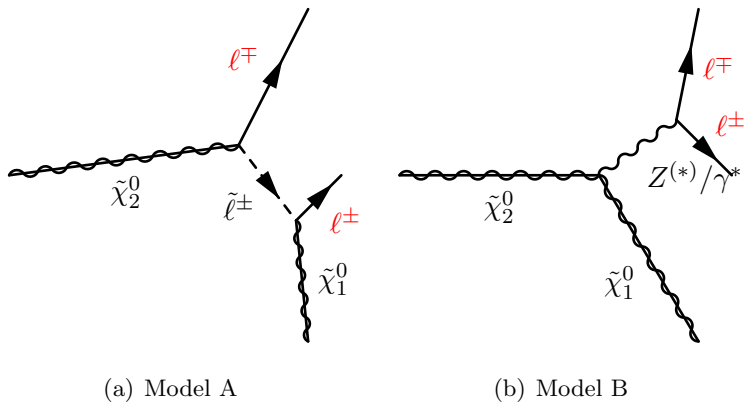


Figure 5.5: SFOS pair from $\tilde{\chi}_2^0$ decays in Model A and B. The invariant mass $m_{\ell\ell}$ from the SFOS pair in (a) has a kinematic endpoint related to the difference between the $\tilde{\chi}_2^0$ and $\tilde{\chi}_1^0$ masses, as discussed further in Section 5.3.5. The invariant mass of the (possibly off-shell) Z boson in (b) is given by $m_{\tilde{\chi}_2^0} - m_{\tilde{\chi}_1^0}$.

no other $m_{\ell\ell}$ requirement, this retains sensitivity to all possible mass splittings.

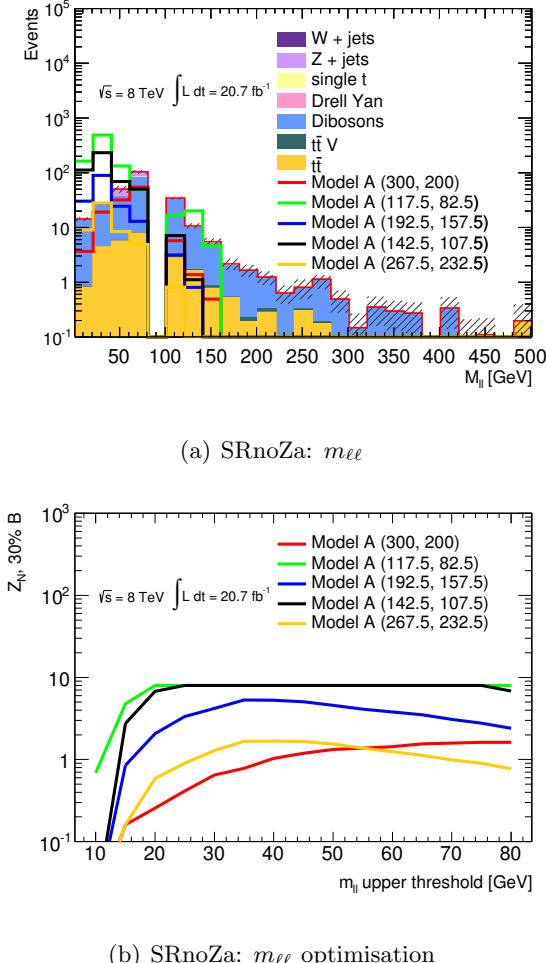
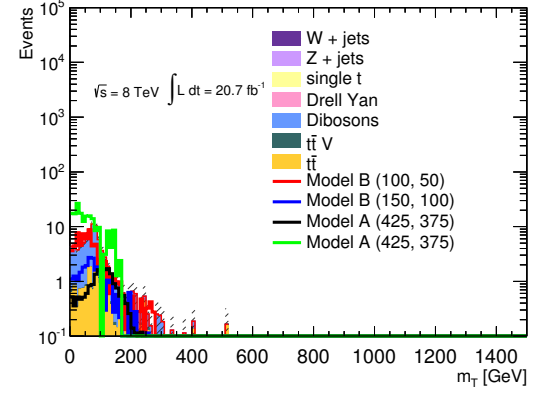
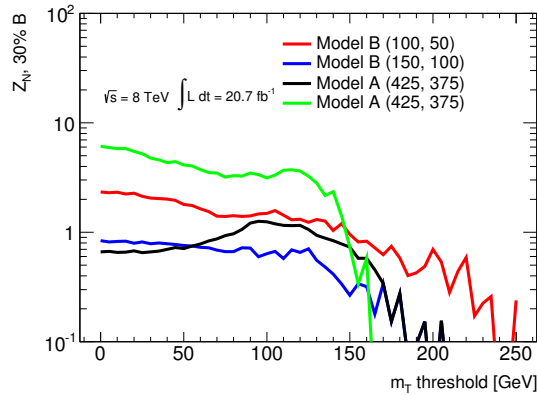
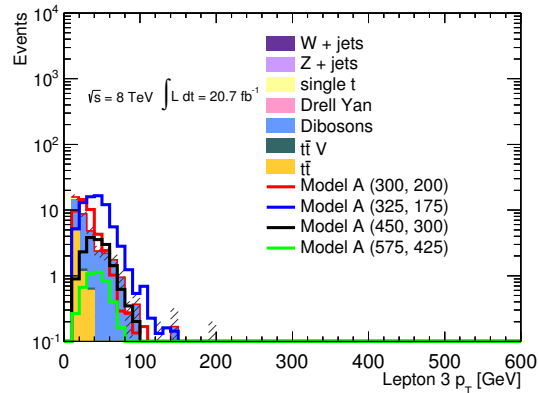
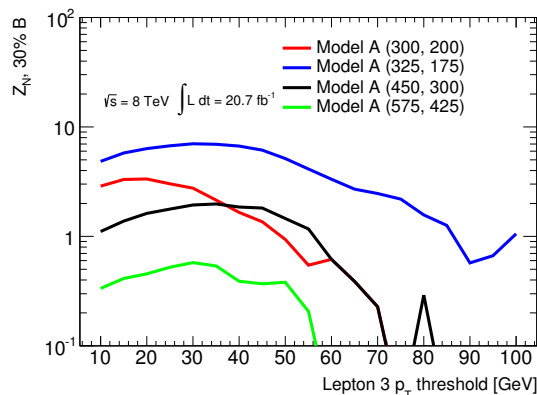


Figure 5.6: The $m_{\ell\ell}$ distribution for three lepton events where a SFOS lepton pair is present, $E_T^{\text{miss}} > 50$ GeV, Z candidates are vetoed, and a b -jet veto is applied (a). The expected significance Z_N for SUSY benchmark points as an upper threshold on $m_{\ell\ell}$ is increased (b). The Z_N is truncated at $Z_N = 8$, leading to the flat behaviour as a function of $m_{\ell\ell}$.

5.3.6 Optimisation of m_T and lepton p_T

Figure 5.7 shows the effect of varying a lower threshold on m_T : in all regions without a Z -candidate, values around 100 GeV are preferred. For signal regions SRnoZc, SRZb, and SRZc, a common cut value of $m_T > 110$ GeV is chosen: SRZa reverses this cut in order to retain sensitivity to signals with lower mass splitting. In SRnoZc, lepton $p_T > 30$ GeV is required, in order to optimise sensitivity to scenarios with large mass splitting: Figures 5.7(c) and 5.7(d) motivate this choice.

(a) SRnoZc: m_T (b) SRnoZc: m_T optimisation(c) SRnoZc: $p_T^{\ell_3}$ (d) SRnoZc: $p_T^{\ell_3}$ optimisationFigure 5.7: The m_T distribution with a SFOSS lepton pair is present. $E_{\text{miss}}^{\text{miss}} > 75 \text{ GeV}$, a

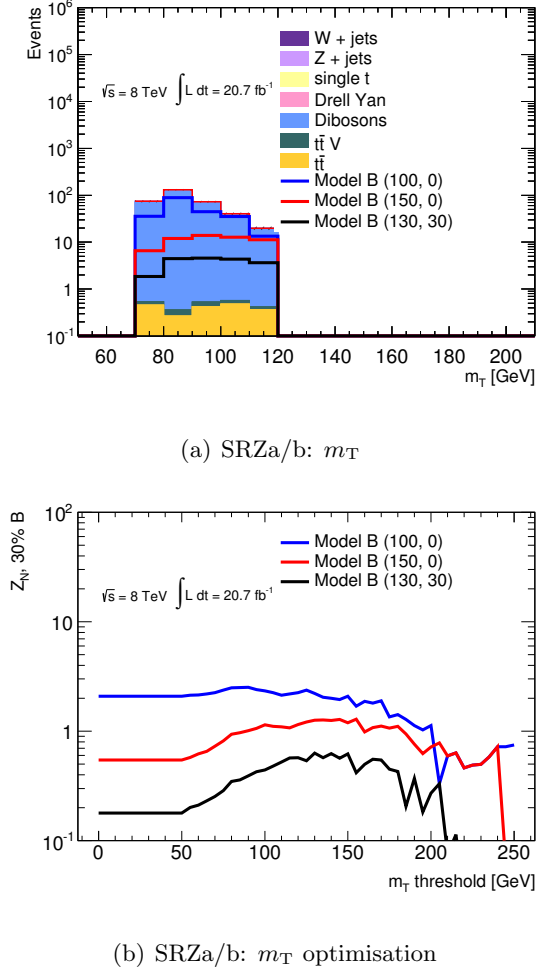


Figure 5.8: The m_T distribution with a SFOS lepton pair, $75 < E_T^{\text{miss}} < 120 \text{ GeV}$, a b -jet veto is applied and Z candidates are requested (a). The expected significance for SUSY benchmark points as a cut on m_T is varied (b). Statistical fluctuations in the number of available events manifest as sharp peaks and troughs in Z_N , visible in (b) above approximately $m_T > 150 \text{ GeV}$.

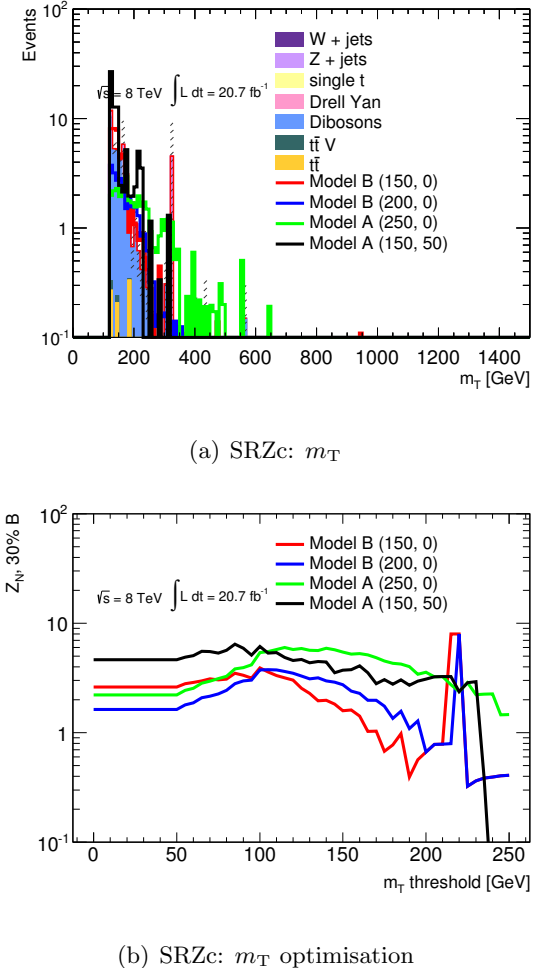


Figure 5.9: The m_T distribution for the lepton with a SFOS lepton pair is present, $E_T^{\text{miss}} > 120$ GeV, a b -jet veto is applied and Z candidates are requested (a). The expected significance for SUSY benchmark points as a cut on m_T is varied (b). Statistical fluctuations in the number of available events manifest as sharp peaks and troughs in Z_N , visible in (b) above approximately $m_T > 200$ GeV.

5.3.7 Signal region choices

The set of three signal regions (SR1a, SR1b, SR2) used in 2011 is given in Table 5.6. A single, moderate, E_T^{miss} requirement (75 GeV) is used instead of the 50, 75 and 120 GeV cuts used in the 2012 signal regions. Since $t\bar{t}$ is not a dominant background in Z -request signal regions, no b -jet veto was imposed in SR2. Relative to 2011, the 2012 m_T cuts are

Selection	SR1a	SR1b	SR2
Targeted intermediate decay	$\tilde{l}^{(*)}$ or Z^*	on-shell Z	
$m_{\ell\ell}$ [GeV]	< 81.2, > 101.2	[81.2:101.2]	
E_T^{miss} [GeV]		> 75	
m_T	–	> 90 GeV	
$p_T^{\ell_3}$ [GeV]	> 10	> 30	> 10
Number of b -jets	0	0	–

Table 5.6: The selection requirements for the 2011 signal regions. SR1a and SR1b are not disjoint, while SR1a and SR1b are both orthogonal with SR2.

higher (110 GeV compared to 90 GeV): the increased pileup in 2012 broadened the W m_T peak. The final set of six 2012 signal regions is given in Table 5.7.

Selection	SRnoZa	SRnoZb	SRnoZc	SRZa	SRZb	SRZc
Main sensitivity	Model A				Model B	
$m_{\ell\ell}$ [GeV]	< 60	60–81.2	< 81.2 or > 101.2	81.2–101.2	81.2–101.2	81.2–101.2
E_T^{miss} [GeV]	> 50	> 75	> 75	75–120	75–120	> 120
m_T [GeV]	–	–	> 110	< 110	> 110	> 110
$p_T^{\ell_3}$ [GeV]	> 10	> 10	> 30	> 10	> 10	> 10
Signal region veto	Not in SRnoZc		–	–	–	–

Table 5.7: The selection requirements for the 2012 signal regions. All regions are disjoint.

5.3.8 Removing overlap between signal regions

SRs used in a statistical combination (discussed in Section 7.3.6) are not allowed to have overlapping selection criteria. Such SRs are said to be *disjoint* or orthogonal. Since each SR is composed of a sequence of cuts, it is only necessary to reverse one cut ($E_T^{\text{miss}} < X$ GeV $\rightarrow E_T^{\text{miss}} > X$ GeV, for example) to make the SRs disjoint. It is possible to use the **AND** of several cut reversals: since several conditions have to be met, this means that fewer events will be vetoed, thus increasing the selection efficiency of the region containing

the veto. SRnoZa and SRnoZb explicitly veto SRnoZc by requiring that any event in SRnoZa/b does not pass at least one of the selection criteria for SRnoZc. SRZa/b/c are disjoint by construction, as are the SRnoZ and SRZ regions. The 2011 SRs SR1a and SR1b are not disjoint: SR1b is a subset of SR1a. However, SR2 is disjoint with SR1a and SR1b due to a Z -candidate request.

5.4 Cutflows for final signal regions

The sequence of cuts defining an SR is known as a *cutflow*. The cutflow for each background and SR at $\sqrt{s} = 8$ TeV with 20.7 fb^{-1} of data is shown separately in Tables 5.8, 5.9, 5.10, 5.11, 5.12 and 5.13. These tables demonstrate the effectiveness of the chosen cuts at reducing the SM background. The total SM background, as well as the different contributions is shown for each SR. SUSY points are also tabulated to demonstrate the effectiveness of the chosen cut values. The naming convention for each point is “Model X: $m_{\tilde{\chi}_2^0}, m_{\tilde{\chi}_1^\pm}, m_{\tilde{\chi}_1^0}$ ”, with entries such as “Model A: 100, 0”. Underneath each SUSY point the expected significance, Z_N , is shown.

As previously discussed, the different SRs are statistically combined to produce the final exclusion limits. This combination is ignored in the simplified Z_N calculation. Figures 5.10, 5.11 and 5.12 and 5.13 show the expected Z_N for the complete Model A and Model B grids in each SR. Since all SRs are statistically combined, the true sensitivity is greater. Overall, the SRnoZ signal regions are designed to have the greatest sensitivity to Model A, and SRZ regions have the greatest sensitivity to Model B. As seen in Figure 5.12(a), SRnoZa also has sensitivity to points with low mass near the diagonal.

Requiring or vetoing a Z candidate reduces the total SFOS background by a factor of two. The softest E_T^{miss} cut ($E_T^{\text{miss}} > 50$ GeV in SRnoZa) reduces the total SM background by almost a factor of ten (from 3327.5 ± 77.6 to 455.4 ± 13.2) - similar factors of background reduction are found for all other SRs. In the Z -request SRs, initially dominated by $Z + \text{jets}$, the E_T^{miss} distribution extends to higher values, requiring higher E_T^{miss} cuts (up to 120 GeV) for a similar background reduction. The application of a b -jet veto in all SRs reduces the $t\bar{t}$ and $t\bar{t} + V$ backgrounds by up to a factor of five (from $t\bar{t} + t\bar{t} + V = 50.8 \pm 2.5$ to 10.7 ± 1.2 in SRnoZa).

5.4.1 SRnoZa

Requiring that events in SRnoZa do not pass SRnoZc selection leads to a small reduction in both signal and background events. For instance, Model A: (225, 125) falls from 164.7 ± 7.3

to 143.0 ± 6.8 , a reduction of over 10%. The expected significance for this point changes from $Z_N = 5.1$ to $Z_N = 4.7$. The invariant mass cut ($m_{\ell\ell} < 60$ GeV) reduces $Z + X$ (ZZ , WZ and $Z+\text{jets}$) by more than a factor of two. SRnoZa has the best reach in Model A close to the diagonal, where the mass splitting is small, as can be seen in Figure 5.10(a). SRnoZa also has sensitivity to the Model B (100, 50) and (150, 100) points, as seen in Figure 5.12(a), since the invariant mass of the Z boson produced is constrained by the neutralino mass difference $m_{\tilde{\chi}_2^0} - m_{\tilde{\chi}_1^0}$ (see Figure 5.5(a)). The cutflow for SRnoZa is shown in Table 5.8.

5.4.2 SRnoZb

Since events in SRnoZb, like those in SRnoZa, are required not to pass SRnoZc selection, there is a decrease in signal sensitivity for several points, which is recovered in the final statistical combination. The double-sided invariant mass cut (60 GeV $< m_{\ell\ell} < 81.2$ GeV) reduces all $Z + X$ background by more than a factor of two. SRnoZb increases the sensitivity near to the line $m_{\tilde{\chi}_2^0} - m_{\tilde{\chi}_1^0} = m_Z$: see for example the points (150, 50) and (200, 100) in Figure 5.12(b). The cutflow for SRnoZb is shown in Table 5.9.

5.4.3 SRnoZc

SRnoZc imposes a tight m_T requirement ($m_T > 110$ GeV), reducing WZ (the dominant background at this point) from 81.9 ± 3 events to 11.6 ± 1.1 . At this stage, $t\bar{t}$ is then the dominant background (15.4 ± 1.4 events); its contributions are reduced by more than a factor of ten by requiring $p_T^{\ell_3} > 30$ GeV. SRnoZc has the lowest overall predicted background (4.0 ± 0.6). SRnoZc has the highest predicted sensitivity across the bulk of Model A, as seen in Figure 5.10(c). The cutflow for SRnoZc is shown in Table 5.10.

5.4.4 SRZa

Since SRZa has a moderate E_T^{miss} requirement (75 GeV $< E_T^{\text{miss}} < 120$ GeV) and an upper threshold on m_T ($m_T < 110$ GeV), it is most useful as an auxiliary SR, selecting events lost by the harder cuts in SRZb and SRZc. In particular, it is sensitive to the lowest mass point, (100, 0), as seen in Figure 5.13(a). It also has some coincidental sensitivity to Model A, visible in 5.11(a). The cutflow for SRZa is shown in Table 5.11.

5.4.5 SRZb

SRZb has the same E_T^{miss} requirement as SRZa but a harder m_T cut ($m_T > 110 \text{ GeV}$), reducing the dominant background WZ by a factor of ten (from 299.8 ± 5.7 to 22.6 ± 1.6). SRZb has enhanced sensitivity to points near 5.13(b).

5.4.6 SRZc

SRZc has the tightest E_T^{miss} and m_T requirements of any SR ($E_T^{\text{miss}} > 120 \text{ GeV}$ and $m_T > 110 \text{ GeV}$), and consequently has a low overall SM background (6.1 ± 0.8). SRZc has the highest predicted sensitivity in the bulk of Model B, rising to a maximum of $Z_N = 3.5$ for the point (200, 0), as seen in 5.13(c).

SRnoZa	SFOS	Z veto	$E_T^{\text{miss}} > 50 \text{ GeV}$	$m_{\ell\ell} < 60 \text{ GeV}$	b -jet veto	Not in SRnoZc
$t\bar{t}$	249.4 ± 5.7	216.6 ± 5.3	143.8 ± 4.4	47.8 ± 2.5	10.5 ± 1.2	10.3 ± 1.2
$t\bar{t} + V$	50.9 ± 0.6	19.7 ± 0.4	15.1 ± 0.4	3.0 ± 0.2	0.2 ± 0.04	0.2 ± 0.04
WW	6.8 ± 0.6	6.1 ± 0.6	3.2 ± 0.4	0.9 ± 0.2	0.6 ± 0.2	0.6 ± 0.2
ZZ	1564.0 ± 10.2	1099.5 ± 8.6	42.7 ± 1.6	15.8 ± 1.0	13.9 ± 0.9	13.7 ± 0.9
$ZZ \rightarrow \ell\ell\nu\nu$	0.4 ± 0.1	0.1 ± 0.05	0.1 ± 0.03	0.0 ± 0.0	0.0 ± 0.0	0.0 ± 0.0
WZ	2398.6 ± 16.3	489.2 ± 7.3	194.0 ± 4.6	62.8 ± 2.6	50.1 ± 2.3	49.5 ± 2.3
Tribosons	16.3 ± 0.2	12.6 ± 0.2	8.4 ± 0.1	1.9 ± 0.1	1.8 ± 0.1	1.7 ± 0.1
Drell-Yan	138.3 ± 30.0	135.8 ± 29.9	1.5 ± 1.4	1.5 ± 1.4	1.5 ± 1.4	1.5 ± 1.4
Single t	14.3 ± 2.5	11.3 ± 2.2	6.9 ± 1.7	1.0 ± 0.9	0.3 ± 0.8	0.3 ± 0.8
$Z + \text{jets}$	2734.7 ± 98.2	1336.5 ± 70.5	39.8 ± 11.3	12.5 ± 6.9	12.5 ± 6.9	12.5 ± 6.9
$\Sigma \text{ SM}$	7173.6 ± 104.7	3327.5 ± 77.6	455.4 ± 13.2	147.2 ± 8.0	91.3 ± 7.6	90.3 ± 7.6
Model A: 225,125	881.5 ± 16.9	550.7 ± 13.4	406.8 ± 11.5	185.3 ± 7.9	164.7 ± 7.3	143.0 ± 6.8
Z_N	0.4	0.6	2.9	3.9	5.3	4.7
Model A: 192.5,157.5	536.8 ± 17.9	519.4 ± 17.6	187.0 ± 10.4	164.4 ± 9.8	141.1 ± 8.9	141.1 ± 8.9
Z_N	0.2	0.5	1.3	3.5	4.6	4.6
Model B: 150,100	137.0 ± 3.8	130.5 ± 3.7	57.0 ± 2.4	48.3 ± 2.2	43.7 ± 2.1	43.5 ± 2.1
Z_N	0.1	0.1	0.4	1.0	1.5	1.5
Model B: 100, 50	551.0 ± 16.3	530.7 ± 16.1	200.3 ± 9.8	176.3 ± 9.2	158.3 ± 8.6	158.3 ± 8.6
Z_N	0.3	0.5	1.4	3.7	5.1	5.1

Table 5.8: Cutflow for SRnoZa at $\sqrt{s} = 8 \text{ TeV}$ with 20.7 fb^{-1} of data. Errors are statistical only. Expected significances are calculated assuming a 30% uncertainty on the number of background events.

5.5 Potential improvements to choice of SRs

While the manual optimisation of SRs is a transparent technique, there are other ways to choose SRs. The signal regions chosen here are effectively “binned” in several kinematic

SRnoZb	SFOS	Z veto	$E_T^{\text{miss}} > 75 \text{ GeV}$	$60 < m_{\ell\ell} < 81.2 \text{ GeV}$	b-jet veto	Not in SRnoZc
$t\bar{t}$	249.4 ± 5.7	216.6 ± 5.3	85.5 ± 3.4	17.2 ± 1.5	4.3 ± 0.8	4.3 ± 0.8
$t\bar{t} + V$	50.9 ± 0.6	19.7 ± 0.4	11.1 ± 0.3	1.9 ± 0.1	0.1 ± 0.03	0.1 ± 0.03
WW	6.8 ± 0.6	6.1 ± 0.6	1.8 ± 0.3	0.2 ± 0.1	0.1 ± 0.1	0.1 ± 0.1
ZZ	1564.0 ± 10.2	1099.5 ± 8.6	6.0 ± 0.6	2.1 ± 0.4	1.8 ± 0.3	1.8 ± 0.3
$ZZ \rightarrow \ell\ell\nu\nu$	0.4 ± 0.1	0.1 ± 0.05	0.0 ± 0.0	0.0 ± 0.0	0.0 ± 0.0	0.0 ± 0.0
WZ	2398.6 ± 16.3	489.2 ± 7.3	81.9 ± 3.0	25.4 ± 1.7	20.0 ± 1.5	19.5 ± 1.5
Tribosons	16.3 ± 0.2	12.6 ± 0.2	5.3 ± 0.1	0.8 ± 0.05	0.8 ± 0.04	0.6 ± 0.04
Drell-Yan	138.3 ± 30.0	135.8 ± 29.9	0.0 ± 0.0	0.0 ± 0.0	0.0 ± 0.0	0.0 ± 0.0
Single t	14.3 ± 2.5	11.3 ± 2.2	3.3 ± 1.2	1.2 ± 0.6	0.2 ± 0.2	0.2 ± 0.2
$Z + \text{jets}$	2734.7 ± 98.2	1336.5 ± 70.5	0.2 ± 0.2	0.0 ± 0.0	0.0 ± 0.0	0.0 ± 0.0
$\Sigma \text{ SM}$	7173.6 ± 104.7	3327.5 ± 77.6	195.1 ± 4.7	48.9 ± 2.4	27.4 ± 1.7	26.6 ± 1.7
Model A: 250, 0	663.3 ± 11.8	588.0 ± 11.1	431.4 ± 9.5	50.8 ± 3.3	47.1 ± 3.2	24.4 ± 2.3
Z_N	0.3	0.6	6.8	2.9	4.1	2.2
Model A: 250, 100	620.4 ± 11.4	482.5 ± 10.1	308.9 ± 8.1	68.4 ± 3.8	62.2 ± 3.6	37.3 ± 2.8
Z_N	0.3	0.5	4.9	3.9	5.3	3.4
Model A: 300, 200	269.8 ± 5.1	169.8 ± 4.0	93.6 ± 3.0	43.3 ± 2.0	39.0 ± 1.9	32.4 ± 1.8
Z_N	0.1	0.2	1.5	2.5	3.5	2.9
Model A: 142.5, 107.5	1626.2 ± 56.2	1580.1 ± 55.5	221.0 ± 20.6	29.7 ± 7.5	27.7 ± 7.3	27.7 ± 7.3
Z_N	0.8	1.6	3.6	1.7	2.6	2.6
Model B: 100, 0	1070.9 ± 22.9	88.8 ± 6.6	19.6 ± 3.1	15.8 ± 2.8	12.6 ± 2.3	12.6 ± 2.3
	0.5	0.1	0.3	0.9	1.1	1.1

Table 5.9: Cutflow for SRnoZb at $\sqrt{s} = 8 \text{ TeV}$ with 20.7 fb^{-1} of data. Errors are statistical only. Expected significances are calculated assuming a 30% uncertainty on the number of background events.

SRnoZc	SFOS	Z veto	$E_T^{\text{miss}} > 75 \text{ GeV}$	$m_T > 110 \text{ GeV}$	$p_T^{\ell_3} > 30 \text{ GeV}$	b -jet veto
$t\bar{t}$	249.4 ± 5.7	216.6 ± 5.3	85.5 ± 3.4	15.4 ± 1.4	1.5 ± 0.5	0.6 ± 0.3
$t\bar{t} + V$	50.9 ± 0.6	19.7 ± 0.4	11.1 ± 0.3	3.7 ± 0.2	1.8 ± 0.1	0.1 ± 0.04
WW	6.8 ± 0.6	6.1 ± 0.6	1.8 ± 0.3	0.7 ± 0.2	0.2 ± 0.1	0.1 ± 0.04
ZZ	1564.0 ± 10.2	1099.5 ± 8.6	6.0 ± 0.6	0.7 ± 0.2	0.4 ± 0.2	0.2 ± 0.1
$ZZ \rightarrow \ell\ell\nu\nu$	0.4 ± 0.1	0.1 ± 0.05	0.0 ± 0.0	0.0 ± 0.0	0.0 ± 0.0	0.0 ± 0.0
WZ	2398.6 ± 16.3	489.2 ± 7.3	81.9 ± 3.0	11.6 ± 1.1	4.1 ± 0.7	2.1 ± 0.4
Tribosons	16.3 ± 0.2	12.6 ± 0.2	5.3 ± 0.1	1.9 ± 0.1	0.9 ± 0.05	0.8 ± 0.05
Drell-Yan	138.3 ± 30.0	135.8 ± 29.9	0.0 ± 0.0	0.0 ± 0.0	0.0 ± 0.0	0.0 ± 0.0
Single t	14.3 ± 2.5	11.3 ± 2.2	3.3 ± 1.2	0.4 ± 0.3	0.0 ± 0.0	0.0 ± 0.0
$Z + \text{jets}$	2734.7 ± 98.2	1336.5 ± 70.5	0.2 ± 0.2	0.0 ± 0.0	0.0 ± 0.0	0.0 ± 0.0
$\Sigma \text{ SM}$	7173.6 ± 104.7	3327.5 ± 77.6	195.1 ± 4.7	34.5 ± 1.9	8.9 ± 0.9	4.0 ± 0.6
Model A: 350, 0	157.7 ± 2.7	147.5 ± 2.7	122.0 ± 2.4	95.9 ± 2.1	85.6 ± 2.0	77.1 ± 1.9
Z_N	0.1	0.1	2.0	6.8	8.0	8.0
Model A: 425, 75	63.4 ± 1.1	59.8 ± 1.1	52.2 ± 1.0	43.3 ± 0.9	40.8 ± 0.9	37.0 ± 0.8
Z_N	0.0	0.1	0.9	3.2	6.9	8.0
Model A: 500, 0	28.5 ± 0.5	27.5 ± 0.5	25.2 ± 0.5	21.6 ± 0.4	20.7 ± 0.4	18.4 ± 0.4
Z_N	0.0	0.0	0.4	1.7	3.9	5.1
Model A: 450, 300	45.0 ± 0.8	35.4 ± 0.7	24.3 ± 0.6	15.5 ± 0.5	12.3 ± 0.4	10.8 ± 0.4
Z_N	0.0	0.0	0.4	1.2	2.5	3.2
Model A: 500, 250	28.1 ± 0.5	25.4 ± 0.5	21.1 ± 0.4	16.6 ± 0.4	15.3 ± 0.4	13.5 ± 0.3
Z_N	0.0	0.0	0.4	1.3	3.1	4.0
Model A: 625, 125	7.8 ± 0.1	7.5 ± 0.1	7.0 ± 0.1	6.1 ± 0.1	6.0 ± 0.1	5.4 ± 0.1
Z_N	0.0	0.0	0.1	0.4	1.1	1.7

Table 5.10: Cutflow for SRnoZc at $\sqrt{s} = 8 \text{ TeV}$ with 20.7 fb^{-1} of data. Errors are statistical only. Expected significances are calculated assuming a 30% uncertainty on the number of background events.

SRZa	SFOS	Z request	$E_T^{\text{miss}} > 75 \text{ GeV}$	$E_T^{\text{miss}} < 120 \text{ GeV}$	$m_T < 110 \text{ GeV}$	b -jet veto
$t\bar{t}$	249.4 ± 5.7	32.8 ± 2.1	10.9 ± 1.2	9.0 ± 1.1	7.8 ± 1.0	2.2 ± 0.5
$t\bar{t} + V$	50.9 ± 0.6	31.1 ± 0.5	13.4 ± 0.3	7.5 ± 0.2	6.3 ± 0.2	0.4 ± 0.1
WW	6.8 ± 0.6	0.7 ± 0.2	0.3 ± 0.1	0.2 ± 0.1	0.2 ± 0.1	0.1 ± 0.1
ZZ	1564.0 ± 10.2	464.4 ± 5.6	14.5 ± 1.0	11.5 ± 0.9	10.3 ± 0.8	8.9 ± 0.8
$ZZ \rightarrow \ell\ell\nu\nu$	0.4 ± 0.1	0.2 ± 0.1	0.1 ± 0.03	0.1 ± 0.03	0.0 ± 0.0	0.0 ± 0.0
WZ	2398.6 ± 16.3	1909.4 ± 14.5	403.2 ± 6.6	299.8 ± 5.7	277.2 ± 5.5	234.9 ± 5.0
Tribosons	16.3 ± 0.2	3.7 ± 0.1	1.7 ± 0.1	1.1 ± 0.04	0.6 ± 0.03	0.5 ± 0.03
Drell-Yan	138.3 ± 30.0	2.5 ± 2.5	0.0 ± 0.0	0.0 ± 0.0	0.0 ± 0.0	0.0 ± 0.0
Single t	14.3 ± 2.5	3.0 ± 1.3	1.5 ± 0.9	1.5 ± 0.9	1.0 ± 0.7	1.0 ± 0.7
$Z + \text{jets}$	2734.7 ± 98.2	1398.2 ± 68.4	16.2 ± 8.0	16.2 ± 8.0	8.0 ± 5.5	8.0 ± 5.5
$\Sigma \text{ SM}$	7173.6 ± 104.7	3846.1 ± 70.2	461.9 ± 10.6	347.0 ± 10.0	311.3 ± 7.9	256.0 ± 7.5
Model A: 112.5, 12.5	9363.4 ± 210.3	2664.9 ± 114.0	649.4 ± 55.0	440.6 ± 44.9	363.9 ± 41.0	363.8 ± 41.0
Z_N	4.3	2.3	4.6	4.1	3.8	4.5
Model A: 130, 30	6138.0 ± 130.2	1952.1 ± 73.6	642.0 ± 42.3	485.4 ± 36.5	413.0 ± 33.9	392.7 ± 32.9
Z_N	2.8	1.7	4.5	4.5	4.3	4.9
Model A: 155, 5	3548.6 ± 70.8	911.2 ± 36.0	433.5 ± 25.0	287.3 ± 20.6	148.5 ± 15.0	130.8 ± 13.8
Z_N	1.6	0.8	3.1	2.7	1.5	1.6
Model A: 150, 50	3891.2 ± 79.0	1324.2 ± 46.4	417.7 ± 25.9	300.7 ± 22.1	231.5 ± 19.5	214.9 ± 18.6
Z_N	1.8	1.1	2.9	2.8	2.4	2.7

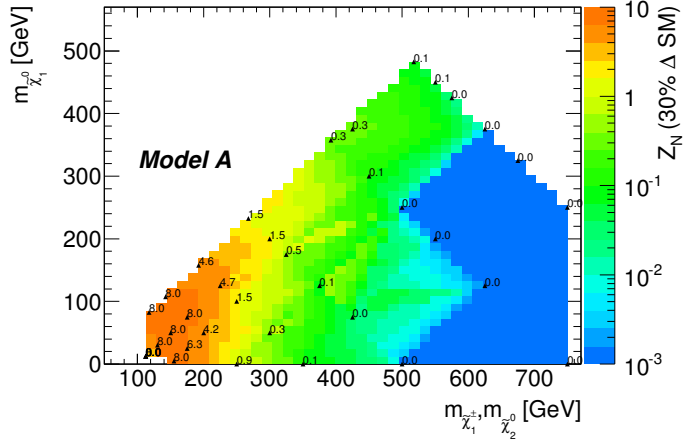
Table 5.11: Cutflow for SRZa at $\sqrt{s} = 8 \text{ TeV}$ with 20.7 fb^{-1} of data. Errors are statistical only. Expected significances are calculated assuming a 30% uncertainty on the number of background events.

SRZb	SFOS	Z request	$E_T^{\text{miss}} > 75 \text{ GeV}$	$E_T^{\text{miss}} < 120 \text{ GeV}$	$m_T > 110 \text{ GeV}$	b -jet veto
$t\bar{t}$	249.4 ± 5.7	32.8 ± 2.1	10.9 ± 1.2	9.0 ± 1.1	1.2 ± 0.4	0.5 ± 0.3
$t\bar{t} + V$	50.9 ± 0.6	31.1 ± 0.5	13.4 ± 0.3	7.5 ± 0.2	1.2 ± 0.1	0.1 ± 0.02
WW	6.8 ± 0.6	0.7 ± 0.2	0.3 ± 0.1	0.2 ± 0.1	0.0 ± 0.0	0.0 ± 0.0
ZZ	1564.0 ± 10.2	464.4 ± 5.6	14.5 ± 1.0	11.5 ± 0.9	1.3 ± 0.3	0.9 ± 0.2
$ZZ \rightarrow \ell\ell\nu\nu$	0.4 ± 0.1	0.2 ± 0.1	0.1 ± 0.03	0.1 ± 0.03	0.0 ± 0.0	0.0 ± 0.0
WZ	2398.6 ± 16.3	1909.4 ± 14.5	403.2 ± 6.6	299.8 ± 5.7	22.6 ± 1.6	18.7 ± 1.4
Tribosons	16.3 ± 0.2	3.7 ± 0.1	1.7 ± 0.1	1.1 ± 0.04	0.5 ± 0.03	0.4 ± 0.03
Drell-Yan	138.3 ± 30.0	2.5 ± 2.5	0.0 ± 0.0	0.0 ± 0.0	0.0 ± 0.0	0.0 ± 0.0
Single t	14.3 ± 2.5	3.0 ± 1.3	1.5 ± 0.9	1.5 ± 0.9	0.6 ± 0.6	0.0 ± 0.0
$Z + \text{jets}$	2734.7 ± 98.2	1398.2 ± 68.4	16.2 ± 8.0	16.2 ± 8.0	8.3 ± 5.9	8.3 ± 5.9
$\Sigma \text{ SM}$	7173.6 ± 104.7	3846.1 ± 70.2	461.9 ± 10.6	347.0 ± 10.0	35.7 ± 6.1	28.9 ± 6.0
Model B: 150, 0	259.7 ± 5.2	244.2 ± 5.1	114.0 ± 3.5	73.3 ± 2.8	29.9 ± 1.8	27.8 ± 1.7
Z_N	0.1	0.2	0.8	0.7	2.2	2.4
Model B: 100, 0	1070.9 ± 22.9	982.1 ± 22.0	251.1 ± 11.0	181.2 ± 9.4	11.4 ± 2.2	11.4 ± 2.2
Z_N	0.5	0.8	1.8	1.7	0.9	1.0
Model B: 150, 50	261.7 ± 5.2	247.5 ± 5.1	80.3 ± 2.9	59.1 ± 2.5	13.8 ± 1.2	13.0 ± 1.2
Z_N	0.1	0.2	0.6	0.6	1.0	1.1
Model B: 200, 0	92.8 ± 1.8	88.0 ± 1.7	58.7 ± 1.4	29.7 ± 1.0	14.1 ± 0.7	13.0 ± 0.7
Z_N	0.0	0.1	0.4	0.3	1.0	1.1
Model B: 200, 50	92.2 ± 1.8	87.5 ± 1.7	52.1 ± 1.3	26.9 ± 1.0	13.5 ± 0.7	12.6 ± 0.6
Z_N	0.0	0.1	0.4	0.2	1.0	1.1

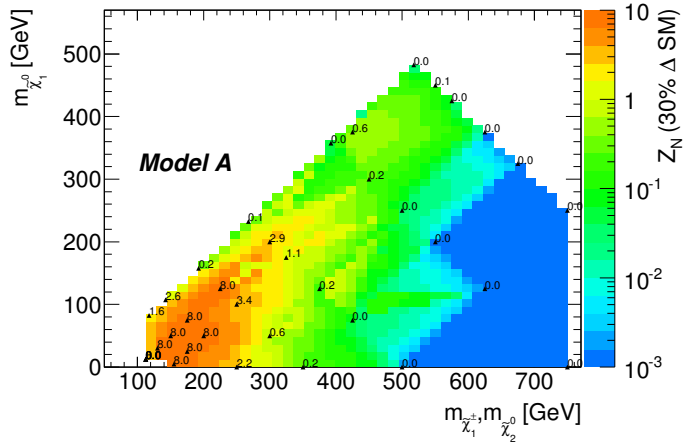
Table 5.12: Cutflow for SRZb at $\sqrt{s} = 8 \text{ TeV}$ with 20.7 fb^{-1} of data. Errors are statistical only. Expected significances are calculated assuming a 30% uncertainty on the number of background events.

SRZc	SFOS	Z request	$E_T^{\text{miss}} > 120 \text{ GeV}$	$m_T > 110 \text{ GeV}$	b -jet veto
$t\bar{t}$	249.4 ± 5.7	32.8 ± 2.1	1.9 ± 0.5	0.3 ± 0.2	0.2 ± 0.2
$t\bar{t} + V$	50.9 ± 0.6	31.1 ± 0.5	5.9 ± 0.2	1.4 ± 0.1	0.1 ± 0.03
WW	6.8 ± 0.6	0.7 ± 0.2	0.1 ± 0.1	0.1 ± 0.05	0.1 ± 0.05
ZZ	1564.0 ± 10.2	464.4 ± 5.6	3.0 ± 0.5	0.5 ± 0.2	0.4 ± 0.2
$ZZ \rightarrow \ell\ell\nu\nu$	0.4 ± 0.1	0.2 ± 0.1	0.0 ± 0.0	0.0 ± 0.0	0.0 ± 0.0
WZ	2398.6 ± 16.3	1909.4 ± 14.5	103.3 ± 3.4	7.1 ± 0.9	5.0 ± 0.7
Tribosons	16.3 ± 0.2	3.7 ± 0.1	0.6 ± 0.03	0.3 ± 0.02	0.3 ± 0.02
Drell-Yan	138.3 ± 30.0	2.5 ± 2.5	0.0 ± 0.0	0.0 ± 0.0	0.0 ± 0.0
Single t	14.3 ± 2.5	3.0 ± 1.3	0.0 ± 0.0	0.0 ± 0.0	0.0 ± 0.0
$Z + \text{jets}$	2734.7 ± 98.2	1398.2 ± 68.4	0.0 ± 0.0	0.0 ± 0.0	0.0 ± 0.0
$\Sigma \text{ SM}$	7173.6 ± 104.7	3846.1 ± 70.2	114.9 ± 3.4	9.7 ± 0.9	6.1 ± 0.8
Model B: 150, 0	259.7 ± 5.2	244.2 ± 5.1	40.7 ± 2.1	15.0 ± 1.3	13.7 ± 1.2
Z_N	0.1	0.2	1.1	2.8	3.3
Model B: 200, 0	92.8 ± 1.8	88.0 ± 1.7	29.1 ± 1.0	16.5 ± 0.8	14.4 ± 0.7
Z_N	0.0	0.1	0.8	3.1	3.5
Model B: 200, 50	92.2 ± 1.8	87.5 ± 1.7	25.2 ± 0.9	13.1 ± 0.7	12.3 ± 0.6
Z_N	0.0	0.1	0.7	2.4	3.0
Model B: 250, 0	39.9 ± 0.7	37.5 ± 0.7	19.5 ± 0.5	13.1 ± 0.4	11.9 ± 0.4
Z_N	0.0	0.0	0.5	2.4	3.0

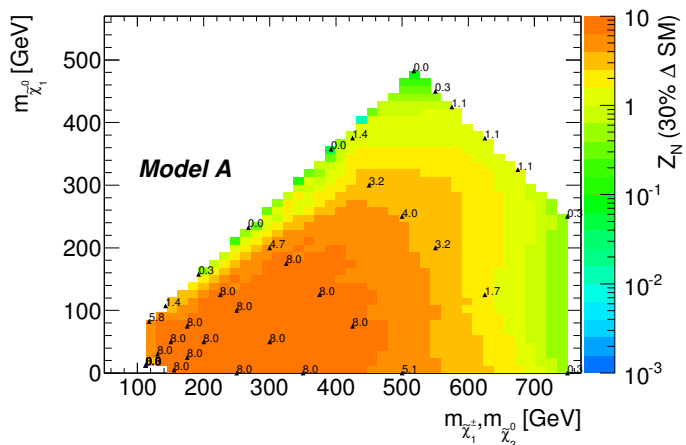
Table 5.13: Cutflow for SRZc at $\sqrt{s} = 8 \text{ TeV}$ with 20.7 fb^{-1} of data. Errors are statistical only. Expected significances are calculated assuming a 30% uncertainty on the number of background events.



(a) SRnoZa



(b) SRnoZb



(c) SRnoZc

Figure 5.10: Expected significance (Z_N) in Model A, for the 2012 SRnoZs. SRnoZa is most effective near the diagonal, while SRnoZb is most effective slightly further away from the diagonal. SRnoZc has good sensitivity to the bulk of the grid. Expected significances are calculated assuming a 30% uncertainty on the number of background events.

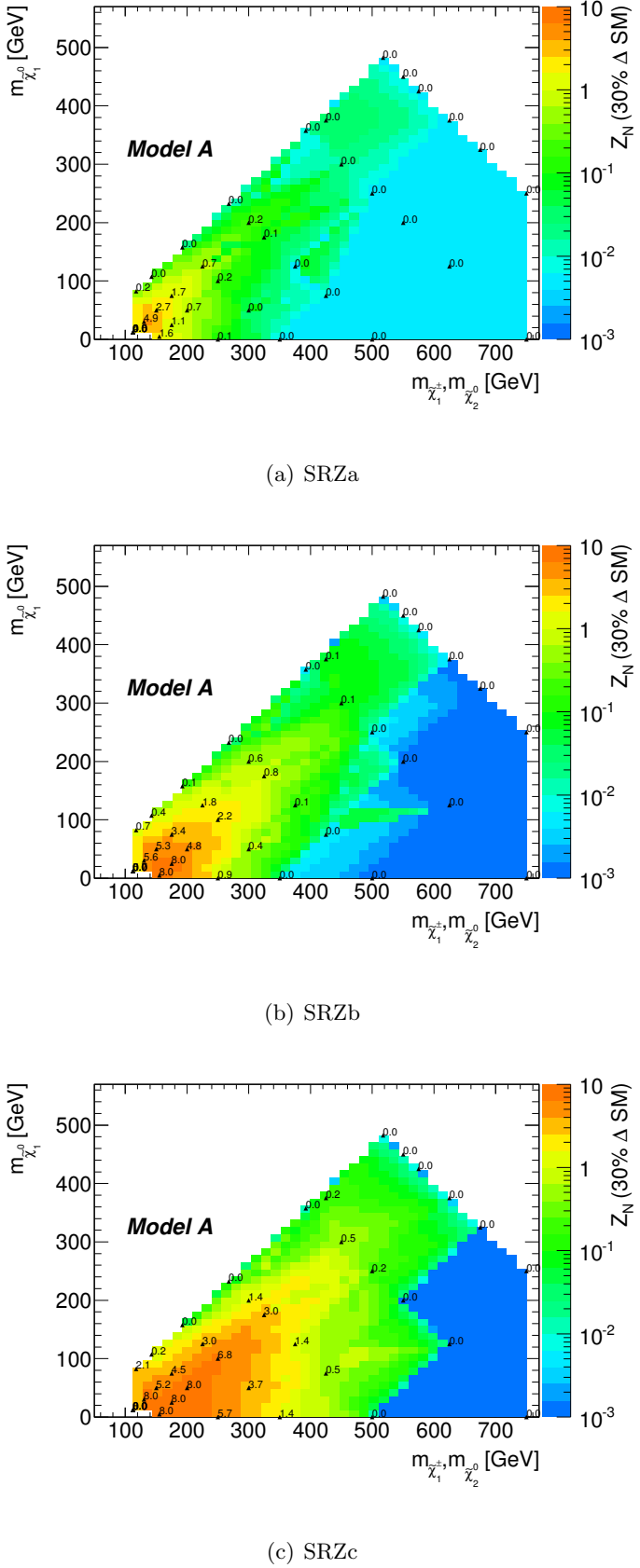
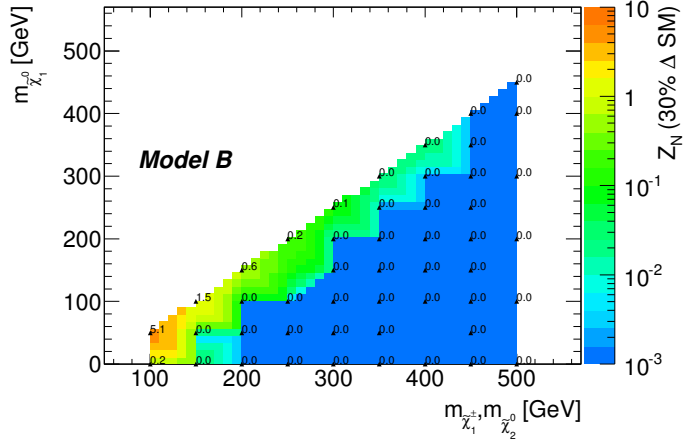
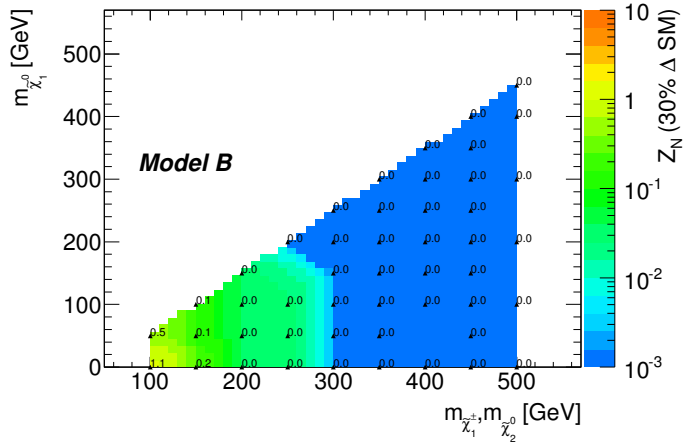


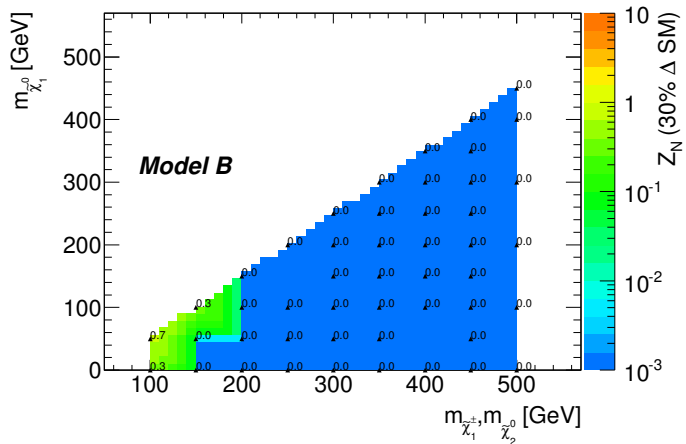
Figure 5.11: Expected significance (Z_N) in Model A, for the 2012 SRZs. SRZa, SRZb and SRZc have some sensitivity to the bulk regions, but this is coincidental. Expected significances are calculated assuming a 30% uncertainty on the number of background events.



(a) SRnoZa

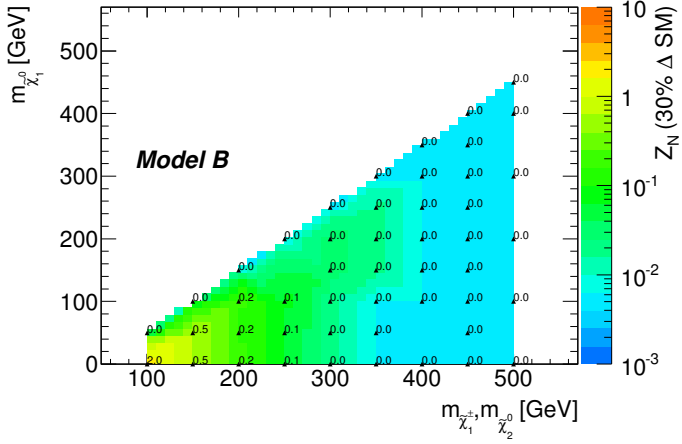


(b) SRnoZb

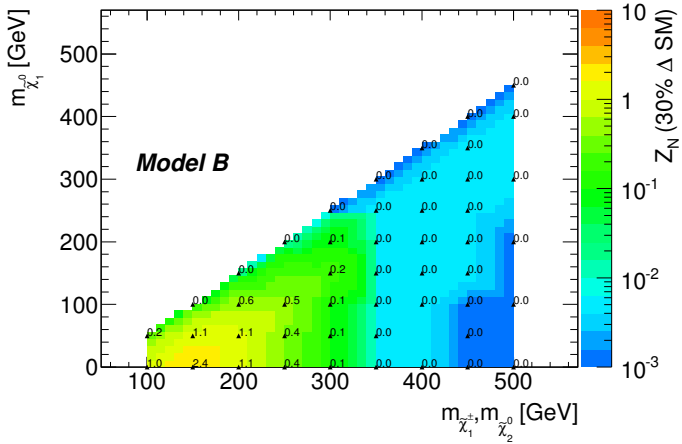


(c) SRnoZc

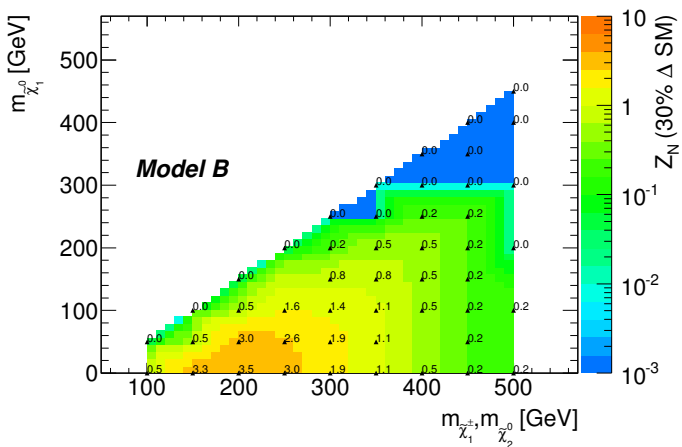
Figure 5.12: Expected significance (Z_N) in Model B, for the 2012 SRnoZs. Only SRnoZa is effective for signal points on the diagonal. Expected significances are calculated assuming a 30% uncertainty on the number of background events.



(a) SRZa



(b) SRZb



(c) SRZc

Figure 5.13: Expected significance (Z_N) in Model B, for the 2012 SRZs. SRZa, SRZb and SRZc are sensitive to the bulk region. Expected significances are calculated assuming a 30% uncertainty on the number of background events.

variables:

$$m_{\ell\ell}(\text{SRnoZ}) = \{< 60, 60 - 81.2, < 81.2 \text{ OR } > 101.2\} \text{ GeV} \quad (5.5)$$

$$m_T(\text{SRZ}) = \{< 110, > 110\} \text{ GeV} \quad (5.6)$$

$$E_T^{\text{miss}}(\text{SRZ}) = \{75 - 120, > 120\} \text{ GeV} \quad (5.7)$$

A more systematic approach would be to define SRs with (for example):

$$m_{\ell\ell} = \{< 81.2, 81.2 - 101.2, > 101.2\} \text{ GeV} \quad (5.8)$$

$$E_T^{\text{miss}} = \{> 50, 75 - 100, > 100\} \text{ GeV} \quad (5.9)$$

$$m_T = \{< 110, > 110\} \text{ GeV}. \quad (5.10)$$

There are eighteen possible combinations of $m_{\ell\ell}$, E_T^{miss} and m_T , leading to eighteen SRs. Increasing the number of SRs can increase sensitivity, but at the cost of increased computational demands, particularly for the calculation of exclusion limits. Also, the probability to observe an excess or deficit due to a random fluctuation increases, potentially leading to a false exclusion or discovery claim [203]. The Bonferroni correction [204] accounts for the presence of N signal regions by, increasing the expected significance required for a discovery by a factor of N . Systematic binning of SRs was not adopted in this work due to computational limitations but does represent an interesting avenue for future work.

SRs may also be defined by assigning events a score according to how signal- or background-like they are. The score may be calculated using a multivariate technique, such as a BDT or ANN. Control and validation regions may then be defined by selecting highly background-like events, and SRs by selecting highly signal-like events. A disadvantage to such techniques is that the initial signal and background samples used to train the multivariate technique must be statistically independent from those used in the final analysis, which leads to (as a minimum) doubling of the number of simulated events required. Again, multivariate techniques may prove fruitful for the future.

Chapter 6

Background estimation and systematic uncertainties

Far better an approximate answer to the right question, which is often vague, than an exact answer to the wrong question, which can always be made precise.

John Tukey [205]

6.1 Background estimation

The sources of leptons in reducible and irreducible backgrounds are discussed in Section 6.1.1. The framework used to estimate reducible backgrounds is the *matrix method*, discussed in Section 6.1.2. Additionally, a control region for WZ , the largest irreducible background, is discussed in Section 6.2.

6.1.1 Sources of leptons in SM backgrounds

The sources of electrons and muons in simulated SM backgrounds are shown in Figure 6.1. The selection used is the base selection for all the analyses presented here: exactly three leptons are selected including at least one same flavour opposite charge sign (SFOS) pair, and E_T^{miss} is required to exceed 50 GeV. Figures 6.2(a)-(c) show the proportions of real and fake leptons, for highest, second-highest and lowest p_T lepton respectively. The proportion of fake leptons is lowest for the highest- p_T leptons, which are found to be

more than 98% composed of real leptons. For the purposes of background estimation, the highest- p_T lepton is therefore assumed to always be real.

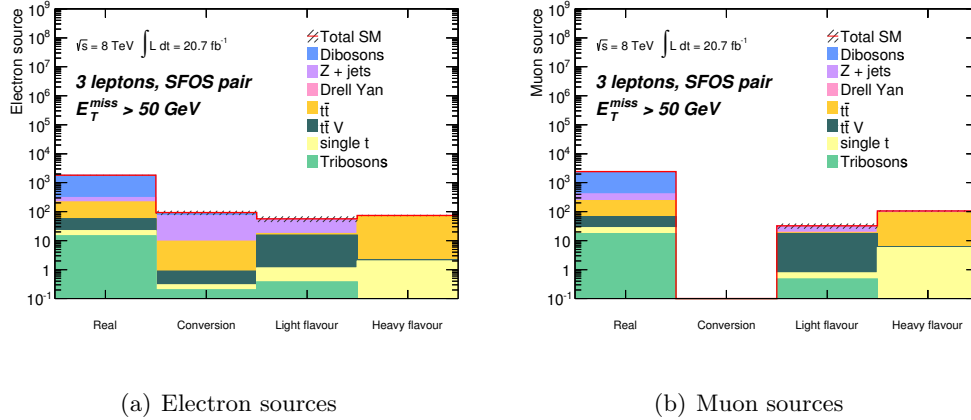


Figure 6.1: Sources of electrons (a) and muons (b) in simulated SM events with three leptons and at least one same SFOS pair. Errors are statistical only.

6.1.2 Matrix method

The matrix method relates samples of loosely and tightly identified leptons (loose and tight for brevity) to their composition in terms of real and fake leptons. The requirements for loose and tight leptons are given in Sections 4.4.4.3 and 4.4.5.3. This composition can be expressed in terms of

- the *reconstruction efficiency* ϵ : the probability of a real lepton passing tight identification
- the *fake rate* f : the probability of a fake lepton passing tight identification

Since a given lepton must either pass or fail tight identification, the other possible outcomes may be expressed in terms of ϵ and f . As a concrete example, consider a sample of events with three tight leptons N_{TTT} . The composition of this sample may then be expressed as a linear combination of samples with real (R) and fake (F) leptons:

$$N_{TTT} = \epsilon^3 N_{RRR} + \epsilon^2 f N_{RRF} + \epsilon f^2 N_{RFF} + f^3 N_{FFF} \quad (6.1)$$

For brevity, it is assumed here that each lepton has the same ϵ and f : in general, these are strongly dependent on the kinematics of a given lepton, as well as the type of object faking the lepton. Higher p_T leptons are generally less likely to be fake since possible sources of fakes (hadrons, electrons from photon conversions) have a lower mass scale than $W/Z/\gamma^*$ bosons and SUSY particles.

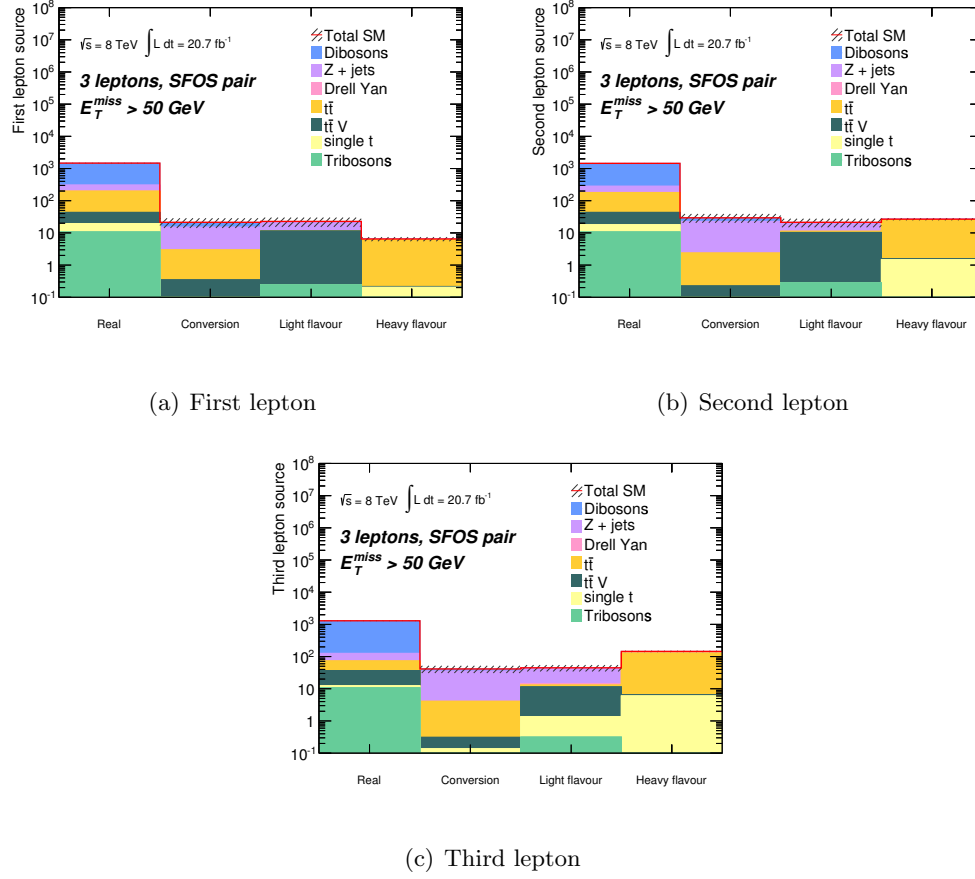


Figure 6.2: Sources of leptons in simulated SM events with three leptons, at least one SFOS pair and $E_T^{\text{miss}} > 50 \text{ GeV}$. Histograms (a), (b) and (c) show the background composition for the highest, second-highest and lowest p_T lepton respectively. Errors are statistical only.

There are eight equations similar to (6.1) for the various combinations (N_{TTT} , N_{TLL} , N_{TLT} etc) of real and fake leptons, which may be expressed as a single 8×8 matrix equation. For three lepton events with a tight leading lepton, the leading lepton was shown to be real in $> 98\%$ of cases in Section 6.1.1. This simplification reduces the dimensionality of the matrix to 4×4 . Under this assumption, the number of events with a leading tight lepton and any combination of two additional tight/loose leptons (denoted 1 and 2) is given by

$$\begin{pmatrix} N_{TT} \\ N_{TL} \\ N_{LT} \\ N_{LL} \end{pmatrix} = \begin{pmatrix} \epsilon_1 \epsilon_2 & \epsilon_1 f_2 & f_1 \epsilon_2 & f_1 f_2 \\ \epsilon_1 (1 - \epsilon_2) & \epsilon_1 (1 - f_2) & f_1 (1 - \epsilon_2) & f_1 (1 - f_2) \\ (1 - \epsilon_1) \epsilon_2 & (1 - \epsilon_1) f_2 & (1 - f_1) \epsilon_2 & (1 - f_1) f_2 \\ (1 - \epsilon_1)(1 - \epsilon_2) & (1 - \epsilon_1)(1 - f_2) & (1 - f_1)(1 - \epsilon_2) & (1 - f_1)(1 - f_2) \end{pmatrix} \cdot \begin{pmatrix} N_{RR} \\ N_{RF} \\ N_{FR} \\ N_{FF} \end{pmatrix}. \quad (6.2)$$

Inverting equation (6.2) gives the sum of events with at least one fake lepton:

$$\begin{aligned} N_{Fake} = N_{RF} + N_{FR} + N_{FF} &= \frac{1}{(\epsilon_1 - f_1)(\epsilon_2 - f_2)} [(\epsilon_1\epsilon_2 - \epsilon_1f_2 - f_1\epsilon_2 + f_1 + f_2 - 1)N_{TT} \\ &\quad + (\epsilon_1\epsilon_2 - \epsilon_1f_2 - f_1\epsilon_2 + f_2)N_{TL} + (\epsilon_1\epsilon_2 - \epsilon_1f_2 - f_1\epsilon_2 + f_1)N_{LT} \\ &\quad + (\epsilon_1\epsilon_2 - \epsilon_1f_2 - f_1\epsilon_2)N_{LL}] \end{aligned} \quad (6.3)$$

The presence of the factors $1/(\epsilon - f)$ can lead to numerical instability if the fake rates and efficiencies are not well-separated. This instability is enhanced in the more general case that the leading lepton may not be real, due to additional factors of $1/(\epsilon - f)$, justifying the use of this assumption. Since only tight leptons are used in the final analysis, contributions to N_{Fake} from loose leptons are ignored. The salient prediction is therefore $N_{Fake|TT}$, the number of events with at least one fake lepton, and all three leptons passing tight selection:

$$N_{Fake|TT} = \epsilon_1f_2 \times N_{RF} + f_1\epsilon_2 \times N_{FR} + f_1f_2 \times N_{FF}. \quad (6.4)$$

In summary, for the correction of MC predicted backgrounds, only the real efficiency and the fake rates for the various different types of fake leptons are required.

6.1.3 Measurement of weighted average fake rates

The fake rate f for a given lepton depends on the type of fake (light flavour, heavy flavour or electron conversion) as well as the lepton kinematics. The kinematics vary depending on the process considered: for instance, the p_T spectra of fake leptons from heavy flavour produced in $Z + b$ events are softer than those in $t\bar{t}$ events due to the lower mass scale of the $Z + b$ process. The different compositions of the various signal and validation regions will lead to different predictions for the various fakes.

Since the origin and type of each real and fake lepton is recorded in MC, simulated fake rates can be found unambiguously. However, the fake rate in MC will not necessarily match that in data. A weighted average fake rate, taking into account differences between data and MC and the different fake proportions, is given by

$$f_{XR}^\ell = \Sigma_{i,j} (\mathcal{S}^i \times R_{XR}^{ij} \times f_{truth}^{ij}) \quad (6.5)$$

Here $XR=(SR,VR)$ refers either to a validation or a signal region. The index i refers to the type of fake, j indicates the process (t decay, W , Z). Indices reflecting dependence on p_T and η are suppressed.

The **scale factor** \mathcal{S}^i is a scale factor for the fake rate of origin i to correct the MC prediction to the fake rate in data.

The **fake fraction** R_{XR}^{ij} gives the proportion of different fake leptons by origin i and type j in a given region XR.

The **truth fake rate** f_{truth}^{ij} is the fake rate found in simulation. It is given by the ratio of tight to loose leptons of a given origin i and type j .

The measurement of the scale factor $\mathcal{S}_{\text{conv}}$ for electron conversion is discussed in Section 6.1.4.2, and the treatment of light/heavy flavour scale factors and the real lepton efficiency, are discussed in Sections 6.1.5.1, 6.1.5.3 and 6.1.5.2. The calculation of the truth fake rates and final matrix method calculation was performed by another analysis group member.

6.1.4 Measurement of the electron conversion scale factor

There are two types of lepton conversion processes: *internal conversion*, involving a virtual photon ($\gamma^* \rightarrow e^+e^-$), and *external conversion*, an interaction between a real photon and detector material. Feynman diagrams for internal conversion in Z/γ^* production are shown in Figure 6.4. There is no observable distinction between internal and external conversion, since both processes lead to the same final state. However, one difference is that internal conversion is equally likely for electrons and muons (above the mass threshold for muon pair creation), while external conversion is more likely to occur for electrons. The kinematic properties of internal conversion also differ if the conversion is initial or final state radiation (ISR/FSR, shown in Figure 6.4(a) and (b) respectively). The four leptons from final state internal conversion form the invariant mass of the Z boson, while the four leptons from initial state internal conversion can only form this by accident. Highly asymmetric internal conversions, in which one lepton has too low p_T to be reconstructed, can form an important background to multilepton SUSY production, due to the presence of $E_{\text{T}}^{\text{miss}}$ from the unreconstructed lepton [206]. Since the unreconstructed lepton is soft, the three reconstructed leptons can still have a mass close to the Z mass window if the process is FSR. The overall strategy to estimate electron external conversion is as follows:

1. Validate MC treatment of internal conversion in a sample of asymmetric muon conversions, since this will be almost totally free of external conversion contamination.
2. Measure a combination of external and internal electron conversion events in data, subtracting the internal conversion contribution from MC.
3. Extract the data/MC scale factor for external conversion, $\mathcal{S}_{\text{conv}}$: this is the ratio between the data and MC fake rates.

6.1.4.1 Muon conversion validation region

Since internal conversion is insensitive to the flavour of the lepton produced, and muons very rarely externally convert, a sample of asymmetric internal conversion events with approximately 80% purity can be selected. The requirements for this region are as follows:

- Standard quality requirements defined in Section 5.2, but without electron triggers (since no electrons are selected)
- Exactly three tight muons, with one opposite sign pair $\mu^+\mu^-$
- Trimuon invariant mass $m_{\mu\mu\mu}$ compatible with an on-shell Z decay ([81.2–101.2] GeV)
- All muon $m_T < 40$ GeV and $E_T^{\text{miss}} < 50$ GeV (rejecting WZ)
- b -jet veto (rejecting $t\bar{t}$)

The number of events in data and MC in the validation region are summarised in Table 6.1 (for the 2012 dataset), and the p_T and η distributions for the lowest p_T muon are shown in Figure 6.5. The invariant mass formed by the three muons is shown in Figure 6.6. It is not possible to directly subtract the pure muon conversion sample from the real external conversion contribution, since the acceptance and efficiency of electron and muon reconstruction are different and, at low invariant masses, the probability of conversion of a virtual photon to an electron-positron pair is greater than that of photon conversion to a muon pair. There is some discrepancy between the data and MC prediction in this region, but the errors on the MC prediction are statistical only. Systematic uncertainties, if evaluated, would add to the error. In the case of the electron conversion control region, detailed in Section 6.1.4, the total systematic and statistical uncertainty is 22%: since the largest systematic uncertainty follows from increasing the Z mass window, this is also likely to apply in the case of the muon conversion validation region. In conclusion, the level of agreement seen between the data and MC prediction is sufficient to validate the electron conversion control region.

6.1.4.2 Electron conversion control region

The rate of electron conversion is measured in a dedicated control region similar to the muon conversion validation region, with selection criteria as follows:

- Standard quality requirements defined in Section 5.2
- Exactly 1 loose electron

Selection	Muon conversion validation region
$t\bar{t}$	0.3 ± 0.2
WZ	4.7 ± 0.7
ZZ	189.8 ± 3.8
$Z + \text{jets}$	42.0 ± 11.4
$\Sigma \text{ SM}$	236.9 ± 12.0
Data	180

Table 6.1: Observed events in the muon conversion validation region in data and MC samples with the 2012 dataset. Errors are statistical only.

- Trilepton invariant mass $m_{\mu\mu e}$ in Z mass window [81.2–101.2] GeV
- $E_T^{\text{miss}} < 50$ GeV and electron $m_T < 40$ GeV (rejecting WZ)
- b -jet veto (rejecting $t\bar{t}$)

These requirements are designed to select a sample of $Z \rightarrow \mu\mu + \gamma$ events with final state asymmetric electron conversions. The fake rate is then defined as

$$f_{\text{conv}} = \frac{N_{\text{tight}}(\text{CR})}{N_{\text{loose}}(\text{CR})} \quad (6.6)$$

which is the fraction of events in the control region with a tight electron divided by the fraction of events with a loose electron. The p_T and η distributions of loose (left) and tight (right) electrons for the full 2012 dataset are shown in Figure 6.7. The invariant mass of the dimuon pair and electron conversion candidate is shown in Figure 6.8.

The scale factor between data and MC is then defined as

$$\mathcal{S}_{\text{conv}} = \frac{f(\text{Data})_{\text{conv}} - f(\text{Real})_{\text{conv}}}{f(\text{EC})_{\text{conv}}} \quad (6.7)$$

“Real” is a set of samples ($t\bar{t}$, ZZ , WZ) containing non-external conversion electrons. The denominator ($f(\text{EC})$) contains only $Z/\gamma^* + \text{jets}$ samples which include external conversions.

6.1.4.3 Systematic uncertainties for the electron conversion scale factor

Systematic uncertainties on the method were evaluated by altering the selection criteria. The relative shifts in the event acceptance were then summed in quadrature separately for the data and MC and then together to give a single overall systematic uncertainty on the scale factor. The selection criteria varied were:

- The Z mass window - this was moved by ± 5 GeV increments from the central value of [81.2–101.2] GeV, to [76.2–106.2] GeV and [86.2–96.2] GeV
- The b -jet veto was removed
- The electron m_T cut was removed

The statistical uncertainties on the data and MC samples were also used. The percentage changes in the event acceptance are summarised in Table 6.2. Here the largest uncertainties arise from moving the Z mass window: the Z peak is sharp, so it follows that small changes can have a large effect on the acceptance. The uncertainties were also evaluated in two different $|\eta|$ and p_T bins, as shown in Figure 6.9. To within the systematic and statistical uncertainties applied, no significant dependence on the electron η and p_T was observed. A single unbinned scale factor was extracted:

$$\mathcal{S}_{\text{conv}} = 1.22 \pm 0.27$$

and used in the matrix method. This scale factor is compatible with 1 and implies that the treatment of conversion in this kinematic regime is well treated in MC.

Source of uncertainty	Data	MC
Z window up 5 GeV	17.0%	10.0%
Z window down 5 GeV	-10.6%	-11.6%
Remove b -jet veto	1.7%	-1.5%
Remove m_T cut	-0.5%	-1.8%
Statistical	4.6%	8.5%
Sum	20.6%	17.7%

Table 6.2: Statistical and systematic uncertainties for the electron conversion scale factor. The systematic uncertainties are expressed as a percentage change in the event acceptance. Systematic uncertainties are added in quadrature with the statistical errors to obtain the total uncertainty for the data and MC fake rates, and these are then added in quadrature to obtain the error on the scale factor.

6.1.5 Measurements of real lepton efficiency and weighted average fake rates

As discussed in Section 6.1.2, only the fake rates for each type of fake contribution, f and the real lepton efficiency ϵ are independent probabilities and must be measured in data. The measurements of these quantities are summarised briefly here.

6.1.5.1 Measurement of real lepton efficiency

Real lepton efficiency is measured using a tag-and-probe method. In this method, a sample of events with two loose quality objects whose invariant mass is close to a resonance (generally J/ψ or Z) is selected. One of the objects is then required to pass tight quality requirements - this is referred to as the *tag*. The other object, known as the *probe* is then required to pass/fail tight quality criteria. This then gives a reconstruction efficiency relative to the loose identification requirement. The real lepton efficiency was measured in a Z control region and found to be

$$\begin{aligned}\epsilon_{\text{Real}}^e &= 0.996 \pm 0.001 \\ \epsilon_{\text{Real}}^\mu &= 0.995 \pm 0.001\end{aligned}$$

where errors quoted are statistical only. No significant dependence on p_T or η was observed.

6.1.5.2 Measurement of heavy flavour fake rates

Light leptons produced in semi-leptonic b and c quark (collectively Heavy Flavour, HF) decays can form an important background to multilepton searches. Such leptons are generally produced within a jet and can be removed by isolation and ΔR requirements, as discussed in Section 4.4.10.1. In order to select semi-leptonic b and c quark decays, a tag-and-probe method is used, similarly to Section 6.1.5.1. The uncertainties quoted are the systematic uncertainty from the subtraction of backgrounds with real leptons and the statistical uncertainty arising from the data and MC sample size. The scale factor and associated uncertainty is applied in the matrix method.

- Standard quality requirements defined in Section 5.2
- Exactly two loose leptons
- Exactly one b -tagged jet
- $E_T^{\text{miss}} > 60 \text{ GeV}$
- $m_T < 40 \text{ GeV}$

The fake rate is defined similarly to the conversion fake rate:

$$S_{\text{HF}} = \frac{f_{\text{HF}}^{\text{Data}} - f_{\text{HF}}^{\text{RMC}}}{f_{\text{HF}}^{\text{HFMC}}} \quad (6.8)$$

where RMC refers to real (i.e. non-heavy flavour) MC contributions and HFMC are the $b\bar{b}$ and $c\bar{c}$ samples. The subtraction is performed in order to obtain a data sample pure in

HF events. No kinematic dependence was observed, allowing the extraction of unbinned scale factors:

$$\begin{aligned}\mathcal{S}_\mu^{\mathrm{mathrm{HF}}} &= 0.86 \pm 0.03 \\ \mathcal{S}_e^{\mathrm{mathrm{HF}}} &= 0.75 \pm 0.04\end{aligned}$$

which are then applied in the matrix method. The uncertainties quoted are the systematic uncertainty arising from the subtraction of real leptons and the statistical uncertainty arising from the data and MC sample sizes.

6.1.5.3 Measurement of light flavour fake rates

Fake leptons from light flavour are sub-dominant in most signal regions, as shown in Figure 6.3. Since the contribution is small, a flat scale factor of $\mathcal{S}^{LF} = 1.0 \pm 0.1$ is applied. This is conservatively chosen to be larger than the 3–6% uncertainties on the heavy flavour scale factor.

6.2 WZ normalisation (2011 only)

In the 2011 analysis, the overall yield of WZ , the largest irreducible background, was normalised to a WZ -rich control region. The advantage of this technique is to remove uncertainties on the normalised background. The reducible backgrounds to WZ production in the control region are estimated using the matrix method and control regions detailed above. A scale factor is obtained by taking the ratio of the data yield (with non- WZ MC subtracted) divided by the WZ MC yield:

$$sf_{WZNR} = \frac{N^{\mathrm{Data}} - N^{\mathrm{non-WZMC}} - N^{\mathrm{reducible}}}{N^{WZ}} = 1.25 \pm 0.12 \quad (6.9)$$

This scale factor is then used to rescale the WZ yield in the signal and validation regions. The treatment of the WZ normalisation in the statistical interpretation is discussed in Section 7.3.5. The disadvantage of the method is that it leads to a reduction in sensitivity to WZ -like signals – in the 2012 analysis, this was felt to outweigh the advantage of the reduced systematic uncertainties, so the method was not used.

6.2.1 Summary of background estimation

Events with three or more real, prompt leptons (“irreducible backgrounds”) such as WZ and ZZ production, are estimated using MC simulation only. In the 2011 analysis the total WZ contribution was normalised to a control region, as discussed in Section 6.2.

Contributions from events with fewer than three real, prompt leptons (“reducible backgrounds”) such as heavy flavour decays and electron conversions, are estimated in control regions. The various data/MC fake rate scale factors \mathcal{S} , as well as the real lepton efficiency ϵ , are given in Table 6.3. The electron conversion scale factor $\mathcal{S}_{\text{conv}}$ has the largest uncertainty (22%): this is mainly due to the changes in acceptance from raising and lowering the Z window, shown in Table 6.2.

Quantity	Electron	Muon
\mathcal{S}_{LF}	1.0 ± 0.1	1.0 ± 0.1
\mathcal{S}_{HF}	0.75 ± 0.04	0.86 ± 0.03
$\mathcal{S}_{\text{conv}}$	1.22 ± 0.27	
ϵ_{Real}	0.996 ± 0.001	0.995 ± 0.001

Table 6.3: Summary of scale factors and efficiencies in the 2012 analysis. The light flavour scale factor, \mathcal{S}_{LF} , is an assumption chosen to have a similar degree of uncertainty to the other scale factors.

6.3 Systematic uncertainties

Uncertainties on the irreducible and reducible background are calculated separately. Standard uncertainties for the irreducible background were provided by ATLAS performance groups. All uncertainties are then propagated to the likelihood used to calculate limits on SUSY scenarios and summed in quadrature bin-by-bin to produce the figures and tables in the validation/signal regions. Unless stated otherwise, the procedures detailed are those adopted for the 2012 analysis.

6.3.1 Uncertainties on the irreducible background

6.3.1.1 MC generator

Uncertainties arising from the theoretical description of processes were evaluated by comparing the kinematic distributions of the same process in two different generators. The difference between the two predictions is then taken as the $1-\sigma$ variation. The SHERPA WZ and ZZ samples were compared to POWHEG samples. Since no alternate samples of triboson production were available, a full 100% uncertainty was applied to these samples.

6.3.1.2 MC cross section

For $t\bar{t}+V$ samples the 30% uncertainty evaluated in [170, 171] was applied. An uncertainty of 5% for ZZ and 7% for WZ was applied: these are recommended by ATLAS and found by comparing the results of calculations with the MCFM and MC@NLO generators and MSTW [207] and CTEQ PDF sets. No error calculations were available for the triboson production: the uncertainties were therefore conservatively taken to be 10% (larger than the diboson uncertainties). The triboson uncertainties are in any case dominated by the 100% MC generator systematic.

6.3.1.3 PDF

The PDF uncertainties for the SHERPA WZ and ZZ samples were calculated using the PDF4LHC recommendations [208]. Since WZ and ZZ are dominated by quark-antiquark contributions, these must be precisely known. The PDF set used was provided by the CTEQ collaboration [209]. The CTEQ PDF set is based on 26 free parameters and the resulting 90% confidence level variations in these parameters form the “error set” $\{q\}$ for the PDF. The zeroth member of the set, $q^{(0)}$, is the nominal prediction of the observable, while the odd members form the positive part of the CL interval. The even members form the negative part of the CL interval. There are $N^{CTEQ} = 52$ even and odd members in the set. The notation $O[q^{(i)}]$ refers to the observable O rescaled to the prediction from the set member $q^{(i)}$. Since each event will have a different parton centre of mass energy, each observable will have, in general, a different dependence on the PDF prediction. The total $\pm 1\sigma$ variation in the observable is found by summing the largest variations in O in quadrature:

$$\begin{aligned}\sigma^{CTEQ}(+)[O] &= \frac{1}{C_{90}} \sqrt{\sum_{i=1}^{N^{CTEQ}/2} (\max\{O[q^{(2i-1)}] - O[q^{(0)}], O[q^{(2i)}] - O[q^{(0)}], 0\})^2} \\ \sigma^{CTEQ}(-)[O] &= \frac{1}{C_{90}} \sqrt{\sum_{i=1}^{N^{CTEQ}/2} (\max\{O[q^{(0)}] - O[q^{(2i-1)}], O[q^{(0)}] - O[q^{(2i)}], 0\})^2}\end{aligned}$$

$C_{90} = 1.64485$ is a rescaling factor to convert the 90% CL variations into 1σ variations. For the other irreducible backgrounds, the uncertainty on the cross section also includes the PDF uncertainty. The PDF uncertainty is applied to each bin of the distributions shown in Sections 7.1 and 7.2, and as overall event weights for tables and interpretation of results.

6.3.1.4 Electrons

Electron energy scale and energy resolution were measured in selections of Z , W and J/ψ events by the ATLAS electron performance group. The resulting uncertainties are η and p_T dependent, and the largest uncertainty is present in the 10–20 GeV p_T bin, since the statistics from W and J/ψ events are lowest in this region. An uncertainty for electron identification efficiency is also applied.

6.3.1.5 Muons

Since muon momentum is measured in the ID and MS systems, there are two different associated energy scale systematics. These are evaluated independently: in each case, the muon momentum is smeared up/down according to a data-driven energy scale determination provided by the ATLAS muon performance group.

6.3.1.6 Taus

Although tau leptons are not selected for these analyses, events containing medium quality tau leptons are vetoed to facilitate a future combination with analyses selecting tau leptons. Changing the energy scale can therefore change the overall number of events accepted for given signal and validation regions. The uncertainty due to the tau energy scale was evaluated using single hadron calorimeter response measurements (as evaluated for the jet energy scale) and correcting for the known composition of tau jets - these measurements were performed by the ATLAS tau performance group. No systematics were evaluated for tau identification.

6.3.1.7 Jets

The jet energy scale was estimated from the 1σ variations obtained from jet energy scale measurements discussed in Section 4.4.6.1 performed by the ATLAS jet performance group. To account for jet energy resolution, jet p_T was smeared according to a Gaussian distribution. The mean and width of the Gaussian were varied according to the p_T and η of the jet.

6.3.1.8 b -tagging efficiency

The b -tagging algorithm performance was evaluated by the ATLAS flavour-tagging performance group using MC light and heavy jet samples: the associated uncertainty on the

real efficiency and mis-tag rates for the 2011 and 2012 algorithms (JetFitterCombNN and MV1) was then propagated as an overall scale factor.

6.3.1.9 MET

The uncertainties on electron, muon, tau and jet energy scales and resolutions are propagated directly to the MET. There are additional systematics from the calorimeter cells not associated with any objects (“CellOut” term), and from soft jets ($p_T < 20$ GeV): in the former case, a 5% uncertainty on the energy scale is applied, as is an uncertainty for the resolution. Since the effect of soft jets was found to be negligible, no systematic uncertainty was applied.

6.3.1.10 Luminosity

The uncertainty on the luminosity is 3.6% for 2012 data, and 3.9% for 2011 data. This uncertainty was calculated using the methods detailed in [210, 211].

6.3.1.11 Trigger

Trigger reweighting was used in the 2011 analysis, and the $\pm 1\sigma$ band from the statistical error on the MC and data samples used was found to be $< 1\%$, and applied as a systematic uncertainty. In the 2012 analysis, trigger simulation was used directly, and a 5% systematic uncertainty was applied to account for the small discrepancies between data and MC observed.

6.3.1.12 WZ normalisation (2011 only)

WZ was normalised in a control region (WZNR) defined in Section 6.2: this normalisation was then allowed to fluctuate simultaneously in each signal region as discussed in Section 7.3.5. The systematic uncertainties used were simply those detailed in Section 6.3.1.

6.3.2 Summary of irreducible background uncertainties

Tables 6.4 and 6.5 show the main systematics (any individual contributions above 10%) on the irreducible background for the 2012 analysis: systematics with a contribution greater than 5% are included. Full tables may be found in Appendix B. The triboson samples have the largest ($> 100\%$) overall systematics in most regions: this is dominated by the 100% uncertainty on the choice of MC generator. The $t\bar{t} + V$ samples also have large uncertainties: the fluctuations in each SR are due to the small overall number of MC

events selected. This also leads to statistical fluctuations in systematic uncertainties that change the total number of events accepted.

	Triboson	ZZ	$t\bar{t} + V$	WZ	Total
SRZa					
Expected events	0.54	8.88	0.43	235.05	244.9
Jet energy scale	3.3,-2.64%	1.34,-7.25%	26.64,-21.24%	1.71,-1.04%	1.74,-1.3%
Jet energy resolution	2.95,-2.95%	7.76,-7.76%	19.64,-19.64%	2.88,-2.88%	3.08,-3.08%
E_T^{miss} soft term scale	-1.35,-0.32%	10.88,-6.69%	0.0,-0.0%	2.61,-2.35%	2.9,-2.5%
b -tagging	2.56,-2.63%	3.33,-3.43%	46.28,-56.32%	3.07,-3.17%	3.15,-3.28%
MC statistics	5.92,-5.92%	8.51,-8.51%	40.41,-40.41%	2.13,-2.13%	2.07,-2.07%
Generator	100.0 %	10.7 %	0.0 %	1.6 %	2.14%
Cross section	10.0 %	5.0 %	30.0 %	12.0 %	11.77%
Total	101.05,-101.1%	21.26,-21.24%	80.74,-85.60%	14.83,-15.62%	14.82,-15.57%
SRZb					
Expected events	0.43	0.95	0.22	18.68	20.29
Electron energy scale	2.06,-2.58%	21.65,-20.82%	0.0,-0.0%	2.08,-7.7%	2.97,-8.12%
Jet energy scale	-0.06,-3.66%	17.68,-10.14%	0.0,-18.39%	1.7,-7.57%	2.39,-6.77%
Jet energy resolution	0.34,-0.34%	15.47,-15.47%	4.64,-4.64%	4.84,-4.84%	5.24,-5.24%
E_T^{miss} soft term scale	1.55,-2.07%	6.16,-4.82%	0.0,-0.0%	13.73,-16.89%	12.97,-15.37%
b -tagging	2.95,-3.0%	1.86,-1.9%	38.4,-64.33%	3.3,-3.45%	3.61,-4.03%
MC statistics	6.62,-6.62%	25.45,-25.45%	57.33,-57.33%	7.46,-7.46%	7.0,-7.0%
Generator	100.0 %	16.8 %	0.0 %	5.9 %	8.36%
Cross section	10.0 %	5.0 %	30.0 %	12.0 %	11.83%
Total	100.99,-101.17%	45.88,-43.30%	75.64,-93.42%	22.79,-27.10%	23.15,-26.69%
SRZc					
Expected events	0.29	0.39	0.1	5.01	5.79
Jet energy resolution	2.85,-2.85%	4.52,-4.52%	38.25,-38.25%	2.77,-2.77%	3.51,-3.51%
E_T^{miss} soft term scale	-0.84,-1.11%	0.0,-32.99%	0.0,-0.0%	3.94,-4.74%	3.37,-6.26%
E_T^{miss} soft term resolution	-1.22,-1.22%	-33.02,-33.02%	0.0,-0.0%	-3.3,-3.3%	-5.13,-5.13%
MC statistics	6.37,-6.37%	41.46,-41.46%	95.95,-95.95%	14.22,-14.22%	12.73,-12.73%
Generator	100.0 %	35.4 %	0.0 %	12.9 %	18.55%
Cross section	10.0 %	5.0 %	30.0 %	12.0 %	11.74%
Total	101.0,-101.13%	64.98,-72.56%	108.02,-108.07%	27.62,-27.38%	29.40,-29.77%

Table 6.4: The % effect of the dominant ($> 10\%$ for any background) systematic uncertainties on irreducible SM yields in SRZ for the 2012 analysis.

6.3.3 Uncertainties on the reducible background

The systematic uncertainties on the matrix method estimation of the background come from several sources. The statistical uncertainty on data and MC samples varies between 7.3% and 71%, depending on the region considered. The highest uncertainties are found in SRnoZc and SRZc, which have the tightest selection criteria. The fake fraction(R_{XR}^{ij}) is the proportion of different fake leptons by origin i and type j in a given region XR: an uncertainty of 10% is assigned to the fake fractions from each MC sample to account for potential differences between data and MC. An uncertainty of up to 5% on the real lepton efficiency was also assigned by considering the largest deviation from the fitted value as a function of η . Finally, uncertainties on the truth fake rates arising from different proportions of fakes as a function of E_T^{miss} were evaluated by finding the relative differences in truth fake rate for leptons of all origins and types in each E_T^{miss} bin. These uncertainties range between 5 and 26%.

	Triboson	$Z Z$	$t\bar{t} + V$	$W Z$	Total
SRnoZa					
Expected events	1.69	13.76	0.23	49.56	65.23
Jet energy resolution	0.67,-0.67%	7.3,-7.3%	36.0,-36.0%	6.73,-6.73%	6.8,-6.8%
E_T^{miss} soft term scale	0.42,-0.46%	21.93,-15.72%	0.0,0.0%	4.27,-2.97%	7.86,-5.58%
b -tagging	2.23,-2.31%	2.94,-3.02%	61.48,-76.77%	3.11,-3.2%	3.26,-3.4%
MC statistics	3.94,-3.94%	6.37,-6.37%	54.76,-54.76%	4.59,-4.59%	3.74,-3.74%
Generator	100.0 %	49.4 %	0.0 %	6.9 %	18.25%
Cross section	10.0 %	5.0 %	30.0 %	12.0 %	10.54%
Total	100.79,-101.0%	56.50,-54.48%	94.94,-105.72%	18.31,-19.27%	25.22,-25.3%
SRnoZb					
Expected events	0.63	1.76	0.21	19.52	22.11
Jet energy scale	2.78,0.09%	10.61,-7.47%	0.0,46.9%	4.31,6.1%	4.73,5.23%
Jet energy resolution	1.35,1.35%	16.77,16.77%	43.16,43.16%	6.73,6.73%	7.71,7.71%
E_T^{miss} soft term scale	1.57,-1.05%	34.57,-23.63%	0.0,0.0%	7.22,-1.82%	9.16,-3.52%
b -tagging	2.25,-2.29%	2.18,-2.19%	28.75,-29.03%	3.28,-3.38%	3.4,-3.49%
MC statistics	6.41,-6.41%	18.29,-18.29%	54.86,-54.86%	7.54,-7.54%	6.84,-6.84%
Generator	100.0 %	38.4 %	0.0 %	7.0 %	12.09%
Cross section	10.0 %	5.0 %	30.0 %	12.0 %	11.55%
Total	101.0,-101.08%	59.19,-53.41%	81.47,-94.123%	20.78,-20.56%	23.58,-22.60%
SRnoZc					
Expected events	0.81	0.25	0.21	2.12	3.4
Jet energy resolution	3.09,3.09%	0.0,0.0%	103.23,103.23%	11.33,11.33%	14.2,14.2%
E_T^{miss} soft term scale	-0.04,-2.1%	3.11,0.0%	0.0,0.0%	11.51,-2.32%	7.41,-1.95%
b -tagging	2.35,-2.43%	6.32,-6.32%	10.39,-10.67%	3.98,-4.12%	4.16,-4.28%
MC statistics	5.64,-5.64%	54.82,-54.82%	51.78,-51.78%	20.6,-20.6%	13.93,-13.93%
Generator	100.0 %	14.4 %	0.0 %	65.9 %	66.2%
PDF	0.0,0.0%	9.12,-8.29%	0.0,0.0%	1.86,2.27%	1.83,0.81%
Cross section	10.0 %	5.0 %	30.0 %	12.0 %	12.12%
Total	100.81,-100.9%	58.28,-68.2%	119.83,-144.83%	73.27,-72.34%	71.3,-71.54%

Table 6.5: The % effect of all systematic uncertainties on irreducible SM yields in SRZ for the 2012 analysis.

The overall uncertainty from the reducible background estimate varied between 37 and 78% in the 2012 analysis, depending on the signal region considered. Table 6.6 shows the different uncertainties for each signal region.

	SRnoZa	SRnoZb	SRnoZc	SRZa	SRZb	SRZc
Expected events	31.0	7.1	1.0	4.3	1.7	0.5
Statistics	+7.3,-7.3%	+12,-12%	+38,-38%	+34,-34%	+35,-35%	+71,-71%
Fake fractions	+12,-12%	+19,-19%	+5,-14%	+29,-29%	+8,-9%	+20,-26%
E_T^{miss} dependence	+42,-36%	+64,-64%	+10,-9%	+33,-26%	+6,-5%	+16,-13%
Scale factors	+7,-6%	+13,-13%	+1,-1%	+4,-4%	+0,-0%	+1,-1%
Total	+45,-39%	+66,-50%	+40,-42%	+84,-111%	+37,-38%	+76,-78%

Table 6.6: Systematic uncertainties for the reducible background in the signal regions.

6.3.4 Uncertainties on the SUSY signal samples

The uncertainty on the SUSY signal production includes contributions from the PDF errors (evaluated using both the CTEQ and MSTW PDF sets) and variations in the

theoretical parameters used in the cross section calculation. The procedure to evaluate these errors is detailed in [212].

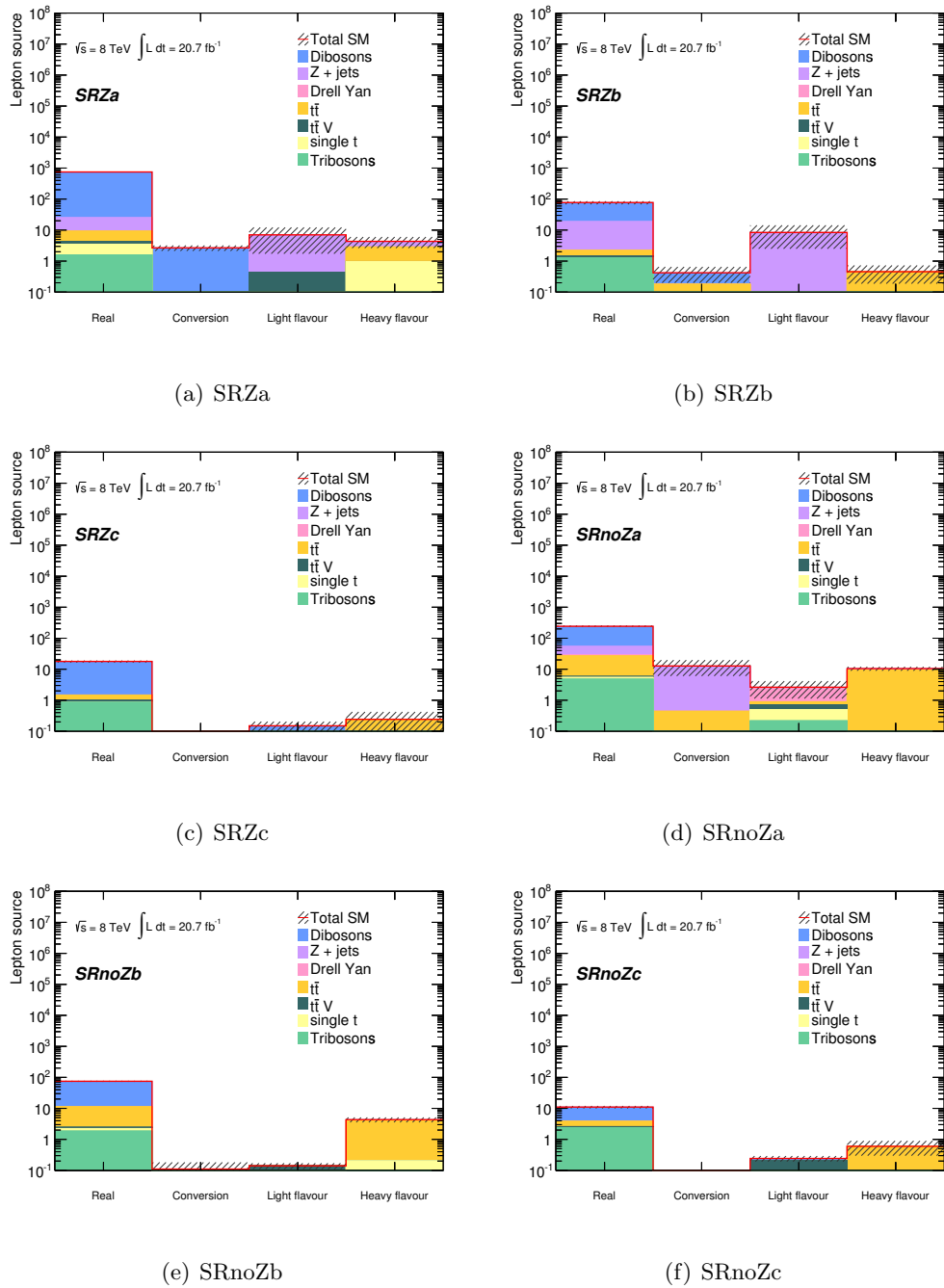


Figure 6.3: Sources of leptons in 2012 signal regions. Errors are statistical only.

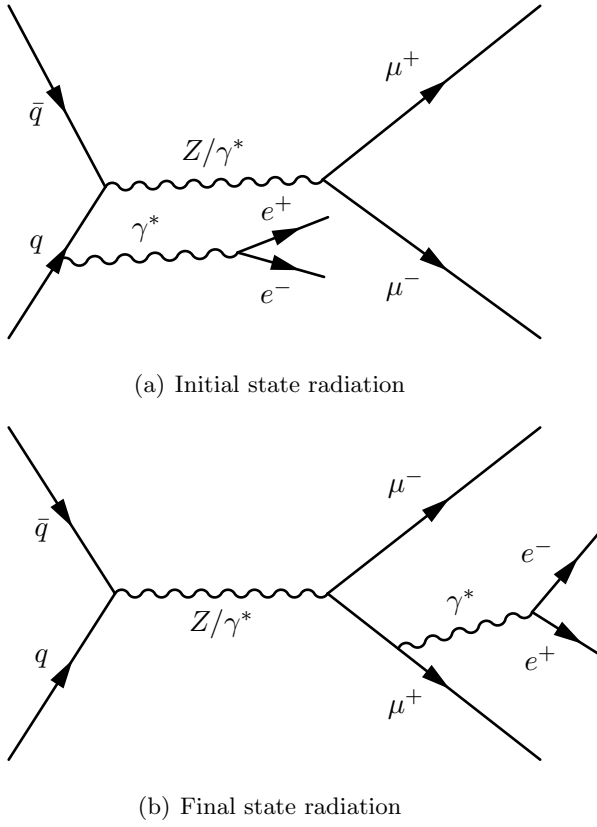


Figure 6.4: Feynman diagrams for initial and final state internal conversion. In a), the internal conversion radiates from the initial quark leg, while in b) the internal conversion radiates from a final state lepton.

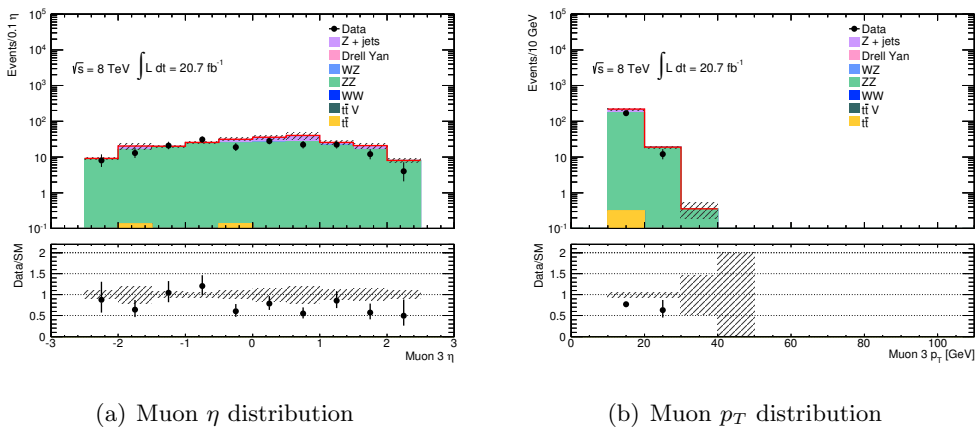


Figure 6.5: Data/MC comparison for the muon conversion validation region defined in Section 6.1.4.1. Errors are statistical only.

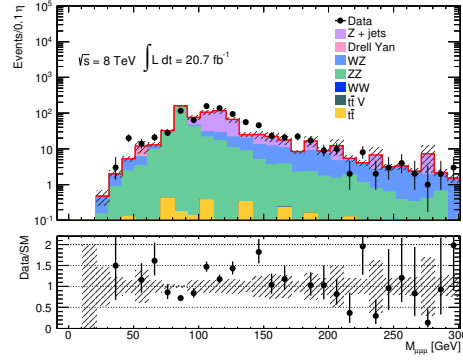


Figure 6.6: Invariant mass of dimuon pair and muon conversion candidate defined in Section 6.1.4.1 in the muon conversion validation region, with all cuts except $m_{\mu\mu\mu}$ within the range [81.2–101.2] GeV applied. Some fluctuation is observed on either side of the range [81.2–101.2] GeV used to define the validation region. Errors are statistical only.

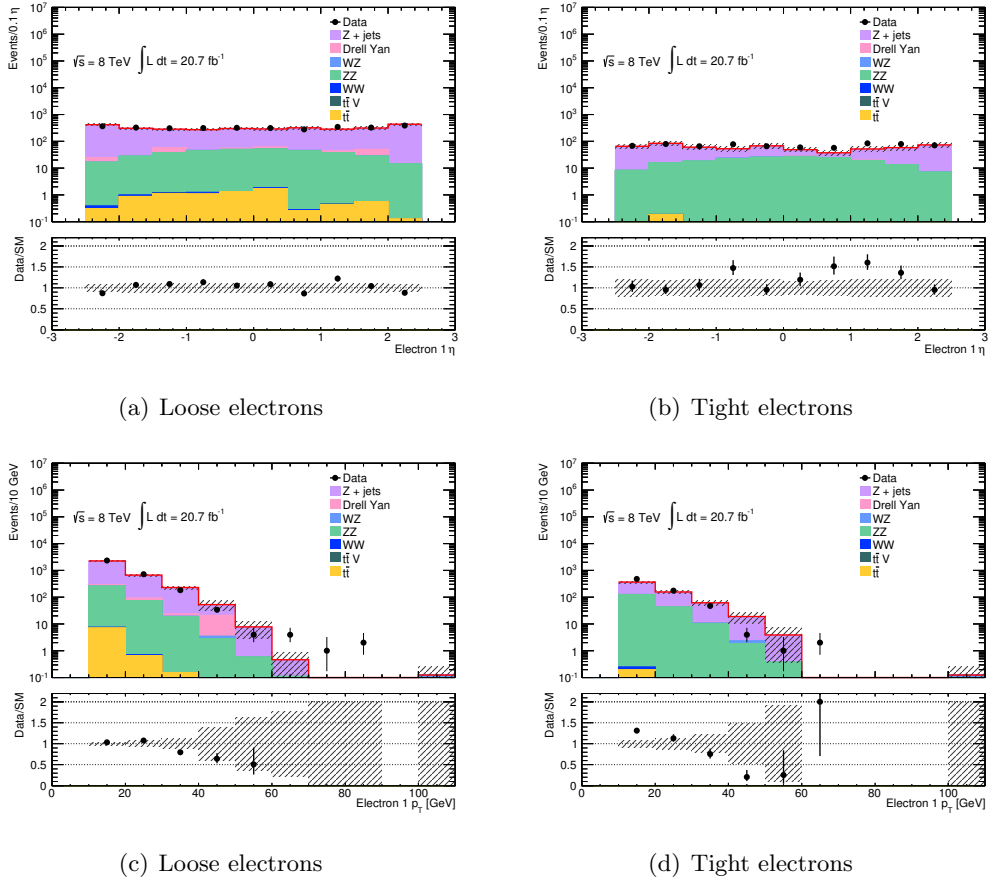


Figure 6.7: η (top) and p_T (bottom) of electron conversion candidate in the conversion control region. Errors are statistical only.

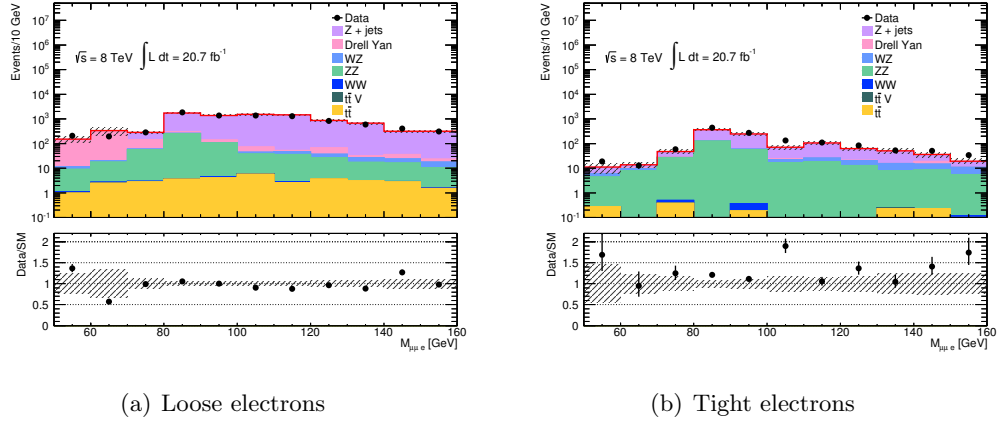


Figure 6.8: Invariant mass of dimuon pair and electron conversion candidate in the conversion control region, with all cuts except [81.2:101.2] GeV applied. Errors are statistical only.

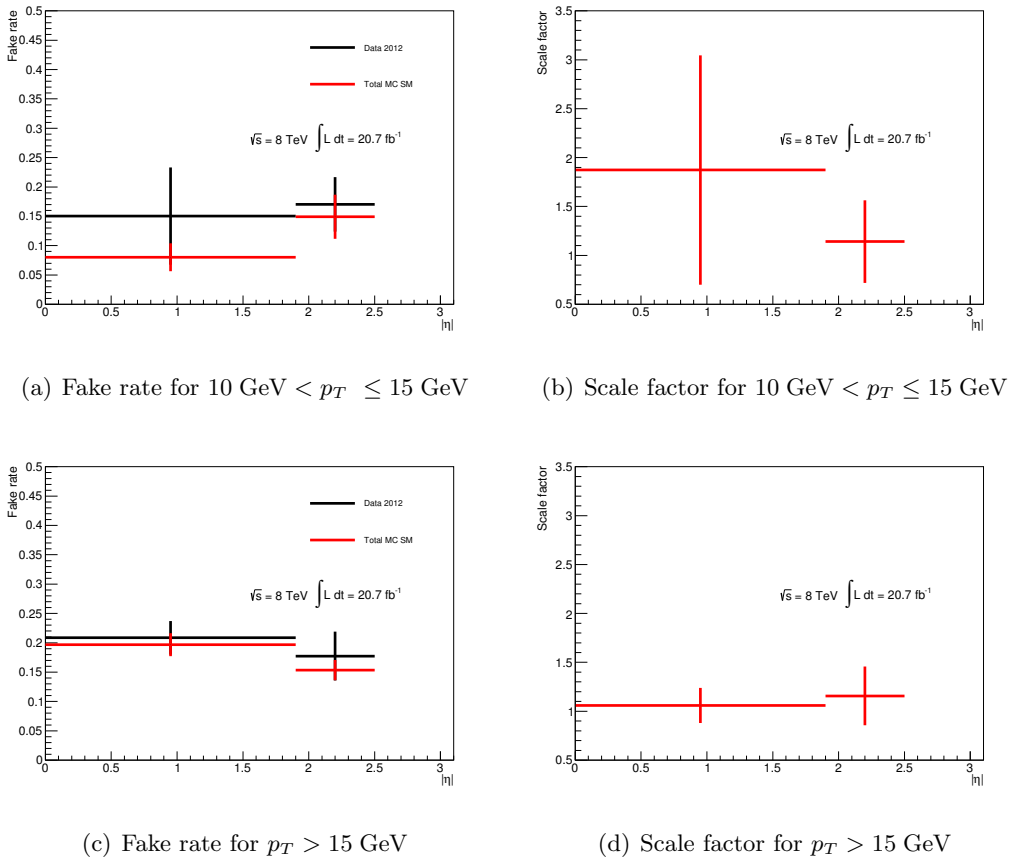


Figure 6.9: Fake rates and scale factors for conversion electrons. In the fake rate plots (left) data fake rates are shown in black, while MC fake rates are shown in red. Errors shown are statistical and systematic, summed in quadrature.

Chapter 7

Results and interpretation

In the beginning, there was
simply the event and its
consequences.

Paul Auster [213]

7.1 Validation of background prediction

As this is a blind analysis the background modelling, including the data-driven background estimates for fake leptons and treatment of systematic uncertainties, is verified using dedicated validation regions (VRs) enriched in relevant background sources, before the analysis of the data in the signal regions.

7.1.1 2011 analysis

The selection criteria for the 2011 validation regions are summarised in Table 7.1.

Selection	VR1	VR2	VR3
Targeted background	Drell-Yan, WZ^*	$t\bar{t}$	on-shell WZ
$m_{\ell\ell}$ [GeV]	$< 81.2, > 101.2$	Veto SFOS pairs	[81.2:101.2]
E_T^{miss} [GeV]	$30 < E_T^{\text{miss}} < 75$	> 50	$50 < E_T^{\text{miss}} < 75$

Table 7.1: The selection requirements for the 2011 signal regions.

7.1.2 2012 analysis

The 2012 validation regions, like the signal regions, are subdivided into Z -veto and Z -request regions. They are then defined by reversing one of two selection criteria:

Selection	VR1	VR2	VR3
$t\bar{t} + V$	0.787 ± 0.52	0.84 ± 0.51	1.20 ± 0.90
ZZ	17 ± 15	0.10 ± 0.05	3.9 ± 0.6
WZ	46 ± 8	0.93 ± 0.29	98 ± 12
Reducible background	50 ± 28	13 ± 7	$3.1^{+4.7}_{-3.1}$
Total background	114 ± 32	15 ± 7	106 ± 13
Data	126	18	109

Table 7.2: Expected numbers of events from SM backgrounds and observed numbers of events in 2011 data, for 4.7 fb^{-1} , in validation regions VR1, VR2 and VR3. Both statistical and systematic uncertainties are included. Adapted from [196].

- (a) $E_T^{\text{miss}} < 50 \text{ GeV}$ rather than the high E_T^{miss} selection in the signal regions (VRnoZa, VRZa)
- (b) At least one b -tagged jet, rather than the veto across all signal regions (VRnoZb, VRZb)

The regions (VRnoZb, VRZb) with at least one b -jet preferentially select events with large heavy flavour contributions ($Z+b$ -jets, $t\bar{t}$, $t\bar{t} + V$ etc), while VRnoZa and VRZa preferentially select events with large light flavour contributions. The regions are summarised in Table 7.3.

Selection	VRnoZa	VRnoZb	VRZa	VRZb
Z candidate	Veto		Request	
$E_T^{\text{miss}} [\text{ GeV}]$	$< 50 \text{ GeV}$	$> 50 \text{ GeV}$	$< 50 \text{ GeV}$	$> 50 \text{ GeV}$
b -jet	Veto	Request	Veto	Request

Table 7.3: The selection requirements for the 2012 signal regions.

The error bars shown for data events are, by convention, Poisson 68% upper and lower confidence levels. As shown in Table 7.4, VRnoZa and VRZa have the largest contributions from reducible backgrounds. WZ is the dominant background in all VRs except VRnoZa, where ZZ is dominant. The reducible background prediction from the matrix method can fluctuate negatively: this is visible in VRnoZa, shown in the last bin of Figure 7.1(a). This fluctuation in the reducible background prediction is covered by uncertainties. In Figures 7.1(b), 7.2(a) and 7.2(b), the negative prediction is spread across several bins and therefore no longer visible. A slight excess is visible in the final bin of Figure 7.1(b): this is compensated for by a deficit in the second bin. Figures 7.2(a) and 7.2(b) show

Selection	VRnoZa	VRnoZb	VRZa	VRZb
Triboson	1.41 ± 0.19	0.51 ± 0.11	0.6 ± 0.6	0.26 ± 0.05
$t\bar{t}+V$	2.9 ± 0.8	21.2 ± 2.1	7.4 ± 1.3	25.9 ± 2.6
ZZ	128 ± 24	4.5 ± 1.3	108 ± 13	6.9 ± 1.4
WZ	110 ± 17	34 ± 6	545 ± 79	138 ± 22
Reducible background	146 ± 55	72 ± 45	376 ± 138	27 ± 13
Total background	388 ± 63	132 ± 45	1038 ± 160	198 ± 26
Data	463	141	1131	171

Table 7.4: Expected numbers of events in the validation regions from SM backgrounds and observed numbers of events in 2012 data. Both statistical and systematic uncertainties are included. Adapted from [3].

slight excesses and deficits distributed across several bins. In VRnoZb there are slight excesses between $140 \text{ GeV} < m_T < 280 \text{ GeV}$, followed by several bins with zero data events (shown in Figure 7.3(a)): these bins have a prediction of one background event or fewer. The distribution of data events as a function of E_T^{miss} is smooth, as shown in Figure 7.3(b), while there are fluctuations in the $m_{\ell\ell}$ and $p_T^{\ell_3}$ distributions (Figures 7.2(a) and 7.2(b) respectively). In VRZa, as shown in Figure 7.5(a) the reducible background is seen to have the largest contribution at low m_T : this region is dominated by $Z+\text{jets}$, which is expected to have low E_T^{miss} and hence low m_T . The data in each bin of 7.5(a) and 7.5(b) are contained within the envelope of the uncertainties on the background prediction. In VRZb, the data events in the b -jet multiplicity distribution (Figure 7.6(b)) follow the shape of the background prediction. Small fluctuations are visible in some bins of the m_T distribution (Figure 7.6(a)) but do not appear to follow a systematic shape.

7.1.3 Summary

Very good agreement between the background predictions and data results is observed in both 2011 and 2012 analyses. In the 2012 analysis, all background predictions agree with data within uncertainties. There are slight over-fluctuations in all regions except VRnoZb, where there is an underfluctuation. The observed and expected numbers of events are shown in Tables 7.2 and 7.4 for the 2011 and 2012 analysis respectively. Kinematic distributions for the 2012 analysis are shown in Figures 7.1, 7.2, 7.3, 7.4, 7.5 and 7.6.

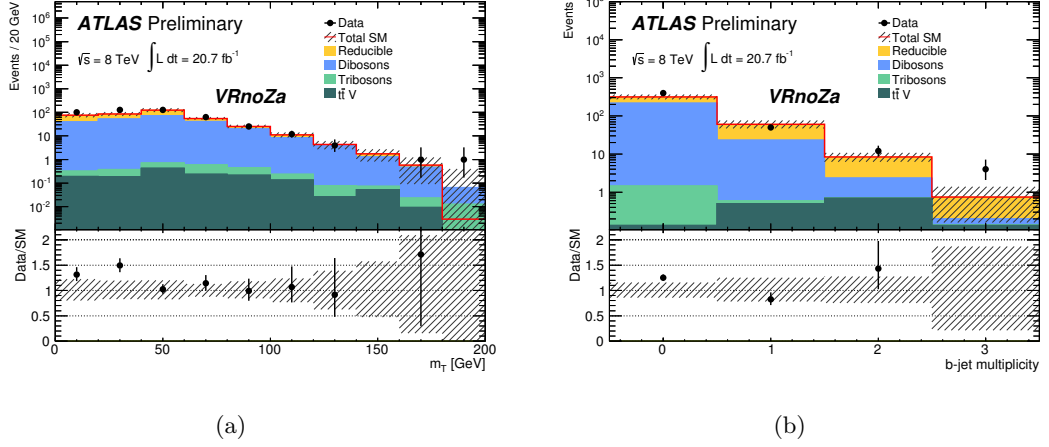


Figure 7.1: The (a) m_T and (b) b -jet multiplicity distributions for VRnoZa in the 2012 analysis. The uncertainty band includes both statistical and systematic uncertainties on the SM prediction. A negative prediction from the matrix method is visible in the final bin of histogram (a). The data plotted correspond to Table 7.4. Result made public in [3].

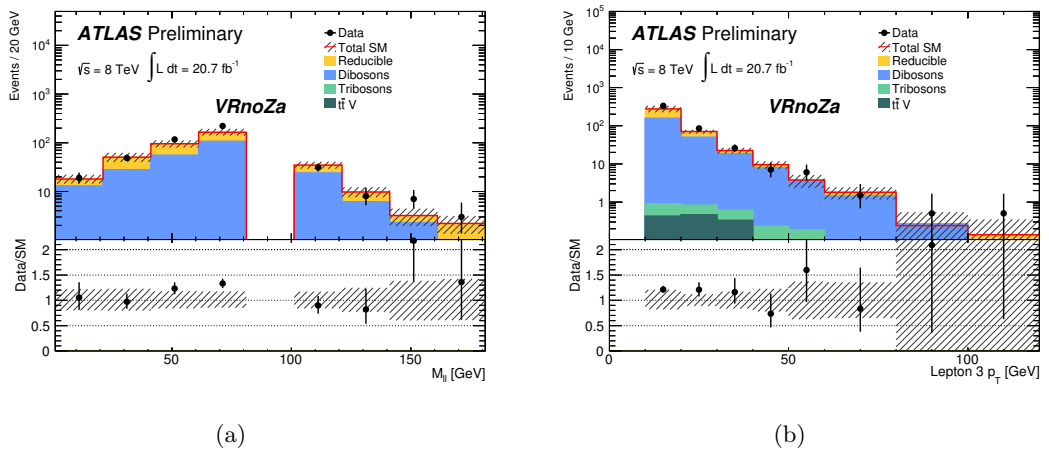


Figure 7.2: The (a) $m_{\ell\ell}$ and (b) $p_T^{\ell_3}$ distributions for VRnoZa in the 2012 analysis. The uncertainty band includes both statistical and systematic uncertainties on the SM prediction. The data plotted correspond to Table 7.4. Result made public in [3].

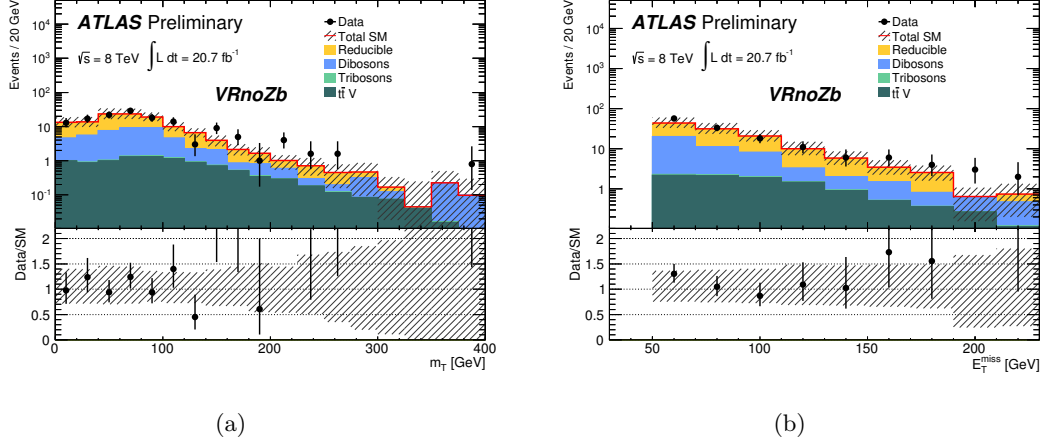


Figure 7.3: The (a) m_T and (b) E_T^{miss} distributions for VRnoZb. The uncertainty band includes both statistical and systematic uncertainties on the SM prediction. A slight over-fluctuation is visible in a single bin of (c). The data plotted correspond to Table 7.4. Result made public in [3].

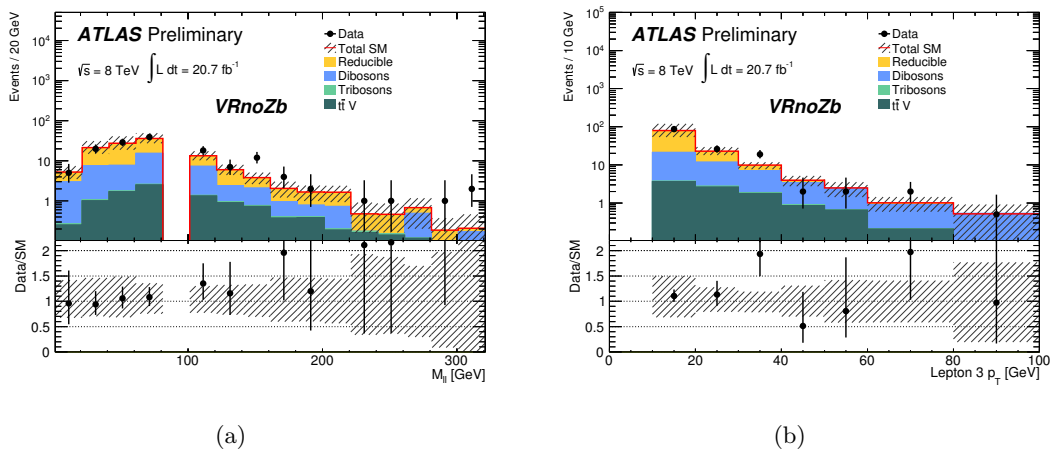


Figure 7.4: The (a) $m_{\ell\ell}$ and (b) third lepton p_T distributions for VRnoZb. The uncertainty band includes both statistical and systematic uncertainties on the SM prediction. The data plotted correspond to Table 7.4. A slight over-fluctuation is visible in a single bin of (b). Result made public in [3].

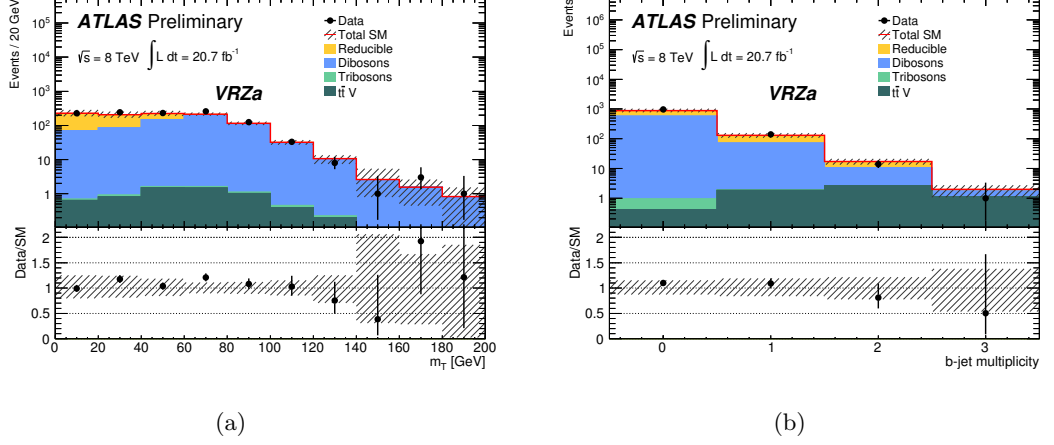


Figure 7.5: The (a) m_T and (b) b -jet multiplicity distributions for VRZa. The uncertainty band includes both statistical and systematic uncertainties on the SM prediction. Result made public in [3].

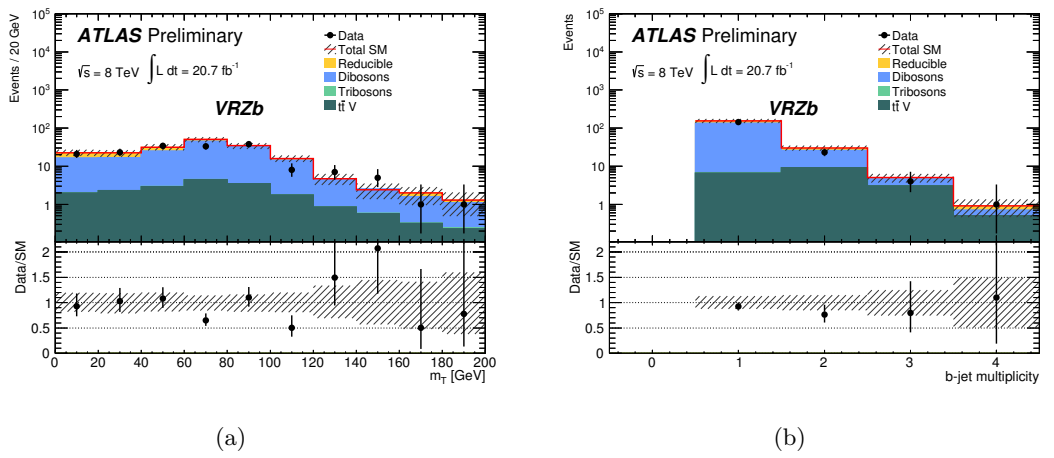


Figure 7.6: The (a) m_T and (b) b -jet multiplicity distributions for VRZb. The uncertainty band includes both statistical and systematic uncertainties on the SM prediction. The data plotted correspond to Table 7.4. Result made public in [3].

7.2 Results in signal regions

In the following sections the full results of 2011 and 2012 analyses in the signal region are given. The plots with associated systematics are my own work, while the tables were produced by another member of the analysis team.

7.2.1 2011 analysis

The observed events in data agree well with the background prediction, as shown in Table 7.5: this is true for all signal regions. In SR1b there is a slight underfluctuation.

Selection	SR1a	SR1b	SR2
$t\bar{t}+V$	0.43 ± 0.29	0.13 ± 0.008	0.70 ± 0.51
ZZ	0.67 ± 0.21	0.09 ± 0.08	0.34 ± 0.17
WZ	13.5 ± 3.2	1.1 ± 0.28	9.3 ± 2.2
SM irreducible	15 ± 3	1.3 ± 0.29	10 ± 2
SM reducible	10 ± 5	0.35 ± 0.34	$0.5^{+1.0}_{-0.5}$
Σ SM	25 ± 6	1.6 ± 0.5	10.9 ± 2.4
Data	24	0	11

Table 7.5: Expected numbers of events from SM backgrounds and observed numbers of events in 2011 data in signal regions SR1a, SR1b and SR2. Both statistical and systematic uncertainties are included. Adapted from [196].

7.2.2 2012 analysis

The observed events in data are in full agreement with the background prediction, as shown in 7.6: there is a modest excess in all signal regions except SRZc, where there is a slight underfluctuation. Of the Z -veto SRs, SRnoZa has the highest number of expected (96 ± 17) and observed (101) events. The E_T^{miss} distribution is well described by the background prediction, with every bin agreeing within uncertainties (shown in 7.7(a)). SRnoZb has a moderate number of expected (29 ± 6) and observed (32) events. Like SRnoZa, the E_T^{miss} distribution is well described by the background prediction, as shown in Figure 7.7(b). SRnoZc is the tightest Z -veto SR, and therefore has the lowest number of expected (4.4 ± 1.2) and observed (5) events. There is no event in the 110 to 150 GeV bin, with approximately two expected (shown in Figure 7.7(d)), but there is no systematic shift towards higher E_T^{miss} events (shown in Figure 7.7(c)). SRZa has the highest number

of expected (249 ± 32) and observed (273) events in any SR. There is a slight excess in the first m_T bin, followed by a slight deficit in the third bin (shown in Figure 7.8(a)). In the high- m_T region, there is a moderate number of expected (22 ± 5) and observed (23) events. No significant excess or deficit is observed in the three broad m_T bins shown in Figure 7.8(b). SRZc is the tightest Z -request SR, with the lowest number of expected (6.3 ± 1.3) and observed (6) events. No excess or deficit is seen in the m_T or E_T^{miss} distributions (Figures 7.8(c) and 7.8(d) respectively).

Selection	SRnoZa	SRnoZb	SRnoZc	SRZa	SRZb	SRZc
$t\bar{t} + V$	0.23 ± 0.24	0.21 ± 0.19	0.21 ± 0.30	0.4 ± 0.4	0.22 ± 0.21	0.10 ± 0.11
Triboson	1.7 ± 1.7	0.6 ± 0.6	0.8 ± 0.8	0.5 ± 0.5	0.4 ± 0.4	0.29 ± 0.29
ZZ	14 ± 4	1.8 ± 0.8	0.25 ± 0.17	8.9 ± 1.7	1.0 ± 0.4	0.39 ± 0.25
WZ	50 ± 8	20 ± 4	2.1 ± 0.7	235 ± 32	19 ± 5	5.0 ± 1.2
Σ SM irreducible	65 ± 9	22 ± 4	3.4 ± 1.1	245 ± 32	20 ± 5	5.8 ± 1.2
SM reducible	31 ± 14	7 ± 5	1.0 ± 0.4	4 ± 5	1.7 ± 0.7	0.5 ± 0.4
Σ SM	96 ± 17	29 ± 6	4.4 ± 1.2	249 ± 32	22 ± 5	6.3 ± 1.3
Data	101	32	5	273	23	6

Table 7.6: Expected numbers of events from SM backgrounds and observed numbers of events in data in 2012 signal regions. Both statistical and systematic uncertainties are included. The number of signal events N_{signal} and visible cross-section σ_{visible} that can be excluded with 95% CL are also shown. Adapted from [3].

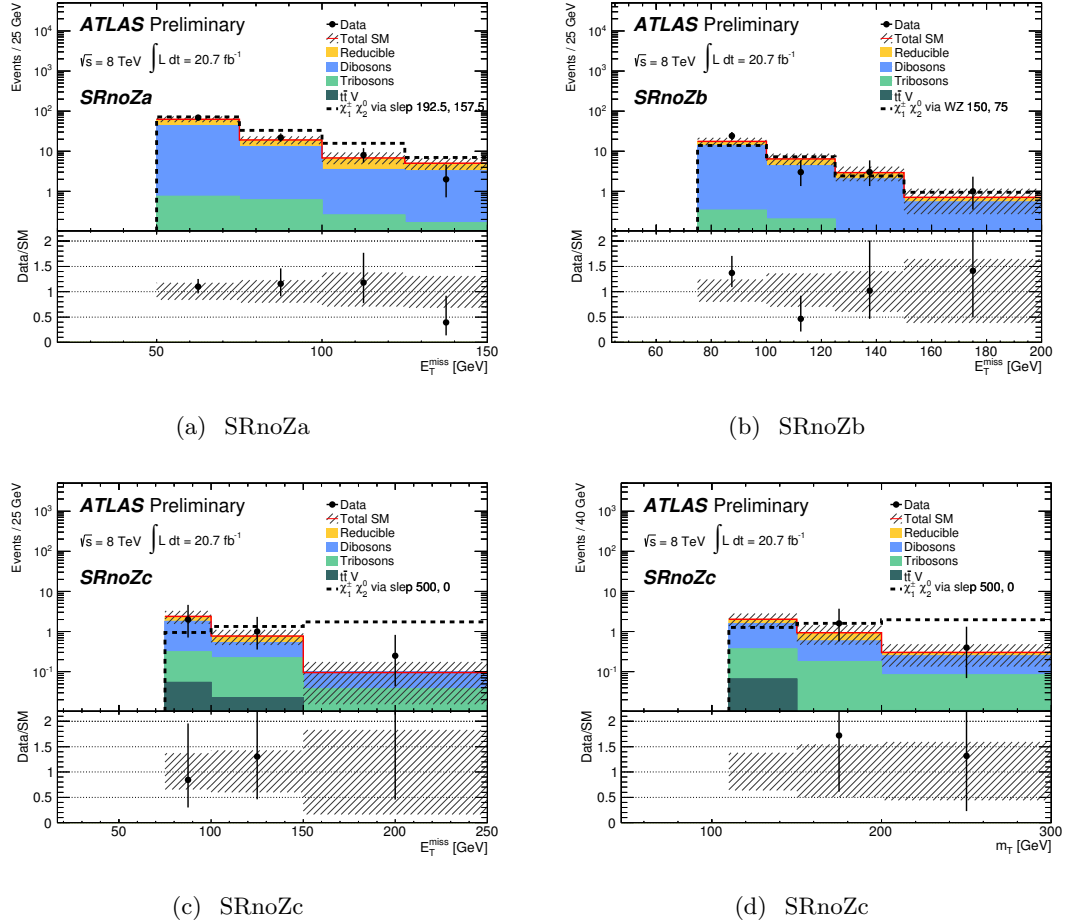


Figure 7.7: The E_T^{miss} distributions for events in signal regions (a) SRnoZa, (b) SRnoZb, (c) SRnoZc, as well as (d) the m_T distribution in SRnoZc are shown. The data plotted correspond to Table 7.6. Preliminary result made public in [3].

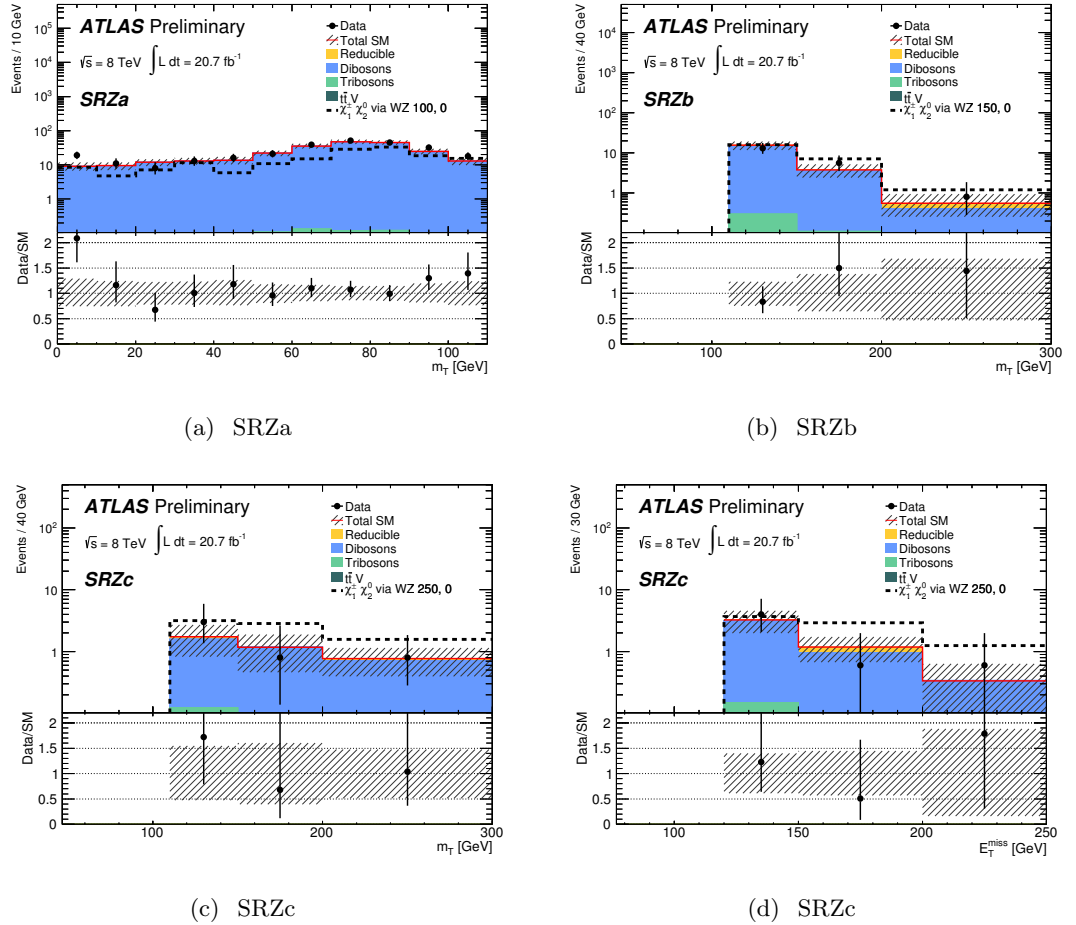


Figure 7.8: The m_T distributions for events in signal regions (a) SRZa, (b) SRZb, (c) SRZc. The data plotted correspond to Table 7.6. Preliminary result made public in [3].

7.3 Statistical interpretation

7.3.1 Introduction

The results obtained with the 2011 and 2012 datasets are interpreted as limits on SUSY signal scenarios. The models were discussed extensively in Sections 2.4.1.1, 2.4.2.1, 2.4.3, and their phenomenological properties relevant to the statistical interpretation are briefly reviewed below (Section 7.3.2). The statistical techniques used are reviewed in Section 7.3.3, while the following Sections are devoted to interpretation in specific scenarios. As with the preceding Sections, emphasis is placed on results I had significant involvement in. Firstly, I used the results of the 2011 analysis to derive limits in GGM scenarios (Section 7.4.1). The second interpretation (Section 7.4.2) again used the 2011 dataset, this time to derive limits in pMSSM scenarios. I then combined these limits with a complementary two-lepton analysis: this is discussed in Section 7.4.2.1). Finally, the results of the 2012 analysis were used to derive limits in simplified model scenarios: the optimisation of the signal regions discussed in Chapter 5.3, substantially improved upon the 2011 analysis.

7.3.2 SUSY models

The cross section for each scenario is dependent on the mass of the intermediate particles produced, and on the type of interaction (strong or weak). Only the GGM scenarios contain significant contributions from strong production.

7.3.2.1 General gauge mediation

The GGM scenario was discussed in more detail in Section 2.4.1. Two scenarios are considered here: one with higgsino NLSP and one with degenerate wino co-NLSPs. The \tilde{H} masses vary between 110 and 890 GeV and \tilde{g} masses between 300 and 900 GeV in increments of 100 GeV. The \tilde{W} masses vary between 120 and 790 GeV, \tilde{g} masses between 300 and 1000 GeV in increments of 100 GeV. The first two \tilde{W} masses are 120 and 150 GeV, and subsequent masses are incremented by 100 GeV, starting at 200 GeV. As $m_{\tilde{g}}$ increases, weak production becomes dominant, as shown in Figures 7.9 and 7.10.

7.3.2.2 The phenomenological MSSM

The pMSSM scenarios was discussed in more detail in Section 2.4.2. The pMSSM model considered here is parameterised by the gaugino mass parameters M_1 , M_2 and μ defined in Section 2.3.1. Three values are chosen for M_1 (100, 140 and 250 GeV), defining three

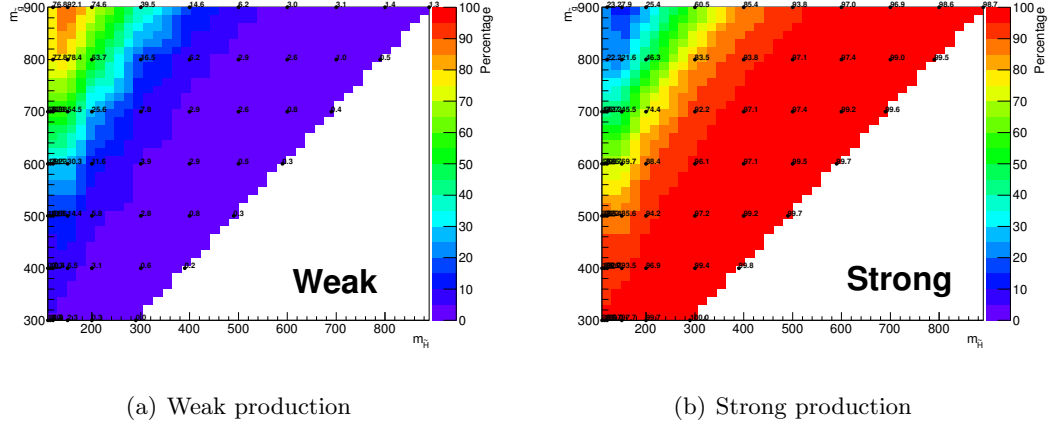


Figure 7.9: Percentages of weak (a) and strong (b) production in GGM higgsino co-NLSP grid.

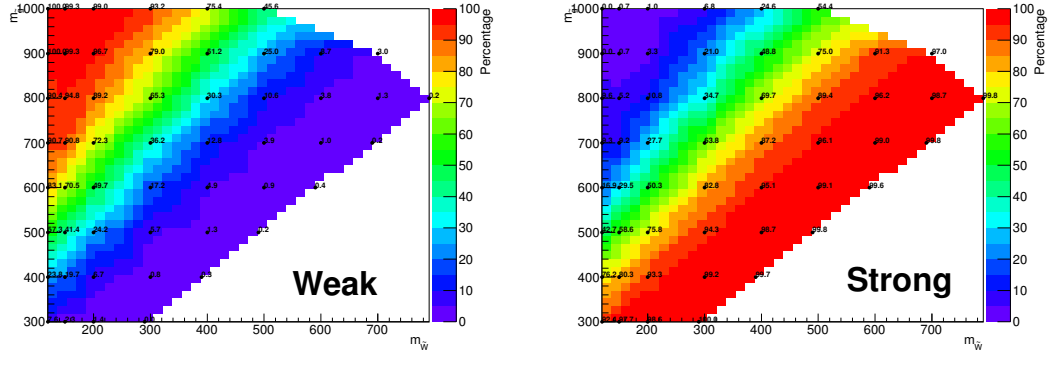


Figure 7.10: Percentages of weak (a) and strong (b) production in GGM wino co-NLSP grid.

grids. The values of M_2 and μ are between 100 and 500 GeV for $M_1 = 100$ and 140 GeV, and between 100 and 350 GeV for $M_1 = 250$ GeV, with spacing shown in Figure 7.11. As M_1 and μ simultaneously increase, the cross section for gaugino production decreases. If μ is greater than M_1 and M_2 , the gaugino masses are approximately independent of μ : there is only a slight decrease in cross section as a function of μ . This is not present in the $M_1 = 250$ GeV grid, since $\mu < M_1$ for most generated points. These features may be seen in Figure 7.11, where the MC cross sections for each grid point are plotted.

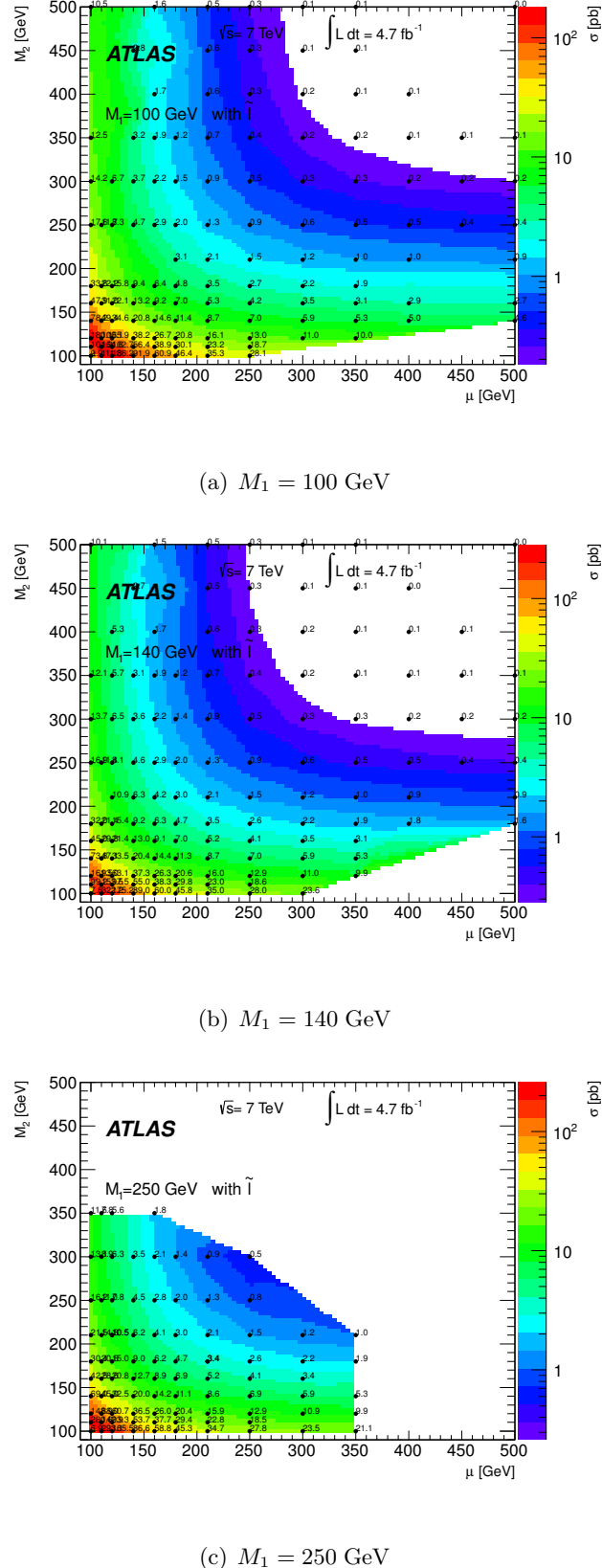


Figure 7.11: Cross sections for the three pMSSM scenarios ($M_1=100$ (a), 140 (b) and 250 (c) GeV), calculated at NLO. Details about the calculations used are given in Section 4.3.1.2. Taken from [196].

7.3.2.3 Simplified models

Simplified models were discussed in more detail in Section 2.4.3.1. As previously discussed, the phenomenology of simplified models is drastically reduced relative to GGM or the pMSSM: only a single process ($\tilde{\chi}_2^0 \tilde{\chi}_1^\pm$ production) is simulated, and decays are constrained to occur via sleptons (Model A) or gauge bosons (Model B) only. The relevant model parameters are $m_{\tilde{\chi}_2^0}$ (constrained to equal $m_{\tilde{\chi}_1^\pm}$) and $m_{\tilde{\chi}_1^0}$. Model A points are simulated with $m_{\tilde{\chi}_1^\pm}, m_{\tilde{\chi}_2^0} = 112.5 \text{ GeV}$ to 750 GeV and $m_{\tilde{\chi}_1^0}$ between 12.5 and 607.5 GeV . Model B points are defined with $m_{\tilde{\chi}_1^\pm}, m_{\tilde{\chi}_2^0}$ between 100 and 500 GeV and $m_{\tilde{\chi}_1^0}$ between 0 and 450 GeV .

Since the $\tilde{\chi}_1^0$ is the LSP, the models must obey $m_{\tilde{\chi}_1^\pm}, m_{\tilde{\chi}_2^0} < m_{\tilde{\chi}_1^0}$. The mass difference constrains the maximum m_{SFOS} available as discussed in Section 5.3.5.

Benchmark points in Model A are defined with masses from $m_{\tilde{\chi}_1^\pm}, m_{\tilde{\chi}_2^0} = 112.5 \text{ GeV}$ to 750 GeV , and $m_{\tilde{\chi}_1^0}$ between 12.5 and 607.5 GeV .

Benchmark points in Model B are defined with $m_{\tilde{\chi}_1^\pm}, m_{\tilde{\chi}_2^0}$ masses between 100 and 500 GeV , with $m_{\tilde{\chi}_1^0}$ between 0 and 450 GeV .

7.3.3 Statistical procedure

The results are interpreted using the profile likelihood ratio formalism [214]. First, the likelihood $L(n_{\text{obs}}|\mu, \mathbf{b}, \eta)$ is defined as

$$L(n_{\text{obs}}|\mu S, B, \eta) = \text{Pois}(n_{\text{obs}}|\mu S + B) \times \prod_{\eta} G_{\text{syst}}(\eta(0), \eta(\alpha), \eta(-\alpha)) \quad (7.1)$$

where

- n_{obs} is the number of observed events in data;
- μS is the number of signal events, with signal strength μ ;
- B is the predicted background;
- $\text{Pois}(n|\mu S + B)$ is a Poisson distribution;
- η are the associated systematic and statistical uncertainties or *nuisance parameters*;
- $G_{\text{syst}}(\eta(0), \eta(\alpha), \eta(-\alpha))$ is a Gaussian centred around the estimated value $\eta(\mathbf{0})$.

Since it is estimated from auxiliary measurements of various types (those for energy scale uncertainties, for instance), the estimated value of the nuisance parameters, $\tilde{\eta}$, is considered to be a measured quantity. A signal strength $\mu = 0$ corresponds to the SM without

SUSY (the background-only hypothesis) and $\mu = 1$ corresponds to the existence of the SUSY model under consideration (the signal hypothesis). The notation may be condensed by referring to the signal and background model (and associated nuisance parameters) as ν , and the likelihood as $L(\mu, \nu(\mu))$. The profile likelihood ratio, $\lambda_p(\mu)$, is then defined as

$$\lambda_p(\mu) = \frac{L(\mu, \hat{\nu}(\mu))}{L(\hat{\mu}, \hat{\nu}(\hat{\mu}))} \quad (7.2)$$

The “hats” ($\hat{\nu}$, $\hat{\mu}$) refer to the optimisation procedure used to maximise each likelihood:

- The numerator is a *conditional* maximum likelihood fit ($\hat{\nu}$): ν is varied while μ is kept fixed.
- The denominator is an *unconditional* maximum likelihood fit($\hat{\nu}$): ν and μ are varied simultaneously.

Each likelihood becomes independent of the nuisance parameters after this maximisation or “profiling” procedure. The profile likelihood ratio tends to unity if the observation is compatible with the hypothesised value of μ .

The *discovery p-value*, p_μ is a measure of the compatibility between the signal hypothesis and the observed data: it is defined as

$$p_\mu = P(n \geq n_{\text{obs}} | \mu), \quad (7.3)$$

that is to say, the probability of observing another dataset at least as compatible with the signal hypothesis. In the case of zero signal ($\mu = 0$), the *background-only p-value* is a measure of the compatibility between the data and background hypothesis:

$$p_0 = P(n \leq n_{\text{obs}} | \mu = 0). \quad (7.4)$$

In the profile log likelihood framework, the *p-value* is defined as a function of the *test statistic* q_μ , defined as follows:

$$q_\mu = \begin{cases} -2 \ln \lambda_p(\mu) & \hat{\mu} \leq \mu \\ 0 & \hat{\mu} > \mu. \end{cases} \quad (7.5)$$

The discovery *p-value* is then defined as

$$p_\mu = \int_{q_{\mu, \text{obs}}}^{\infty} f(q_\mu | \mu) dq_\mu \quad (7.6)$$

where $f(q_\mu | \mu)$ is the probability density function for the test statistic evaluated at a given μ . This form for the *p-value* starts from an initial value of the nuisance parameters but

becomes independent of the nuisance parameters in the large-sample limit. By convention, signal hypotheses are said to be excluded at 95% confidence level (95% CL) if

$$p_\mu < 0.05 \quad (7.7)$$

Confidence levels are not used directly in this work for the following reason: it is possible (though unlikely) to falsely exclude a signal hypothesis to which the analysis has little or no sensitivity. The CL_s [215, 216] method averts this by reducing the signal hypothesis CL by the background-only CL:

$$CL_s = \frac{CL_{s+b}}{CL_b} = \frac{p_{s+b}}{1 - p_b} \quad (7.8)$$

While the CL_s is *not* technically a CL, in this work hypotheses are considered to have been excluded if $CL_s \leq 0.05$, and the term CL is always taken to mean CL_s from now on. Limits obtained in the CL_s formalism are more conservative than those obtained from CL_{s+b} , since $CL_s \geq CL_{s+b}$ for all s and b , reducing the risk of a false exclusion. In the analyses discussed in this work, p -values are usually evaluated by MC sampling of the probability density function for the test statistic. Exact formulae [217] for q_μ and $f(q_\mu|\mu)$ exist and were used to validate the results of MC sampling. These formulae are not used for the final results, since they are only applicable in the limit of a large number of signal and background events, a condition not generally satisfied for the signal regions in this work.

7.3.4 Treatment of systematic uncertainties

The different systematic uncertainties may be correlated between different regions and/or processes (top, WZ/γ^* etc). In each case, different nuisance parameters are introduced into the likelihood used for limit setting. The correlations are treated by introducing four classes of nuisance parameter:

1. A global uncertainty affecting all processes and regions equally: this is the case for the different object energy scales and resolutions, for example. In this case, a single nuisance parameter η is introduced for each SR and process.
2. An uncertainty correlated between regions but not processes: in this case a new nuisance parameter is introduced for every region.
3. An uncertainty correlated between processes but not regions: in this case a new nuisance parameter is introduced for every process.

4. A fully uncorrelated uncertainty: in this case no correlation between processes and regions is expected, and a new nuisance parameter for each process and region is introduced.

The correlations between regions and processes for each nuisance parameter are as follows:

1. All uncertainties relating to electron, muon and tau energy scales, resolutions and identification, triggers, b -tagging, E_T^{miss} , and luminosity are correlated between regions and processes.
2. Uncertainties relating to the electron and muon fake rates are correlated between regions only.
3. Jet energy scale and resolution uncertainties are correlated between processes only.
4. Systematic and statistical uncertainties on the reducible background estimate are uncorrelated.

Since $\mu S(\boldsymbol{\nu})$ and $B(\boldsymbol{\nu})$ are known only at three values of $\boldsymbol{\nu}$ from auxiliary measurements in control regions, interpolation is used to evaluate $\mu S(\boldsymbol{\nu})$ and $B(\boldsymbol{\nu})$ at other values of $\boldsymbol{\nu}$.

7.3.5 Simultaneous fit

In the 2011 analysis, the largest irreducible background, WZ , was normalised to a control region as discussed in Section 6.2). The WZ MC was normalised to the data yield in the WZNR, and the normalisation factor was applied to the WZ yields quoted in tables and figures, both for signal and validation regions. However, in the setting of exclusion limits, the overall WZ yield was allowed to vary simultaneously in the WZNR and SR and then normalised to the value best matching the data in the WZNR and SR. Exclusion limits were also produced while keeping WZ constant in order to verify that no bias was introduced by this procedure.

The procedure led to a decrease in sensitivity to SUSY scenarios with on-shell Z/W decays in the 2011 analysis, as seen in Figure 7.16(b): this should be compared to Figure 7.16(b) from the 2012 analysis, where the normalisation method was not used.

7.3.6 Combining signal regions

If a set of N SRs are disjoint (as defined in Section 5.3.8) then their combined likelihood is given by

$$L(\mu, \boldsymbol{\nu}) = \prod_i^N L_i(\mu, \boldsymbol{\nu}_i) \quad (7.9)$$

Here ν_i represents the set of nuisance parameters in SR i . Note that μ takes the same value in each sub-likelihood: this is clearly true in the case of a hypothesis like SUSY, which is either realised or not realised in Nature. Correlations between nuisance parameters are accounted for in the same way as for a single SR. A combination of SRs of this type is referred to as a *statistical combination*. If an SR is insensitive to the signal hypothesis, its likelihood is no longer a function of μ so does not contribute to the overall likelihood maximisation.

If SRs are not disjoint, it is not possible to create a combined likelihood: a different approach is required. One option is to evaluate the p -value for each SUSY grid point considered separately for each SR, and then choose the region with the lowest p -value for each point. This is referred to as a *graphical combination*, since the overall effect is similar to simply joining up the two 95% CL contours in the exclusion plane. Statistical combinations are denoted in equations by \otimes , while graphical combinations are denoted by **OR**. Other approaches to the combination of p -values are given in [218].

7.3.7 Model-independent limits

In addition to testing the agreement of the data with specific signal hypotheses, the agreement of the data with the background-only hypothesis ($\mu = 0$) was tested for each analysis. Upper limits are then derived by evaluating p_μ at a large (and hence easily excluded) starting value of μ until p_μ exceeds 0.05. This is interpreted as an upper limit on the visible cross section, defined as the total signal cross section multiplied by the detector acceptance and analysis efficiency:

$$\sigma_{\text{vis}} = \text{Signal cross section} \times \text{Detector acceptance} \times \text{Analysis efficiency} \quad (7.10)$$

where the signal cross section is given by $\mu S/\mathcal{L}$. The detector acceptance contains the fiducial restrictions on object reconstruction or identification (η , p_T thresholds etc), while the analysis efficiency contains the specific kinematic and object multiplicity cuts used in the analysis. The 95% CL limits on σ_{visible} are summarised for the 2012 dataset in Table 7.7.

7.4 Interpretation in SUSY scenario grids

The signal grids defined in Section 4.3.1.2 and 4.3.2.2 define SUSY phenomenology for specific scenarios. For each point in these grids, the CL_s limit on the number of expected events for the point is calculated, with both the expected and observed number of data

Selection	SRnoZa	SRnoZb	SRnoZc	SRZa	SRZb	SRZc
Σ SM	96 ± 19	29 ± 6	4.4 ± 1.8	249 ± 35	22 ± 5	6.3 ± 1.5
Data	101	32	5	273	23	6
<i>p</i> -value	0.41	0.37	0.40	0.23	0.44	0.5
N_{signal} excluded (exp)	39.3	16.3	6.2	67.9	13.2	6.7
N_{signal} excluded (obs)	41.8	18.0	6.8	83.7	13.9	6.5
σ_{visible} excluded (exp) [fb]	1.90	0.79	0.30	3.28	0.64	0.32
σ_{visible} excluded (obs) [fb]	2.02	0.87	0.33	4.04	0.67	0.31

Table 7.7: Model independent limits in the 2012 analysis.

events. No nuisance parameters are applied to the signal points. Delaunay interpolation [219] is then used to create contours of 95% CL_s exclusion, in both the expected and observed cases, with associated $\pm 1\sigma$ bands. The two bands are defined as follows:

- The uncertainty band on the observed limit (shown in solid yellow) is calculated by considering the effect of $\pm 1\sigma$ variation of the SUSY signal uncertainty only.
- The uncertainty band on the expected limit (shown as a dashed red band) is calculated by considering the effect of $\pm 1\sigma$ variation of the background model uncertainties only.

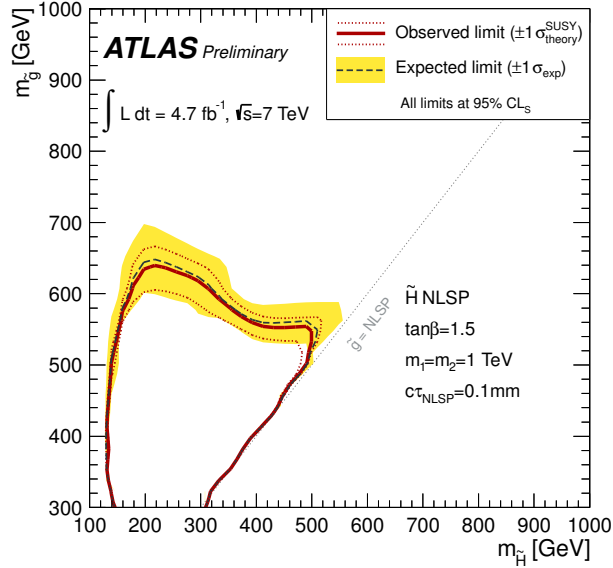
Only considering theoretical uncertainties on the observed limit allows for a straightforward comparison of sensitivity to new signals and is standard practice between ATLAS and CMS [212].

In the next few sections, interpretations in different SUSY models (with theoretical parameters defined in Section 2.4 and model details defined in Section 4.3.1.2 and 4.3.2.2) are shown.

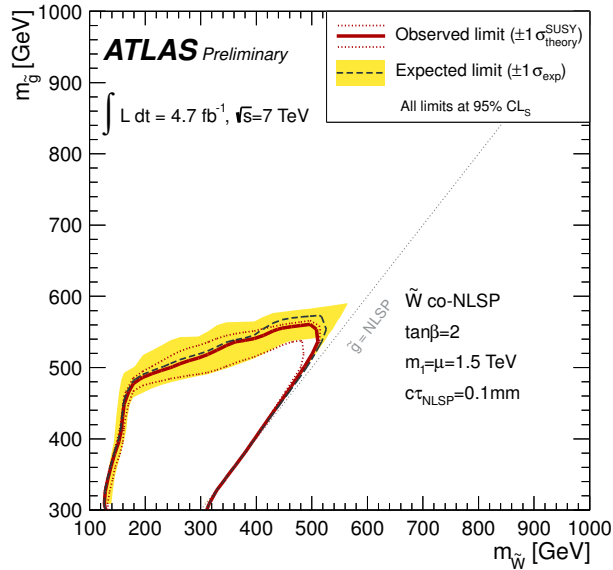
7.4.1 Interpretation in GGM models

The 2011 results, while optimised principally for simplified models and the pMSSM, were also interpreted in the GGM models defined in Section 2.4.1.1, since these also have three-lepton final states. SR2 provides the best sensitivity to the GGM, due to on-shell Z bosons in the higgsino and wino decays. The exclusion limits are shown in Figure 7.12. In the higgsino model (a), the gluino is excluded with masses up to 600 GeV for higgsino masses up to 500 GeV. In the wino co-NLSP model (b), the gluino is excluded with masses up to 520 GeV for common wino co-NLSP masses below 480 GeV. The higgsino NLSP results have been superseded by more optimised ATLAS analyses with jet-rich SRs[220, 221], while

the wino co-NLSP results are, to the best of my knowledge, the only LHC results in such a scenario.



(a) Higgsino NLSP



(b) Wino co-NLSP

Figure 7.12: Excluded regions in two GGM models. Result made public in [197].

7.4.2 Interpretation in the phenomenological MSSM

As discussed in Section 4.3.1.2, three pMSSM grids with $M_1 = 100$ GeV, $M_1 = 140$ GeV and $M_1 = 250$ GeV are defined. Limits in these scenarios were derived in the 2011 analysis.

Analyses with exactly two light leptons (two-lepton analyses) have complementary sensitivities in the pMSSM. A two-lepton analysis was performed with the full 2011 dataset, and interpreted in a variety of scenarios including the pMSSM [195]. The important features of the two lepton analysis [195] are summarised below and the procedure used to combine the two analyses is discussed in Section 7.4.2.1.

7.4.2.0.1 Two-lepton analysis Only one of the two-lepton signal regions (referred to as SR- m_{T2} in [195] and SR2L here) has sensitivity to the direct chargino-chargino production process

$$\tilde{\chi}_1^\pm \tilde{\chi}_1^\mp \rightarrow (\ell^\pm \nu \tilde{\chi}_1^0 \ell^\mp \nu \tilde{\chi}_1^0). \quad (7.11)$$

The estimation of backgrounds for the two-lepton analysis is generally similar to that in the three-lepton analysis: the matrix method is used to estimate the relative contributions of real and fake leptons, as detailed in Section 6.1.2, and the choice of control regions for fake lepton estimation is similar. In SR2L, 20.4 ± 4.7 events were predicted, with 15 observed.

7.4.2.1 Combination of 2011 two and three-lepton pMSSM results

SR2L is statistically combined with the 2011 SR1a and SR1b, as well as the WZNR. The different nuisance parameters in the two- and three-lepton analyses were treated as correlated/uncorrelated as summarised in Section 7.3.4. The overall yield of WZ is allowed to float in the three-lepton signal regions, but not the two-lepton signal regions, where it is not a significant background. Since the 2011 SR1a and SR1b are not disjoint, the total combinations

$$\text{SR23La} = (\text{SR1a} \otimes \text{SR2L} \otimes \text{WZNR}) \quad (7.12)$$

and

$$\text{SR23Lb} = (\text{SR1b} \otimes \text{SR2L} \otimes \text{WZNR}) \quad (7.13)$$

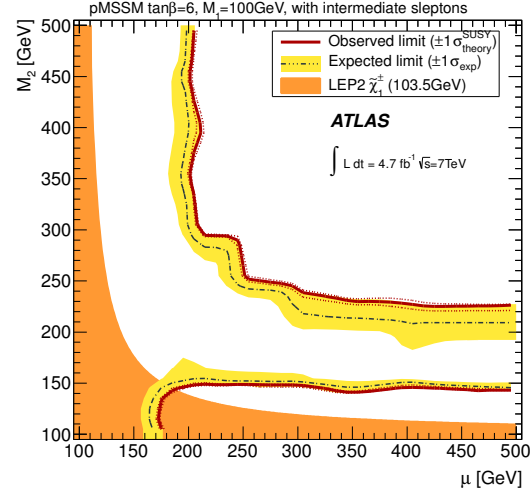
are also not disjoint. The graphical combination

$$\text{SR23La OR SR23Lb} \quad (7.14)$$

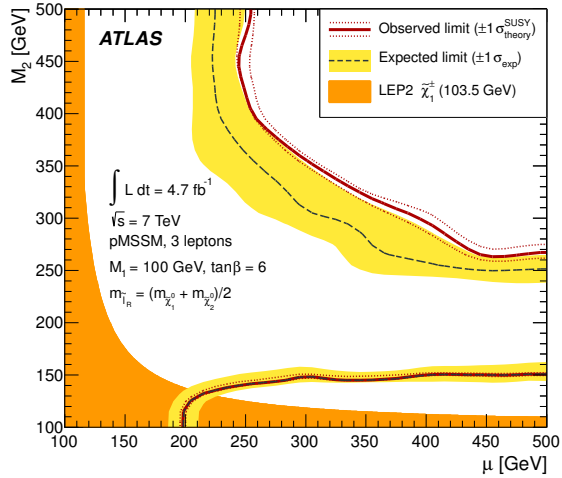
is therefore used to obtain the final results.

Figures 7.13, 7.14 and 7.15 show the two- and three-lepton limits separately, followed by the combined exclusion limits for the $M_1 = 100$ GeV, $M_1 = 140$ GeV and $M_1 = 250$ GeV respectively. As M_1 and μ increase, the cross section for gaugino production decreases

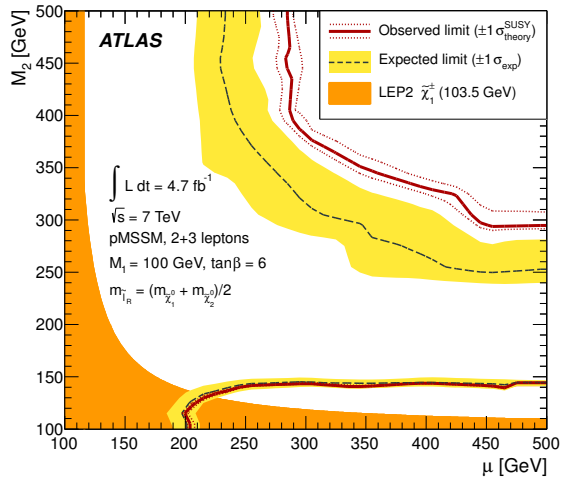
as shown in Figure 7.11 - limits at large M_1 and μ are therefore less stringent. However, when μ exceeds M_1 and M_2 , the gaugino mass becomes independent of μ : in this case the limit is also independent of μ , as seen in the lower right-hand corner of Figure 7.13b/c and 7.14b/c. Since $\mu < M_1$ for most generated points in the $M_1 = 250$ GeV grid, this effect does not occur.



(a) Two-lepton analysis

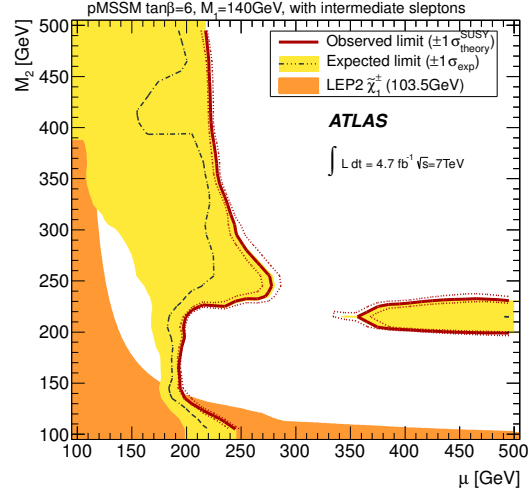


(b) Three-lepton analysis

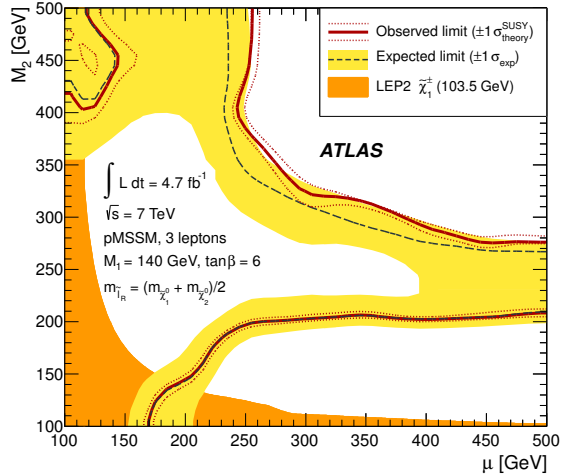


(c) Combination

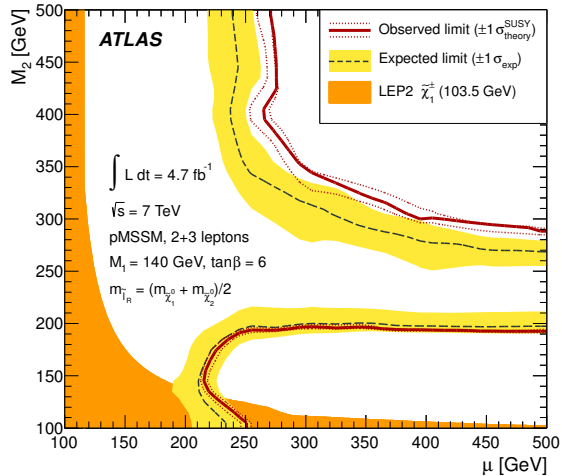
Figure 7.13: Excluded regions in the pMSSM scenario with $M_1 = 100 \text{ GeV}$, with the two-lepton (a), three-lepton (b) and statistically combined (c) two- and three-lepton signal regions. These plots were produced by other analysis group members. Published in [195] (a) and [196] (b,c).



(a) Two-lepton analysis

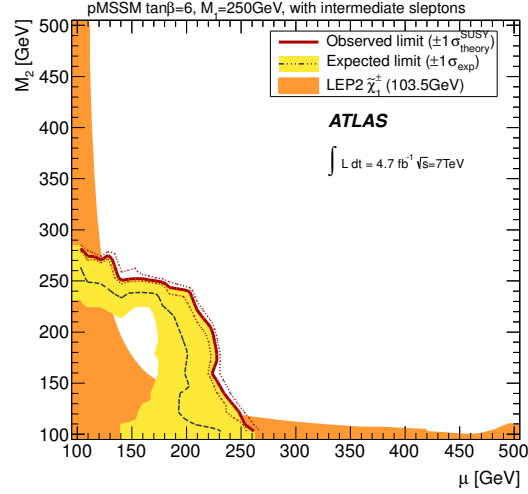


(b) Three-lepton analysis

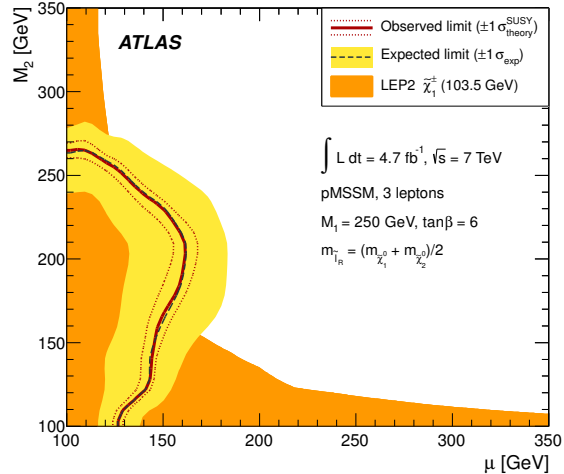


(c) Combination

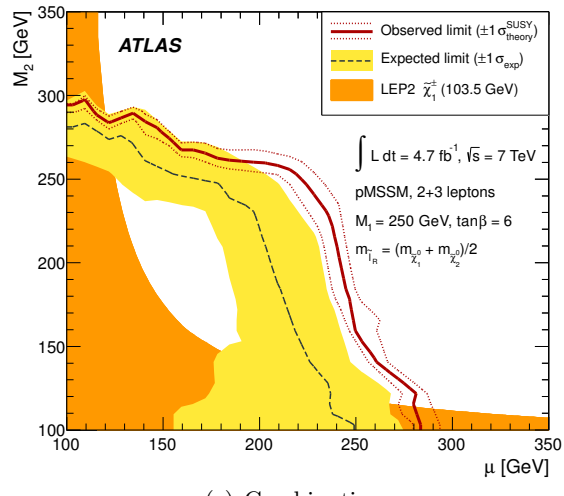
Figure 7.14: Excluded regions in the pMSSM scenario with $M_1 = 140 \text{ GeV}$, with the two-lepton (a), three-lepton (b) and statistically combined (c) two- and three-lepton signal regions. These plots were produced by other analysis group members. Published in [195] (a) and [196] (b,c). Published in [196].



(a) Two-lepton analysis



(b) Three-lepton analysis



(c) Combination

Figure 7.15: Excluded regions in the pMSSM scenario with $M_1 = 250 \text{ GeV}$, with the two-lepton (a), three-lepton (b) and statistically combined (c) two- and three-lepton signal regions. These plots were produced by other analysis group members. Published in [195] (a) and [196] (b,c).

7.4.3 Interpretation in simplified models of direct gaugino production

In the scenario with sleptons (Model A, shown in Figure 7.17b)), degenerate $\tilde{\chi}_1^\pm$ and $\tilde{\chi}_2^0$ masses up to 600 GeV are excluded for $\tilde{\chi}_1^0$ masses up to 200 GeV. The production cross section falls as the gaugino masses increase, explaining the decrease in sensitivity in the upper sections of the plots. In the scenario with W and Z boson decays (Model B, shown in Figure 7.17b), the limits are less stringent: degenerate $\tilde{\chi}_1^\pm$ and $\tilde{\chi}_2^0$ masses up to 320 GeV are excluded for $\tilde{\chi}_1^0$ masses below 100 GeV. Additionally, there is a region where $m_{\tilde{\chi}_2^0} - m_{\tilde{\chi}_1^\pm} = m_Z$, leading to on-shell Z boson decays: points near this line are very difficult to distinguish from SM WZ , even with the dedicated SRnoZb. In both models, only decays with $m_{\tilde{\chi}_2^0}, m_{\tilde{\chi}_1^\pm} > m_{\tilde{\chi}_1^0}$ are simulated: the dashed grey diagonal line indicates the line of equality between the masses. As the mass splitting between the gauginos decreases (near to this line) it becomes increasingly difficult to exclude points. SRnoZc (in particular the cut $m_{\ell\ell} < 60$ GeV) was developed in order to improve sensitivity in this area.

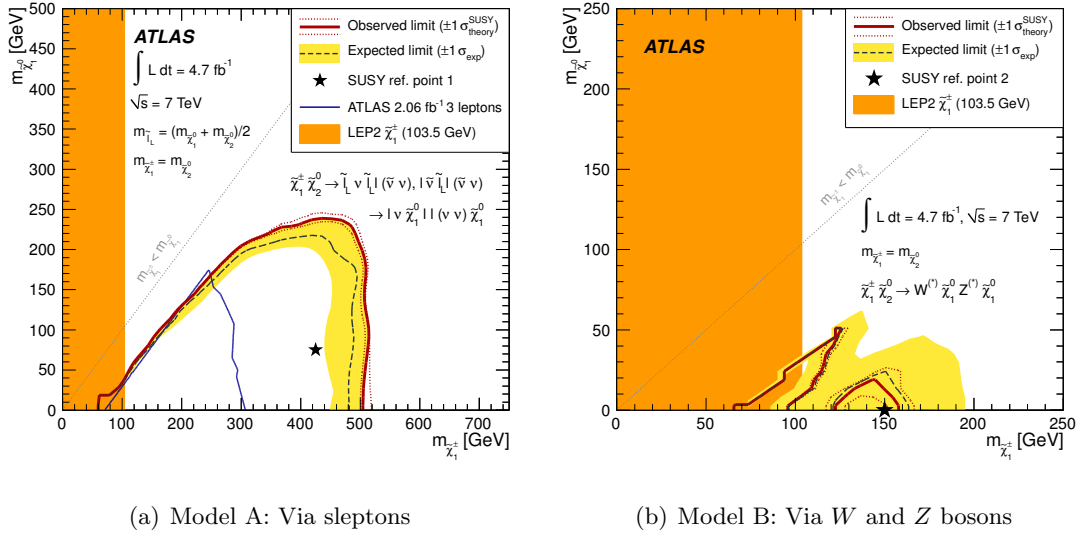


Figure 7.16: Excluded regions in simplified models of direct gaugino production in the 2012 analysis. These plots were produced by other analysis group members. Published in [3].

7.4.4 Summary of interpretations

7.4.4.1 GGM

In the higgsino model, the gluino is excluded with masses up to 600 GeV for higgsino masses up to 500 GeV. In the wino co-NLSP model, the gluino is excluded with masses

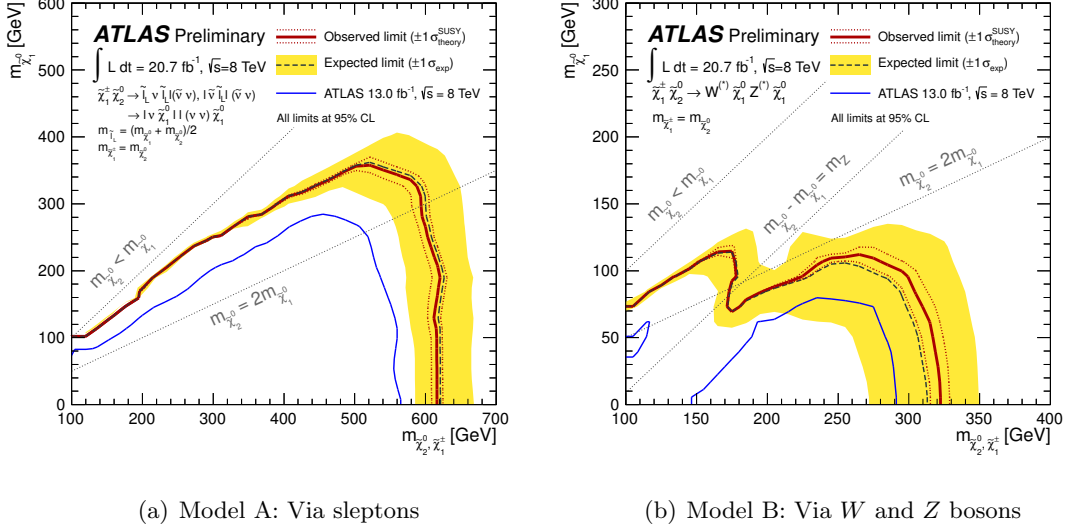


Figure 7.17: Excluded regions in simplified models of direct gaugino production in the 2012 analysis. These plots were produced by other analysis group members. Result made public in [3].

up to 520 GeV for common wino co-NLSP masses below 480 GeV.

7.4.4.2 pMSSM

In the $M_1 = 100$ GeV scenario, values of μ up to 200 GeV are excluded for all values of M_2 , while values of M_2 between 150 and 300 GeV are excluded for all values of μ . In the $M_1 = 140$ GeV scenario, values of μ up to 200 GeV are again excluded for all values of M_2 , while values of M_2 between 200 and 300 GeV are excluded for all values of μ . The limits in the $M_1 = 250$ GeV are less stringent, since $M_1 > M_2, \mu$ for most points. In this scenario, M_2 and μ of up to 300 GeV are excluded for low μ and M_2 respectively.

7.4.4.3 Simplified models

In the scenario with sleptons (Model A, shown in Figure 7.17b)), degenerate $\tilde{\chi}_1^\pm$ and $\tilde{\chi}_2^0$ masses up to 600 GeV are excluded for $\tilde{\chi}_1^0$ masses up to 200 GeV. In the scenario with W and Z boson decays (Model B), degenerate $\tilde{\chi}_1^\pm$ and $\tilde{\chi}_2^0$ masses up to 320 GeV are excluded for $\tilde{\chi}_1^0$ masses below 100 GeV.

7.4.5 Comparison with CMS

A similar analysis ([1]) was performed by the CMS collaboration with 9.2 fb $^{-1}$ of data. Results are also binned in $m_{\ell\ell}$, m_T and E_T^{miss} , with a total of 36 signal and validation

Analysis	ATLAS	CMS
Model A chargino mass observed limit	600 GeV	650 GeV
Model B chargino mass observed limit	320 GeV	270 GeV

Table 7.8: Comparison of the analysis presented here (“ATLAS”) and a similar search by the CMS collaboration. CMS data taken from [1].

regions to compare to the 6 SRs and 6 VRs used in the 2012 search presented here. All signal regions are statistically combined to give final limits. A comparison of the observed limits on chargino production in Model A and Model B for both analyses is shown in Table 7.8.

7.4.6 Implications for dark matter searches

Direct dark matter experiments are usually interpreted as a function of the mass and nucleon-interaction cross section of the WIMP, which, as discussed in Section 2.2.2, may be identified with the SUSY LSP. While SUSY particles may be responsible for all dark matter, it is also possible that other particles such as axions [222] make up some proportion of the dark matter spectrum. Cross section limits are usually expressed in cms^{-2} - the most stringent limits from the XENON experiment [50], at the time of writing, are $< 3.5 \text{ cms}^{-2}$ at 90% CL for a WIMP mass of 45 GeV. This is an order of magnitude lower than the exclusion limits found in this work, which are of the order of 1 fb^{-1} . The results presented here are complementary to direct dark matter searches, since the processes involved in WIMP-nucleon interactions are distinct.

7.4.7 Implications for supersymmetry

The MSSM, the simplest incarnation of SUSY, is a theory with more than 100 free parameters, as previously discussed. The exclusion limits found in this work are found only in two-dimensional planes of a pair of parameters, or as cross sections for any process with a final state matching the signal region used. The results presented here have been used by other authors in combination with other direct and indirect constraints on supersymmetric models [223, 224]. Notably, the viable points for the pMSSM were reduced by roughly 1/3 when taking this and other results into account [225].

7.5 Conclusions

Searches for supersymmetry in $\sqrt{s} = 7$ TeV and 8 TeV proton-proton collisions with the LHC at the ATLAS detector were performed. Events with exactly three light leptons (electrons or muons) and missing transverse energy were selected, since this can be a striking signature of supersymmetry with low background. Background Standard Model processes were simulated by Monte Carlo event generators and several major backgrounds were estimated using data-driven techniques. Before looking at signal regions (selections of events with exactly three light leptons and significant missing transverse energy), the agreement between data and background prediction was validated with selections distinct from the signal regions. With the observation of good agreement between the data and background prediction, the data in the signal regions were analysed. No significant excess was recorded in any of the analyses performed: the results were therefore interpreted as lower bounds on the masses of supersymmetric particles in a variety of different model scenarios.

Appendix A

Details of MC samples

Details of MC samples used in the 2012 analysis are given here. When cross sections (σ) are given at NLO, there is a k -factor ($\sigma(\text{NLO})/\sigma(\text{LO})$) to convert the LO cross section. If a generator filter is applied (for example, requiring exactly two leptons with $p_T > 7 \text{ GeV}$), there is a corresponding factor to convert the cross section without this filter to the appropriate number for the sample. This is known as the filter efficiency ϵ . To summarise, the full NLO cross section is given by

$$\sigma(\text{NLO}) = \sigma(\text{LO}) \times k \times \epsilon \quad (\text{A.1})$$

All three factors, or fewer as appropriate, may be found in the following tables, as well as the effective integrated luminosity ($\int \mathcal{L} dt$) for the samples used.

Process	σ [fb]	k -factor	$\int \mathcal{L} dt \text{ fb}^{-1}$
WWW (167006)	5.10	1.5	9800
ZWW (167007)	1.55	1.5	32250
ZZZ (167008)	0.33	1.5	151500

Table A.1: The triboson samples used for this thesis. The LO cross section and k -factors (for NLO normalisation) are reported. The integrated luminosities corresponding to the total statistics in each sample are also given.

Process	$\int \mathcal{L} dt \text{ fb}^{-1}$		
$t\bar{t} W(\ell\nu)$ Np0 ALPGEN (174233)	2.7×10^{-2}	1.255	443.4
$t\bar{t} W(\ell\nu)$ Np1 ALPGEN (174234)	1.8×10^{-2}	1.255	443.0
$t\bar{t} W(\ell\nu)$ Np2 ALPGEN (174235)	9.5×10^{-3}	1.255	421.0
$t\bar{t} W(\ell\nu)$ Np3+ ALPGEN (174236)	6.5×10^{-3}	1.255	366.1
$t\bar{t} W(qq)$ Np0 ALPGEN (174238)	5.4×10^{-2}	1.255	440.1
$t\bar{t} W(qq)$ Np1 ALPGEN (174239)	3.7×10^{-2}	1.255	432.9
$t\bar{t} W(qq)$ Np2 ALPGEN (174240)	1.9×10^{-2}	1.255	415.5
$t\bar{t} W(qq)$ Np3+ ALPGEN (174241)	1.3×10^{-2}	1.255	390.4
$t\bar{t} Z(\nu\nu)$ Np0 ALPGEN (174243)	1.1×10^{-2}	1.277	740.0
$t\bar{t} Z(\nu\nu)$ Np1 ALPGEN (174244)	1.0×10^{-2}	1.277	390.0
$t\bar{t} Z(\nu\nu)$ Np2 ALPGEN (174245)	6.9×10^{-3}	1.277	226.0
$t\bar{t} Z(\nu\nu)$ Np3+ ALPGEN (174246)	5.0×10^{-3}	1.277	236.3
$t\bar{t} Z(\ell\ell)$ Np0 ALPGEN (174248)	7.9×10^{-3}	1.277	496.6
$t\bar{t} Z(\ell\ell)$ Np1 ALPGEN (174249)	7.7×10^{-3}	1.277	511.7
$t\bar{t} Z(\ell\ell)$ Np2 ALPGEN (174250)	5.3×10^{-3}	1.277	443.8
$t\bar{t} Z(\ell\ell)$ Np3+ ALPGEN (174251)	4.0×10^{-3}	1.277	393.7

Table A.2: The ALPGEN $t\bar{t} + V$ samples used for this thesis. The LO cross section are k -factors (for NLO normalisation) are reported. The integrated luminosities corresponding to the total statistics in each sample are also given.

Process (ID)	$\int \mathcal{L} dt \text{ fb}^{-1}$			
ZZ (4ℓ) SHERPA (126894)	8.74	1.00	1	167.2
ZW (3ℓ) SHERPA (126893)	9.75	1.05	1	258.6
ZZ ($2\ell 2\nu$) SHERPA (126895)	0.50	1.05	1	1465.2
WW ($2\ell 2\nu$) SHERPA (126892)	5.50	1.06	1	454.6
(S) ZZ ($4e$) POWHEG (126937)	0.08	1	0.91	8600.6
(S) ZZ ($2e 2\mu$) POWHEG (126938)	0.18	1	0.83	4131.3
(S) ZZ ($2e 2\tau$) POWHEG (126939)	0.18	1	0.58	5868.7
(S) ZZ (4μ) POWHEG (126940)	0.08	1	0.91	8554.6
(S) ZZ ($2\mu 2\tau$) POWHEG (126941)	0.18	1	0.59	5825.0
(S) ZZ (4τ) POWHEG (126942)	0.08	1	0.11	36813.5
(S) WZ ($e^- \bar{\nu}_e e^+ e^-$) POWHEG (129477)	1.41	1	0.29	458.4
(S) WZ ($e^- \bar{\nu}_e \mu^+ \mu^-$) POWHEG (129478)	0.94	1	0.35	575.1
(S) WZ ($e^- \bar{\nu}_e \tau^+ \tau^-$) POWHEG (129479)	0.17	1	0.17	2609.2
(S) WZ ($\mu^- \bar{\nu}_\mu e^+ e^-$) POWHEG (129480)	1.40	1	0.29	462.7
(S) WZ ($\mu^- \bar{\nu}_\mu \mu^+ \mu^-$) POWHEG (129481)	0.95	1	0.35	567.0
(S) WZ ($\mu^- \bar{\nu}_\mu \tau^+ \tau^-$) POWHEG (129482)	0.17	1	0.17	2581.2
(S) WZ ($\tau^- \bar{\nu}_\tau e^+ e^-$) POWHEG (129483)	1.40	1	0.14	377.1
(S) WZ ($\tau^- \bar{\nu}_\tau \mu^+ \mu^-$) POWHEG (129484)	0.94	1	0.18	443.7
(S) WZ ($\tau^- \bar{\nu}_\tau \tau^+ \tau^-$) POWHEG (129485)	0.17	1	0.06	1888.8
(S) WZ ($e^+ \nu_e e^+ e^-$) POWHEG (129486)	0.98	1	0.30	652.9
(S) WZ ($e^+ \nu_e \mu^+ \mu^-$) POWHEG (129487)	0.64	1	0.35	842.2
(S) WZ ($e^+ \nu_e \tau^+ \tau^-$) POWHEG (129488)	0.11	1	0.16	4230.4
(S) WZ ($\mu^+ \nu_\mu e^+ e^-$) POWHEG (129489)	0.94	1	0.30	682.0
(S) WZ ($\mu^+ \nu_\mu \mu^+ \mu^-$) POWHEG (129490)	0.65	1	0.35	826.9
(S) WZ ($\mu^+ \nu_\mu \tau^+ \tau^-$) POWHEG (129491)	0.11	1	0.16	4216.1
(S) WZ ($\tau^+ \nu_\tau e^+ e^-$) POWHEG (129492)	0.94	1	0.15	548.5
(S) WZ ($\tau^+ \nu_\tau \mu^+ \mu^-$) POWHEG (129493)	0.64	1	0.19	637.4
(S) WZ ($\tau^+ \nu_\tau \tau^+ \tau^-$) POWHEG (129494)	0.11	1	0.06	3029.6

Table A.3: Diboson samples used for this thesis. The LO cross section, k -factors (for NLO normalisation) and filter efficiencies are reported. The integrated luminosities corresponding to the total statistics in each sample are also given. Samples labelled with (S) are used for systematics studies only.

Process	$\int \mathcal{L} dt \text{ fb}^{-1}$			
$t\bar{t}$ not all-hadronic Powheg (105861)	238.06	1	0.54	231.8
Wt MC@NLO (108346)	20.66	1.08	1	78.9
t -channel $e\nu$ AcerMC (117360)	8.60	1.10	1	31.6
t -channel $\mu\nu$ AcerMC (117361)	8.60	1.1	1	31.6
t -channel $\tau\nu$ AcerMC (117362)	8.60	1.1	1	31.6
s -channel $e\nu$ MC@NLO (108343)	0.56	1.07	1	278.9
s -channel $\mu\nu$ MC@NLO (108344)	0.56	1.07	1	278.9
s -channel $\tau\nu$ MC@NLO (108345)	0.56	1.07	1	278.7

Table A.4: Top-quark samples used for this thesis. The samples are generated with 0.111 $W \rightarrow \ell\nu$ branching ratio; for setting the k -factors the $\text{BR}(W \rightarrow \ell\nu)$ reference of 0.1080 is used (in agreement with the PDG2010 value). The $t\bar{t}$ cross section is normalised to approximate NNLO. The integrated luminosities corresponding to the total statistics in each sample are also given.

Process	$\int \mathcal{L} dt \text{ fb}^{-1}$						
$Z + \text{jets}$	(ee+Np0) (117650)	848.29	7.8	Z+jets low mass	(ee+Np0) (146830)	4154.56	0.2
	(ee+Np1) (117651)	207.21	6.4		(ee+Np1) (146831)	129.99	2.3
	(ee+Np2) (117652)	69.44	5.8		(ee+Np2) (146832)	63.05	7.5
	(ee+Np3) (117653)	18.36	6.0		(ee+Np3) (146833)	13.50	10.7
	(ee+Np4) (117654)	4.64	6.5		(ee+Np4) (146834)	3.09	11.7
	(ee+Np5) (117655)	1.42	7.1		(ee+Np5) (146835)	0.83	96.2
	($\mu\mu$ +Np0) (117660)	848.31	7.8		($\mu\mu$ +Np0) (146840)	4154.44	0.2
	($\mu\mu$ +Np1) (117661)	207.46	6.4		($\mu\mu$ +Np1) (146841)	129.93	2.3
	($\mu\mu$ +Np2) (117662)	69.39	5.8		($\mu\mu$ +Np2) (146842)	63.01	7.5
	($\mu\mu$ +Np3) (117663)	18.40	6.0		($\mu\mu$ +Np3) (146843)	13.43	10.8
	($\mu\mu$ +Np4) (117664)	4.61	6.5		($\mu\mu$ +Np4) (146844)	3.11	11.7
	($\mu\mu$ +Np5) (117665)	1.41	7.1		($\mu\mu$ +Np5) (146845)	0.83	96.2
	($\tau\tau$ +Np0) (117670)	848.24	7.8		($\tau\tau$ +Np0) (146850)	4154.44	0.2
	($\tau\tau$ +Np1) (117671)	207.48	6.4		($\tau\tau$ +Np1) (146851)	129.92	2.3
	($\tau\tau$ +Np2) (117672)	69.18	5.9		($\tau\tau$ +Np2) (146852)	63.00	7.5
	($\tau\tau$ +Np3) (117673)	18.30	6.0		($\tau\tau$ +Np3) (146853)	13.53	10.7
	($\tau\tau$ +Np4) (117674)	4.66	6.4		($\tau\tau$ +Np4) (146854)	3.10	70.5
	($\tau\tau$ +Np5) (117675)	1.39	7.2		($\tau\tau$ +Np5) (146855)	0.83	96.6
$Z + bb$	(ee+Np0) (110817)	9.49	15.8	$Z + cc$	(ee+Np0) (110805)	17.83	33.9
	(ee+Np1) (110818)	3.82	21.0		(ee+Np1) (110806)	8.51	30.5
	(ee+Np2) (110819)	1.34	33.5		(ee+Np2) (110807)	3.58	30.7
	(ee+Np3) (110820)	0.58	7.8		(ee+Np3) (110808)	1.39	28.8
	($\mu\mu$ +Np0) (110821)	9.49	15.8		($\mu\mu$ +Np0) (110809)	17.84	33.6
	($\mu\mu$ +Np1) (110822)	3.79	21.1		($\mu\mu$ +Np1) (110810)	8.49	31.2
	($\mu\mu$ +Np2) (110823)	1.35	33.5		($\mu\mu$ +Np2) (110811)	3.58	32.2
	($\mu\mu$ +Np3) (110824)	0.60	8.3		($\mu\mu$ +Np3) (110812)	1.39	28.9
	($\tau\tau$ +Np0) (110825)	9.48	15.8		($\tau\tau$ +Np0) (110813)	17.84	33.6
	($\tau\tau$ +Np1) (110826)	3.81	21.0		($\tau\tau$ +Np1) (110814)	8.50	31.2
	($\tau\tau$ +Np2) (110827)	1.35	33.3		($\tau\tau$ +Np2) (110815)	3.59	32.1
	($\tau\tau$ +Np3) (110828)	0.58	8.6		($\tau\tau$ +Np3) (110816)	1.38	29.0

Table A.5: ALPGEN $Z/\gamma^* + \text{jets}$ samples used for this thesis. The integrated luminosities corresponding to the total statistics in each sample are also given.

Process	$\int \mathcal{L} dt \text{ fb}^{-1}$					
$W+\text{jets}$	($e\nu+Np0$) (117680)	9300.36	0.4	(Np0) (126601)	867.46	7.5
	($e\nu+Np1$) (117681)	2047.68	1.2	(Np1) (126602)	313.46	6.6
	($e\nu+Np2$) (117682)	619.05	6.1	$W+c$	(Np2) (126603)	81.88
	($e\nu+Np3$) (117683)	167.62	6.0		(Np3) (126604)	18.77
	($e\nu+Np4$) (117684)	42.63	5.9		(Np4) (126605)	5.43
	($e\nu+Np5$) (117685)	12.99	5.4			
	($\mu\nu+Np0$) (117690)	9296.48	0.4		(Np0) (126606)	163.53
	($\mu\nu+Np1$) (117691)	2049.06	1.2		(Np1) (126607)	164.23
	($\mu\nu+Np2$) (117692)	618.67	6.1	$W+cc$	(Np2) (126608)	92.31
	($\mu\nu+Np3$) (117693)	167.44	6.0		(Np3) (126609)	41.07
$W+\text{bb}$	($\mu\nu+Np4$) (117694)	42.67	6.0			
	($\mu\nu+Np5$) (117695)	13.05	5.0			
	($\tau\nu+Np0$) (117700)	9299.11	0.4		(Np0) (110801)	59.73
	($\tau\nu+Np1$) (117701)	2050.20	1.2		(Np1) (110802)	52.05
	($\tau\nu+Np2$) (117702)	618.64	6.1		(Np2) (110803)	27.06
	($\tau\nu+Np3$) (117703)	167.43	6.0		(Np3) (110804)	14.32
	($\tau\nu+Np4$) (117704)	42.59	5.9			
	($\tau\nu+Np5$) (117705)	13.19	4.9			

Table A.6: ALPGEN $W+\text{jets}$ samples used for this thesis. The integrated luminosities corresponding to the total statistics in each sample are also given.

Appendix B

Tables of systematics

In this appendix, the full systematic uncertainties on the irreducible backgrounds in the 2012 analysis are given in tabular form.

	Triboson	ZZ	$t\bar{t}V$	WZ	Total
SRZa					
Expected events	0.54	8.88	0.43	235.05	244.9
Electron energy scale	2.68,-2.12%	0.52,-2.99%	0.0,0.0%	0.39,-0.19%	0.4,-0.3%
Electron energy ratio	-0.39,0.49%	1.63,0.91%	0.0,26.64%	0.06,0.04%	0.11,0.12%
Muon spectrometer track p resolution	1.17,-0.28%	0.48,0.15%	26.64,0.0%	-0.13,0.11%	-0.06,0.11%
Muon inner detector track p resolution	0.71,1.18%	0.0,0.15%	0.0,0.0%	-0.03,0.15%	-0.02,0.15%
Jet energy scale	3.3,2.64%	1.34,7.25%	26.64,21.24%	1.71,1.04%	1.74,1.3%
Jet energy resolution	2.95,2.95%	7.76,7.76%	19.64,19.64%	2.88,2.88%	3.08,3.08%
E_T^{miss} soft term scale	-1.35,0.32%	10.88,-6.69%	0.0,0.0%	2.61,-2.35%	2.9,-2.5%
E_T^{miss} soft term resolution	-0.5,-0.5%	1.95,1.95%	-0.94,-0.94%	-0.24,-0.24%	-0.16,-0.16%
Trigger	5.0,-5.0%	5.0,-5.0%	5.0,-5.0%	5.0,-5.0%	5.0,-5.0%
b -tagging	2.56,-2.63%	3.33,-3.43%	46.28,-56.32%	3.07,-3.17%	3.15,-3.28%
Electron ID/reconstruction efficiency	0.36,-4.72%	0.37,-3.61%	0.07,-6.06%	0.41,-4.98%	0.41,-4.93%
Tau energy scale	0.0,0.0%	0.0,0.0%	0.0,0.0%	0.0,0.0%	0.0,0.0%
Muon ID/reconstruction efficiency	-0.1,-1.05%	-0.08,-1.14%	0.05,-0.82%	-0.1,-1.05%	-0.1,-1.05%
MC statistics	5.92,-5.92%	8.51,-8.51%	40.41,-40.41%	2.13,-2.13%	2.07,-2.07%
Luminosity	3.6,-3.6%	3.6,-3.6%	3.6,-3.6%	3.6,-3.6%	3.6,-3.6%
Generator	100.0 %	10.7 %	0.0 %	1.6 %	2.14 %
PDF	0.0,0.0%	1.85,-2.01%	0.0,0.0%	1.74,2.0%	1.74,1.85%
Cross section	10.0 %	5.0 %	30.0 %	12.0 %	11.77%
Total	101.05,-101.1%	21.26,-21.24%	80.74,-85.60%	14.83,-15.62%	14.82,-15.57%
SRZb					
Expected events	0.43	0.95	0.22	18.68	20.29
Electron energy scale	2.06,-2.58%	21.65,-20.82%	0.0,0.0%	2.08,-7.7%	2.97,-8.12%
Electron energy ratio	-0.65,0.29%	0.0,-6.89%	0.0,0.0%	0.3,-0.31%	0.26,-0.6%
Muon spectrometer track p resolution	-0.36,-0.21%	5.51,0.0%	0.0,0.0%	0.1,-0.12%	0.34,-0.12%
Muon inner detector track p resolution	0.2,-0.36%	0.0,0.0%	0.0,0.0%	-1.81,-0.15%	-1.66,-0.14%
Jet energy scale	-0.06,3.66%	17.68,-10.14%	0.018,3.9%	1.7,7.57%	2.39,6.77%
Jet energy resolution	0.34,0.34%	15.47,15.47%	4.64,4.64%	4.84,4.84%	5.24,5.24%
E_T^{miss} soft term scale	1.55,-2.07%	6.16,4.82%	0.0,0.0%	13.73,-16.89%	12.97,-15.37%
E_T^{miss} soft term resolution	0.72,0.72%	2.67,2.67%	0.0,0.0%	3.02,3.02%	2.93,2.93%
Trigger	5.0,-5.0%	5.0,-5.0%	5.0,-5.0%	5.0,-5.0%	5.0,-5.0%
b -tagging	2.95,-3.0%	1.86,-1.9%	38.4,-64.33%	3.3,-3.45%	3.61,-4.03%
Electron ID/reconstruction efficiency	0.03,-4.37%	2.73,-3.99%	0.17,-1.53%	0.65,-3.14%	0.73,-3.19%
Muon ID/reconstruction efficiency	-0.08,-1.01%	-0.05,-0.91%	-0.04,-1.38%	-0.08,-1.13%	-0.08,-1.12%
MC statistics	6.62,-6.62%	25.45,-25.45%	57.33,-57.33%	7.46,-7.46%	7.0,-7.0%
Luminosity	3.6,-3.6%	3.6,-3.6%	3.6,-3.6%	3.6,-3.6%	3.6,-3.6%
Generator	100.0 %	16.8 %	0.0 %	5.9 %	8.36 %
PDF	0.0,0.0%	2.33,-2.82%	0.0,0.0%	2.0,2.15%	1.95,1.84%
Cross section	10.0 %	5.0 %	30.0 %	12.0 %	11.83%
Total	100.99,-101.17%	45.88,-43.30%	75.64,-93.42%	22.79,-27.10%	23.15,-26.69%
SRZc					
Expected events	0.29	0.39	0.1	5.01	5.79
Electron energy scale	0.58,-1.0%	0.0,0.0%	0.0,0.0%	8.44,-10.02%	7.33,-8.73%
Electron energy ratio	-0.02,0.49%	0.0,0.0%	0.0,0.0%	0.0,0.61%	-0.0,0.55%
Muon spectrometer track p resolution	0.44,0.28%	0.0,0.0%	0.0,0.0%	-0.29,0.0%	-0.22,0.01%
Muon inner detector track p resolution	-0.05,0.0%	0.0,0.0%	0.0,0.0%	0.0,0.0%	-0.0,0.0%
Jet energy scale	0.05,2.43%	-7.58,1.46%	0.0,0.0%	8.23,0.99%	6.62,1.08%
Jet energy resolution	2.85,2.85%	4.52,4.52%	38.25,38.25%	2.77,2.77%	3.51,3.51%
E_T^{miss} soft term scale	-0.84,1.11%	0.0,-32.99%	0.0,0.0%	3.94,-4.74%	3.37,-6.26%
E_T^{miss} soft term resolution	-1.22,-1.22%	-33.02,-33.02%	0.0,0.0%	-3.3,-3.3%	-5.13,-5.13%
Trigger	5.0,-5.0%	5.0,-5.0%	5.0,-5.0%	5.0,-5.0%	5.0,-5.0%
b -tagging	3.34,-3.4%	2.35,-2.35%	7.74,-8.19%	6.02,-6.47%	5.67,-6.07%
Electron ID/reconstruction efficiency	0.14,-4.19%	1.04,-1.32%	0.29,-2.03%	0.96,-3.24%	0.91,-3.14%
Muon ID/reconstruction efficiency	-0.04,-1.07%	-0.29,-1.39%	0.03,-1.08%	0.02,-0.95%	-0.01,-0.99%
MC statistics	6.37,-6.37%	41.46,-41.46%	95.95,-95.95%	14.22,-14.22%	12.73,-12.73%
Luminosity	3.6,-3.6%	3.6,-3.6%	3.6,-3.6%	3.6,-3.6%	3.6,-3.6%
Generator	100.0 %	35.4 %	0.0 %	12.9 %	18.55 %
PDF	0.0,0.0%	3.43,-4.47%	0.0,0.0%	1.37,1.67%	1.41,1.15%
Cross section	10.0 %	5.0 %	30.0 %	12.0 %	11.74%
Total	101.0,-101.13%	64.98,-72.56%	108.02,-108.07%	27.62,-27.38%	29.40,-29.77%

Table B.1: The % effect of all systematic uncertainties on irreducible SM yields in SRZ for the 2012 analysis.

	Triboson	ZZ	$t\bar{t}V$	WZ	Total
SRnoZa					
Expected events	1.69	13.76	0.23	49.56	65.23
Electron energy scale	0.17,-0.53%	4.92,-4.27%	0.0,0.0%	1.16,-1.31%	1.92,-1.91%
Electron energy ratio	-0.16,-0.36%	-0.2,0.32%	0.0,0.0%	0.44,-0.26%	0.29,-0.14%
Muon spectrometer track p resolution	0.28,0.04%	0.02,-0.35%	0.0,0.0%	-0.22,0.03%	-0.16,-0.05%
Muon inner detector track p resolution	0.0,-0.31%	0.0,0.02%	0.0,0.0%	-0.27,0.03%	-0.2,0.02%
Jet energy scale	-0.06,1.76%	7.65,-4.39%	0.0,0.0%	2.3,1.42%	3.36,0.19%
Jet energy resolution	0.67,0.67%	7.3,-7.3%	36.0,36.0%	6.73,6.73%	6.8,6.8%
E_T^{miss} soft term scale	-0.42,-0.46%	21.93,-15.72%	0.0,0.0%	4.27,-2.97%	7.86,-5.58%
E_T^{miss} soft term resolution	-0.37,-0.37%	3.39,3.39%	0.0,0.0%	0.15,0.15%	0.82,0.82%
Trigger	5.0,-5.0%	5.0,-5.0%	5.0,-5.0%	5.0,-5.0%	5.0,-5.0%
b -tagging	2.23,-2.31%	2.94,-3.02%	61.48,-76.77%	3.11,-3.2%	3.26,-3.4%
Electron ID/reconstruction efficiency	0.39,-6.0%	1.85,-7.53%	-0.62,-7.02%	0.81,-6.83%	1.01,-6.96%
Tau energy scale	0.0,0.0%	0.0,0.0%	0.0,0.0%	0.0,0.0%	0.0,0.0%
Muon ID/reconstruction efficiency	-0.1,-1.0%	-0.09,-0.99%	-0.05,-0.67%	-0.1,-1.04%	-0.1,-1.03%
MC statistics	3.94,-3.94%	6.37,-6.37%	54.76,-54.76%	4.59,-4.59%	3.74,-3.74%
Luminosity	3.6,-3.6%	3.6,-3.6%	3.6,-3.6%	3.6,-3.6%	3.6,-3.6%
Generator	100.0 %	49.4 %	0.0 %	6.9 %	18.25%
PDF	0.0,0.0%	2.6,-2.71%	0.0,0.0%	1.98,2.18%	2.06,1.08%
Cross section	10.0 %	5.0 %	30.0 %	12.0 %	10.54%
Total	100.79,-101.0%	56.50,-54.48%	94.94,-105.72%	18.31,-19.27%	25.22,-25.3%
SRnoZb					
Expected events	0.63	1.76	0.21	19.52	22.11
Electron energy scale	1.35,-1.11%	0.0,-3.68%	0.0,0.0%	2.99,-2.28%	2.68,-2.33%
Electron energy ratio	1.08,-0.07%	0.0,-0.48%	0.0,0.0%	0.96,-1.28%	0.88,-1.17%
Muon spectrometer track p resolution	-1.11,-0.11%	0.0,0.0%	0.0,0.0%	-0.73,0.63%	-0.67,0.55%
Muon inner detector track p resolution	0.0,-0.62%	0.0,-0.48%	0.0,0.0%	0.82,-0.06%	0.72,-0.11%
Jet energy scale	2.78,0.09%	10.61,-7.47%	0.46,9%	4.31,6.1%	4.73,5.23%
Jet energy resolution	1.35,1.35%	16.77,16.77%	43.16,43.16%	6.73,6.73%	7.71,7.71%
E_T^{miss} soft term scale	1.57,-1.05%	34.57,-23.63%	0.0,0.0%	7.22,-1.82%	9.16,-3.52%
E_T^{miss} soft term resolution	-0.48,-0.48%	-5.36,-5.36%	0.0,0.0%	0.82,0.82%	0.28,0.28%
Trigger	5.0,-5.0%	5.0,-5.0%	5.0,-5.0%	5.0,-5.0%	5.0,-5.0%
b -tagging	2.25,-2.29%	2.18,-2.19%	28.75,-29.03%	3.28,-3.38%	3.4,-3.49%
Electron ID/reconstruction efficiency	0.45,-5.22%	1.01,-5.46%	-0.23,-1.84%	0.41,-4.78%	0.45,-4.82%
Tau energy scale	0.0,0.0%	0.0,0.0%	0.0,0.0%	0.0,0.0%	0.0,0.0%
Muon ID/reconstruction efficiency	-0.07,-1.02%	-0.14,-0.95%	-0.4,-1.74%	-0.11,-1.08%	-0.12,-1.07%
MC statistics	6.41,-6.41%	18.29,-18.29%	54.86,-54.86%	7.54,-7.54%	6.84,-6.84%
Luminosity	3.6,-3.6%	3.6,-3.6%	3.6,-3.6%	3.6,-3.6%	3.6,-3.6%
Generator	100.0 %	38.4 %	0.0 %	7.0 %	12.09%
PDF	0.0,0.0%	2.75,-2.67%	0.0,0.0%	2.28,2.39%	2.23,1.9%
Cross section	10.0 %	5.0 %	30.0 %	12.0 %	11.55%
Total	101.0,-101.08%	59.19,-53.41%	81.47,-94.123%	20.78,-20.56%	23.58,-22.60%
SRnoZc					
Expected events	0.81	0.25	0.21	2.12	3.4
Electron energy scale	1.04,-2.07%	0.0,0.0%	0.0,-29.58%	7.85,-7.57%	5.15,-7.05%
Electron energy ratio	0.58,0.21%	0.0,0.0%	0.0,29.58%	0.0,6.51%	0.14,5.94%
Muon spectrometer track p resolution	0.16,-0.02%	3.11,0.0%	0.0,0.0%	0.0,0.0%	0.27,-0.0%
Muon inner detector track p resolution	0.0,0.17%	0.0,0.0%	0.0,0.0%	5.27,0.0%	3.29,0.04%
Jet energy scale	1.05,-0.02%	0.0,35.9%	0.0,69.5%	5.5,-0.42%	3.68,6.68%
Jet energy resolution	3.09,3.09%	0.0,0.0%	103.23,103.23%	11.33,11.33%	14.2,14.2%
E_T^{miss} soft term scale	-0.04,-2.1%	3.11,0.0%	0.0,0.0%	11.51,-2.32%	7.41,-1.95%
E_T^{miss} soft term resolution	0.78,0.78%	0.0,0.0%	0.0,0.0%	6.68,6.68%	4.36,4.36%
Trigger	0.0,0.0%	0.0,0.0%	0.0,0.0%	0.0,0.0%	0.0,0.0%
b -tagging	2.35,-2.43%	6.32,-6.32%	10.39,-10.67%	3.98,-4.12%	4.16,-4.28%
Electron ID/reconstruction efficiency	-0.0,-3.29%	1.94,0.21%	-0.18,-5.46%	0.72,-2.59%	0.58,-2.73%
Tau energy scale	0.0,0.0%	0.0,0.0%	0.0,0.0%	0.0,0.0%	0.0,0.0%
Muon ID/reconstruction efficiency	-0.05,-1.04%	-0.48,-1.91%	0.2,-0.37%	-0.04,-1.07%	-0.06,-1.08%
MC statistics	5.64,-5.64%	54.82,-54.82%	51.78,-51.78%	20.6,-20.6%	13.93,-13.93%
Luminosity	3.6,-3.6%	3.6,-3.6%	3.6,-3.6%	3.6,-3.6%	3.6,-3.6%
Generator	100.0 %	14.4 %	0.0 %	65.9 %	66.2%
PDF	0.0,0.0%	9.12,-8.29%	0.0,0.0%	1.86,2.27%	1.83,0.81%
Cross section	10.0 %	5.0 %	30.0 %	12.0 %	12.12%
Total	100.81,-100.9%	58.28,-68.2%	119.83,-144.83%	73.27,-72.34%	71.3,-71.54%

Table B.2: The % effect of all systematic uncertainties on irreducible SM yields in SRZ for the 2012 analysis.

Bibliography

- [1] CMS Collaboration Collaboration, *Search for direct EWK production of SUSY particles in multilepton modes with 8TeV data*, Tech. Rep. CMS-PAS-SUS-12-022, CERN, Geneva, 2013. xi, 155, 156
- [2] S. Lem, *Cyberiad*. Harcourt, 1965. 1
- [3] ATLAS Collaboration, *Search for direct production of charginos and neutralinos in events with three leptons and missing transverse momentum in 21fb^{-1} of pp collisions at $\sqrt{s} = 8 \text{ TeV}$ with the ATLAS detector*, Tech. Rep. ATLAS-CONF-2013-035, CERN, Geneva, Mar, 2013. 2, 78, 131, 132, 133, 134, 136, 137, 138, 154, 155
- [4] N. Stephenson, *Quicksilver*. Random House, 2003. 3
- [5] J. Beringer et al., *Particle Data Group*, Physical Review D **86** (2012) 010001+. <http://pdg.lbl.gov>. 3, 18, 31, 35, 40, 69
- [6] M. Dine, *TASI lectures on the strong CP problem*, [arXiv:hep-ph/0011376 \[hep-ph\]](https://arxiv.org/abs/hep-ph/0011376). 4
- [7] S. F. King, *Neutrino mass*, Contemporary Physics **48** (2007) 195–211, [arXiv:0712.1750 \[physics.pop-ph\]](https://arxiv.org/abs/0712.1750). 4
- [8] R. Woodard, *How Far Are We from the Quantum Theory of Gravity?*, Rept.Prog.Phys. **72** (2009) 126002, [arXiv:0907.4238 \[gr-qc\]](https://arxiv.org/abs/0907.4238). 4
- [9] V. Trimble, *Existence and Nature of Dark Matter in the Universe*, Annual Review of Astronomy and Astrophysics **25** no. 1, (1987) 425–472, <http://www.annualreviews.org/doi/pdf/10.1146/annurev.aa.25.090187.002233>. 4
- [10] J. D. Jackson and L. Okun, *Historical roots of gauge invariance*, Rev.Mod.Phys. **73** (2001) 663–680, [arXiv:hep-ph/0012061 \[hep-ph\]](https://arxiv.org/abs/hep-ph/0012061). 4

- [11] C. N. Yang and R. L. Mills, *Conservation of Isotopic Spin and Isotopic Gauge Invariance*, Phys. Rev. **96** (1954) 191–195.
<http://link.aps.org/doi/10.1103/PhysRev.96.191>. 4
- [12] A. Salam and J. C. Ward, *Electromagnetic and weak interactions*, Phys.Lett. **13** (1964) 168–171. 5
- [13] S. Weinberg, *A Model of Leptons*, Phys. Rev. Lett. **19** (1967) 1264–1266.
<http://link.aps.org/doi/10.1103/PhysRevLett.19.1264>. 5
- [14] S. Glashow, *Partial Symmetries of Weak Interactions*, Nucl.Phys. **22** (1961) 579–588. 5
- [15] D. Haidt, *The discovery of neutral currents*, Eur.Phys.J. **C34** (2004) 25–31. 6
- [16] F. Englert and R. Brout, *Broken Symmetry and the Mass of Gauge Vector Mesons*, Phys. Rev. Lett. **13** (1964) 321–323.
<http://link.aps.org/doi/10.1103/PhysRevLett.13.321>. 6
- [17] P. W. Higgs, *Broken Symmetries and the Masses of Gauge Bosons*, Phys. Rev. Lett. **13** (1964) 508–509.
<http://link.aps.org/doi/10.1103/PhysRevLett.13.508>. 6
- [18] P. W. Higgs, *Spontaneous Symmetry Breakdown without Massless Bosons*, Phys. Rev. **145** (1966) 1156–1163.
<http://link.aps.org/doi/10.1103/PhysRev.145.1156>. 6
- [19] G. S. Guralnik, C. R. Hagen, and T. W. B. Kibble, *Global Conservation Laws and Massless Particles*, Phys. Rev. Lett. **13** (1964) 585–587.
<http://link.aps.org/doi/10.1103/PhysRevLett.13.585>. 6
- [20] T. W. B. Kibble, *Symmetry Breaking in Non-Abelian Gauge Theories*, Phys. Rev. **155** (1967) 1554–1561. <http://link.aps.org/doi/10.1103/PhysRev.155.1554>. 6
- [21] C. Quigg, *Unanswered Questions in the Electroweak Theory*, Ann.Rev.Nucl.Part.Sci. **59** (2009) 505–555, [arXiv:0905.3187 \[hep-ph\]](https://arxiv.org/abs/0905.3187). 6
- [22] MuLan Collaboration, *Measurement of the Positive Muon Lifetime and Determination of the Fermi Constant to Part-per-Million Precision*, Phys. Rev.

Lett. **106** (2011) 041803.

<http://link.aps.org/doi/10.1103/PhysRevLett.106.041803>. 6

- [23] P. J. Mohr, B. N. Taylor, and D. B. Newell, *CODATA recommended values of the fundamental physical constants: 2010*, Rev. Mod. Phys. **84** (2012) 1527–1605.
<http://link.aps.org/doi/10.1103/RevModPhys.84.1527>. 7
- [24] B. W. Lee, C. Quigg, and H. B. Thacker, *Weak interactions at very high energies: The role of the Higgs-boson mass*, Phys. Rev. D **16** (1977) 1519–1531.
<http://link.aps.org/doi/10.1103/PhysRevD.16.1519>. 7
- [25] ATLAS Collaboration, *Combined coupling measurements of the Higgs-like boson with the ATLAS detector using up to 25 fb⁻¹ of proton-proton collision data*, Tech. Rep. ATLAS-CONF-2013-034, CERN, Geneva, Mar, 2013. 7
- [26] CMS Collaboration, S. Chatrchyan et al., *Observation of a new boson with mass near 125 GeV in pp collisions at sqrt(s) = 7 and 8 TeV*, [arXiv:1303.4571 \[hep-ex\]](https://arxiv.org/abs/1303.4571). 7
- [27] M. Baak, M. Goebel, J. Haller, A. Hoecker, D. Kennedy, et al., *The Electroweak Fit of the Standard Model after the Discovery of a New Boson at the LHC*, Eur.Phys.J. **C72** (2012) 2205, [arXiv:1209.2716 \[hep-ph\]](https://arxiv.org/abs/1209.2716). 8
- [28] L. W. Jones, *A review of quark search experiments*, Rev. Mod. Phys. **49** (1977) 717–752. <http://link.aps.org/doi/10.1103/RevModPhys.49.717>. 10
- [29] H1 and ZEUS Collaboration, *Combined Measurement and QCD Analysis of the Inclusive e+- p Scattering Cross Sections at HERA*, JHEP **1001** (2010) 109, [arXiv:0911.0884 \[hep-ex\]](https://arxiv.org/abs/0911.0884). 11
- [30] C. M. Will, *The Confrontation between General Relativity and Experiment*, Living Reviews in Relativity **9** no. 3, (2006).
<http://www.livingreviews.org/lrr-2006-3>. 12
- [31] H. Miyazawa, *Baryon Number Changing Currents*, Prog. Theor. Phys. **36** (6) (1966) 1266–1276. 12
- [32] P. Ramond, *Dual Theory for Free Fermions*, Phys. Rev. **D3** (1971) 2415–2418. 12
- [33] Y. A. Gol'fand and E. P. Likhtman, *Extension of the Algebra of Poincare Group Generators and Violation of p Invariance*, JETP Lett. **13** (1971) 323–326. [Pisma Zh.Eksp.Teor.Fiz.13:452-455,1971]. 12

- [34] A. Neveu and J. H. Schwarz, *Factorizable dual model of pions*, Nucl. Phys. **B31** (1971) 86–112. 12
- [35] A. Neveu and J. H. Schwarz, *Quark Model of Dual Pions*, Phys. Rev. **D4** (1971) 1109–1111. 12
- [36] J. Gervais and B. Sakita, *Field theory interpretation of supergauges in dual models*, Nucl. Phys. **B34** (1971) 632–639. 12
- [37] D. V. Volkov and V. P. Akulov, *Is the Neutrino a Goldstone Particle?*, Phys. Lett. **B46** (1973) 109–110. 12
- [38] J. Wess and B. Zumino, *A Lagrangian Model Invariant Under Supergauge Transformations*, Phys. Lett. **B49** (1974) 52. 12
- [39] J. Wess and B. Zumino, *Supergauge Transformations in Four-Dimensions*, Nucl. Phys. **B70** (1974) 39–50. 12
- [40] S. Coleman and J. Mandula, *All Possible Symmetries of the S Matrix*, Phys. Rev. **159** (1967) 1251–1256. <http://link.aps.org/doi/10.1103/PhysRev.159.1251>. 13
- [41] R. Haag, J. T. opuszaski, and M. Sohnius, *All possible generators of supersymmetries of the S-matrix*, Nuclear Physics B **88** no. 2, (1975) 257 – 274. <http://www.sciencedirect.com/science/article/pii/0550321375902795>. 13
- [42] J. H. Oort, *The force exerted by the stellar system in the direction perpendicular to the galactic plane and some related problems*, Bull. Ast. Inst. Netherlands **6** (1932) 249. 13
- [43] F. Zwicky, *Die Rotverschiebung von extragalaktischen Nebeln*, Helvetica Physica Acta **6** (1933) 110–127. 13
- [44] R. Massey, T. Kitching, and J. Richard, *The dark matter of gravitational lensing*, Rept.Prog.Phys. **73** (2010) 086901, [arXiv:1001.1739 \[astro-ph.CO\]](https://arxiv.org/abs/1001.1739). 13
- [45] Planck Collaboration, P. Ade et al., *Planck 2013 results. I. Overview of products and scientific results*, [arXiv:1303.5062 \[astro-ph.CO\]](https://arxiv.org/abs/1303.5062). 13
- [46] B. Famaey and S. S. McGaugh, *Modified Newtonian Dynamics (MOND): Observational Phenomenology and Relativistic Extensions*, Living Reviews in Relativity **15** no. 10, (2012). <http://www.livingreviews.org/lrr-2012-10>. 13

- [47] K. Griest, *Galactic microlensing as a method of detecting massive compact halo objects*, *Astrophys. J.* **366** (1991) 412–421. 13
- [48] G. Bertone and D. Merritt, *Dark matter dynamics and indirect detection*, *Mod.Phys.Lett.* **A20** (2005) 1021, [arXiv:astro-ph/0504422 \[astro-ph\]](https://arxiv.org/abs/astro-ph/0504422). 13
- [49] CDMS Collaboration, R. Agnese et al., *Dark Matter Search Results Using the Silicon Detectors of CDMS II*, *Phys.Rev.Lett.* (2013), [arXiv:1304.4279 \[hep-ex\]](https://arxiv.org/abs/1304.4279). 13
- [50] XENON100 Collaboration, E. Aprile et al., *Limits on spin-dependent WIMP-nucleon cross sections from 225 live days of XENON100 data*, [arXiv:1301.6620 \[astro-ph.CO\]](https://arxiv.org/abs/1301.6620). 13, 156
- [51] H. Goldberg, *Constraint on the photino mass from cosmology*, *Phys. Rev. Lett.* **50** (1983) 1419. 13
- [52] J. Ellis, J. Hagelin, D. Nanopoulos, K. Olive, and M. Srednicki, *Supersymmetric relics from the big bang*, *Nucl. Phys.* **B238** (1984) 453–476. 13
- [53] S. Weinberg, *Implications of Dynamical Symmetry Breaking*, *Phys. Rev.* **D13** (1976) 974–996. 14
- [54] E. Gildener, *Gauge Symmetry Hierarchies*, *Phys. Rev.* **D14** (1976) 1667. 14
- [55] S. Weinberg, *Implications of Dynamical Symmetry Breaking: An Addendum*, *Phys. Rev.* **D19** (1979) 1277–1280. 14
- [56] L. Susskind, *Dynamics of Spontaneous Symmetry Breaking in the Weinberg- Salam Theory*, *Phys. Rev.* **D20** (1979) 2619–2625. 14
- [57] S. Dimopoulos and H. Georgi, *Softly Broken Supersymmetry and SU(5)*, *Nucl. Phys.* **B193** (1981) 150. 14
- [58] E. Witten, *Dynamical Breaking of Supersymmetry*, *Nucl. Phys.* **B188** (1981) 513. 14
- [59] M. Dine, W. Fischler, and M. Srednicki, *Supersymmetric Technicolor*, *Nucl. Phys.* **B189** (1981) 575–593. 14
- [60] S. Dimopoulos and S. Raby, *Supercolor*, *Nucl. Phys.* **B192** (1981) 353. 14
- [61] N. Sakai, *Naturalness in Supersymmetric Guts*, *Zeit. Phys.* **C11** (1981) 153. 14, 15

- [62] R. Kaul and P. Majumdar, *Cancellation of quadratically divergent mass corrections in globally supersymmetric spontaneously broken gauge theories*, Nucl. Phys. **B199** (1982) 36. 14
- [63] S. Dimopoulos, S. Raby, and F. Wilczek, *Supersymmetry and the Scale of Unification*, Phys. Rev. **D24** (1981) 1681–1683. 15
- [64] L. E. Ibanez and G. G. Ross, *Low-Energy Predictions in Supersymmetric Grand Unified Theories*, Phys. Lett. **B105** (1981) 439. 15
- [65] M. B. Einhorn and D. R. T. Jones, *The Weak Mixing Angle and Unification Mass in Supersymmetric SU(5)*, Nucl. Phys. **B196** (1982) 475. 15
- [66] W. J. Marciano and G. Senjanovic, *Predictions of Supersymmetric Grand Unified Theories*, Phys. Rev. **D25** (1982) 3092. 15
- [67] S. P. Martin, *A Supersymmetry primer*, arXiv:hep-ph/9709356 [hep-ph]. 15, 16, 17, 18
- [68] D. H. Perkins, *Proton Decay Experiments*, Annual Review of Nuclear and Particle Science **34** no. 1, (1984) 1–50,
<http://www.annualreviews.org/doi/pdf/10.1146/annurev.ns.34.120184.000245>.
<http://www.annualreviews.org/doi/abs/10.1146/annurev.ns.34.120184.000245>. 15
- [69] D. J. Gross and R. Jackiw, *Effect of Anomalies on Quasi-Renormalizable Theories*, Phys. Rev. D **6** (1972) 477–493.
<http://link.aps.org/doi/10.1103/PhysRevD.6.477>. 15
- [70] DELPHI Collaboration, *Searches for supersymmetric particles in e+ e- collisions up to 208-GeV and interpretation of the results within the MSSM*, Eur.Phys.J. **C31** (2003) 421–479, arXiv:hep-ex/0311019 [hep-ex]. 16
- [71] H. Haber and G. Kane, *The search for supersymmetry: Probing physics beyond the standard model*, Physics Reports **117** no. 24, (1985) 75 – 263.
<http://www.sciencedirect.com/science/article/pii/0370157385900511>. 19
- [72] S. Choi, J. Kalinowski, G. A. Moortgat-Pick, and P. Zerwas, *Analysis of the neutralino system in supersymmetric theories*, Eur.Phys.J. **C22** (2001) 563–579, arXiv:hep-ph/0108117 [hep-ph]. 19

- [73] G. D'Ambrosio, G. Giudice, G. Isidori, and A. Strumia, *Minimal flavor violation: An Effective field theory approach*, Nucl.Phys. **B645** (2002) 155–187, arXiv:hep-ph/0207036 [hep-ph]. 19, 24
- [74] H. Baer, C.-h. Chen, M. Drees, F. Paige, and X. Tata, *Collider phenomenology for supersymmetry with large tan Beta*, Phys.Rev.Lett. **79** (1997) 986–989, arXiv:hep-ph/9704457 [hep-ph]. 20, 28
- [75] H. E. Haber, R. Hempfling, and A. H. Hoang, *Approximating the radiatively corrected Higgs mass in the minimal supersymmetric model*, Z.Phys. **C75** (1997) 539–554, arXiv:hep-ph/9609331 [hep-ph]. 20
- [76] L. J. Hall, D. Pinner, and J. T. Ruderman, *A Natural SUSY Higgs Near 126 GeV*, JHEP **1204** (2012) 131, arXiv:1112.2703 [hep-ph]. 20
- [77] P. Meade, N. Seiberg, and D. Shih, *General Gauge Mediation*, Prog.Theor.Phys.Supppl. **177** (2009) 143–158, arXiv:0801.3278 [hep-ph]. 20
- [78] C. F. Berger, J. S. Gainer, J. L. Hewett, and T. G. Rizzo, *Supersymmetry without prejudice*, Journal of High Energy Physics **2009** no. 02, (2009) 023. <http://stacks.iop.org/1126-6708/2009/i=02/a=023>. 21, 24
- [79] J. Alwall, P. Schuster, N. Toro Phys. Rev. **D79** (2009) 075020. 21
- [80] LHC New Physics Working Group Collaboration, D. Alves et al., *Simplified Models for LHC New Physics Searches*, J.Phys. **G39** (2012) 105005, arXiv:1105.2838 [hep-ph]. 21
- [81] A. H. Chamseddine, R. L. Arnowitt, and P. Nath, *Locally Supersymmetric Grand Unification*, Phys. Rev. Lett. **49** (1982) 970. 21
- [82] R. Barbieri, S. Ferrara, and C. A. Savoy, *Gauge Models with Spontaneously Broken Local Supersymmetry*, Phys. Lett. **B119** (1982) 343. 21
- [83] L. E. Ibanez, *Locally Supersymmetric SU(5) Grand Unification*, Phys. Lett. **B 118** (1982) 73. 21
- [84] L. J. Hall, J. D. Lykken, and S. Weinberg, *Supergravity as the Messenger of Supersymmetry Breaking*, Phys. Rev. **D27** (1983) 2359–2378. 21
- [85] N. Ohta, *Grand unified theories based on local supersymmetry*, Prog. Theor. Phys. **70** (1983) 542. 21

- [86] G. L. Kane, C. F. Kolda, L. Roszkowski, and J. D. Wells, *Study of constrained minimal supersymmetry*, Phys. Rev. **D49** (1994) 6173–6210. 21
- [87] G. F. Giudice, M. A. Luty, H. Murayama, and R. Rattazzi, *Gaugino mass without singlets*, JHEP **9812** (1998) 027, [arXiv:hep-ph/9810442 \[hep-ph\]](https://arxiv.org/abs/hep-ph/9810442). 21
- [88] L. Randall and R. Sundrum, *Out of this world supersymmetry breaking*, Nucl.Phys. **B557** (1999) 79–118, [arXiv:hep-th/9810155 \[hep-th\]](https://arxiv.org/abs/hep-th/9810155). 21
- [89] M. Dine, W. Fischler, and M. Srednicki, *Supersymmetric Technicolor*, Nucl. Phys. **B189** (1981) 575. 21
- [90] S. Dimopoulos and S. Raby, *Supercolor*, Nucl. Phys. **B192** (1981) 353. 21
- [91] L. Alvarez-Gaume, M. Claudson, and M. Wise, *Low-energy Supersymmetry*, Nucl. Phys. **B207** (1982) 96. 21
- [92] C. R. Nappi and B. A. Ovrut, *Supersymmetric Extension of the $SU(3)\times SU(2)\times U(1)$ Model*, Phys. Lett. **B113** (1982) 175. 21
- [93] M. Dine, A. E. Nelson, Y. Nir, and Y. Shirman, *New Tools for Low-energy Dynamical Supersymmetry Breaking*, Phys. Rev. **D53** (1996) 2658. 21
- [94] P. Meade, M. Reece, and D. Shih, *Prompt Decays of General Neutralino NLSPs at the Tevatron*, JHEP **1005** (2010) 105, [arXiv:0911.4130 \[hep-ph\]](https://arxiv.org/abs/0911.4130). 23
- [95] A. Buckley, *PySLHA: a Pythonic interface to SUSY Les Houches Accord data*, 2013. 24, 27
- [96] WMAP Collaboration, E. Komatsu et al., *Five-Year Wilkinson Microwave Anisotropy Probe (WMAP) Observations: Cosmological Interpretation*, Astrophys.J.Suppl. **180** (2009) 330–376, [arXiv:0803.0547 \[astro-ph\]](https://arxiv.org/abs/0803.0547). 25
- [97] LEPSUSYWG, ALEPH, DELPHI, L3 and OPAL experiments note LEPSUSYWG/01-03.1. <http://lepsusy.web.cern.ch/lepsusy/Welcome.html>. 26
- [98] *Search for squarks and gluinos with the ATLAS detector in final states with jets and missing transverse momentum and 20.3 fb^{-1} of $\sqrt{s} = 8\text{ TeV}$ proton-proton collision data*, Tech. Rep. ATLAS-CONF-2013-047, CERN, Geneva, May, 2013. 28
- [99] J. R. Fowles, *The Magus*. Jonathan Cape, 1966. 31

- [100] O. Brüning, Sim, P. Collier, P. Lebrun, S. Myers, R. Ostoja, J. Poole, and P. Proudlock, *LHC Design Report*. CERN, Geneva, 2004. [31](#)
- [101] V. Frigo, “LHC map in 3D. Schma du LHC en 3D.” AC Collection. Legacy of AC. Pictures from 1992 to 2002., Mar, 1997. [32](#)
- [102] ATLAS Collaboration, *Luminosity working group public results*, 2012. <https://twiki.cern.ch/twiki/bin/view/AtlasPublic/LuminosityPublicResults>. [32](#), [34](#)
- [103] ATLAS Collaboration, *The ATLAS Experiment at the CERN Large Hadron Collider*, Journal of Instrumentation **3** no. 08, (2008) S08003. <http://stacks.iop.org/1748-0221/3/i=08/a=S08003>. [32](#), [33](#), [36](#), [37](#), [38](#), [39](#), [40](#), [41](#), [42](#), [43](#), [44](#), [45](#), [47](#), [50](#)
- [104] CMS Collaboration, *The CMS experiment at the CERN LHC. The Compact Muon Solenoid experiment*, J. Instrum. **3** (2008) S08004. 361 p. Also published by CERN Geneva in 2010. [32](#)
- [105] LHCb Collaboration, *The LHCb Detector at the LHC*, J. Instrum. **3** no. LHCb-DP-2008-001. CERN-LHCb-DP-2008-001, (2008) S08005. Also published by CERN Geneva in 2010. [32](#)
- [106] ALICE Collaboration, *The ALICE experiment at the CERN LHC. A Large Ion Collider Experiment*, J. Instrum. **3** (2008) S08002. 259 p. Also published by CERN Geneva in 2010. [32](#)
- [107] P. Jenni, M. Nordberg, M. Nessi, and K. Jon-And, *ATLAS Forward Detectors for Measurement of Elastic Scattering and Luminosity*. Technical Design Report. CERN, Geneva, 2008. [36](#)
- [108] P. Jenni, M. Nessi, and M. Nordberg, *Zero Degree Calorimeters for ATLAS*, Tech. Rep. LHCC-I-016. CERN-LHCC-2007-001, CERN, Geneva, Jan, 2007. [36](#)
- [109] ATLAS Collaboration, *Particle Identification Performance of the ATLAS Transition Radiation Tracker*, [39](#), [40](#)
- [110] E. Abat, E. Arik, M. Arik, N. Becerici, O. Dogan, et al., *The ATLAS TRT electronics*, *JINST* **3** (2008) P06007. [39](#)

- [111] G. Charpak, R. Bouclier, T. Bressani, J. Favier, and . Zupani, *The use of multiwire proportional counters to select and localize charged particles*, Nuclear Instruments and Methods **62** no. 3, (1968) 262 – 268.
<http://www.sciencedirect.com/science/article/pii/0029554X68903716>. 46
- [112] ATLAS Collaboration, G. Aad et al., *Performance of the ATLAS Trigger System in 2010*, Eur.Phys.J. **C72** (2012) 1849, arXiv:1110.1530 [hep-ex]. 48, 49
- [113] R. Achenbach, P. Adragna, et al., *The ATLAS Level-1 Calorimeter Trigger*, Journal of Instrumentation **3** no. 03, (2008) P03001.
<http://stacks.iop.org/1748-0221/3/i=03/a=P03001>. 48
- [114] ATLAS Collaboration, *Performance of the ATLAS muon trigger in 2011*, Tech. Rep. ATLAS-CONF-2012-099, CERN, Geneva, Jul, 2012. 49, 52
- [115] S. Ask, D. Berge, P. Borrego-Amaral, et al., *The ATLAS central level-1 trigger logic and TTC system*, Journal of Instrumentation **3** no. 08, (2008) P08002.
<http://stacks.iop.org/1748-0221/3/i=08/a=P08002>. 49
- [116] ATLAS Collaboration, *Trigger and data acquisition public results*, 2012.
https://twiki.cern.ch/twiki/pub/Atlas/TDAQSpeakersCommitteeCommonReferences/TDAQResources2010_11_12.pdf. 51
- [117] N. P. Konstantinidis, M. Sutton, J. T. M. Baines, D. Emeliyanov, F. Parodi, C. Schiavi, and H. Drevermann, *A Fast Tracking Algorithm for the ATLAS Level 2 Trigger*, Tech. Rep. ATL-COM-DAQ-2006-021, CERN, Geneva, May, 2006. 51
- [118] R. Frühwirth, *Application of Kalman filtering to track and vertex fitting*, Nucl.Instrum.Meth. **A262** (1987) 444–450. 51, 61
- [119] ATLAS Collaboration, *Performance of the ATLAS Jet Trigger in the Early $\sqrt{s} = 7$ TeV Data*, Tech. Rep. ATLAS-CONF-2010-094, CERN, Geneva, Oct, 2010. 52
- [120] ATLAS Collaboration, *Performance of the ATLAS transverse energy triggers with initial LHC runs at $\text{sqrt}s = 7$ TeV*, Tech. Rep. ATLAS-CONF-2011-072, CERN, Geneva, May, 2011. 52
- [121] T. S. Eliot, *Four Quartets*. Harcourt, 1943. 53
- [122] ATLAS Collaboration, *The ATLAS Simulation Infrastructure*, European Physical Journal C **70** (2010) 823–874, arXiv:1005.4568 [physics.ins-det]. 53

- [123] G. Barrand, I. Belyaev, P. Binko, M. Cattaneo, R. Chytracek, et al., *GAUDI - A software architecture and framework for building HEP data processing applications*, *Comput.Phys.Commun.* **140** (2001) 45–55. 53
- [124] A. Buckley, J. Butterworth, S. Gieseke, D. Grellscheid, S. Hoche, et al., *General-purpose event generators for LHC physics*, *Phys.Rept.* **504** (2011) 145–233, [arXiv:1101.2599 \[hep-ph\]](https://arxiv.org/abs/1101.2599). 54, 55
- [125] I. W. Stewart, F. J. Tackmann, and W. J. Waalewijn, *Factorization at the LHC: From PDFs to Initial State Jets*, *Phys.Rev.* **D81** (2010) 094035, [arXiv:0910.0467 \[hep-ph\]](https://arxiv.org/abs/0910.0467). 54
- [126] V. Gribov and L. Lipatov, *Deep inelastic e p scattering in perturbation theory*, *Sov.J.Nucl.Phys.* **15** (1972) 438–450. 54
- [127] G. Altarelli and G. Parisi, *Asymptotic Freedom in Parton Language*, *Nucl.Phys.* **B126** (1977) 298. 54
- [128] Y. L. Dokshitzer, *Calculation of the Structure Functions for Deep Inelastic Scattering and e+ e- Annihilation by Perturbation Theory in Quantum Chromodynamics.*, *Sov.Phys.JETP* **46** (1977) 641–653. 54
- [129] A. M. Cooper-Sarkar, R. Devenish, and A. De Roeck, *Structure functions of the nucleon and their interpretation*, *Int.J.Mod.Phys.* **A13** (1998) 3385–3586, [arXiv:hep-ph/9712301 \[hep-ph\]](https://arxiv.org/abs/hep-ph/9712301). 54
- [130] NLO Multileg Working Group Collaboration, Z. Bern et al., *The NLO multileg working group: Summary report*, [arXiv:0803.0494 \[hep-ph\]](https://arxiv.org/abs/0803.0494). 55
- [131] C. F. Berger and D. Forde, *Multiparton Scattering Amplitudes via On-Shell Methods*, *Annual Review of Nuclear and Particle Science* **60** no. 1, (2010) 181–205, <http://www.annualreviews.org/doi/pdf/10.1146/annurev.nucl.012809.104538>.
<http://www.annualreviews.org/doi/abs/10.1146/annurev.nucl.012809.104538>. 55
- [132] G. Corcella, I. Knowles, G. Marchesini, S. Moretti, K. Odagiri, et al., *HERWIG 6.5 release note*, [arXiv:hep-ph/0210213](https://arxiv.org/abs/hep-ph/0210213). 55
- [133] S. Moretti, K. Odagiri, P. Richardson, M. H. Seymour, and B. R. Webber, *Implementation of supersymmetric processes in the HERWIG event generator*, *JHEP* **04** (2002) 028, [arXiv:hep-ph/0204123](https://arxiv.org/abs/hep-ph/0204123). 55

- [134] M. Bahr et al., *Herwig++ Physics and Manual*, *Eur. Phys. J. C* **58** (2008) 639–707, [arXiv:0803.0883 \[hep-ph\]](https://arxiv.org/abs/0803.0883). 55
- [135] T. Sjöstrand, S. Mrenna, and P. Z. Skands, *PYTHIA 6.4 Physics and Manual*, *JHEP* **0605** (2006) 026, [arXiv:hep-ph/0603175 \[hep-ph\]](https://arxiv.org/abs/hep-ph/0603175). 55
- [136] T. Sjöstrand, S. Mrenna, and P. Z. Skands, *A Brief Introduction to PYTHIA 8.1*, *Comput. Phys. Commun.* **178** (2008) 852. 55
- [137] T. Gleisberg et al., *Event generation with SHERPA 1.1*, *JHEP* **0902** (2009) 007, [arXiv:0811.4622 \[hep-ph\]](https://arxiv.org/abs/0811.4622). 55
- [138] S. Catani, F. Krauss, R. Kuhn, and B. Webber, *QCD matrix elements + parton showers*, *JHEP* **0111** (2001) 063, [arXiv:hep-ph/0109231 \[hep-ph\]](https://arxiv.org/abs/hep-ph/0109231). 55
- [139] M. L. Mangano, M. Moretti, and R. Pittau, *Multijet matrix elements and shower evolution in hadronic collisions: $Wb\bar{b} + n$ jets as a case study*, *Nucl.Phys.* **B632** (2002) 343–362, [arXiv:hep-ph/0108069 \[hep-ph\]](https://arxiv.org/abs/hep-ph/0108069). 55
- [140] CDF Collaboration, R. D. Field, *The Underlying event in hard scattering processes*, eConf **C010630** (2001) P501, [arXiv:hep-ph/0201192 \[hep-ph\]](https://arxiv.org/abs/hep-ph/0201192). 55
- [141] J. Butterworth, J. R. Forshaw, and M. Seymour, *Multiparton interactions in photoproduction at HERA*, *Z. Phys. C* **72** (1996) 637–646, [hep-ph/9601371](https://arxiv.org/abs/hep-ph/9601371). 55
- [142] ATLAS Collaboration, *Further ATLAS tunes of PYTHIA6 and Pythia 8*, Tech. Rep. ATL-PHYS-PUB-2011-014, CERN, Geneva, Nov, 2011. 55
- [143] ATLAS Collaboration, *Summary of ATLAS Pythia 8 tunes*, Tech. Rep. ATL-PHYS-PUB-2012-003, CERN, Geneva, Aug, 2012. 55
- [144] ATLAS tunes of PYTHIA 6 and Pythia 8 for MC11, Tech. Rep. ATL-PHYS-PUB-2011-009, CERN, Geneva, Jul, 2011. 55
- [145] First tuning of HERWIG/JIMMY to ATLAS data, Tech. Rep. ATL-PHYS-PUB-2010-014, CERN, Geneva, Oct, 2010. 55
- [146] New ATLAS event generator tunes to 2010 data, Tech. Rep. ATL-PHYS-PUB-2011-008, CERN, Geneva, Apr, 2011. 55
- [147] S. Frixione and B. R. Webber, *The MC@NLO 3.2 event generator*, [arXiv:hep-ph/0601192](https://arxiv.org/abs/hep-ph/0601192). 56

- [148] P. Nason, *A New method for combining NLO QCD with shower Monte Carlo algorithms*, JHEP **0411** (2004) 040, [arXiv:hep-ph/0409146](https://arxiv.org/abs/hep-ph/0409146). 56
- [149] J. M. Campbell and R. K. Ellis, *$t\bar{t}W^{+-}$ production and decay at NLO*, JHEP **1207** (2012) 052, [arXiv:1204.5678 \[hep-ph\]](https://arxiv.org/abs/1204.5678). 56
- [150] J. M. Campbell and R. K. Ellis, *An Update on vector boson pair production at hadron colliders*, Phys. Rev. **D 60** (1999) 113006, [arXiv:hep-ph/9905386 \[hep-ph\]](https://arxiv.org/abs/hep-ph/9905386). 56
- [151] J. M. Campbell, R. K. Ellis, and C. Williams, *Vector boson pair production at the LHC*, JHEP **1107** (2011) 018, [arXiv:1105.0020 \[hep-ph\]](https://arxiv.org/abs/1105.0020). 56
- [152] K. Melnikov and F. Petriello, *Electroweak gauge boson production at hadron colliders through $O(\alpha(s)^{**2})$* , Phys. Rev. **D 74** (2006) 114017, [arXiv:hep-ph/0609070 \[hep-ph\]](https://arxiv.org/abs/hep-ph/0609070). 56, 59
- [153] C. Anastasiou et al., *High precision QCD at hadron colliders: Electroweak gauge boson rapidity distributions at NNLO*, Phys. Rev. **D 69** (2004) 094008, [arXiv:hep-ph/0312266 \[hep-ph\]](https://arxiv.org/abs/hep-ph/0312266). 56, 59
- [154] TOTEM Collaboration, *The TOTEM Experiment at the CERN Large Hadron Collider*, J. Instrum. **3** (2008) S08007. 57
- [155] GEANT4 Collaboration, *GEANT4: A Simulation toolkit*, Nucl. Instrum. Meth. **A 506** (2003) 250–303. 57
- [156] B. Di Girolamo, A. Dotti, V. Giangiobbe, P. Johansson, L. Pribyl, and M. Volpi, *Beamline instrumentation in the 2004 combined ATLAS testbeam*, Tech. Rep. ATL-TECH-PUB-2005-001. ATL-COM-TECH-2005-001, CERN, Geneva, 2005. 57
- [157] ATLAS Collaboration, T. Cornelissen and W. Liebig, *ATLAS Inner Detector results from the 2004 combined test beam data*, Nucl.Phys.Proc.Suppl. **172** (2007) 292–295. 57
- [158] F. Bauer, L. Chevalier, et al., *ATLAS 2004 Combined Test Beam results: Muon Chamber Alignment and Muon Reconstruction*, Tech. Rep. ATL-MUON-PUB-2007-003. ATL-COM-MUON-2006-012, CERN, Geneva, Apr, 2006. 57, 66

- [159] ATLAS Collaboration, *Readiness of the ATLAS Tile Calorimeter for LHC collisions*, European Physical Journal C **70** (2010) 1193–1236, [arXiv:1007.5423 \[physics.ins-det\]](https://arxiv.org/abs/1007.5423). 57
- [160] ATLAS Collaboration, *The ATLAS Inner Detector commissioning and calibration*, Eur.Phys.J. **C70** (2010) 787–821, [arXiv:1004.5293 \[physics.ins-det\]](https://arxiv.org/abs/1004.5293). 57
- [161] ATLAS Collaboration, *Commissioning of the ATLAS Muon Spectrometer with Cosmic Rays*, Eur.Phys.J. **C70** (2010) 875–916, [arXiv:1006.4384 \[physics.ins-det\]](https://arxiv.org/abs/1006.4384). 57
- [162] ATLAS Collaboration, *Alignment of the ATLAS Inner Detector Tracking System with 2010 LHC proton-proton collisions at $\sqrt{s} = 7 \text{ TeV}$* , [57](#)
- [163] ATLAS Collaboration, *Study of the Material Budget in the ATLAS Inner Detector with K_S^0 decays in collision data at $\sqrt{s}=900 \text{ GeV}$* , Tech. Rep. ATLAS-CONF-2010-019, CERN, Geneva, Jul, 2010. [57](#)
- [164] E. Richter-Was, D. Froidevaux, and L. Poggioli, *ATLFAST 2.0: a fast simulation package for ATLAS*, Tech. Rep. ATL-PHYS-98-131, CERN, Geneva, Nov, 1998. [58](#)
- [165] W. Lukas, *Fast Simulation for ATLAS: Atlfast-II and ISF*, Journal of Physics: Conference Series **396** no. 2, (2012) 022031.
<http://stacks.iop.org/1742-6596/396/i=2/a=022031>. [58](#)
- [166] ATLAS Collaboration, T. Yamanaka, *The ATLAS calorimeter simulation FastCaloSim*, J.Phys.Conf.Ser. **331** (2011) 032053. [58](#)
- [167] ATLAS Collaboration, J. Mechnick, *FATRAS: The ATLAS fast track simulation project*, J.Phys.Conf.Ser. **331** (2011) 032046. [58](#)
- [168] J. Chapman, K. Assamagan, P. Calafiura, D. Chakraborty, D. Costanzo, et al., *The ATLAS detector digitization project for 2009 data taking*, J.Phys.Conf.Ser. **219** (2010) 032031. [58](#)
- [169] M. Aliev et al., *HATHOR: HAdronic Top and Heavy quarks crOss section calculatoR*, Comput. Phys. Commun. **182** (2011) 1034–1046, [arXiv:1007.1327 \[hep-ph\]](https://arxiv.org/abs/1007.1327). [59](#)
- [170] A. Kardos, Z. Trocsanyi, and C. Papadopoulos, *Top quark pair production in association with a Z-boson at NLO accuracy*, Phys. Rev. D **85** (2012) 054015, [arXiv:1111.0610 \[hep-ph\]](https://arxiv.org/abs/1111.0610). [59](#), 119

- [171] J. M. Campbell and R. K. Ellis, *$t\bar{t}W^{+-}$ production and decay at NLO*, **JHEP** **1207** (2012) 052, [arXiv:1204.5678 \[hep-ph\]](https://arxiv.org/abs/1204.5678). 59, 119
- [172] F. E. Paige, S. D. Protopopescu, H. Baer, and X. Tata, *ISAJET 7.69: A Monte Carlo event generator for pp , anti- p p , and $e+e-$ reactions*, [arXiv:hep-ph/0312045 \[hep-ph\]](https://arxiv.org/abs/hep-ph/0312045). 59
- [173] M. Muhlleitner, A. Djouadi, and Y. Mambrini, *SDECAY: A Fortran code for the decays of the supersymmetric particles in the MSSM*, **Comput.Phys.Commun.** **168** (2005) 46–70, [arXiv:hep-ph/0311167 \[hep-ph\]](https://arxiv.org/abs/hep-ph/0311167). 59
- [174] B. P. Kersevan and E. Richter-Was, *The Monte Carlo event generator AcerMC version 1.0 with interfaces to PYTHIA 6.2 and HERWIG 6.3*, **Comput. Phys. Commun.** **149** (2003) 142–194, [arXiv:hep-ph/0201302 \[hep-ph\]](https://arxiv.org/abs/hep-ph/0201302). 59
- [175] S. S. Haykin, S. S. Haykin, S. S. Haykin, and S. S. Haykin, *Neural networks and learning machines*, vol. 3. Prentice Hall, 2009. 61
- [176] B. P. Roe, H.-J. Yang, J. Zhu, Y. Liu, I. Stancu, and G. McGregor, *Boosted decision trees as an alternative to artificial neural networks for particle identification*, **Nuclear Instruments and Methods in Physics Research A** **543** (2005) 577–584, [arXiv:physics/0408124](https://arxiv.org/abs/physics/0408124). 61
- [177] *Performance of the ATLAS Inner Detector Track and Vertex Reconstruction in the High Pile-Up LHC Environment*, Tech. Rep. ATLAS-CONF-2012-042, CERN, Geneva, Mar, 2012. 61
- [178] W. Lampl, S. Laplace, D. Lelas, P. Loch, H. Ma, S. Menke, S. Rajagopalan, D. Rousseau, S. Snyder, and G. Unal, *Calorimeter Clustering Algorithms: Description and Performance*, Tech. Rep. ATL-LARG-PUB-2008-002. ATL-COM-LARG-2008-003, CERN, Geneva, Apr, 2008. 63, 67
- [179] ATLAS Collaboration, G. Aad et al., *Electron performance measurements with the ATLAS detector using the 2010 LHC proton-proton collision data*, **Eur.Phys.J.** **C72** (2012) 1909, [arXiv:1110.3174 \[hep-ex\]](https://arxiv.org/abs/1110.3174). 64, 83
- [180] ATLAS Electromagnetic Barrel Calorimeter Collaboration, M. Aharrouche et al., *Energy linearity and resolution of the ATLAS electromagnetic barrel calorimeter in an electron test-beam*, **Nucl.Instrum.Meth.** **A568** (2006) 601–623, [arXiv:physics/0608012 \[physics\]](https://arxiv.org/abs/physics/0608012). 64

- [181] ATLAS Collaboration, *Electron combined performance public results*, 2012.
<https://atlas.web.cern.ch/Atlas/GROUPS/PHYSICS/EGAMMA/PublicPlots/20120611/ElectronEfficiency2012/ATL-COM-PHYS-2011-783/index.html>. 65
- [182] *Muon Performance in Minimum Bias pp Collision Data at $s = 7 \text{ TeV}$ with ATLAS*, Tech. Rep. ATLAS-CONF-2010-036, CERN, Geneva, Jul, 2010. 66
- [183] ATLAS Collaboration, *ATLAS muon spectrometer: Technical Design Report*. Technical Design Report ATLAS. CERN, Geneva, 1997. distribution. 66
- [184] ATLAS Collaboration, *Muon combined performance public results*, 2012.
<https://atlas.web.cern.ch/Atlas/GROUPS/PHYSICS/MUON/PublicPlots/2012/June/index.html>. 67
- [185] *Properties of Jets and Inputs to Jet Reconstruction and Calibration with the ATLAS Detector Using Proton-Proton Collisions at $\sqrt{s} = 7 \text{ TeV}$* , Tech. Rep. ATLAS-CONF-2010-053, CERN, Geneva, Jul, 2010. 67, 68
- [186] ATLAS Collaboration, *Jet energy measurement with the ATLAS detector in proton-proton collisions at $\sqrt{s} = 7 \text{ TeV}$* , arXiv:1112.6426 [hep-ex]. 68
- [187] M. Cacciari, G. P. Salam, and G. Soyez, *The anti- k_t jet clustering algorithm*, Journal of High Energy Physics 4 (2008) 63, arXiv:0802.1189 [hep-ph]. 68
- [188] *Measurement of the Mistag Rate with 5fb^{-1} of Data Collected by the ATLAS Detector*, Tech. Rep. ATLAS-CONF-2012-040, CERN, Geneva, Mar, 2012. 69, 83
- [189] *Measurement of the b-tag Efficiency in a Sample of Jets Containing Muons with 5fb^{-1} of Data from the ATLAS Detector*, Tech. Rep. ATLAS-CONF-2012-043, CERN, Geneva, Mar, 2012. 69, 83
- [190] *Measuring the b-tag efficiency in a top-pair sample with 4.7fb^{-1} of data from the ATLAS detector*, Tech. Rep. ATLAS-CONF-2012-097, CERN, Geneva, Jul, 2012. 69, 83
- [191] *b-jet tagging calibration on c-jets containing D^{*+} mesons*, Tech. Rep. ATLAS-CONF-2012-039, CERN, Geneva, Mar, 2012. 69
- [192] ATLAS Collaboration, *Performance of the Reconstruction and Identification of Hadronic Tau Decays in ATLAS with 2011 Data*, Tech. Rep. ATLAS-CONF-2012-142, CERN, Geneva, Oct, 2012. 70

- [193] *Determination of the tau energy scale and the associated systematic uncertainty in proton-proton collisions at $\sqrt{s} = 8$ TeV with the ATLAS detector at the LHC in 2012*, Tech. Rep. ATLAS-CONF-2013-044, CERN, Geneva, Apr, 2013. [71](#)
- [194] *Performance of Missing Transverse Momentum Reconstruction in ATLAS with 2011 Proton-Proton Collisions at $\sqrt{s} = 7$ TeV*, Tech. Rep. ATLAS-CONF-2012-101, CERN, Geneva, Jul, 2012. [72](#)
- [195] ATLAS Collaboration, *Search for direct slepton and gaugino production in final states with two leptons and missing transverse momentum with the ATLAS detector in pp collisions at $\sqrt{s} = 7$ TeV*, Phys.Lett. **B718** (2013) 879–901, [arXiv:1208.2884 \[hep-ex\]](https://arxiv.org/abs/1208.2884). [77](#), [149](#), [151](#), [152](#), [153](#)
- [196] ATLAS Collaboration, *Search for direct production of charginos and neutralinos in events with three leptons and missing transverse momentum in pp collisions with the ATLAS detector*, Physics Letters B **718** no. 3, (2013) 841 – 859.
<http://www.sciencedirect.com/science/article/pii/S037026931201204X>.
[78](#), [130](#), [135](#), [141](#), [151](#), [152](#), [153](#)
- [197] ATLAS Collaboration, *Search for direct production of charginos and neutralinos in events with three leptons and missing transverse momentum in $\sqrt{s} = 7$ TeV pp collisions with the ATLAS detector*, Tech. Rep. ATLAS-CONF-2012-077, CERN, Geneva, Jul, 2012. [78](#), [148](#)
- [198] *Performance of the ATLAS Electron and Photon Trigger in p-p Collisions at $\sqrt{s} = 7$ TeV in 2011*, Tech. Rep. ATLAS-CONF-2012-048, CERN, Geneva, May, 2012. [80](#)
- [199] *Selection of jets produced in proton-proton collisions with the ATLAS detector using 2011 data*, Tech. Rep. ATLAS-CONF-2012-020, CERN, Geneva, Mar, 2012. [81](#)
- [200] *Muon reconstruction efficiency in reprocessed 2010 LHC proton-proton collision data recorded with the ATLAS detector*, Tech. Rep. ATLAS-CONF-2011-063, CERN, Geneva, Apr, 2011. [83](#)
- [201] J. T. Linnemann, *Measures of Significance in HEP and Astrophysics*, arXiv:physics/0312059. [86](#)

- [202] C. G. Lester, M. A. Parker, and M. J. White, *Determining SUSY model parameters and masses at the LHC using cross-sections, kinematic edges and other observables*, *JHEP* **0601** (2006) 080, [arXiv:hep-ph/0508143 \[hep-ph\]](https://arxiv.org/abs/hep-ph/0508143). 88
- [203] E. Gross and O. Vitells, *Trial factors for the look elsewhere effect in high energy physics*, *Eur.Phys.J.* **C70** (2010) 525–530, [arXiv:1005.1891 \[physics.data-an\]](https://arxiv.org/abs/1005.1891). 107
- [204] S. Holm, *A Simple Sequentially Rejective Multiple Test Procedure*, Scandinavian Journal of Statistics **6** no. 2, (1979) pp. 65–70.
<http://www.jstor.org/stable/4615733>. 107
- [205] J. Tukey, *The future of data analysis*, *Ann. Math. Stat.* **33** (1) (1962). 108
- [206] R. C. Gray, C. Kilic, M. Park, S. Somalwar, and S. Thomas, *Backgrounds To Higgs Boson Searches from $W\gamma^*l\nu l(l)$ Asymmetric Internal Conversion*, [arXiv:1110.1368 \[hep-ph\]](https://arxiv.org/abs/1110.1368). 112
- [207] A. Martin, W. Stirling, R. Thorne, and G. Watt, *Parton distributions for the LHC*, *Eur.Phys.J.* **C63** (2009) 189–285, [arXiv:0901.0002 \[hep-ph\]](https://arxiv.org/abs/0901.0002). 119
- [208] S. Alekhin, S. Alioli, R. D. Ball, V. Bertone, J. Blumlein, et al., *The PDF4LHC Working Group Interim Report*, [arXiv:1101.0536 \[hep-ph\]](https://arxiv.org/abs/1101.0536). 119
- [209] H.-L. Lai, M. Guzzi, J. Huston, Z. Li, P. M. Nadolsky, et al., *New parton distributions for collider physics*, *Phys.Rev.* **D82** (2010) 074024, [arXiv:1007.2241 \[hep-ph\]](https://arxiv.org/abs/1007.2241). 119
- [210] ATLAS Collaboration, *Luminosity Determination in pp Collisions at $\sqrt{s} = 7$ TeV using the ATLAS Detector in 2011*, ATLAS-CONF-2011-116.
<http://cdsweb.cern.ch/record/1376384>. 121
- [211] ATLAS Collaboration, G. Aad et al., *Luminosity Determination in pp Collisions at $\sqrt{s}=7$ TeV Using the ATLAS Detector at the LHC*, *Eur.Phys.J.* **C71** (2011) 1630, [arXiv:1101.2185 \[hep-ex\]](https://arxiv.org/abs/1101.2185). 121
- [212] M. Kramer, A. Kulesza, R. van der Leeuw, M. Mangano, S. Padhi, et al., *Supersymmetry production cross sections in pp collisions at $\sqrt{s} = 7$ TeV*, [arXiv:1206.2892 \[hep-ph\]](https://arxiv.org/abs/1206.2892). 124, 147
- [213] P. Auster, *The New York Trilogy*. Faber and Faber, 1987. 129

- [214] N. Reid, *Likelihood Inference in the Presence of Nuisance Parameters*, eConf **C030908** (2003) THAT001. [142](#)
- [215] A. L. Read, *Modified frequentist analysis of search results (the CL_s method)*,. [144](#)
- [216] A. L. Read, *Presentation of search results: the CL_s technique*, Journal of Physics G: Nuclear and Particle Physics **28** no. 10, (2002) 2693.
<http://stacks.iop.org/0954-3899/28/i=10/a=313>. [144](#)
- [217] G. Cowan, K. Cranmer, E. Gross, and O. Vitells, *Asymptotic formulae for likelihood-based tests of new physics*, European Physical Journal C **71** (2011) 1554, [arXiv:1007.1727 \[physics.data-an\]](https://arxiv.org/abs/1007.1727). [144](#)
- [218] R. D. Cousins, *Annotated Bibliography of Some Papers on Combining Significances or p-values*, ArXiv e-prints (2007), [arXiv:0705.2209 \[physics.data-an\]](https://arxiv.org/abs/0705.2209). [146](#)
- [219] B. Delaunay, *Sur la sphère vide.*, Bull. Acad. Sci. URSS, VII. Ser. **1934** no. 6, (1934) 793–800. [147](#)
- [220] *Search for supersymmetry in events with four or more leptons in 21fb^{-1} of pp collisions at $\sqrt{s} = 8\text{ TeV}$ with the ATLAS detector*, Tech. Rep. ATLAS-CONF-2013-036, CERN, Geneva, Mar, 2013. [147](#)
- [221] *Search for supersymmetry in final states with jets, missing transverse momentum and a Z boson at $\sqrt{s} = 8\text{ TeV}$ with the ATLAS detector*, Tech. Rep. ATLAS-CONF-2012-152, CERN, Geneva, Nov, 2012. [147](#)
- [222] J. E. Kim, *A Review on axions and the strong CP problem*, AIP Conf.Proc. **1200** (2010) 83–92, [arXiv:0909.3908 \[hep-ph\]](https://arxiv.org/abs/0909.3908). [156](#)
- [223] M. Buchkremer, G. Cacciapaglia, A. Deandrea, and L. Panizzi, *Model Independent Framework for Searches of Top Partners*, Nucl.Phys. **B876** (2013) 376–417, [arXiv:1305.4172 \[hep-ph\]](https://arxiv.org/abs/1305.4172). [156](#)
- [224] A. Choudhury and A. Datta, *Neutralino dark matter confronted by the LHC constraints on Electroweak SUSY signals*, JHEP **09** (2013) 119, [arXiv:1305.0928 \[hep-ph\]](https://arxiv.org/abs/1305.0928). [156](#)
- [225] M. W. Cahill-Rowley, J. L. Hewett, A. Ismail, and T. G. Rizzo, *More Energy, More Searches, but the pMSSM Lives On*, Phys.Rev. **D88** (2013) 035002, [arXiv:1211.1981 \[hep-ph\]](https://arxiv.org/abs/1211.1981). [156](#)